

DISSERTATION

NUMERICAL SIMULATIONS OF BINARY MIXTURES UNDER GRAVITY
DEPOSITION USING THE DISCRETE ELEMENT METHOD

Submitted by

Chao Jiang

Department of Civil and Environmental Engineering

In partial fulfillment of the requirements

For the Degree of Doctor of Philosophy

Colorado State University

Fort Collins, Colorado

Summer 2021

Doctoral Committee:

Advisor: Paul Heyliger

Christopher Bareither
Bruce R. Ellingwood
Karan Venayagamoorthy
Kirk McGilvray

Copyright by Chao Jiang 2021

All Rights Reserved

ABSTRACT

NUMERICAL SIMULATIONS OF BINARY MIXTURES UNDER GRAVITY DEPOSITION USING THE DISCRETE ELEMENT METHOD

Binary granular mixtures are frequently used in manufacturing, geotechnical engineering, and construction. Applications for these materials include dams, roads, and railway embankments. The mixing process requires dealing with particles with varying sizes and properties, and the complex composite nature of these mixtures can bring unpredictable results in overall performance. At present, there are no specifications for mixing these materials that can be used to quantify the levels of mixing and give estimates of the overall bulk properties. In this study, the Discrete Element Method (DEM) is used to examine the mechanics of the mixing process and give guidelines on how to achieve a well-mixed aggregate.

A comprehensive non-linear visco-elastic damping collision model was developed to better represent the interactions between two dissimilar particles. A general Hertz model was applied for describing the normal force but a refined non-linear spring model was generated to imitate the friction force behavior without having to consider the entire loading history. A transition zone revealing the interactions between static and dynamic friction forces was shown in our numerical results. A moment resistance model was also added to capture the behavior of particle surface asperities and the damping force was calculated using relative motion. An alternative condition was applied to determine the end of a collision. Excellent agreement was found with well-established benchmark solutions and new results are also provided for future comparisons.

Using this new DEM model, the mixing process of binary unbonded particles was studied using the effects of the number and position of geometric mixing obstacles and the number of mixing iterations. It was found that the mixing degree can be best quantified by measuring the spatial variation of the volume ratio ϕ_v . It was also found that small adjustments in the geometric position of the mixing obstacles could have a significant impact on the final mixing parameters. Surprisingly, the results indicate that two mixing iterations provided almost identical levels of mixing regardless of the number and nature of mixing obstacles. Estimates of the bulk elastic constants were provided and showed a high level of anisotropy as measured by the Poisson ratios for the horizontal versus vertical planes of the control volume.

Particle crushing is a typical characteristic of many granular materials and can influence the mixing process, and it is possible to model non-particulate materials by bonding individual spheres together. The particle interactions and possibly impact with mixing barriers can result in the fracture of these solids as the allowable bond strength is exceeded. Therefore, the strength of the bond between individual particles that can be part of the mixing process is a critical parameter. The parallel bond model of Potyondy and Cundall (2004) was extended with the present DEM model was used to study the effects of bond strength on the mixing and mechanical properties of binary mixtures. Three types of particle blocks were studied for this purpose: unbonded, weakly bonded, and strongly bonded particles. The bonded particles result in a wider range of reflection angles as the particles interact with geometric mixers and simultaneously change and improve the level of mixing.

Overall, these simulations serve to established specific guidelines and provide a basis for field-level mixing operations. They also provide some levels of expectation for the final

mixing and bulk elastic behavior for the final aggregates.

ACKNOWLEDGMENTS

I would like to thank all committee members who help me complete this work. A special thanks to my advisor Dr. Paul R. Heyliger for his careful instruction, patient teaching, and constant supports. All his advice not only helps me finish this research, but also illuminates my way forward. Will make me benefit for life. Another special thanks goes to Dr. Christopher Bareither for working to acquire the funding that supported me financially while completing this research and his effort on revising my dissertation.

TABLE OF CONTENTS

ABSTRACT.....	ii
ACKNOWLEDGMENTS.....	v
LIST OF TABLES.....	ix
LIST OF FIGURES.....	x
CHAPTER 1: EXECUTIVE SUMMARY.....	1
1.1 Introduction.....	1
1.2 Problem Statement.....	3
1.3 Major Findings.....	6
CHAPTER 2: DEM MODEL AND THEORY.....	9
2.1 Particle Types.....	10
2.1.1 Sphere particles.....	11
2.1.2 Crushable aggregates.....	12
2.2 Force Detection.....	13
2.3 Force Calculation.....	14
2.3.1 Normal contact response.....	15
2.3.2 Tangential contact response.....	17
2.3.3 Rolling resistance behavior.....	21
2.3.4 Bond/cement behavior.....	23
2.4 Kinematic Motion.....	25
2.4.1 Acceleration calculation.....	25
2.4.2 Position updating.....	26
2.5 Damping Effect.....	27
2.5.1 Mass damping.....	27
2.5.2 Local non-viscous damping.....	29
2.5.3 Viscous damping.....	30
2.6 Time Increments.....	32
2.7 Boundary Conditions.....	33

2.7.1 Finite rigid wall boundary conditions.....	34
2.7.2 Rigid moving wall boundary conditions.....	35
2.7.3 Periodic inlet boundary conditions.....	36
2.8 Post-analysis.....	37
2.8.1 Identify the mixing parameters of a mixture.....	38
2.8.2 Evaluate the effective elastic properties.....	41
CHAPTER 3: A MODIFICATION OF NON-LINEAR VISCO-ELASTIC DAMPING MOD- ELS APPLIED IN DISCRETE ELEMENT SIMULATIONS.....	55
3.1 Overview.....	55
3.2 Introduction.....	56
3.3 DEM model and Description.....	59
3.3.1 Normal contact model.....	59
3.3.2 Tangential contact model.....	60
3.3.3 Rolling resistant model.....	62
3.3.4 Viscous damping model.....	63
3.4 Investigation of Tangential force response.....	65
3.4.1 Alternative condition for checking the end of a collision.....	66
3.4.2 Tangential force-displacement response.....	67
3.4.3 Transition between stick and sliding regions.....	72
3.5 Numerical results for Benchmark tests.....	73
3.6 Summary and Conclusions.....	81
CHAPTER 4: MIXING PROPERTIES OF BINARY GRANULAR MIXTURES UNDER GRAVITY DEPOSITION.....	116
4.1 Overview.....	116
4.2 Introduction.....	117
4.3 DEM model Description.....	119
4.3.1 Contact models.....	120
4.3.2 Boundary conditions.....	123
4.3.3 Post-mixing analysis.....	124
4.4 Sample Generation.....	128

4.4.1	Number of obstacles.....	131
4.4.2	Obstacle position.....	132
4.4.3	Affect of mixing iterations in filling.....	133
4.5	Results and Discussion.....	133
4.5.1	Mixing parameters.....	134
4.5.2	Effective elastic properties.....	137
4.6	Summary and Conclusions.....	138
CHAPTER 5: MIXING PROPERTIES OF BINARY GRANULAR MIXTURES WITH BONDED PARTICLES.....		159
5.1	Overview.....	159
5.2	Introduction.....	160
5.3	DEM model Description.....	163
5.3.1	Contact behavior.....	163
5.3.2	Bond behavior.....	165
5.3.3	Post-analysis.....	167
5.4	Sample Generation.....	169
5.5	Results and Discussion.....	175
5.5.1	Internal mixing degree.....	175
5.5.2	Effective elastic properties.....	178
5.6	Summary and Conclusions.....	180
CHAPTER 6: SUMMARY OF THE DISSERTATION AND FUTURE STUDIES.....		206
6.1	Summary and Conclusions.....	206
6.2	Future Research.....	208
6.2.1	An advanced study of the proposed Discrete Element Model.....	208
6.2.2	Effect of particle rearrangement on mixing properties.....	209
6.2.3	A modification of the parallel bond model.....	209
6.2.4	The quantitative analysis of bond strength on mixing properties of binary mixtures.....	210
REFERENCES.....		214

LIST OF TABLES

Table 3-1: Summary of Benchmark test problems (Chung and Ooi, 2011).....	83
Table 3-2: DEM input parameters of benchmark tests (Chung and Ooi, 2011).....	84
Table 4-1: Summary of input parameters.....	140
Table 4-2: Point locations for measuring mixing parameters and the equivalent elastic properties.....	140
Table 4-3: The mean value and related standard deviation of the effective elastic modulus E (N/m^2) for each model after different mixing iterations.....	141
Table 4-4: The mean value and related standard deviation of the effective Poisson ratio ν_{xy} for each model after different mixing iterations.....	141
Table 4-5: The mean value and related standard deviation of the effective Poisson ratio ν_{xz} or ν_{yz} for each model after different mixing iterations.....	142
Table 5-1: Summary of input parameters.....	182
Table 5-2: Point locations for measuring mixing parameters and the equivalent elastic properties.....	183
Table 5-3: The mean values and the related standard deviations of mixing ratios measured at the middle clips for the present six models in each group.....	183
Table 5-4: The mean values and the related standard deviations of equivalent elastic modulus E (N/m^2) measured at the middle clips for the present six models in each group.....	184
Table 5-5: The mean values and the related standard deviations of equivalent Poisson ratios measured at the middle clips for the present six models in each group.....	185

LIST OF FIGURES

Figure 1-1: A figure showing the existing mixing process in the industry field and a numerical simulation.....	4
Figure 2-1: A flow chart showing sequence of calculations in a DEM simulation.....	45
Figure 2-2: Concept of simulating crushable particles using bonded aggregates.....	46
Figure 2-3: A contact detection using “binning algorithm”.....	46
Figure 2-4: Force-displacement responses for normal contact model.....	47
Figure 2-5: The deviation of contact area respect to tangential force.....	47
Figure 2-6: The decompose of calculating the relative tangential velocity.....	48
Figure 2-7: Force-displacement response for tangential contact model.....	48
Figure 2-8: A figure shows unbalance distribution of stresses over the contact area and the related relative rotational motions.....	49
Figure 2-9: Force-displacement response for rolling resistance model.....	50
Figure 2-10: Cement behavior for bonded aggregates.....	50
Figure 2-11: The scheme giving the dynamic equation at the mass center of the contact system.....	51
Figure 2-12: Condition for checking effective contacts within the finite rigid walls.....	51
Figure 2-13: An example illustrating the application of rigid moving walls in 2D biaxial compression tests.....	52
Figure 2-14: A scheme showing periodic boundary condition in 2D (O’Sullivan, 2011).....	52
Figure 2-15: Particle behavior for periodic boundary condition in 1D.....	53
Figure 2-16: Application of periodic boundary condition for simulating inlet/entrance behavior.....	53
Figure 2-17: A scheme illustrating the algorithm of area calculation.....	54
Figure 2-18: A flow chart illustrating sequence of calculations in simulated compression tests.....	54
Figure 3-1: Normal force-time response in arbitrary units as a function of different damping ratios (Luding, 1998).....	85
Figure 3-2: Evolution of tangential forces during the impact at intermediate angle of inci-	

dence $\psi_1 = 1.2$ for spheres of various radii of gyration χ (Maw et al., 1976).... 85

Figure 3-3: Evolution of tangential forces during different impact regimes for a combination of the normal model by Tomas and a tangential force calculated from the model by Brilliantov: (a) nearly frontal contact at a small impact angle and (b) grazing impact at larger impact angle. (Kruggel-Emden et al., 2008)..... 86

Figure 3-4: Evolution of tangential forces during different impact regimes for a combination of the normal model by Tomas and a tangential force calculated from an unconstrained spring limited by the Coulomb condition: (a) small impact angle, (b) intermediate impact angle, and (c) large impact angle. (Kruggel-Emden et al., 2008)..... 86

Figure 3-5: Evolution of tangential forces during different impact regimes for a combination of the normal model by Tomas and a tangential force calculated from a spring according to Brendel and Dippel (1998): (a) Small impact angle, (b) intermediate impact angle and (c) large impact angle. (Kruggel-Emden et al., 2008)..... 86

Figure 3-6: Evolution of tangential forces during different impact regimes for a combination of the normal model by Tomas and a tangential force calculated from a constrained spring limited by the Coulomb condition: (a) Small impact angle, (b) intermediate impact angle and (c) large impact angle. (Kruggel-Emden et al., 2008)..... 87

Figure 3-7: Evolution of tangential forces during different impact regimes for a combination of the extended linear spring damping normal model and a tangential force calculated from an unconstrained spring limited by the Coulomb condition. Impact angle increases from (a) to (f) (Kruggel-Emden et al., 2008)..... 87

Figure 3-8: Evolution of tangential forces during different impact regimes for a combination of the extended linear spring damping normal model and a tangential force calculated from a constrained spring limited by the Coulomb condition. Impact angle increases from (a) to (e) (Kruggel-Emden et al., 2008)..... 88

Figure 3-9: Evolution of tangential forces during the impact with different impact angles by using the proposed models and the input parameters from Benchmark Test 6. Results are checked at $\omega = 0.175, 2, 4,$ and 8 rad/s..... 89

Figure 3-10: Schematic picture of the velocity ratio Ψ_1 versus Ψ_2 for the different force laws (Luding, 1998).....	90
Figure 3-11: An example showing a schematic picture of the velocity ratio Ψ_1 versus Ψ_2 from the presented numerical model.....	90
Figure 3-12: The definition of positive directions and symbols of linear and angular velocities before and after impact (Chung and Ooi, 2011).....	91
Figure 3-13: Test 1(Prior study): elastic normal impact of two identical spheres: (a) force-displacement curve; (b) force-time curve.....	92
Figure 3-14: Test 1(Present DEM): elastic normal impact of two identical spheres: (a) force-displacement curve; (b) force-time curve.....	93
Figure 3-15: Test 2(Prior study): elastic normal impact of a sphere with a rigid plane: (a) force-displacement curve; (b) force-time curve.....	94
Figure 3-16: Test 2(Present DEM): elastic normal impact of a sphere with a rigid plane: (a) force-displacement curve; (b) force-time curve.....	95
Figure 3-17: Test 3(Prior study): comparison between simulated velocity ratio and input value of the restitution coefficient.....	96
Figure 3-18: Test 3(Present DEM): comparison between simulated velocity ratio and input value of the restitution coefficient.....	96
Figure 3-19: Test 4(Prior study): simulated, theoretical and experimental tangential restitution coefficient e for varying incident angles θ	97
Figure 3-20: Test 4(Present DEM): simulated, theoretical and experimental tangential restitution coefficient e for varying incident angles θ	97
Figure 3-21: Test 4(Prior study): simulated, theoretical and experimental post-collision angular velocity ω'_1 for varying incident angles θ	98
Figure 3-22: Test 4(Present DEM): simulated, theoretical and experimental post-collision angular velocity ω'_1 for varying incident angles θ	98
Figure 3-23: Test 4(Prior study): simulated, theoretical and experimental rebound angles φ for varying incident angles θ	99
Figure 3-24: Test 4(Present DEM): simulated, theoretical and experimental rebound angles φ for varying incident angles θ	99

Figure 3-25: Test 5(Prior study): oblique impact for varying tangential velocities: (a) normalized recoil angle versus normalized incident angle; (b) normalized post-collision angular velocity versus normalized incident angle..... 100

Figure 3-26: Test 5(Present DEM): oblique impact for varying tangential velocities: (a) normalized recoil angle versus normalized incident angle; (b) normalized post-collision angular velocity versus normalized incident angle..... 101

Figure 3-27: Test 6(Prior study): simulated and theoretical tangential restitution coefficient β versus the quantity $[3.5\mu(1 + e_n)\frac{V_n}{V_s}]$ 102

Figure 3-28: Test 6(Present DEM): simulated and theoretical tangential restitution coefficient β versus the quantity $[3.5\mu(1 + e_n)\frac{V_n}{V_s}]$ 102

Figure 3-29: Test 6(Prior study): simulated and theoretical tangent of recoil angle $\frac{V'_{st}}{V'_{cn}}$ for varying tangent of incident angles $\frac{V_s}{V_n}$ 103

Figure 3-30: Test 6(Present DEM): simulated and theoretical tangent of recoil angle $\frac{V'_{st}}{V'_{cn}}$ for varying tangent of incident angles $\frac{V_s}{V_n}$ 103

Figure 3-31: Test 6(Present DEM): simulated tangential restitution coefficient β varying as a function of the quantity $[3.5\mu(1 + e_n)\frac{V_n}{V_s}]$ with different restitution coefficients ε respect to Al. alloy..... 104

Figure 3-32: Test 6(Present DEM): simulated tangent of recoil angle $\frac{V'_{st}}{V'_{cn}}$ versus various tangent of incident angles $\frac{V_s}{V_n}$ with different restitution coefficients ε respect to Al. alloy..... 104

Figure 3-33: Test 6(Present DEM): simulated tangential restitution coefficient β varying as a function of the quantity $[3.5\mu(1 + e_n)\frac{V_n}{V_s}]$ with different restitution coefficients ε respect to Nylon..... 105

Figure 3-34: Test 6(Present DEM): simulated tangent of recoil angle $\frac{V'_{st}}{V'_{cn}}$ versus various tangent of incident angles $\frac{V_s}{V_n}$ with different restitution coefficients ε respect to Nylon..... 105

Figure 3-35: Test 7(Prior study): post-collision tangential velocity at the mass center for varying pre-collision angular velocities..... 106

Figure 3-36: Test 7(Present DEM): post-collision tangential velocity at the mass center for varying pre-collision angular velocities..... 106

Figure 3-37: Test 7(Prior study): post-collision angular velocity for varying pre-collision angular velocities.....	107
Figure 3-38: Test 7(Present DEM):post-collision angular velocity for varying pre-collision angular velocities.....	107
Figure 3-39: Test 8(Prior study): Al.alloy, simulated and theoretical tangential restitution coefficient β versus quantity $[3.5\mu(1 + e_n)\frac{V_n}{V_s}]$	108
Figure 3-40: Test 8(Present DEM): Al.alloy, simulated and theoretical tangential restitution coefficient β versus quantity $[3.5\mu(1 + e_n)\frac{V_n}{V_s}]$	108
Figure 3-41: Test 8(Prior study): Al.alloy, simulated and theoretical tangent of recoil angle $\frac{V'_{st}}{V'_{cn}}$ versus tangent of incident angle $\frac{V_s}{V_n}$ for the small sphere.....	109
Figure 3-42: Test 8(Present DEM): Al.alloy, simulated and theoretical tangent of recoil angle $\frac{V'_{st}}{V'_{cn}}$ versus tangent of incident angle $\frac{V_s}{V_n}$ for the small sphere.....	109
Figure 3-43: Test 8(Prior study): Nylon, simulated and theoretical tangential restitution coefficient β versus quantity $[3.5\mu(1 + e_n)\frac{V_n}{V_s}]$	110
Figure 3-44: Test 8(Present DEM): Nylon, simulated and theoretical tangential restitution coefficient β versus quantity $[3.5\mu(1 + e_n)\frac{V_n}{V_s}]$	110
Figure 3-45: Test 8(Prior study): Nylon, simulated and theoretical tangent of recoil angle $\frac{V'_{st}}{V'_{cn}}$ versus tangent of incident angle $\frac{V_s}{V_n}$ for the small sphere.....	111
Figure 3-46: Test 8(Present DEM): Nylon, simulated and theoretical tangent of recoil angle $\frac{V'_{st}}{V'_{cn}}$ versus tangent of incident angle $\frac{V_s}{V_n}$ for the small sphere.....	111
Figure 3-47: Test 8(Present DEM): simulated tangential restitution coefficient β varying as a function of the quantity $[3.5\mu(1 + e_n)\frac{V_n}{V_s}]$ with different restitution coefficients ε respect to Al. alloy for Case A.....	112
Figure 3-48: Test 8(Present DEM): simulated tangent of recoil angle $\frac{V'_{st}}{V'_{cn}}$ versus various tangent of incident angles $\frac{V_s}{V_n}$ with different restitution coefficients ε respect to Al. alloy for Case A.....	112
Figure 3-49: Test 8(Present DEM): simulated tangential restitution coefficient β varying as a function of the quantity $[3.5\mu(1 + e_n)\frac{V_n}{V_s}]$ with different restitution coefficients ε respect to Al. alloy for Case B.....	113
Figure 3-50: Test 8(Present DEM): simulated tangent of recoil angle $\frac{V'_{st}}{V'_{cn}}$ versus various	

tangent of incident angles $\frac{V_s}{V_n}$ with different restitution coefficients ε respect to Al. alloy for Case B.....	113
Figure 3-51: Test 8(Present DEM): simulated tangential restitution coefficient β varying as a function of the quantity $[3.5\mu(1 + e_n)\frac{V_n}{V_s}]$ with different restitution coefficients ε respect to Nylon for Case A.....	114
Figure 3-52: Test 8(Present DEM): simulated tangent of recoil angle $\frac{V'_{st}}{V'_{cn}}$ versus various tangent of incident angles $\frac{V_s}{V_n}$ with different restitution coefficients ε respect to Nylon for Case A.....	114
Figure 3-53: Test 8(Present DEM): simulated tangential restitution coefficient β varying as a function of the quantity $[3.5\mu(1 + e_n)\frac{V_n}{V_s}]$ with different restitution coefficients ε respect to Nylon for Case B.....	115
Figure 3-54: Test 8(Present DEM): simulated tangent of recoil angle $\frac{V'_{st}}{V'_{cn}}$ versus various tangent of incident angles $\frac{V_s}{V_n}$ with different restitution coefficients ε respect to Nylon for Case B.....	115
Figure 4-1: A scheme illustrating the algorithm of area calculation for 2D virtual samples.....	143
Figure 4-2: The application of cylindrical mixers helps particle dispersion in space. By changing the trajectory of the granular flow, different particles have more chance to interact with each other and promote interacting collisions in particles.....	144
Figure 4-3: Model 1: A filling under pure gravity deposition was investigated at specific times: (a) t=1 s, (b) t=2 s, (c) t=3 s, (d) t=6 s, and (e) t=11 s; and (f) a middle clip showing the final stacking state after mixed with the 1 st iteration.....	145
Figure 4-4: Model 2: A filling under gravity deposition with one obstacle placed at locations x=0.5 m and z=1.2 m was investigated at specific times: (a) t=1 s, (b) t=2 s, (c) t=3 s, (d) t=6 s, and (e) t=11 s; and (f) a middle clip showing the final stacking state after mixed with the 1 st iteration.....	146
Figure 4-5: Model 3: A filling under gravity deposition with one obstacle placed at locations x=0.3 m and z=1.5 m was investigated at specific times: (a) t=1 s, (b) t=2 s, (c) t=3 s, (d) t=6 s, and (e) t=11 s; and (f) a middle clip showing the final stacking state after mixed with the 1 st iteration.....	147

Figure 4-6: Model 4: A filling under gravity deposition with one obstacle placed at locations $x=0.4$ m and $z=1.2$ m was investigated at specific times: (a) $t=1$ s, (b) $t=2$ s, (c) $t=3$ s, (d) $t=6$ s, and (e) $t=11$ s; and (f) a middle clip showing the final stacking state after mixed with the 1 st iteration.....	148
Figure 4-7: Model 5: A filling under gravity deposition with two obstacles placed at locations $x=0.3$ m & $z=1.5$ m and $x=0.7$ m & $z=1.2$ m was investigated at specific times: (a) $t=1$ s, (b) $t=2$ s, (c) $t=3$ s, (d) $t=6$ s, and (e) $t=11$ s; and (f) a middle clip showing the final stacking state after mixed with the 1 st iteration.....	149
Figure 4-8: Model 6: A filling under gravity deposition with two obstacles placed at locations $x=0.3$ m & $z=1.5$ m and $x=0.6$ m & $z=1.2$ m was investigated at specific times: (a) $t=1$ s, (b) $t=2$ s, (c) $t=3$ s, (d) $t=6$ s, and (e) $t=11$ s; and (f) a middle clip showing the final stacking state after mixed with the 1 st iteration.....	150
Figure 4-9: Middle clips showing the final stacking states of the previously studied 6 models after re-filling with the 2 nd iteration.....	151
Figure 4-10: Different types of influence area.....	152
Figure 4-11: Mixing parameters measured in nine spherical regions for the presented six models after filling with the 1 st iteration.....	153
Figure 4-12: Mixing parameters measured in nine spherical regions for the presented six models after re-filling with the 2 nd iteration.....	154
Figure 4-13: The effective elastic modulus E measured in nine cubic regions for the presented six models after mixing with the 1 st iteration.....	155
Figure 4-14: The distribution of the calculated effective elastic properties E and ν for each model as mixing with the 1 st iteration.....	156
Figure 4-15: The effective elastic modulus E measured in nine cubic regions for the presented six models after mixing with the 2 nd iteration.....	157
Figure 4-16: The distribution of the calculated effective elastic properties E and ν for each model as mixing with the 2 nd iteration.....	158
Figure 5-1: Force-displacement behavior of the presented DEM model for simulating crushable aggregates.....	186
Figure 5-2: A planar cut showing the extended version of using Bardet and Proubet (1991)	

algorithm to calculate the volume ratio ϕ_v in 3D samples.....	187
Figure 5-3: A planar cut showing our strategy for doing element compression tests. Detected points are distributed within the final aggregates. Cubic regions with the detected points placed at the center are used for measuring. Each cubic region is surrounded by five rigid walls, while the top one is movable. The white arrows illustrate the location for applied the uniaxial stress.....	187
Figure 5-4: The front-view, side-view and a 3D view of particles in the repeated section. Crushable particles are bonded with 32 basic spheres where white short lines indicate the pattern of connecting bonds.....	188
Figure 5-5: Group 1 (Model 1): A filling without applying crushable particles was simulated with unbonded spheres and under pure gravity deposition. The mixing process was investigated at specific times: (a) $t=1$ s, (b) $t=3$ s, (c) $t=9$ s; and (d) a middle clip showing the final stacking state.....	189
Figure 5-6: Group 1 (Model 2): A filling without applying crushable particles was simulated with unbonded spheres and under gravity deposition with one obstacle placed at locations $x=0.5$ m and $z=1.2$ m. The mixing process was investigated at specific times: (a) $t=1$ s, (b) $t=3$ s, (c) $t=9$ s; and (d) a middle clip showing the final stacking state.....	189
Figure 5-7: Group 1 (Model 3): A filling without applying crushable particles was simulated with unbonded spheres and under gravity deposition with one obstacle placed at locations $x=0.3$ m and $z=1.5$ m. The mixing process was investigated at specific times: (a) $t=1$ s, (b) $t=3$ s, (c) $t=9$ s; and (d) a middle clip showing the final stacking state.....	190
Figure 5-8: Group 1 (Model 4): A filling without applying crushable particles was simulated with unbonded spheres and under gravity deposition with one obstacle placed at locations $x=0.4$ m and $z=1.2$ m. The mixing process was investigated at specific times: (a) $t=1$ s, (b) $t=3$ s, (c) $t=9$ s; and (d) a middle clip showing the final stacking state.....	190
Figure 5-9: Group 1 (Model 5): A filling without applying crushable particles was simulated with unbonded spheres and under gravity deposition with two obstacles placed	

at locations $x=0.3$ m & $z=1.5$ m and $x=0.7$ m & $z=1.2$ m, respectively. The mixing process was investigated at specific times: (a) $t=1$ s, (b) $t=3$ s, (c) $t=9$ s; and (d) a middle clip showing the final stacking state..... 191

Figure 5-10: Group 1 (Model 6): A filling without applying crushable particles was simulated with unbonded spheres and under gravity deposition with two obstacles placed at locations $x=0.3$ m & $z=1.5$ m and $x=0.6$ m & $z=1.2$ m, respectively. The mixing process was investigated at specific times: (a) $t=1$ s, (b) $t=3$ s, (c) $t=9$ s; and (d) a middle clip showing the final stacking state..... 191

Figure 5-11: Group 2 (Model 1): A filling with crushable particles which was simulated with bonded aggregates using weak bonds and under pure gravity deposition. The mixing process was investigated at specific times: (a) $t=1$ s, (b) $t=3$ s, (c) $t=9$ s; and (d) a middle clip showing the final stacking state..... 192

Figure 5-12: Group 2 (Model 2): A filling with crushable particles which was simulated with bonded aggregates using weak bonds and under gravity deposition with one obstacle placed at locations $x=0.5$ m and $z=1.2$ m. The mixing process was investigated at specific times: (a) $t=1$ s, (b) $t=3$ s, (c) $t=9$ s; and (d) a middle clip showing the final stacking state..... 192

Figure 5-13: Group 2 (Model 3): A filling with crushable particles which was simulated with bonded aggregates using weak bonds and under gravity deposition with one obstacle placed at locations $x=0.3$ m and $z=1.5$ m. The mixing process was investigated at specific times: (a) $t=1$ s, (b) $t=3$ s, (c) $t=9$ s; and (d) a middle clip showing the final stacking state..... 193

Figure 5-14: Group 2 (Model 4): A filling with crushable particles which was simulated with bonded aggregates using weak bonds and under gravity deposition with one obstacle placed at locations $x=0.4$ m and $z=1.2$ m. The mixing process was investigated at specific times: (a) $t=1$ s, (b) $t=3$ s, (c) $t=9$ s; and (d) a middle clip showing the final stacking state..... 193

Figure 5-15: Group 2 (Model 5): A filling with crushable particles which was simulated with bonded aggregates using weak bonds and under gravity deposition with two obstacles placed at locations $x=0.3$ m & $z=1.5$ m and $x=0.7$ m & $z=1.2$ m,

respectively. The mixing process was investigated at specific times: (a) $t=1$ s, (b) $t=3$ s, (c) $t=9$ s; and (d) a middle clip showing the final stacking state.... 194

Figure 5-16: Group 2 (Model 6): A filling with crushable particles which was simulated with bonded aggregates using weak bonds and under gravity deposition with two obstacles placed at locations $x=0.3$ m & $z=1.5$ m and $x=0.6$ m & $z=1.2$ m, respectively. The mixing process was investigated at specific times: (a) $t=1$ s, (b) $t=3$ s, (c) $t=9$ s; and (d) a middle clip showing the final stacking state.... 194

Figure 5-17: Group 3 (Model 1): A filling with crushable particles which was simulated with bonded aggregates using strong bonds and under pure gravity deposition. The mixing process was investigated at specific times: (a) $t=1$ s, (b) $t=3$ s, (c) $t=9$ s; and (d) a middle clip showing the final stacking state..... 195

Figure 5-18: Group 3 (Model 2): A filling with crushable particles which was simulated with bonded aggregates using strong bonds and under gravity deposition with one obstacle placed at locations $x=0.5$ m and $z=1.2$ m. The mixing process was investigated at specific times: (a) $t=1$ s, (b) $t=3$ s, (c) $t=9$ s; and (d) a middle clip showing the final stacking state..... 195

Figure 5-19: Group 3 (Model 3): A filling with crushable particles which was simulated with bonded aggregates using strong bonds and under gravity deposition with one obstacle placed at locations $x=0.3$ m and $z=1.5$ m. The mixing process was investigated at specific times: (a) $t=1$ s, (b) $t=3$ s, (c) $t=9$ s; and (d) a middle clip showing the final stacking state..... 196

Figure 5-20: Group 3 (Model 4): A filling with crushable particles which was simulated with bonded aggregates using strong bonds and under gravity deposition with one obstacle placed at locations $x=0.4$ m and $z=1.2$ m. The mixing process was investigated at specific times: (a) $t=1$ s, (b) $t=3$ s, (c) $t=9$ s; and (d) a middle clip showing the final stacking state..... 196

Figure 5-21: Group 3 (Model 5): A filling with crushable particles which was simulated with bonded aggregates using strong bonds and under gravity deposition with two obstacles placed at locations $x=0.3$ m & $z=1.5$ m and $x=0.7$ m & $z=1.2$ m, respectively. The mixing process was investigated at specific times: (a) $t=1$ s,

	(b) t=3 s, (c) t=9 s; and (d) a middle clip showing the final stacking state....	197
Figure 5-22:	Group 3 (Model 6): A filling with crushable particles which was simulated with bonded aggregates using strong bonds and under gravity deposition with two obstacles placed at locations $x=0.3$ m & $z=1.5$ m and $x=0.6$ m & $z=1.2$ m, respectively. The mixing process was investigated at specific times: (a) t=1 s, (b) t=3 s, (c) t=9 s; and (d) a middle clip showing the final stacking state....	197
Figure 5-23:	An example showing the created void coming from our Model 1 in Group 3.....	198
Figure 5-24:	The distribution of volume ratio ϕ_v in measured regions for Group 1 mixed with unbonded particles.....	199
Figure 5-25:	The distribution of volume ratio ϕ_v in measured regions for Group 2 mixing with crushable particle simulated using weak bonds.....	200
Figure 5-26:	The distribution of volume ratio ϕ_v in measured regions for Group 3 mixing with crushable particle simulated using strong bonds.....	201
Figure 5-27:	The distribution of the effective elastic modulus E measured at the middle clip for the presented three groups.....	202
Figure 5-28:	The distribution of the calculated effective elastic modulus E and two Poisson ratios ν_{xy} and ν_{xz} for six mixing models in Group 1 as mixed with non-crushable particles.....	203
Figure 5-29:	The distribution of the calculated effective elastic modulus E and two Poisson ratios ν_{xy} and ν_{xz} for six mixing models in Group 2 as mixed with crushable particles containing weak bonds.....	204
Figure 5-30:	The distribution of the calculated effective elastic modulus E and two Poisson ratios ν_{xy} and ν_{xz} for six mixing models in Group 3 as mixed with crushable particles containing strong bonds.....	205
Figure 6-1:	A filling under pure gravity deposition bonded with 32 basic spheres using rigid cements is investigated at specific times: (a) t=1 s, (b) t=3 s, (c) t=9 s, and (d) a middle clip showing the final packing state.....	212
Figure 6-2:	A filling under gravity deposition bonded with 32 basic spheres using rigid cements and a obstacle located at $x=0.3$ m & $z=1.5$ m is investigated at specific	

times: (a) $t=1$ s, (b) $t=3$ s, (c) $t=9$ s, and (d) a middle clip showing the final packing state..... 212

Figure 6-3: A modified version for simulating bond behaviors..... 213

CHAPTER 1: EXECUTIVE SUMMARY

1.1 Introduction

Binary granular mixtures are widely used in geotechnical engineering and construction. This idea is attractive as it offers an economic and sustainable method over some traditional approaches but it also brings challenges. The general idea is to mix coarse-grained and fine-grained particles into a new deposit and use this material in specific applications. The complex composite nature of these mixtures influences overall performance and their related evaluations. To solve this problem, large-scale tests have been constructed to explore the mechanical behavior of binary mixtures. Early studies include developing effective mixing methods (Wilson, 2001; Fines et al., 2003; Williams et al., 2003). Advanced techniques makes it possible to evaluate strength properties of the new deposit (Wilson et al., 2000; Wilson et al., 2003). Moreover, field tests with mesoscale column studies in the laboratory were executed to gain a fundamental understanding of mixture response (Wickland et al., 2003; Wickland and Wilson, 2005; Wickland et al., 2006). However, even though traditional experimental methods combined with laboratory tests are conducted as a primary tool for evaluation, this method contains uncertainty and non-reproducibility although limited laboratory- and field-scale tests have proven useful (Khalili et al., 2010; Leduc et al., 2004; Wickland et al., 2010; Jehring and Bareither, 2016). The strength of the mixed deposit is unpredictable and is usually tested only in the final state. In general it has been found that the mechanical properties of binary mixtures highly influenced by the level of mixing. Consequently, attention has been drawn to evaluate the effect of mixing ratio on material properties. This effect is difficult to be explored with many existing methods but many of

these problems can be addressed using a numerical method named the Discrete Element Method (DEM).

The DEM is a numerical modeling approach that is used to study the behavior of individual particles and their interactions. Compared with physical experiments, the simulation process is reproducible. The input parameters can be controlled while eliminating unexpected variables. In contrast with the traditional Finite Element Method (FEM), the DEM method gives a look inside the micro-mechanical interactions and can produce qualitative results at the particle level rather than the bulk solid. Zhou et al. (2015) constructed DEM models to explore the undrained behavior of binary granular mixtures as a function of fines contents. Their analysis indicates that the local isotropy, local anisotropy, sphericity of the Voronoi cells and radial distribution functions are all related to the fraction of smaller particles. The proportion of the sliding contacts was contact-type dependent. The microscopic characteristics and internal stability of binary mixtures were investigated by Nie et al. (2019) including the effects of the size ratio and fine content. After significant examination, the two stability criteria utilized in their model did not satisfied the required features of the micro-field. Consequently, a new stability criterion for evaluating the internal stability was proposed for assessing mixtures.

When the final product is composed of binary materials and used in construction applications, the expected state is to require no large variations of the internal mixing and mechanical properties. This sort of aggregate is also known as being well-distributed. Currently, there are no specifications for determining the level of mixing. Hence the main objective of this research is to study the mixing and mechanical properties of binary granular mixtures, provide quantitative specifications to determine the mixing degree, and propose

effective ways to enhance the mixing properties to meet engineering requirements. There are few, if any, results of this nature in the literature and this research is expected to provide significant knowledge that will supplement results of full-scale field test data.

1.2 Problem Statement

By far, the Discrete Element Method (DEM) has been the most well-established method in the study of particulate media and has more advantages than other traditional approaches. In DEM simulations, dynamic equations are listed at the mass center of individual particles. By summing all acting forces, particle motions are updated at discrete time intervals. The primary differences between various DEM models are rooted in the force-displacement model used to describe the contacting forces between particles or a particle-wall interface. Numerous published models have been used to advance the knowledge base on how particle packings respond to various forcing functions. A number of different models have been used to appropriately simulate the contact forces. To imitate the normal force response, widely used models include the Hertz model (Hertz, 1882), a piecewise elastic-plastic model (Maugis and Pollock, 1984), and Walton and Braun model (Walton and Braun, 1986). Considering the tangential force on the particle, which is more complicated than the normal force, friction forces in the sliding region can be recovered while the behavior of static friction force remains unknown in the dynamic field. Damping force and moment resistance are unresolved and are still under active investigation. Moreover, in practical applications, the combination of those models is multifarious. Regardless of how these models differ, it is crucial that results obtained by DEM simulations are consistent with those obtained by experimental evidence. Therefore, to conduct our further research, we firstly need to develop an accurate

and friendly-used DEM model that can successfully simulate the general mechanical behavior of binary granular mixtures as illustrated in **Fig. 1-1**.



(a) The mixing process

(b) The numerical simulation

Figure 1-1: A figure showing the existing mixing process in the industry field and a numerical simulation

Although binary mixtures have been widely used in various fields in industry, the large local variability of the effective bulk properties the complex composite nature is known to bring unpredictable influences on overall performance. It is reasonable to expect that the optimal mixed aggregate would limit any large variations in mixing and mechanical properties. Yet few studies have appeared to show effective methods to determine the mixing properties of such mixtures. At present, there is no specification that can be used to quantify mixing properties to meet engineering requirements. Through the traditional experimental approaches that contain both uncertainty and non-reproducibility, both stiffness and strength properties are remaining unknown until it is possible to physically test final product. As it occurs, the mixing process is affected by many factors that include but are not limited

to the geometric positions of any mixing obstacles, the number of such obstacles, and the number of times the mixture of particles is cycled through the mixing process. Research into these factors using physical measurements or field tests can be costly. It is also a challenge to determine the effects of different variables on these final deposits. Even though the DEM simulations can help provide information at the particulate level, virtual samples are normally generated by an algorithm that is a simplification and idealization of the actual mixture. Hence, to account for all these effects and provide useful recommendation to assist future studies, it is an urgent to generate an overall binary particle mixing simulation starting from sample generation to the subsequent testing, and finally estimate the mixing and mechanical properties of the final aggregates.

In addition to the mixing process for unbonded spherical particles, it is also true that particle or material breakage is a significant characteristic of many granular materials and cannot be neglected. Particle interactions, or the interactions of other volumes that can be modeled as a collection of particles, can occur during the construction and operating process. It is relatively easy to create the breakage, even with low confining stresses (Potyondy and Cundall, 2004). Particle breakage and the resultant factors can induce additional unpredictable behavior on material mechanical properties. Because of the complexity of this phenomenon, studies of these materials are in the early stages and laboratory testing has been used as the primary method for understanding this process. Through the parallel bond model proposed by Potyondy and Cundall (2004), the analysis of using DEM to study particle crushing has become possible. Hence existing DEM models can be modified to account for particle or material breakage/fracture that occurs during the mixing process.

1.3 Major Findings

The purpose of this study is to address the aforementioned concerns and enhance the understanding of mixing properties within gravity-deposited binary mixtures. The research can be divided into two parts. The first part aimed at developing a comprehensive DEM program that will support the objective of this dissertation and improve existing DEM models. The second part contains the main body of this dissertation and focuses on the particle mixing process.

The first part of this document reviews the entire theoretical foundation of DEM simulations in the context of introducing a new model for more accurately capturing dynamic particle behavior. The general simulation process, detailed principles, employed models, and selected parameters are detailed in Chapter 2. Following this review, a series of objectives are outlined that include 1) developing a comprehensive DEM program for studies of binary granular mixtures, 2) applying this DEM model to the mixing process, evaluating existing mixing procedures, determining the level of influence that mixing can have on the homogeneity of the final aggregate, and providing a sequence of effective recommendations for future mixing designs, and 3) studying the properties of binary mixtures when mixed with crushable particles. Each of the aforementioned objectives are discussed in Chapters 3 to Chapter 5 of this dissertation. Each chapter has been prepared as a journal paper for subsequent submission.

Chapter 3 is titled “A modification of non-linear visco-elastic damping models applied in discrete element simulations”. In this section, a DEM model was established for studies of binary mixtures. The novel feature of this work is a refined nonlinear viscoelastic damping model that is proposed for simulating the behavior of the tangential force. This includes both

particle-particle contacts and particle-wall contacts. The commonly used Hertz model was applied to describe the normal force behavior. An improved non-linear spring tangential model was proposed for recovering the friction force response. The damping force was calculated based on the relative velocity during a contact using an alternative condition to evaluate the end of a collision. This has extended the application of the present model to fit the over-damped system. Since this model can successfully predict the friction force response in the stick and sliding regions, a transition zone has clearly been shown in the numerical results. Through this analysis, a hypothesis revealing the relationship between the static and the dynamic coefficients was proposed. Good performance was achieved as our results are compared with the empirical data, finite element results, and analytical solutions. Finally, additional numerical results have been provided as a supplement to existing benchmark tests.

Chapter 4 is titled “Mixing properties of binary granular mixtures under gravity deposition using the discrete element method”. The DEM model was applied to simulate the mixing process that involves two different particle cohorts entering a control volume and being mixed together using gravity deposition and physical obstacles. Mixing properties of the final products were investigated in regards to the number and position of the obstacles and the number of mixing iterations. A sub-volume algorithm was proposed and simulated compression tests were applied to evaluate the effective elastic properties within the mixtures. During the mixing process, it was found that for a single mixing iteration, fixed mixers can improve the mixing only if the mixer increasing particle collisions rather than separating the particle cohorts. Compared with increasing the number of obstacles and changing the applied positions, increasing the number of mixing iterations seems more effective. Through our analysis, results show that the mixing degree of the final aggregate can be quantified

by measuring the volume ratio ϕ_v which is calculated by the volume ratio of large particles versus smaller particles. For well-mixed mixtures, the measured volume ratios are consistent distributed over their variation ranges and with small fluctuations. Otherwise, assuming the final aggregate is an isotropic material, research on the effective stiffness shows that a high level of anisotropy is given in mixtures subjected to the gravity deposition.

Chapter 5 is titled “Mixing properties of binary granular mixtures with bonded particles”. This section shows the results of studying the variations in the mixing and mechanical properties of binary aggregates when made of crushable particles. Two groups were generated with different strength properties, and another without bonded particles is served as a reference for comparison. Each group is subjected to six mixing conditions for studying the effects of adding obstacles. Studies were conducted to determine the influence of bond strength on mixing volume ratio and the effective elastic properties of the final composite aggregate. Results show that the strength in bonds is an important parameter for quantifying the influence of using crushable particles. Mixing with crushable particles can improve the mixing degree by increasing the range of reflection angles, while the increment is associated with the applied bond strength. In such case, the introduction of mixing obstacles within the control volume can help improve the mixing properties of the final composite aggregate. An increase in the strength in bonds can decrease the effective elastic modulus and reduce the level of anisotropy in the final particle aggregate.

The primary conclusions of this entire body of work are summarized in Chapter 6, which also includes suggestions for future work.

CHAPTER 2: DEM MODEL AND THEORY

A model using the Discrete element method (DEM) is conducted to reveal the interaction behavior between particle contacts and predict the potential material properties while avoiding the construction of physical models. The general procedure is highlighted at the beginning of this chapter. More detailed information will be given in the subsequent sections.

In a DEM simulation, before running an analysis the initial geometry of the system should be given including system geometry, material properties, and boundary conditions. Advanced condition contains scheduled loading or deformations. Although the entire evolution of the system is continuous, the simulation over a period of time is examined at the segmented time intervals. During the simulation, large numbers of particles are interacting with each other. At each time step, contact detection and contact resolution strategies are invoked between interacting particles. Both of these calculations depend on the initial geometry described above. The main characteristic of contact detection is forming the efficient algorithms to keep trajectory of individual particles and detecting contacting particles or particles with likelihood coming into contact. Because of the intermittent connection form and breakage, this methodology makes the resolution enrolling local deformation and large-displacement problems becomes possible. Through this strategy, contact resolution is the most memory-cost and time-consuming process in DEM simulations. Exact calculation of contacting force is a necessary condition to guarantee the real physical situation has successfully been recovered. At this point, all acting forces need to be accounted relied on the interested field and the model complexity. Using the Newton's second law, the resultant external force acts as a driving force for updating particles motion. Knowing the inherent

mass and the moment inertia, translational and rotational accelerations can be calculated. After twice applications of the central-difference integration, finally particle displacements and positions are renewed. The consequent geometry will be used for the analysis in the next time step.

A flow chart showing the sequence of calculations involved in a DEM simulation is illustrated in **Fig. 2-1**. Procedures encapsulated by the dashed box illustrate all calculations involved in the current time step. These calculations are repeated over every time cycles. The output files can be exported for doing the post-analysis.

2.1 Particle Types

In DEM, instead of considering the deformation of each particle, studies are focusing on the relative motion. Particles are assumed to be rigid. Through the effect that particles movement is significant and dominates the granular material response, the assumption of rigid body motion is reasonable. More benefits can be achieved with this assumption. Simulation will involve large numbers of particles which is the primary limitation when applying DEM methods in geotechnique. More degrees of freedom are used to describe particles motion, less numbers of particles can be accounted in analysis. In our program, where the dynamic governing equilibrium equations are applied, only translational and rotational movements are considered at segmented time intervals.

If particles are only treated to be rigid, DEM method is close to “hard sphere” theory which starts from the momentum exchange equation but fails to depict the real philosophy (Campbell, 2006). In realistic, deformation appears at the contact point between contacting particles. To cover this physical phenomenon, DEM method uses overlap length or volume to

imitate the deformed shapes. This tiny improvement makes the application of the Newton's second law come true. Forces are introduced at contacts. The overlap volume is more fit for simulating the situation of distributed stresses. No matter which one is utilized, force calculation is sensitive to the overlap or particle geometries. For irregular particles, besides of centroid locations and radii, additional information needs to be provided for describing particle edges. Therefore, choosing particle type for analysis needs to balance the competition of calculating accuracy and computational cost.

2.1.1 Sphere particles

Spheres, by far, are the most commonly used particle type in DEM models due to their geometry is easily applied. The contacting point and the induced overlap can quickly be determined. Many thanks to the assumption that the general movement is more significant than the deformation of individual particles, the influence of this spherical idealization is small or even can be neglected.

Where spherical particles are employed, the overlap δ_n is calculated by

$$\delta_n = R_a + R_b - \sqrt{(x_a - x_b)^2 + (y_a - y_b)^2 + (z_a - z_b)^2} \quad (1)$$

Following the same sign convention as O'Sullivan (2011) and other authors did in geotechnique, the positive overlap always induces a compression force. R_a and R_b are particle radii where coordinates are setting at (x_a, y_a, z_a) and (x_b, y_b, z_b) , respectively. For spheres, the mass (m_p) and moment of inertia (I_p) in 3D case are given as

$$\begin{aligned}
m_p &= \rho \frac{4}{3} \pi R_p^3 \\
I_p &= \frac{2}{5} m_p R_p^2
\end{aligned}
\tag{2}$$

where the subscript p is the abbreviation of “particle”; ρ stands for material density; and R_p represents the radius respect to that particle.

Even though using spheres for analysis takes many advantages, an inherent shortage associates with this application. That’s the main reason as introducing moment resistance to our model. Spherical particles will automatically lose the inter-lock phenomenon due to the application of smooth surfaces (O’Sullivan, 2011). Additionally, since the normal force always goes through particle centroids, particles cannot provide resistance to inhibit rotational motion transmitted from other particles. As a result, simulating using spheres always overestimates the rotation of real soils. The number of contacts per sphere experienced is greater than the real ones (O’Sullivan and Bray, 2002). The increased number of contacts leads to an incremental strength appeared in the overall material response.

2.1.2 Crushable aggregates

Some researchers are interested in investigating the effect caused by the application of irregular particles or particles in loose form. For loose soils, particle crushing and rearrangement are main characteristics. As the analysis of single particle fracture is complicated, time-consuming, and highly expensive in Finite element method (FEM), Cleary (2000) stated that particle crushing is a primary motivation as driving the DEM application to the mining industry field.

One powerful method to imitate crushable particle behavior is forming bonds between basic spheres to model the internal cohesive force inside the cluster. These can be seen as black short lines generated at the contact points in **Fig. 2-2**. Discussed by Potyondy and Cundall (2004), this model can effectively mimic the irregular geometry of real particles, recover the behavior of sands, and reduce the computational time. In this model, base spheres are still moving independently, including translational and rotational movements. Bonds at the contacts can carry loads and break automatically. Tension force or generalized elastic force-displacement law is utilized to imitate the internal actions. When the internal forces exceed the strength of bonds, aggregates will break into smaller pieces.

There is a limitation associated with this model. The powder size or the particle minimum dimension is determined by the base spheres forming the aggregates/clusters. In contrast to the rigid clusters, for crushing particles each aggregate is a multiple-degree-of-freedom system. Although the system is filled with bonded particles, only the dynamic equilibrium equations of individual basic spheres need to be considered. The acting forces consist contribution from contacts with adjacent spheres and the forces achieved by connecting bonds. In advance, by removing the internal bonds or spheres, flaws can be introduced into the aggregates (Cheng et al., 2003).

2.2 Force Detection

Before calculating contact forces, automatically identifying the contacting particles or particles are likely coming into contact in the current time step is needed. This procedure becomes a necessary condition especially for running analysis with large numbers of particles. The associated memory should be well organized and managed. This detecting algorithm

allows particles to skip the unnecessary loop for force calculation instead of checking every particles in the system. Efficiency is the typical requirement for this step.

A general “binning algorithm” is applied to detect contacting particles. A regular rigid is placed on the analysis domain. Dimensions of each cell should be big enough to completely contain the largest particles. The procedure is close to put rectangular boxed within the problem area. Then, each particle centroid is placed in a given one. In order to build the neighbor list, a single particle needs to check with particles within the same box and other particles in the neighboring boxes. The size of the box is depended on the maximum particle radius. **Fig. 2-3** shows a 2D instance. The gray area indicates the region that particles in the center box need to be checked with. However, a limitation appears when particle dimension has a wide range in the studying domain. More smaller particles will fall into the same box. The benefit getting from this detecting filter doesn't apparent.

2.3 Force Calculation

Force calculation is the most time-consuming procedure and an important condition to guarantee that particle positions are updated correctly. The essence is summarizing the resultant force and moment acting on particles. For unbonded particles, only particle or grain behavior (Potyondy and Cundall, 2004) needs to be considered. Energy is transmitted through three interactions: normal contact, tangential contact, and moment resistance. For bonded aggregates/clusters, additional force and moment introduced by bonds/cements need to be taken into account.

2.3.1 Normal contact response

Hertzian contact mechanics is the basic theory for describing stresses distribution and deformation evolution between two contacting particles along the normal direction. For solid bodies with any geometry, this theory assumes an initial point contact. Then, provide the growth expression of contact area. Two assumptions associated with this theory. First, particle surface is idealized which is assumed to be smooth and non-convex. This condition ensures point contact which avoids multiple contacts happen at the same time for one collision. This phenomenon is well known as “non-conforming contact”. Second, the contact area or the induced deformation is much smaller than particle dimensions. So contact behavior can be dealt independently. For the simplest case, the performance of force-displacement response is treated as linear elastic.

Similar to the constitutive law applied in continuum model to describe the relation between stress and strain, a linear elastic spring is utilized for imitating the force-displacement response in DEM simulations. A very stiff spring is placed at the contact points to mimic the repulsing force. Large amount of force can be generated by tiny penetration. Depending on the complexity of the simulated force, two kinds of models are generally utilized (Munjiza, 2004). One setting the acting force relates to the magnitude of the overlap length, whereas, the other is related to the contact area or the acting volume. The latter one is more fit for the interest of describing distributed stresses.

A simplest model without damper and slider is illustrated in **Fig. 2-4**. A spring is located along the line joined the center of two contacting spheres. When a linear elastic spring is employed, the developed relation between the force and the displacement keeps a straight line. This approach is restricted to the effect that contact stiffness is difficult to link

with material properties. Instead, simplified Hertzian contact model is applied. A series of non-linear formulations are formed.

At each contact, the normal contact force F_n is calculated by

$$F_n = K_n \delta_n \quad (3)$$

where K_n is the normal contact stiffness of the spring; and δ_n represents the overlap length along the line joining the centers of two contacting particles.

For each particle, the associated stiffness is given in non-linear format

$$K_p = \left(\frac{2G_p \sqrt{2R_p}}{3(1 - \nu_p)} \right) \sqrt{\delta_n} \quad (4)$$

G_p , R_p and ν_p are elastic shear modulus, radius and Poisson's ratio related to Particle p . For a sphere-sphere contact involving Particles a and b , the effective stiffness of the contact spring is

$$K_n = \frac{2K_a K_b}{K_a + K_b} \quad (5)$$

The equation illustrates that the effective stiffness is in a series connection of individual particle spring stiffnesses.

For a sphere-wall contact, $K_n = 2K_p$. Referring to Cundall and Strack's early work (1979a), keep the same expression for the particle-particle contact and the particle-wall contact. Since the overlap is half smaller, the normal effective stiffness for wall condition is doubled.

2.3.2 Tangential contact response

Friction resistance is an inherent property during particle contacts due to particle relative translational motion and surface asperity. As smooth particle hypothesis is used in Hertzian model, the ability of friction resistance is consequently lost in the tangential direction. In order to produce the same effect, two words “shear force” and “tangential force” are exchangeable terms to indicate the friction force used to protect the relative translational movement. Mindlin (1949) and Mindlin and Deresiewicz (1953) provided the detailed description of tangential response that is widely employed in DEM simulations. A central assumption is that the normal and the tangential forces are decoupled, which makes the independent analysis of friction force come true. Without influencing the calculation of the normal force, an additional tangential model is allocated at the contact points.

Referred to Hertzian theory, the active contacting area is shown as circles for spheres. Normal force and tangential force are acting in the same area. Mindlin (1949) and Maw et al. (1976) declared that for friction force the contact area generally contains “slip” and “stick” regions which are illustrated in **Fig. 2-5**. The word “stick” means that within the contacting region there is no relative movement or displacement between two particles. Similar to simulate the normal force response, tangential contact springs are placed at the contact point perpendicular to the normal direction to mimic the friction force behavior in the stick region. Through the early results proposed by Di Renzo and Di Maio (2004), regardless of the velocity difference at the end of every collision there is no significant improvement when simulating tangential force using more complicated models, such as applying the complete Mindlin and Deresiewicz theory. More advanced, a linear model can get even better results than a no-slip model as applied in commercial PFC3D or EDEM code. However, this condition only works

when input parameters are precisely evaluated (Di Renzo and Di Maio, 2004). This shortage is overcome by assuming particles have the same properties in every direction. Setting $K_t = K_n$, the tangential stiffness is automatically linked to particle properties.

To update the tangential force, besides of the contact spring stiffness a real overlap spring along tangential direction is needed. Different from the word “overlap” used for describing the relative normal displacement, another phrase “the cumulative tangential displacement” is employed to depict the relative tangential motion. If a contact is firstly detected, both of the cumulative tangential displacement and the corresponding tangential force are set to zero. When effective collision happens, particles are moving in different rates. This relative velocity will generate relative movements acting in the opposite direction for each particle. It has the contribution coming from translational velocity and rotational velocity at particle centers. In a three-dimensional (3D) case, the relative velocity $\dot{\delta}_i$ of Particle a according to Particle b at the contact point is

$$\dot{\delta}_i = [v_i^b + e_{ijk}\omega_j^b (x_k^C - x_k^b)] - [v_i^a + e_{ijk}\omega_j^a (x_k^C - x_k^a)] \quad (6)$$

where v^b and v^a are translational velocities; e_{ijk} is known as the alternating tensor; x_k^C , x_k^b and x_k^a present the locations for the contact point C, and the centroids of particles b and a , respectively; ω^b and ω^a are rotational velocities provided at the mass center. Subscripts i , j and k mean these values are given in indicial notation. Relative tangential velocities are calculated by subtracting the normal components. A 2D example is illustrated in **Fig. 2-6**.

$$\dot{\delta}_i^t = \dot{\delta}_i - \dot{\delta}_i^n \quad (7)$$

$$\dot{\delta}_i^t = \dot{\delta}_i - \dot{\delta}_j n_j n_i \quad (8)$$

$\dot{\delta}_i$ are the total relative velocities including components from the normal and the tangential directions. $\dot{\delta}_j n_j$ represents the resultant relative velocity that is given in tensor notation. When this relative velocity is multiplied by the unit normal vector n_i , the normal components $\dot{\delta}_i^n$ is obtained. By subtracting the normal parts, $\dot{\delta}_i^t$ represents the relative tangential velocity components.

The cumulative displacement is a summation of the incremental relative displacement over the active time period. It happens at the contact point and goes over every time increments from the moment when the contact is formed. This value is calculated by integrating particle relative velocity at the contact. For a spring with tangential stiffness K_t , the tangential/shear force at time t is given by

$$F_t(\delta_t, \dot{\delta}_t) = K_t \int_{t_0}^t \dot{\delta}_t dt \simeq K_t \sum_{t_0}^t \dot{\delta}_t \Delta t \quad (9)$$

$F_t(\delta_t, \dot{\delta}_t)$ means the tangential force is a function of the tangential displacement δ_t and the relative tangential velocity $\dot{\delta}_t$. t_0 is the initiated time accounted at the starting point of a collision. DEM simulations exam values at segregated time intervals, so the integration can be replaced to a summation. The necessity of using cumulative displacement to calculate tangential force is emphasized by Vu-Quoc et al. (2000) and O'Sullivan and Bray (2002).

Once sliding occurs, there is no need to calculate the tangential force in this way. Served as a threshold, if contact region starts to “slip”, value given by the Coulomb equation provides a yielding point illustrating as a slider in **Fig. 2-7**. The force is calculated by

$$F_t = \mu F_n \quad (10)$$

here, μ is a friction coefficient related to the property of particle asperities. F_t and F_n are the tangential force and the related normal force acting at the that point. The tangential force is always acting as a resistant force, so the complete format is shown as

$$F_t = -\min(|\mu F_n|, F_t(\delta_t, \dot{\delta}_t)) \frac{\dot{\delta}_t}{|\dot{\delta}_t|} \quad (11)$$

$|\mu F_n|$ and $F_t(\delta_t, \dot{\delta}_t)$ are the magnitude of shear forces acting in slip and stick regions, respectively. The component $-\frac{\dot{\delta}_t}{|\dot{\delta}_t|}$ reveals the phenomenon that the tangential force is always acting as a resistant force which is in the opposite direction of the relative velocity. An important emphasize. The determination of this value needs to be checked at every time steps. The relevant forces calculated at time t will be used for updating the same parameters at time $t + \Delta t$.

To calculate tangential forces between particles, additional information needs to be recorded in the previous time step. As increasing number of particles, the required storing memory becomes extremely large. In order to condense this symmetric matrix, a new index $k = \frac{(j-1)(j-2)}{2} + i$ is utilized for recording tangential force between particles i and j .

2.3.3 Rolling resistance behavior

Moments between contacting particles are transmitted not only by tangential friction but also rolling resistance. When angular particles, especially for rocks, are coming into contact, multiple contacts may occur at the same time for one collision. This phenomenon is also known as conforming contact. Force from different directions will provide resistance to particle motion. In realistic, forces are acting on a finite area instead of a point. So, moments are also transmitted by unbalance distributed stresses. Such unbalance can be produced in two ways.

One is caused by the asymmetric distribution of normal stresses. The resultant normal force doesn't go through particle centroids that is plotted in **Fig. 2-8(a)**. The dash line indicates the conforming surface appeared in real life. Normal stresses distribution over the contacting area is represented by a sequence of solid lines. Big arrow here represents the resultant force, which will introduce a rotational motion to particles. Two particles are rolling with each other in a plane and generating a relative angular motion about an axis parallel to the tangent plane. Same notations are applied for tangential stresses shown in **Fig. 2-8(b)**, and a torsion is induced. Particles are spin at the contact with an axis perpendicular to their contact plane along the normal direction.

Similar to the tangential contact model, a rolling resistance model is added at the contacts to mimic these physical phenomena. A well-known Iwashita-Oda rotational resistance model is utilized paralleled with the normal and tangential contact springs (Iwashita and Oda, 1998). Ai et al. (2011), whose overviewed frequently used rolling resistance models in DEM simulations, highlighted the advantage of Iwashita-Oda's model. It explicitly considered the viscous damping effect and could provide stable torques even in critical situations. Without

damper, the configuration of this model and the associated moment-angle curve are displayed in **Fig. 2-9**.

Where a relative rotation is generated between two contacting particles, the rolling resistance spring transmit a moment M_r from one to the other. Prior to pure-sliding occurs, the moment is calculated by the following equation.

$$M_r(\theta_r, \dot{\theta}_r) = K_r \int_{t_0}^t \dot{\theta}_r dt \simeq K_r \sum_{t_0}^t \dot{\theta}_r \Delta t \quad (12)$$

K_r is the rotational spring stiffness and θ_r describes the relative angular velocity between two contacting particles. Iwashita and Oda (1998) explained that the incremental relative rotational velocity has the same definition of particles incremental relative velocity applied in calculation of tangential force, but with the form of $\omega_i^b - \omega_i^a$. A fantastic hypothesis appears. Since the incremental rotation has the same format as the relative tangential increment, assuming the torque caused by rolling resistance has the same magnitude of the moment in friction Iwashita and Oda proposed the rolling stiffness is expressed as $K_r = K_t r^2$ (1998).

The maximum value of M_r is controlled by ηF_n , where F_n is the normal contact force as denoted before and η is the rolling friction coefficient related to the surface asperities or the eccentricity of particle centroid (Ai et al., 2011). Following the same format of tangential force, the transmitted moment is written as

$$M_r = -\min(|\eta F_n|, M_r(\theta_r, \dot{\theta}_r)) \frac{\dot{\theta}_r}{|\dot{\theta}_r|} \quad (13)$$

2.3.4 Bond/cement behavior

Rock fragments coming from quarries always have angular and rough faces, but with uniform distributed size. Even though the size of waste rock is big, these fragments are easy to breakage into smaller pieces. So, cement is employed between non-cohesive particles to simulate the mechanical behavior of irregular particles or crushable aggregates. If cement/bond doesn't present, the force-displacement models described above are enough for application. Otherwise, an additional model needs to be added to the previous ones to imitate cement/bond behavior. The model firstly proposed by Potyonday and Cundall is well-developed and frequently utilized, such as PFC2D and PFC3D (Potyondy and Cundall, 2004). Since bonds are located parallel with contact springs, this model is also known as "parallel bonds". Cements connecting the adjacent particles in aggregates play the role of beams, which is demonstrated in **Fig. 2-10**. Forces and moments can be transmitted through parallel bonds. The action of those bonds can be imagined as an elastic beam with circular cross-section in 3D or composed of a series of elastic springs those are uniformly distributed over the acting area, while the latter one is more fit for describing the distributed stresses.

The capacity of a parallel bond is decided by five parameters: normal and shear stiffness given in force per unit area (\bar{k}_n and \bar{k}_t); tensile and shear strengths carried by bonds ($\bar{\sigma}_c$ and $\bar{\tau}_c$); and bond-radius multiplier used for describing the acting area ($\bar{\lambda}$).

The acting radius is given by

$$\bar{R} = \bar{\lambda} \min(R_a, R_b) \quad (14)$$

This parameter determines the acting area of bonds. Consequently, the geometry capacities of this imaged beam are shown as

$$\begin{aligned}
 A &= \pi \bar{R}^2 \\
 I &= \frac{1}{4} \pi \bar{R}^4 \\
 J &= \frac{1}{2} \pi \bar{R}^4
 \end{aligned} \tag{15}$$

A , I and J represent the acting area, moment of inertia and polar moment of inertia of the cross-section, respectively.

Dividing the acting force and moment into normal and tangential components, each relative movement will generate increments to current variables. Since elastic behavior are used, values are given in the following forms:

$$\begin{aligned}
 \Delta \bar{F}_n &= -\bar{k}_n A \Delta \delta_n \\
 \Delta \bar{F}_t &= -\bar{k}_t A \Delta \delta_t \\
 \Delta \bar{M}_n &= -\bar{k}_t J \Delta \theta_n \\
 \Delta \bar{M}_t &= -\bar{k}_n J \Delta \theta_t
 \end{aligned} \tag{16}$$

The maximum capacity of bonds are determined through the beam theory. The maximum tensile and shear stresses are calculated by

$$\begin{aligned}
 \bar{\sigma}^{max} &= \frac{-\bar{F}_n}{A} + \frac{|\bar{M}_t| \bar{R}}{I} \\
 \bar{\tau}^{max} &= \frac{\bar{F}_t}{A} + \frac{|\bar{M}_n| \bar{R}}{J}
 \end{aligned} \tag{17}$$

Therefore, if either the maximum tensile stress or the maximum shear stress exceeds the

allowable strength, for example $\bar{\sigma}^{max} \geq \bar{\sigma}_c$ or $\bar{\tau}^{max} \geq \bar{\tau}_c$, the bond breaks. Then, this bond will be removed associated with other forces or moments. The contact response between particles will come back to the unbonded contact condition.

2.4 Kinematic Motion

Newton's second law is the basic rule applied in DEM simulations. As particles motions are decoupled, DEM method considers dynamic equilibrium equations of individual particles instead of the equation solving for the whole system. In 3D case, particles are free to move and rotate. Therefore, each particle has six degrees of freedom: three in translations and three in rotations.

2.4.1 Acceleration calculation

Referring to Zhu et al.'s (2007) work the general expression for the governing equation in translation is given as

$$m\ddot{x}_i = \sum_{c=1}^{N_c} F_{ic}^{con} + \sum_{n=1}^{N_{nc}} F_{in}^{non-con} + F_i^f + F_i^g + F_i^{app} \quad (18)$$

\ddot{x}_i are the global accelerations of this particle, where i varies from 1 to 3 denoting the x, y and z directions, respectively. F_{ic}^{con} are the contact forces including normal and tangential components due to the c th contact. In addition, rather than explicitly considering damping forces, those were contained in the calculation of contact forces. N_c means there are total N_c contacts either caused by the adjacent particles or contact boundaries. $F_{in}^{non-con}$ are the non-contact forces. N_{nc} gives the number of this kind of contacts. F_i^f are the fluid interaction forces; F_i^g give the particle gravity; and F_i^{app} denote the specified applied force. All forces

acting on this particle p should be taken into account.

The angular motion is calculated by the summation of the applied moment/torque. Moments can be transmitted through the normal and tangential forces at the contacts. However, tangential force always imports a moment, while normal force only generates a moment when it doesn't go through the centroid of this particle. The corresponding equation for calculating rotation is shown as

$$I \frac{d\omega_i}{dt} = \sum_{j=1}^{N_{mom}} M_{ij} \quad (19)$$

where ω is the angular velocity or known as $\dot{\theta}_r$ denoted before. M_{ij} are the moments applied by the j th moment transmitting contact force. A total number of N_{mom} moment transmitting contacts occurs.

2.4.2 Position updating

The central-difference integration is used for updating particle positions. To update particle positions at time $t_{n+1} = (n+1)\Delta t$, the resultant force and moment for each particle at time $t_n = n\Delta t$ need to be clearly calculated. Condense the dynamic equilibrium equations by only considering the contact force.

$$\begin{aligned} m\ddot{x}_i^n &= \Sigma F_i^n \\ I\ddot{\theta}_i^n &= \Sigma M_i^n \end{aligned} \quad (20)$$

Here, the superscript n indicates these values are given at time t_n . When time step is small enough, assuming \ddot{x}_i^n and $\ddot{\theta}_i^n$ are constants over the current time step Δt becomes reasonable. Integrating above equations one time can get velocities at mid-time step.

$$\begin{aligned}\dot{x}_i^{n+\frac{1}{2}} &= \dot{x}_i^{n-\frac{1}{2}} + [\Sigma F_i^n / m] \Delta t \\ \dot{\theta}_i^{n+\frac{1}{2}} &= \dot{\theta}_i^{n-\frac{1}{2}} + [\Sigma M_i^n / I] \Delta t\end{aligned}\tag{21}$$

Using the central-difference algorithm one more time, particle positions and rotations can be achieved for the next time step.

$$\begin{aligned}x_i^{n+1} &= x_i^n + \dot{x}_i^{n+\frac{1}{2}} \Delta t \\ \theta_i^{n+1} &= \theta_i^n + \dot{\theta}_i^{n+\frac{1}{2}} \Delta t\end{aligned}\tag{22}$$

Once particle new positions are updated, these output values will be served as input variables for the next time cycle. Force detection and calculations are repeated over every time steps.

2.5 Damping Effect

Currently, models are elastic before yielding meanwhile no energy is dissipated prior to sliding. Damping effect is accounted for factors before the rupture of spring, such as conforming contact, initial plastic deformation at the contact, or surface damage (Cavarretta, 2009; Cavarretta et al., 2010). Without damping, particles will oscillate at their original locations. To damp out this non-physical phenomenon (Munjiza, 2004), damper is added associated with contact springs. Here is an overview of three damping approaches which are commonly used in DEM simulations: mass damping, non-viscous damping, and viscous damping.

2.5.1 Mass damping

Mass damping is firstly introduced by Cundall and Strack (1979a). It is also known as global damping. Particles are connected to the ground by springs and dashpots. So damper

is operated on the absolute velocities directly. Once only considering the contact forces, for individual particles the dynamic equations become

$$\begin{aligned} m\ddot{x}_i &= \Sigma(F_i^n - C\dot{x}_i) \\ I\ddot{\theta}_i &= \Sigma(M_i^n - C^*\dot{\theta}_i) \end{aligned} \tag{23}$$

where C and C^* are the operating mass damping coefficients operated on the translational velocity \dot{x}_i and rotational velocity $\dot{\theta}_i$, simultaneously.

The damping parameters are related to the intrinsic property of contact particles. These coefficients are taken to be proportional to particle mass and moment of inertia respectively, where α is the proportional coefficient.

$$C = \alpha m, C^* = \alpha I \tag{24}$$

Consequently, the velocities at the mid-time step are rewritten to be

$$\begin{aligned} \dot{x}_i^{n+\frac{1}{2}} &= \{\dot{x}_i^{n-\frac{1}{2}}[1 - \alpha\frac{\Delta t}{2}] + \Sigma F_i^n \frac{\Delta t}{m}\} / \{1 + \alpha\frac{\Delta t}{2}\} \\ \dot{\theta}_i^{n+\frac{1}{2}} &= \{\dot{\theta}_i^{n-\frac{1}{2}}[1 - \alpha\frac{\Delta t}{2}] + \Sigma M_i \frac{\Delta t}{I}\} / \{1 + \alpha\frac{\Delta t}{2}\} \end{aligned} \tag{25}$$

Clarified by Cundall (1987), serial limitations are associated with this method. Damping coefficients are connected with particle intrinsic properties, so damping force will be introduced as a body force and is equivalently applied on all particles. Also, it's difficult to link the proportional coefficient α to particle properties.

2.5.2 Local non-viscous damping

Instead of applying damper to the absolute velocity, Cundall (1987) proposed an alternative model that damping force is treated as a component of contact forces. Equations have been transmitted to

$$\begin{aligned} m\ddot{x}_i &= \Sigma(F_i^n - F_{di}^n) \\ I\ddot{\theta}_i &= \Sigma(M_i^n - M_{di}^n) \end{aligned} \tag{26}$$

F_{di}^n are the components of damping force related to the contact force F_i^n . Consequently, moments M_{di}^n generated by damping force should also be included for updating angular velocities.

The damping force is setting to be proportional to the magnitude of the out-of-balance force. This model is utilized in commercial code PFC3D (Itasca, 2008). Damping force is given by the following equation.

$$F_d = -\alpha^*|F|sign(v) \tag{27}$$

where α^* is the damping constant, normally set as 0.7 for soils. v gives the velocity for this particle. The negative sign means the damping force is always acting on the opposite direction of this particle velocity. Here, F is named as the resultant or out-of-balance force. Referred to Teufelsbauer and his colleagues's study, they did a comparison between the analytical solution and the results from PFC3D (Teufelsbauer et al., 2009). This out-of-balance force is given as $2\sqrt{K\langle m \rangle}$ as they listed the governing differential equation at the effective mass center $\langle m \rangle$ of the contact system showing in **Fig. 2-11**.

This method overcomes the shortage of mass damping. Since the damping force is proportional to the unbalanced force, it is easy to apply. There is no erroneous forces induced in the steady-state. Itasca (2008) also highlighted the feature of this model. It recovers the realistic of the damping effect that the energy loss per cycle is independent of the rate as which cycle is executed. But it's difficult for us to find the value of α^* . And this method fails to depict the fact that damping force is correlated with particle contacting relative velocities.

2.5.3 Viscous damping

Viscous damping force is calculated based on the relative velocities at the contact points. Dashpots are placed on the normal and tangential directions parallel to the contact springs. The relevant coefficients are given as C_n and C_t . Dashpots stop working after spring breakage or sliding occurrence. The damping forces along both directions are provided by

$$\begin{aligned} F_{dn} &= C_n \dot{\delta}_n \\ F_{dt} &= C_t \dot{\delta}_t \end{aligned} \tag{28}$$

F_{dn} and F_{dt} are normal and tangential components of the damping force. The value $\dot{\delta}_n$ here should be calculated by using $\dot{\delta}_j n_j n_i$; and $\dot{\delta}_t$ is calculated by subtracting the normal components $\dot{\delta}_i - \dot{\delta}_j n_j n_i$. The amount of energy dissipated is dependent on the relative velocity between contacting particles, which is fit for the condition that less energy is dissipated during the high velocity impact (Brilliantov et al., 1996; Delaney et al., 2007).

Applying Cleary's model (2000), the selection of the damping coefficient is a function of restitution coefficient ε , where ε is a parameter measured energy dissipated per cycle (O'Sullivan, 2011) or a percentage ratio calculated by the velocity before and after a collision

(Luding, 1998). These two coefficients are calculated by

$$\begin{aligned} C_n &= 2\gamma\sqrt{\langle m \rangle K_n} \\ C_t &= 2\gamma\sqrt{\langle m \rangle K_t} \end{aligned} \quad (29)$$

here $\langle m \rangle$ is the reduced mass declared in Cleary's paper (2000) or named as the effective mass of the contact system determined by $\frac{m_a m_b}{m_a + m_b}$ (Luding, 1998). γ is a parameter linked with the restriction coefficient and expressed as

$$\gamma = -\frac{\ln(\varepsilon)}{\sqrt{\pi^2 + \ln(\varepsilon)^2}} \quad (30)$$

As a consequence, the complete form of normal and tangential forces with damper are presented as

$$\begin{aligned} F_n &= K_n \delta_n + C_n \dot{\delta}_n \\ F_t &= -\min\{|\mu F_n|, K_t \int \dot{\delta}_t dt + C_t \dot{\delta}_t\} \frac{\dot{\delta}_t}{|\dot{\delta}_t|} \end{aligned} \quad (31)$$

Similar to forces, Ai et al. (2011) highlighted that an additional “rolling damper” was a necessary term to control particle oscillations respect to rolling resistance. Referred to Iwashita and oda (1998), Ai et al. (2011) and Wensrich and Katterfelf (2012), the expression of a damping rate C_r is

$$C_r = 2\gamma\sqrt{\langle I \rangle K_r} \quad (32)$$

$\langle I \rangle$ is the effective moment of inertia calculated through $\langle I \rangle = \frac{I_a I_b}{I_a + I_b}$. Therefore, the format

of calculating moment becomes

$$M_r = -\min\{|\eta F_n|, K_r \int \dot{\theta}_r dt + C_r \dot{\theta}_r\} \frac{\dot{\theta}_r}{|\dot{\theta}_r|} \quad (33)$$

2.6 Time Increments

The DEM simulation uses a different solving strategy than the traditional FEM approach. It solves the dynamic equilibrium equations of individual particles instead of solving the matrix of the entire system; whereas a risk of numerical instability is introduced.

While in reality, the evolution of particle position and force are developed continuously; in DEM simulations, a series of calculation involving information about current particle configuration is used to step forward or predict the state at a further time. The system is examined at specific time locations rather than the real time. Since central differential integration is applied for updating particle positions, a truncated error is induced that is a second-order effect of the discretized time Δt .

Therefore, determining an appropriate value for Δt becomes a big issue; otherwise, the calculation makes no sense (Luding, 1998). Cundall and Strack (1979a) declared that the chosen time increment should be small enough to make sure that a particle motion over a single time step cannot propagate through the contacting particle and only influences its neighboring particles immediately. Since contacts are formed and broke at every time intervals, the stiffness of the whole system shows non-linearity. In other words, the time increment is not limited to its initial state. The increment should be small enough in order to capture the formation of new contacts, breakage of existing contacts, and the initial

sliding.

The critical time increment is defined as Δt_{crit} . Thornton (2000) and Thornton and Antony (2000) selected their simulation time intervals based on the minimum particle size R_{min} and the Rayleigh wave speed. Choosing $\alpha = 0.1631\nu + 0.876605$, the critical time increment in Hertzian model with spheres is expressed as

$$\Delta t_{crit} = \frac{\pi R_{min}}{\alpha} \sqrt{\rho/G} \quad (34)$$

It is obvious that decreasing minimum particle radius and density Δt_{crit} reduces. If analyzed particle size varies in large range, time increment becomes so small. Moreover, the Rayleigh time step does not taken into account the relative movement of particles and it may turn out to be too large to ensure numerical stability. If particles are contacting with high relative velocities, the time step should be reduced further. Using a small amount of the Rayleigh time step for analysis will enhance the simulation time, a typical 20% of the Rayleigh time step is utilized (Bossy and Safuryn, 2016). Luding also declared that the time interval should be smaller than the contact time, typically 3-4 steps are included for one collision (1998).

2.7 Boundary Conditions

Currently, three types of boundary conditions are enrolled in our studies: finite rigid walls, rigid moving walls, and periodic inlets. Either of them are given in four points located in counterclockwise order.

2.7.1 Finite rigid wall boundary conditions

Using any three points those are not collinear with each other, the unit normal vector of this plane can be found. Knowing the unit vector and a point (x_w, y_w, z_w) that doesn't go through it, the plane can be expressed as

$$Ax + By + Cz + D = 0 \quad (35)$$

A , B , and C are components of this normal vector; while D is equal to $-Ax_w - By_w - Cz_w$. Having particle centroids and the expression of this plane, the projection or the contact points locations are given as

$$\begin{aligned} x_i^C &= x_i^p - A \frac{Ax_i^p + By_i^p + Cz_i^p + D}{\sqrt{A^2 + B^2 + C^2}} \\ y_i^C &= y_i^p - B \frac{Ax_i^p + By_i^p + Cz_i^p + D}{\sqrt{A^2 + B^2 + C^2}} \\ z_i^C &= z_i^p - C \frac{Ax_i^p + By_i^p + Cz_i^p + D}{\sqrt{A^2 + B^2 + C^2}} \end{aligned} \quad (36)$$

Here, i means the i th number of particles. (x_i^p, y_i^p, z_i^p) are the correlated particle locations. A challenge of this boundary condition is to decide whether particles fall into the region of this plane or not. A map showing the determinate criterion is illustrated in **Fig. 2-12**. P1-P4 are four dominant points determining the effective contact area. The coordinates at a contact point C are calculated by the above equations. On each side of this plane, two vectors can be calculated; for example, for point P_1 , we have $\vec{P_1P_2}$ and $\vec{P_1C}$. If the cross product of these two vectors on every sides has the same sign, the projected point is treated within the plane. Each plane has an "active" and an "inactive" sides, and only one of them is physically reasonable. When the cross product is in the same direction of the unit normal

vector, an effective contact happens. In the figure, P1-P4 are given in counterclockwise direction. Assume upward vector has a positive value. If $P_1\vec{P}_2 \cdot P_1\vec{C}$ is positive, it means Point C is on the left of vector $P_1\vec{P}_2$. Same criterion is applied for other sides.

For particles satisfied the checking condition, distance between particle centroid and the project point is calculated. If this distance is less than particle radius, particles are contacting with rigid walls. Then, the normal and tangential forces on individual particles are calculated. These forces will be used for updating particle positions at the next time step.

An advance application of this boundary is cylindrical obstacles. Instead of giving four points, the cylinder surface is decided by two points denoting the longitudinal direction and a radius. Similar checking condition is applied to make sure the projected points are within the contact surface of the cylinder. Other calculations are following the same rule of sphere-sphere contacts.

2.7.2 Rigid moving wall boundary conditions

The main propose of applying rigid moving walls is for post-analysis. Rigid moving wall is an extend application of finite rigid walls. It is also known as Servo-controlled rigid boundaries and widely used in simulating element tests (Cheng et al., 2003; O’Sullivan, 2011). An example illustrating the implementation of this boundary in biaxial compression tests is shown in **Fig. 2-13**. A representative sample is encapsulated with a moving wall and other three rigid walls. At each time step, the stress distributed on the top plane is measured. It is calculated by the summation of the contact forces along the relevant boundaries while dividing over the boundary length/area. If this measured stress σ_{ii}^{meas} is

greater than the user-specified required stress σ_{ii}^{req} , the rigid moving wall will move outwards; otherwise, the wall is moved inwards in order to achieve the required stress. The wall velocity is proportional to the magnitude of the stress difference, $V_i^{wall} = \bar{\alpha}|\sigma_{ii}^{meas} - \sigma_{ii}^{req}|$, where $\bar{\alpha}$ is the calculated proportionality constant. When this stress difference is within the user-specified tolerance, such as $|\sigma_{ii}^{meas} - \sigma_{ii}^{req}| \leq \epsilon$, the wall stops moving. Appropriate selection of these two parameters is a necessary condition to guarantee the required stress is achievable. However, this condition is getting worse for bonded aggregates due to cements spontaneous breakage (Carolan, 2005).

2.7.3 Periodic inlet boundary conditions

General periodic boundary condition allows the simulation of a very large number of particle by using a much smaller repeated subdomain. A potential cognition is that for each subdomain it keeps the identical internal structure. Using the periodic boundary condition can avoid the repeated input work, focus on the main analysis area and decrease the computational time. An example in 2D is illustrated in **Fig. 2-14**.

Essentially, because the subdomain is surrounded by identical units, it is reasonable to say every unit keeps the same behavior. If a particle passes through the periodic boundary, it will re-enter on the opposite side of this subdomain. This relation is demonstrated in **Fig. 2-15** for 1D case. When particle A' exits the periodic boundary 2-2, identical particle A enters boundary 1-1.

In our model, different from the normal ones, periodic boundary conditions have been converted to periodic inlets/entrances. Given as an initial condition, there is a specific area with length L used to decide the repeated section. If particle doesn't go through the periodic

boundary, a non-zero value associated with the number of inlet is assigned for this particle playing as a function of switch. Therefore, this DEM program can easily handle a mixing process with multiple inlets in the future. Moreover, at each time interval, if this number is detected to be non-zero, related particles will jump out of force detection and calculation loops. This procedure can effectively save the computational time.

An example of this process is shown in **Fig. 2-16**. When this specific number is non-zero, the function of adding particles is “closed”. Referring to this point, a vector from particle centroid to the periodic inlet needs to be determined. Relevant calculations can be referred to wall contacts. If the vector is on the opposite direction of the unit normal vector for the wall, particles are moving out of the inlet and force calculation should be taken into account. After that, zero will be set to that value. New particle will be added at $x_{add} = x_{old} - L$. All mechanical properties will be copied to the new one. Additionally, for an inclined plane with rotational angles $(\theta_x, \theta_y, \theta_z)$, the new location along x axis is given by $x_{add} = x_{old} - L\cos(\theta_x)$. Same calculations are presented for other axes.

2.8 Post-analysis

The main characteristics of DEM simulations is helping us look inside the internal structures and providing particle level information. Converting the particulate measurements to continuum mechanics parameters can improve our understanding of macro-scope phenomena and reveal the micro-level physics behind.

2.8.1 Identify the mixing parameters of a mixture

O’Sullivan (2011) noted that the mixing properties within the mixture can be inhomogeneous. The detailed information on the internal structure level can be evaluated at any point within the granular materials by using DEM simulations (O’Sullivan, 2011). The mixing property of a granular materials can be quantified by the volume ratio (ϕ_v), mass ratio (ϕ_m), void ratio (e), porosity (n), the dry bulk density (ρ_b), and the coordination number (Z). Those are also conventional parameters utilized in soil mechanics.

Algorithm of volume calculation

The numerical determination of volume ratio is obtained from the γ -ray absorption technique that measures the material density in the path of a beam (Bardet and Proubet, 1991). In 1991, Bardet and Proubet applied this method to evaluate the void ratio of 2D virtual samples which is illustrated in **Fig. 2-17**. Only areas within the circular sample of radius r and center C are taken into account.

The area of i th particle covering the selected area is shown as

$$A_i = \begin{cases} 0, & d_i > R_i + r \\ \pi R_i^2, & d_i \leq r - R_i \\ \frac{R_i^2}{2}(\theta_2 - \sin\theta_2) + \frac{r^2}{2}(\theta_1 - \sin\theta_1), & r - R_i < d_i \leq R_i + r \end{cases} \quad (37)$$

where d_i is the distance between center C and the centroid of the i th particle, and θ_1 and θ_2 are denoted as

$$\begin{aligned}\theta_2 &= 2 \arccos \left\{ \frac{d_i^2 + R_i^2 - r^2}{2d_i R_i} \right\} \\ \theta_1 &= 2 \arcsin \left\{ \frac{R_i}{r} \sin \frac{\theta_2}{2} \right\}\end{aligned}\tag{38}$$

In our 3D sample, the covered volume V_i of the i th particle is calculated by

$$V_i = \begin{cases} 0, & d_i \geq R_i + r \\ \frac{4}{3}\pi R_i^3, & d_i \leq r - R_i \\ \frac{1}{3}\pi(3r - h_1)h_1^2 + \frac{1}{3}\pi(3R_i - h_2)h_2^2, & r - R_i < d_i < R_i + r \end{cases}\tag{39}$$

while h_1 and h_2 are the heights of the relevant crown

$$\begin{aligned}\theta_2 &= 2 \arccos \left\{ \frac{d_i^2 + R_i^2 - r^2}{2d_i R_i} \right\} & \text{and} & & h_2 &= R_i - R_i \cos\left(\frac{\theta_2}{2}\right) \\ \theta_1 &= 2 \arcsin \left\{ \frac{R_i}{r} \sin \frac{\theta_2}{2} \right\} & & & h_1 &= r - r \cos\left(\frac{\theta_1}{2}\right)\end{aligned}\tag{40}$$

Mixing parameter calculations

The volume ratio ϕ_v is a dimensionless quantity and is provided by the percentage of different materials occupied the analysis domain without considering the volume of voids. For binary mixing, this value is given as $\frac{V_{big}}{V_{small}}$ in our results, where “big” and “small” present the relative dimension of particle radius.

More generally, for each material, the occupied volume is given as

$$V_m = \sum_{i=1}^{N_s} V_i\tag{41}$$

N_s is the total number of investigated particles contained in the spherical subdomain. After the summation, V_m represents the amount of this material in space. Multiplying by the

relevant mass densities, the mass ratio is illustrated as $\phi_m = \frac{m_{big}}{m_{small}}$.

The void ratio e is related to the packing density and calculated by

$$e = \frac{V_v}{V_s} \quad (42)$$

V_s is the volume of solids shown as $\sum V_m$; while V_v is the volume of voids and calculated by $V_v = \frac{4}{3}\pi r^3 - V_s$. The void ratio demonstrates the porosity of the internal structure, while the porosity is computed by the equation $n = \frac{V_v}{\frac{4}{3}\pi r^3}$.

The dry bulk density illustrates the compaction of the deposit and is given as

$$\rho_b = \frac{M_s}{V_t} \quad (43)$$

M_s is the mass of soil and is shown as $\sum \rho_s V_s$, where ρ_s is the corresponding density of such solid. V_t represents the total volume of the investigated area. For a control volume in the shape of a sphere, $V_t = \frac{4}{3}\pi r^3$.

The parameters above quantify the particle packing density. The coordinate number quantifies the number of contact per particle and is written as

$$Z = 2 \frac{N_c}{N_p} \quad (44)$$

Here, N_c indicates the total number of contacts within the measured subdomain and N_p is the number of particles. The value 2 represents that each contact is shared by two contacting particles.

2.8.2 Evaluate the effective elastic properties

In addition to the mixing ratio, the mechanical behavior of the final packing is of interest. Simulated compression tests are employed for this investigation. Parts of the full sample is taken out for analysis. Cubic sub-regions are used. The sub-region is confined by five rigid walls. A rigid-moving wall condition described above is added. A control volume is placed around the final packing - which now is motionless and in static equilibrium. The top wall of the container will be lowered onto the particles. When the top plane moves downward, particles near the rigid walls experience translational and rotational movements. Under the compression, expansion forces will be generated at the center and push the surrounding particles moving outwards. The calculation process is demonstrated in **Fig. 2-18**.

Stress

Referring to Bagi (1999b) and O’Sullivan (2011), for a closed continuous domain with volume V and boundary area S , the average stress within the material $\bar{\sigma}_{ij}$ is given as

$$\bar{\sigma}_{ij} = \frac{1}{V} \sum_{k=1}^{N_{BF}} x_i^k f_j^k \quad (45)$$

where f_j^k is the boundary force applied at position x_i^k and there is a total number of N_{BF} forces acting along the boundary surface.

Strain

Generally, the strain for a simulated element test can be calculated by considering the boundary positions. The distance between the top and bottom planes can be used to calculate the overall axial strain, $\bar{\epsilon}_{zz} = \frac{\Delta H_{zz}}{H_{zz}}$ where H_{zz} is the original height and ΔH_{zz} is the change in height. However, in order to investigate the difference between the macro-

and micro-scale fields, the best fit approach is utilized as an another approach to find the approximate equation for describing the observed particle displacements within the investigated regions (O’Sullivan, 2011). Itasca (2008) and Potyondy and Cundall (2004) used this method to find the deformation gradient rates, while Marketos and Bolton (2010) extended this approach to calculate actual strains described particle incremental displacements.

To get the average deformation gradients or strains $\bar{\epsilon}_{ij}$, the incremental relative displacements need to be considered. The incremental displacement of each particle over the time increment t_1 to $t_2 = t_1 + n\Delta t$ ($n = 1, 2, \dots$) is calculated by $\Delta u_i^p = x_i^{p,t_2} - x_i^{p,t_1}$, where x_i^{p,t_1} and x_i^{p,t_2} are particle positions at time t_1 and t_2 respectively. Then, the incremental relative displacements relative to the centroid of the selected region is estimated. The mean incremental displacement $\overline{\Delta u}_i$ and mean position \bar{x}_i within the region are given as

$$\begin{aligned}\overline{\Delta u}_i &= \frac{\sum \Delta u_i^p}{N_p} \\ \bar{x}_i &= \frac{\sum x_i^p}{N_p}\end{aligned}\tag{46}$$

N_p is the number of particles within the measured volume and x_i^p are particle position vector provided at time t_2 . Therefore, the incremental displacements and positions of every particles relative to the mean values are calculated by

$$\begin{aligned}\Delta u_i^{p,rel} &= \Delta u_i^p - \overline{\Delta u}_i \\ x_i^{p,rel} &= x_i^p - \bar{x}_i\end{aligned}\tag{47}$$

Assuming particles moved with a uniform displacements and a linear expression is applied to fit the actual movements, the relative incremental displacements of one particle is shown

as

$$\Delta u_i^{p,rel} = \bar{\epsilon}_{ij} x_j^{p,rel} \quad (48)$$

A least squares approach is employed to find the minimum value of $\bar{\epsilon}_{ij}$.

$$\sum_{N_p} (\Delta u_i^{p,rel} - \bar{\epsilon}_{ij} x_j^{p,rel})(\Delta u_i^{p,rel} - \bar{\epsilon}_{ij} x_j^{p,rel}) \rightarrow \min \quad (49)$$

In 3D, this above equation is expressed by solving the following equations.

$$\begin{pmatrix} \sum_{N_p} x_1^{p,rel} x_1^{p,rel} & \sum_{N_p} x_1^{p,rel} x_2^{p,rel} & \sum_{N_p} x_1^{p,rel} x_3^{p,rel} \\ \sum_{N_p} x_2^{p,rel} x_1^{p,rel} & \sum_{N_p} x_2^{p,rel} x_2^{p,rel} & \sum_{N_p} x_2^{p,rel} x_3^{p,rel} \\ \sum_{N_p} x_3^{p,rel} x_1^{p,rel} & \sum_{N_p} x_3^{p,rel} x_2^{p,rel} & \sum_{N_p} x_3^{p,rel} x_3^{p,rel} \end{pmatrix} \begin{pmatrix} \bar{\epsilon}_{i1} \\ \bar{\epsilon}_{i2} \\ \bar{\epsilon}_{i3} \end{pmatrix} = \begin{pmatrix} \sum_{N_p} \Delta u_i^{p,rel} x_1^{p,rel} \\ \sum_{N_p} \Delta u_i^{p,rel} x_2^{p,rel} \\ \sum_{N_p} \Delta u_i^{p,rel} x_3^{p,rel} \end{pmatrix} \quad (50)$$

Both Bagi and Bojtar (2001) and Cambou et al. (2000) clarified that this method underestimated the globally applied strain since only translational motions are included.

Effective E and ν

Applying an orthogonal Hooke's law in continuum mechanics and assuming $\nu_{xz} = \nu_{yz}$, the equivalent elastic properties E and ν can be found using

$$\begin{Bmatrix} \bar{\epsilon}_{xx} \\ \bar{\epsilon}_{yy} \\ \bar{\epsilon}_{zz} \end{Bmatrix} = \begin{bmatrix} \frac{1}{E} & -\frac{\nu_{xy}}{E} & -\frac{\nu_{xz}}{E} \\ -\frac{\nu_{xy}}{E} & \frac{1}{E} & -\frac{\nu_{yz}}{E} \\ -\frac{\nu_{xz}}{E} & -\frac{\nu_{yz}}{E} & \frac{1}{E} \end{bmatrix} \begin{Bmatrix} \bar{\sigma}_{xx} \\ \bar{\sigma}_{yy} \\ \bar{\sigma}_{zz} \end{Bmatrix} \quad (51)$$

Once again, these parameters can be computed at various locations within the final particle packing.

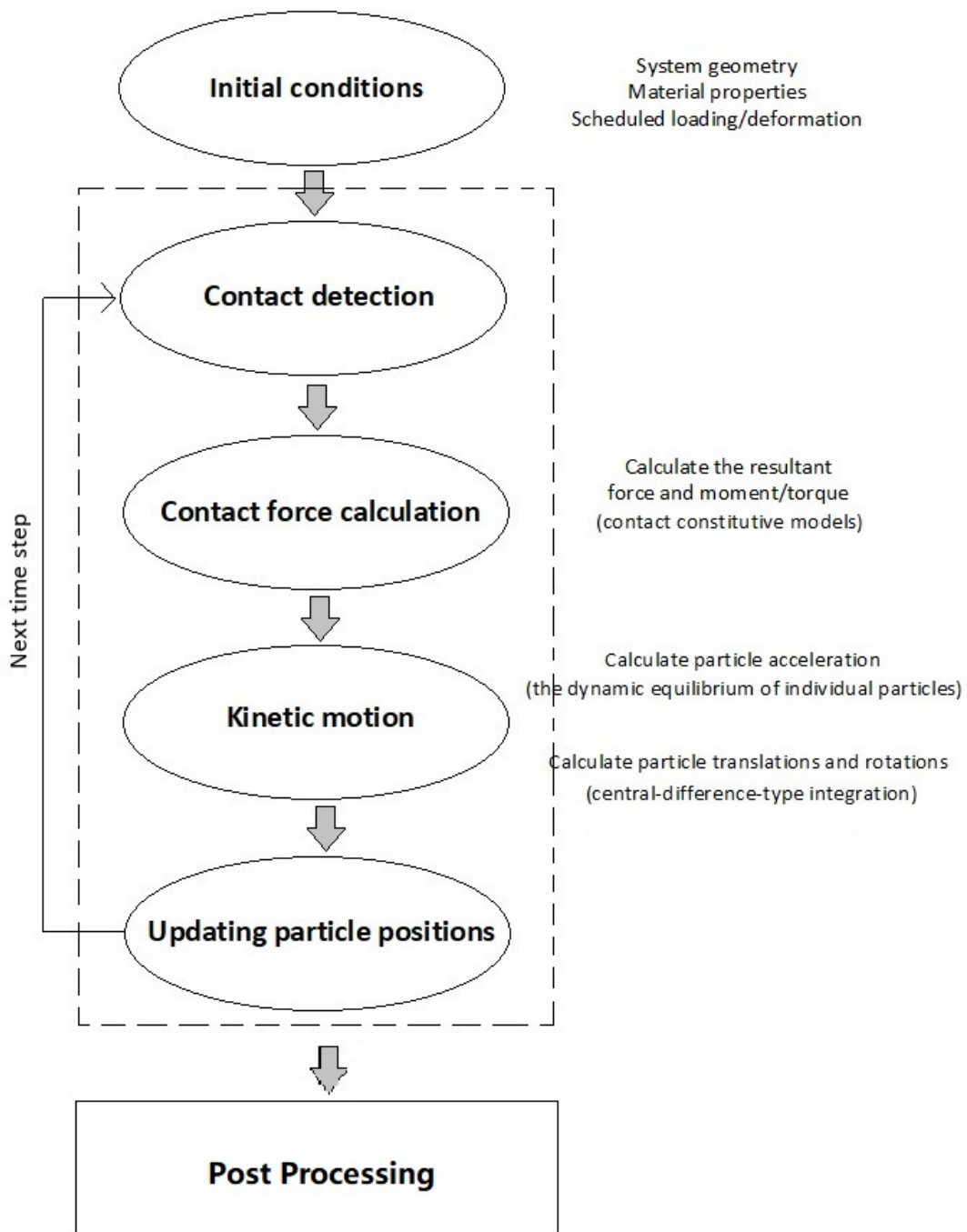


Figure 2-1: A flow chart showing sequence of calculations in a DEM simulation

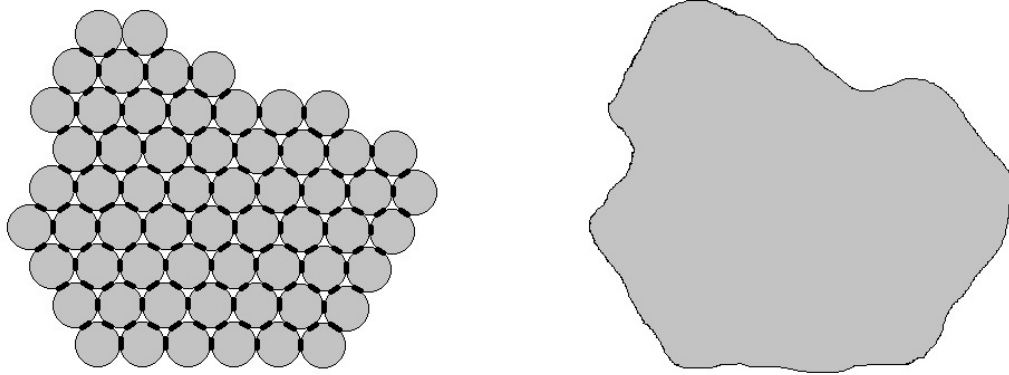


Figure 2-2: Concept of simulating crushable particles using bonded aggregates

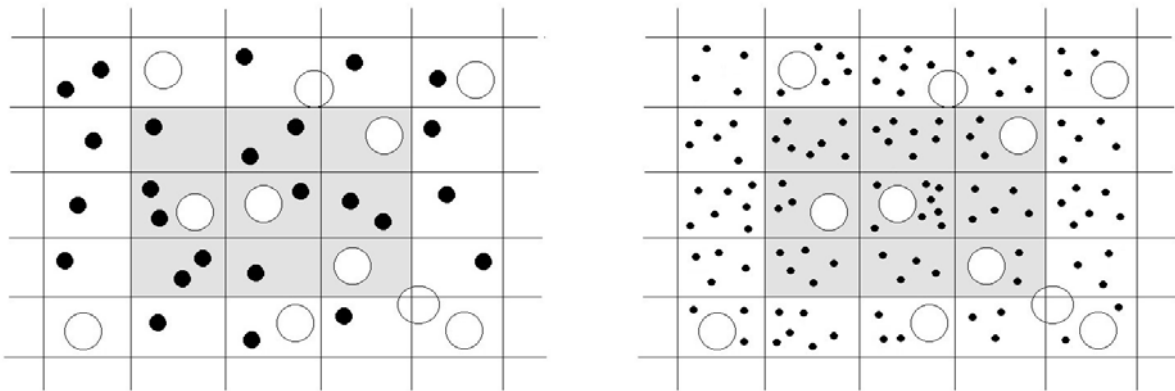


Figure 2-3: A contact detection using “binning algorithm”

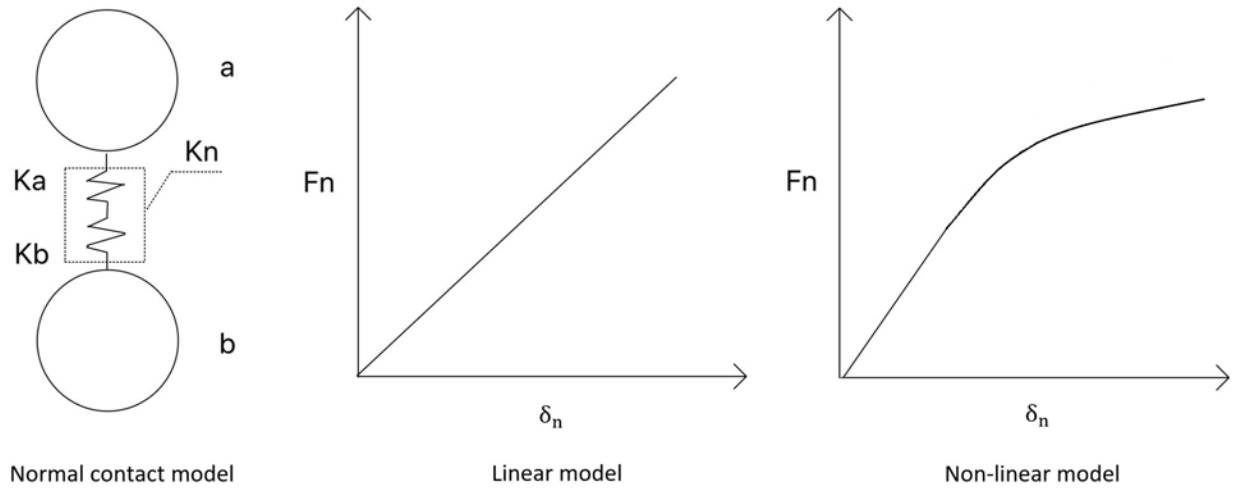


Figure 2-4: Force-displacement responses for normal contact model

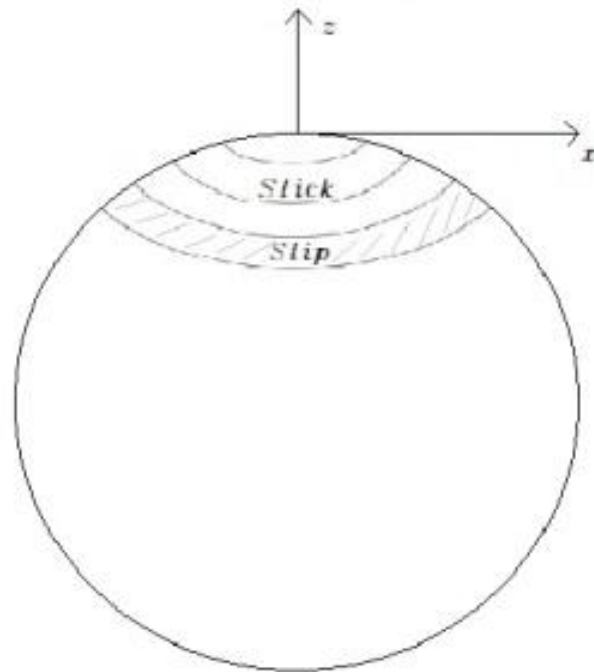


Figure 2-5: The deviation of contact area respect to tangential force

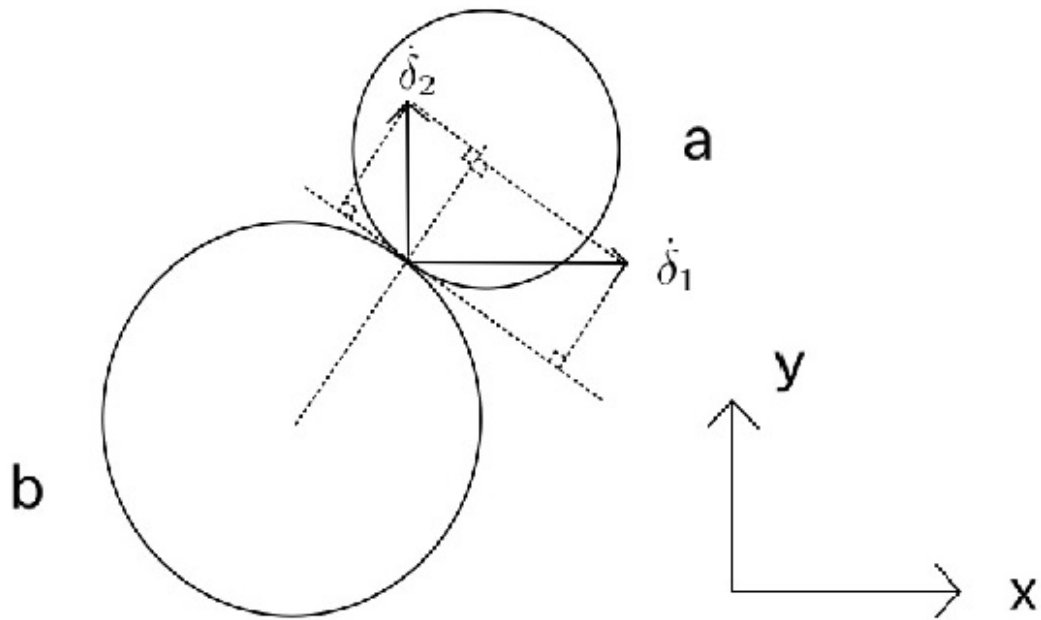
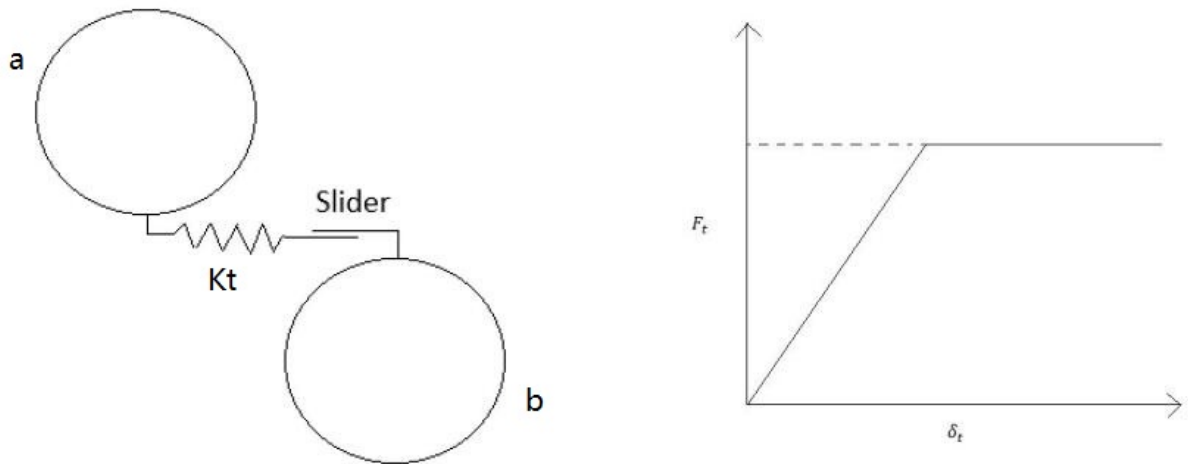


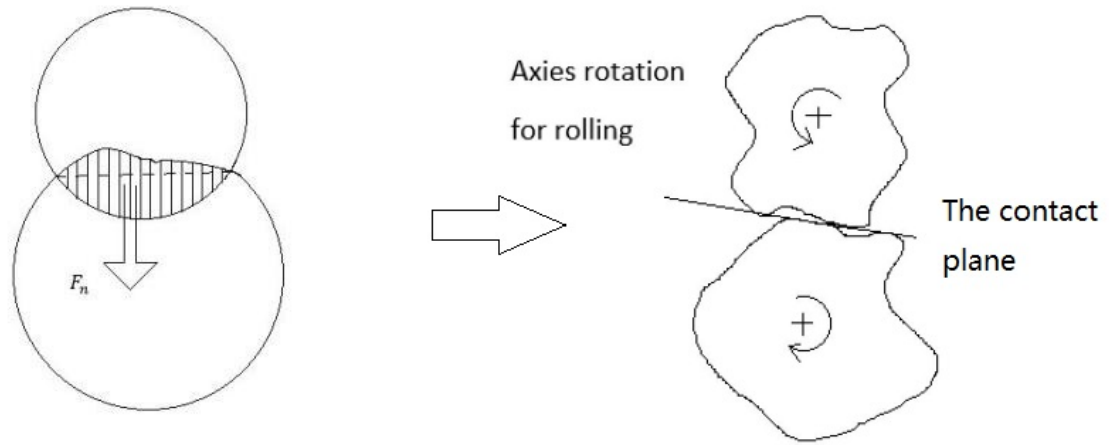
Figure 2-6: The decompose of calculating the relative tangential velocity



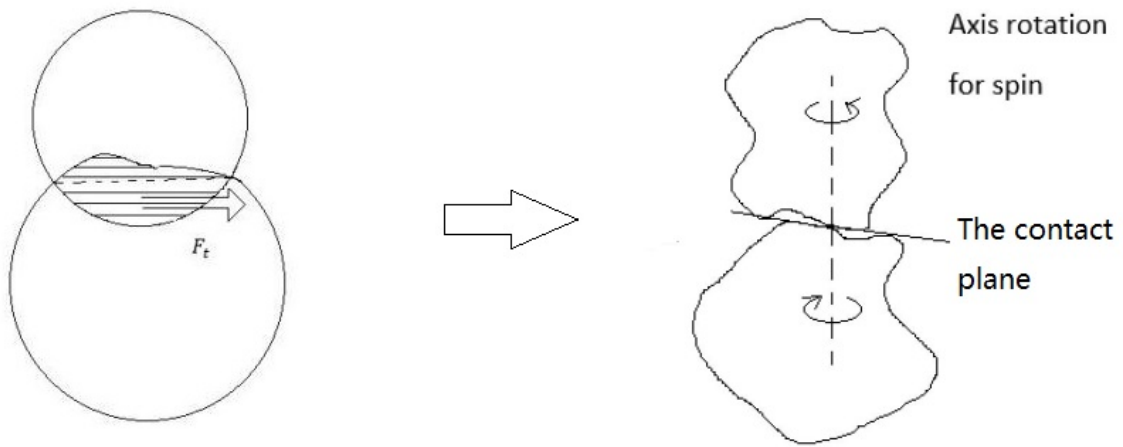
Tangential contact model

force-displacement relationship

Figure 2-7: Force-displacement response for tangential contact model

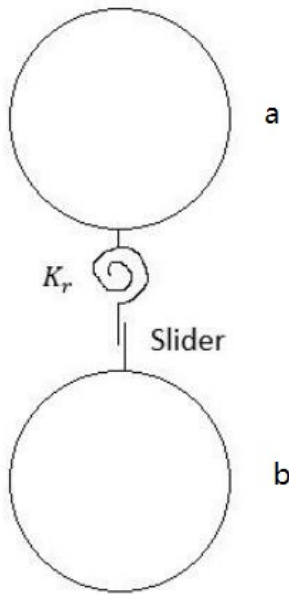


(a) The distributed normal stresses

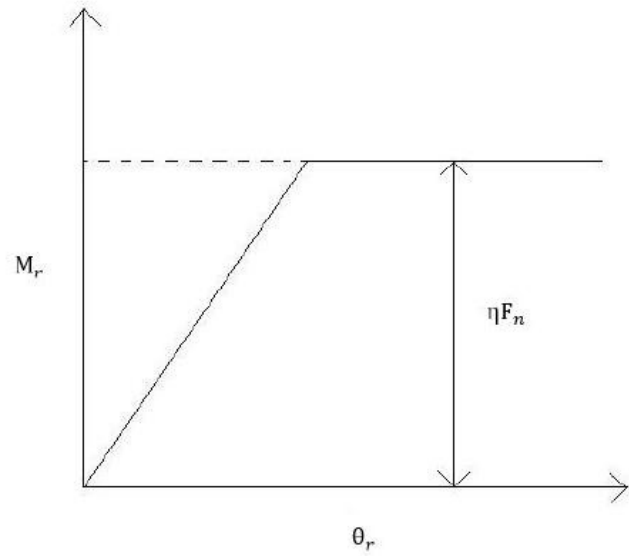


(b) The distributed tangential stresses

Figure 2-8: A figure shows unbalance distribution of stresses over the contact area and the related relative rotational motions

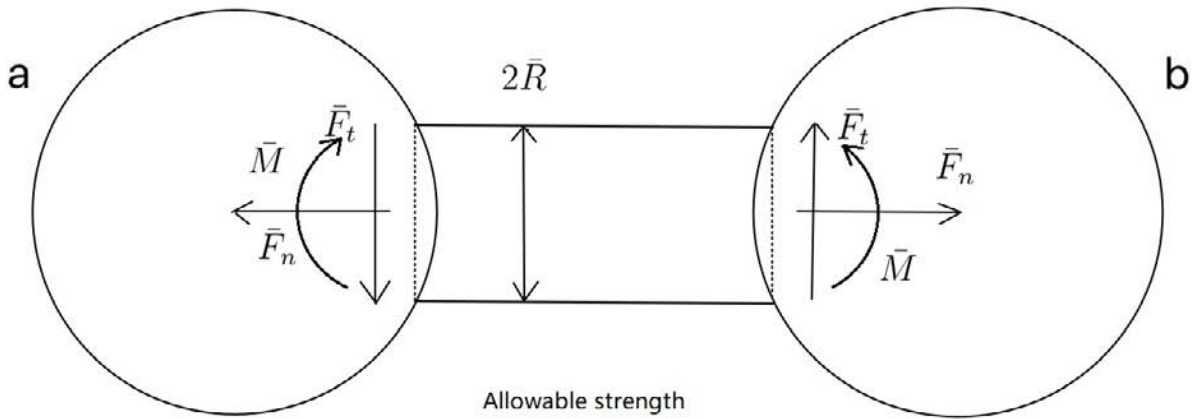


Rolling resistance model



force-displacement relationship

Figure 2-9: Force-displacement response for rolling resistance model



$$\bar{\sigma}^{max} = \frac{-\bar{F}_n}{A} + \frac{|\bar{M}_t|\bar{R}}{I}$$

$$\bar{\tau}^{max} = \frac{\bar{F}_t}{A} + \frac{|\bar{M}_n|\bar{R}}{J}$$

Figure 2-10: Cement behavior for bonded aggregates

$$\langle m \rangle \ddot{x} + C \dot{x} + Kx = 0$$

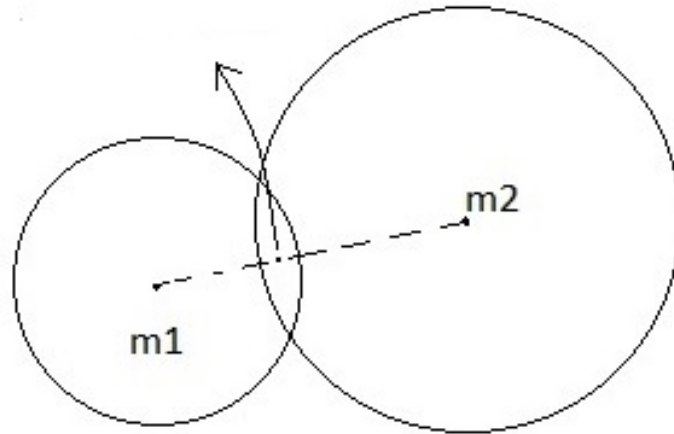


Figure 2-11: The scheme giving the dynamic equation at the mass center of the contact system

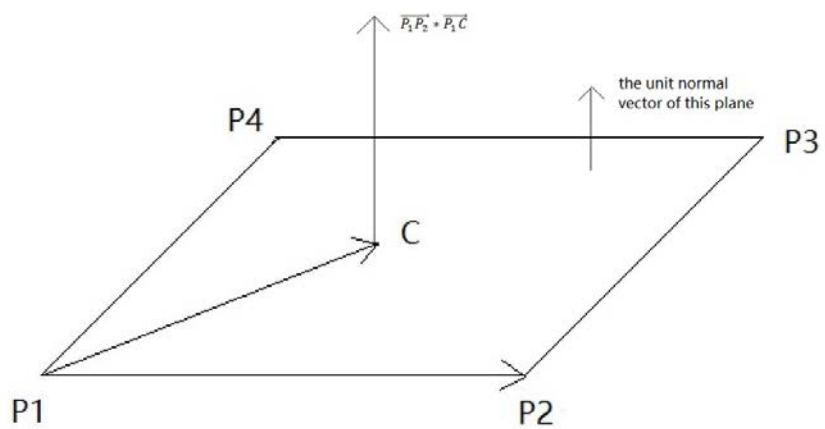


Figure 2-12: Condition for checking effective contacts within the finite rigid walls

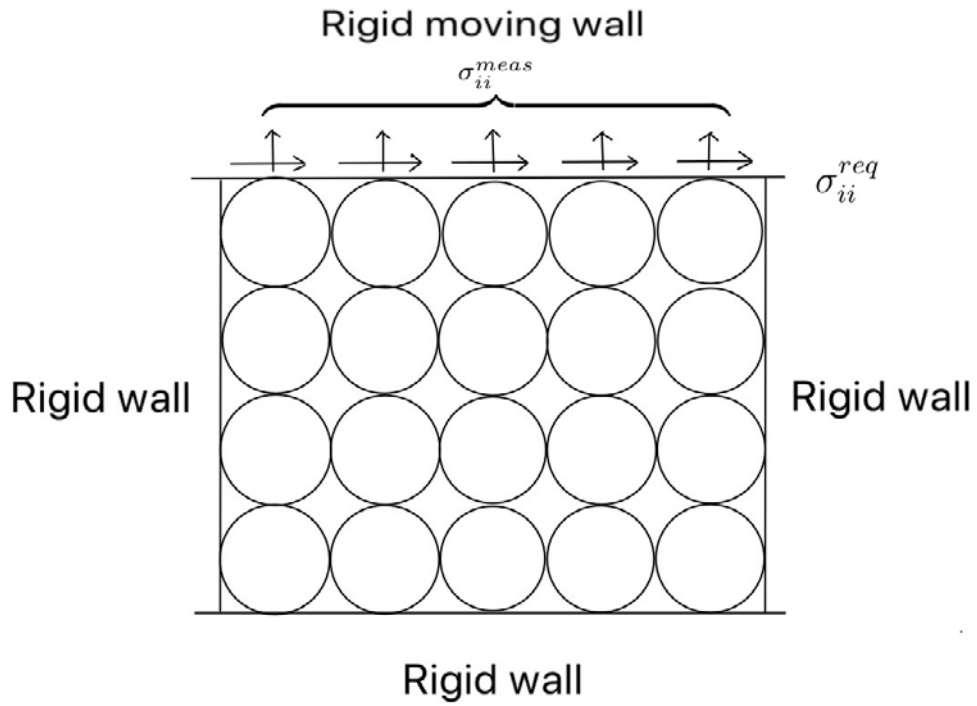


Figure 2-13: An example illustrating the application of rigid moving walls in 2D biaxial compression tests

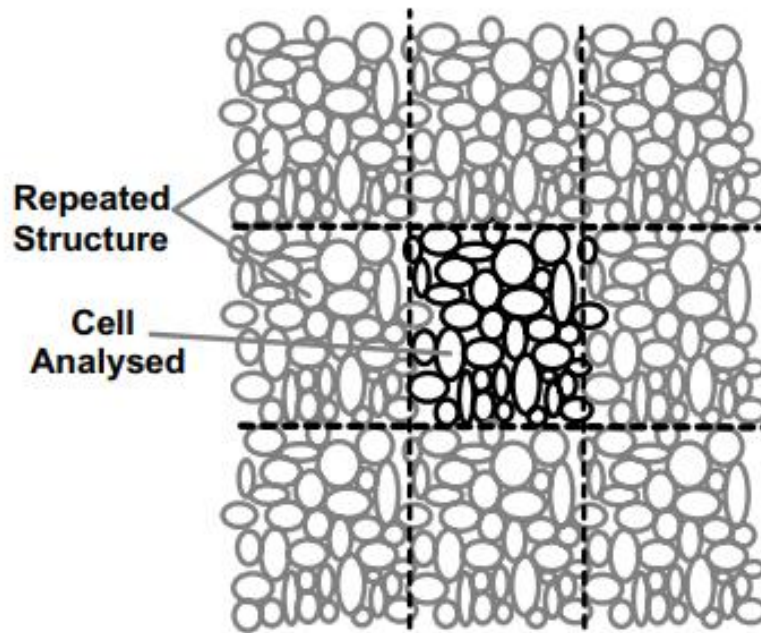


Figure 2-14: A scheme showing periodic boundary condition in 2D (O'Sullivan, 2011)

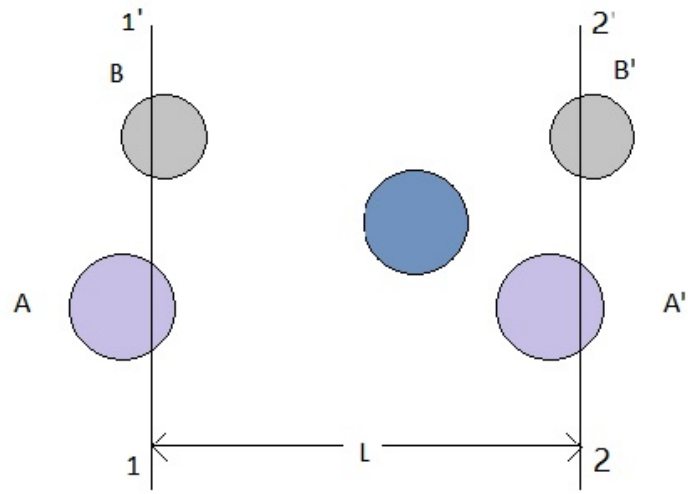


Figure 2-15: Particle behavior for periodic boundary condition in 1D

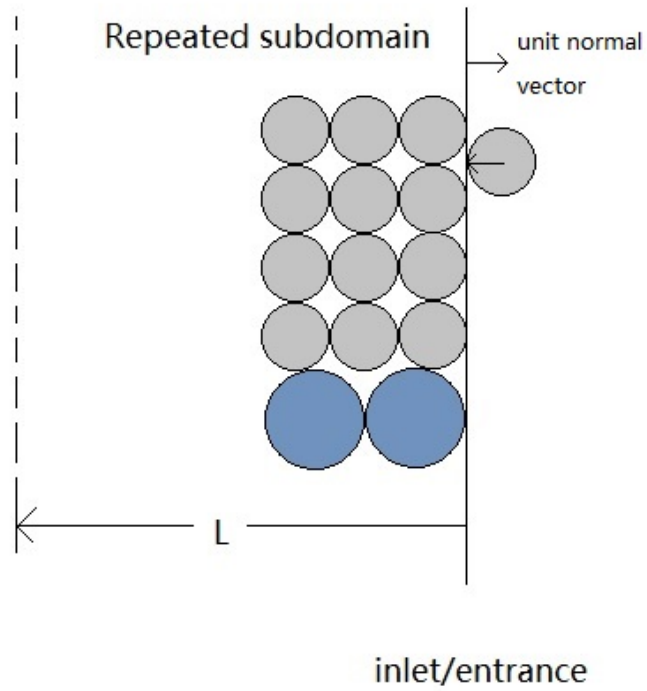


Figure 2-16: Application of periodic boundary condition for simulating inlet/entrance behavior

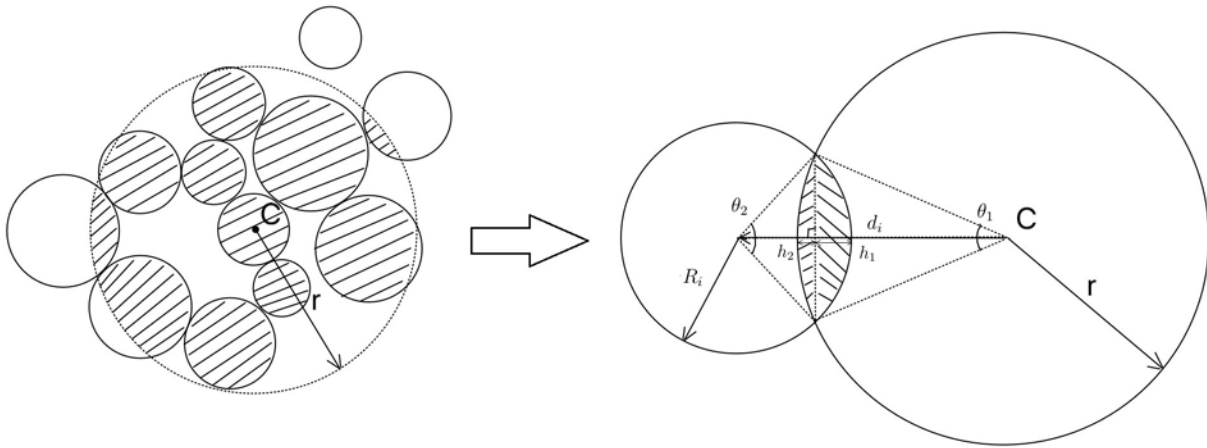


Figure 2-17: A scheme illustrating the algorithm of area calculation

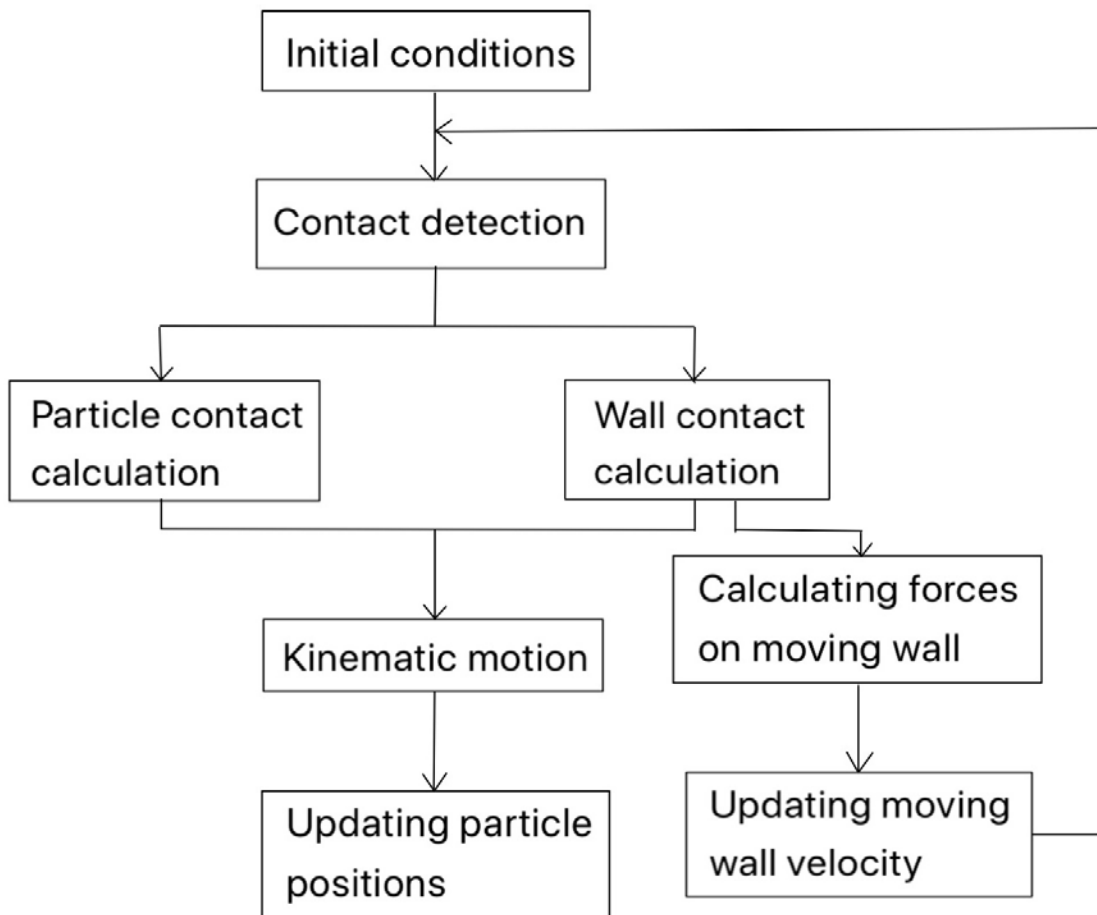


Figure 2-18: A flow chart illustrating sequence of calculations in simulated compression tests

CHAPTER 3: A MODIFICATION OF NON-LINEAR VISCO-ELASTIC DAMPING MODELS APPLIED IN DISCRETE ELEMENT SIMULATIONS

3.1 Overview

The Discrete element method (DEM) is a numerical modeling methodology which studies the behavior of individual particles and their interactions with other adjacent contacting particles. The general purpose of this method is to assist laboratory analysis to save testing time and space, reduce cost, and control output parameters.

In DEM simulations, dynamic equations are written for the mass center of individual particles. By summing all acting forces, particle motions are updated at distinct time intervals. So, the main difference between various studying models is dependent on the described force-displacement response between contacting particles. Up to now, numerous models are published for simulating the individual contacting forces/moments, including the normal force, tangential force, damping force, rolling resistance moment and so on. In practical applications, the combination uses of those models are also multifarious. However, no matter which one is applied, the selection criteria are easy for implementation and accurate for recovering physical phenomena. In this paper, a modified non-linear visco-elastic damping model is proposed. Non-linear springs are placed in the normal and tangential directions to imitate the contact forces. An additional non-linear spring is added for simulating the behavior of moment resistance. A viscous damping model which is relevant to the relative motion between contacting particles is employed for accounting the energy dissipation in the system. In our model, an alternative condition is utilized for checking the end of a collision, which extends the application of current DEM model to the over-damped system.

Through our analysis, it shows that the presented model can successfully imitate the tangential force behavior both in the stick and the sliding regions. A hypothesis unified the using of static and dynamic coefficients is provided for revealing the friction force behavior behind the contact phenomenon. Rather than using the static and the dynamic coefficients to determine the friction force behavior, the force response is determined by the relative motion. Finally, to validate the accuracy of current model, our DEM results are checked with authoritative benchmark tests. As a result, an updated version of benchmark tests is posed for future studies.

3.2 Introduction

The Discrete element method (DEM) by far is a well-developed approach for investigating the microscopic contacts between discrete elements. Different from the traditional Finite element method (FEM) which treats objects as continue materials, DEM is a powerful tool for analyzing materials made of granules and providing detailed information of internal structures.

DEM uses Newton's second law to describe the motion of individual particles. The summation of all acting forces on each particle is served as a driving power of particle motion. Although the general force types are clear, due to their difficult observation it is far from clear to know the micro-forces acting at particle level. As a consequence, in the past few decades, researchers have searched for approximate models to mimic the collision forces. The model for describing the contact force in normal direction was firstly proposed by Hertz while applying a set of non-linear formulations (Hertz, 1882). But Hertz theory is only fit for the elastic condition. As an advanced attempt, Maugis and Pollock (1984) considered a

piecewise elastic-plastic model. The inclined slope of the force-displacement response during loading is divided into two linear stages. Considering the complete loading history, using different spring stiffness Walton and Braun (1986) posed a linear elastic model to account the loading and unloading paths. Moreover, Tomas (1999) described his visco-plastic model which was able to calculate the dissipated energy in every collision along the normal direction. For the tangential force which is more complicated than the normal force, Mindlin and Deresiewicz (1953) laid the theoretical foundation. However, due to its unknown loading history and the difficult application, Cundall and Strack (1979a) provided their linear elastic spring model and limit the maximum tangential force by using the Coulomb friction force law. Unfortunately, mentioned by Di Renzo and Di Maio (2004), finding the linear spring stiffness from material properties is difficult. To overcome this shortage, Vu-Quoc et al. (2000) demonstrated a simplified version of the Mindlin-Deresiewicz model. The tangential stiffness is non-linear and is related to both of the normal contact force and the tangential force at the previous time step. In advance, another simplified version is proposed by Tsuji et al. (1992) and Di Renzo and Di Maio (2005) while the tangential force is calculated by using the normal displacement. More detailed information of developed history associated with this part is described later in this paper. In 1998, Iwashita and Oda treated their rolling resistant model as a necessary condition to consider the moment resistance effect. Inspired by Iwashita and Oda's work, a series of rolling resistance models was proposed by different researchers (Ai et al., 2011). Jiang et al. (2005) proposed a rolling resistance model which relates the application of Iwashita-Oda model to the contact area. Damping force model is an inevitable condition since it can damp out the non-physical phenomenon and simulate the energy dissipation during each contact. Mass damping are firstly applied by Cundall and

Strack (1979a). Since significant body forces are introduced, the application of this model is limited (Cundall, 1987; O'Sullivan, 2011). As a substitute, local non-viscous damping which treats the damping force as a component of the contact force is provided (Cundall, 1987) and utilized in commercial code PFC3D (Itasca, 2008). Recently, viscous damping model is developed (Cleary, 2000; Iwashita and Oda, 1998). The damping force is dependent on the relative motion of contact particles.

More complicated, the combinations of those models in real life is various. It's difficult for people to judge the accuracy of individual model combinations. Sometimes, because of model inaccuracy, the selection of related parameters is based on fitting the material overall response. This uncertainty may lose the insufficient to reveal the hidden truth. The application is based on the user-friendly, while the reliability of a DEM model depends on the accuracy of simulating the contact forces. To summarize the characteristics of previous models, a convenient applied and systematic model is provided in this paper.

The present paper is organized as follows. In Sec. 3, numerical models, model characteristics, and parameters selection are presented. The necessity of using an additional condition for determining the end of a collision in over-damped systems is clarified in Sec. 4. Subsequently, by describing the developed history of modeling tangential force, our purpose is aimed at checking the correction of current models and helping us make the judgment. As an advanced verification, our results are compared with the published benchmark tests in Sec. 5. Detailed discussion are made and a refined version is provided in this section. Finally, several conclusions are highlighted in Sec. 6.

3.3 DEM model Description

In DEM simulations, instead of considering the deformation of individual particles, particles are assumed to be rigid bodies. Assuming the relative movement is much more significant than particles deformation, studies are focusing on the relative motion. Dynamic equations are listed at the mass center of each particle. The interacting forces are introduced by the imagined tiny overlap at the contacts. A series of investigation are conducted by spherical particles in this paper.

3.3.1 Normal contact model

Simplified Hertzian contact model is applied for calculating the normal force between contacting particles. Without damping, the normal contact force is given as

$$F_n = K_n \delta_n \quad (52)$$

where K_n is the normal stiffness of the contact spring and δ_n is the overlap length along the line joining the centers of two particles. This equation aims at replicating the actual repulsing force between two elastic spheres with an easily applied non-linear format since $K_n \propto \delta_n^{\frac{1}{2}}$.

For individual particles p , the associated spring stiffness is calculated by

$$K_p = \frac{2G_p \sqrt{2R_p}}{3(1 - \nu_p)} \sqrt{\delta_n} \quad (53)$$

Meanwhile, the contact stiffness is a function of particle elastic shear modulus G_p , radius R_p and the Poisson's ratio ν_p . However, for a sphere-sphere contact with given particles a and b ,

the effective stiffness is in a series connection of individual springs; while, for wall contacts, the normal stiffness is doubled as the overlap is half smaller.

$$K_n = \begin{cases} \frac{2K_a K_b}{K_a + K_b}, & \text{for particle contacts} \\ 2K_p, & \text{for wall contacts} \end{cases} \quad (54)$$

3.3.2 Tangential contact model

A modified version of the simplified Mindlin-Deresiewicz tangential contact model has been proposed for describing the tangential force response during a collision. The tangential force and the normal force are sharing the same acting area. Explained by Mindlin (1949) and insight by Maw et al. (1976), generally for tangential forces the contact area is containing "sticking" and "slipping" regions.

In the same viewpoint of calculating the normal force, the primary objective is to correctly find the stiffness of the tangential contact spring and the overlap length between two particles along the tangential direction. As in the real phenomenon spheres should have same properties in every directions, the tangential stiffness in our model is setting as $K_t = K_n$. Therefore, the tangential stiffness is consequently linked to particle properties that easily overcomes the drawback of using linear spring models. In stick regions, particles at contact points are moving at different rates. The relative velocity results in the relative movement at the contacts which is acting in the opposite directions for the relevant particles. This relative velocity has the contribution both coming from the translational velocity of particles and the rotational velocity respect to each particle centroid. In the three-dimensional (3D) case, the relative velocity $\dot{\delta}_i$ of particle a respect to particle b at the contact point is calculated by

$$\dot{\delta}_i = [v_i^b + e_{ijk}\omega_j^b (x_k^C - x_k^b)] - [v_i^a + e_{ijk}\omega_j^a (x_k^C - x_k^a)] \quad (55)$$

where v^b and v^a are translational velocities; e_{ijk} is the alternating tensor; x_k^C , x_k^b and x_k^a are the locations of the contact point C and the centroids of particles a and b , respectively; ω^b and ω^a are the rotational velocities. The subscript i , j and k mean variables are given in indicial notation. To find the tangential part, variables need to subtracting the normal components. An example of calculating the relative tangential velocity δ_i^t in 2D case is

$$\dot{\delta}_i^t = \dot{\delta}_i - \dot{\delta}_i^n = \dot{\delta}_i - \dot{\delta}_j n_j n_i \quad (56)$$

$\dot{\delta}_i$ is the total relative velocity at the contacts; while $\dot{\delta}_j n_j$ give this variable in tensorial notation. When this value is multiplied by the unit vector n_i , it represents the normal components which acting along the line connecting particle centroids. By integrating this tangential relative velocity over the acting time, a phase “the cumulative tangential displacement” is able to depict the tangential overlap which records the relative tangential motion at the contacts. Hence, if an effective collision happens and the contact region remains “stick”, the tangential force at time t is given by

$$F_t(\delta_t, \dot{\delta}_t) = K_t \int_{t_0}^t \dot{\delta}_t dt \simeq K_t \sum_{t_0}^t \dot{\delta}_t \Delta t \quad (57)$$

$F_t(\delta_t, \dot{\delta}_t)$ means the tangential force is given in a form of the tangential displacement δ_t and the relative tangential velocity $\dot{\delta}_t$. t_0 is the initial time when a contact is firstly detected or

formed. Since the DEM simulation studies values at time intervals, the integration can be replaced to a summation.

Once sliding occurs, same as Cundall and Strack (1979a) presented, the tangential force is limited by the Coulomb friction force law which calculates the tangential force in a case of the normal force.

$$F_t = \mu F_n \quad (58)$$

where μ is the dynamic friction coefficient related to particle asperities. This force is still acting on the opposite direction of the relative tangential velocity as a resistance. Following the same format provided by O’Sullivan (2011), the general form of tangential force is illustrated as

$$F_t = -\min(|\mu F_n|, F_t(\delta_t, \dot{\delta}_t)) \frac{\dot{\delta}_t}{|\dot{\delta}_t|} \quad (59)$$

A significant emphasize. The determination of this minimum value needs to be checked in every time steps instead of the overall value. The relevant force calculated at time t will be used for updating the corresponding value at time $t + \Delta t$.

3.3.3 Rolling resistant model

Moments between contacting particles can be transmitted by not only forces but also the rolling resistance due to surface asperity or unbalancing stresses distribution. Taking account such effects, a well-known Iwashita-Oda rotational resistance model is located at the contact points parallel with the normal and tangential springs (Iwashita and Oda, 1998).

Similar to the tangential force, when a relative rotation is generated the rolling resistance spring transmits a moment M_r from one to the other. Prior to sliding, the moment is provided by the following form

$$M_r(\theta_r, \dot{\theta}_r) = K_r \int_{t_0}^t \dot{\theta}_r dt \simeq K_r \sum_{t_0}^t \dot{\theta}_r \Delta t \quad (60)$$

K_r is the rolling spring stiffness; $\dot{\theta}_r$, which is also known as ω , gives the relative angular velocity between moving particles. Iwashita and Oda (1998) explained that the definition of incremental relative rotational velocity keeps the same meaning as particle incremental relative velocity, but it gives as $\omega_i^b - \omega_i^a$. An amazing hypothesis. Since the incremental rotation has the same format as the used relative tangential increment, assuming the torque induced by the rolling resistance has the same magnitude as the moment caused by friction, Iwashita and Oda (1998) proposed that the expression of the rolling stiffness is $K_r = K_t r^2$.

The maximum value of M_r is ηF_n , where F_n is the normal contact force as described before and η is the rolling friction coefficient that is related to the surface asperity or the eccentricity of particle centroid. Keeping the same format as the provided tangential force, the transmission moment can be written as

$$M_r = -\min(|\eta F_n|, M_r(\theta_r, \dot{\theta}_r)) \frac{\dot{\theta}_r}{|\dot{\theta}_r|} \quad (61)$$

3.3.4 Viscous damping model

Currently, models are elastic before yielding. Meanwhile, no energy is dissipated prior to sliding. In this case, particles will keep oscillating at their original places. To avoid

this non-physical phenomenon, damping needs to be included in order to damp out these non-physical vibrations (Munjiza, 2004).

Different from the traditional uses of the local non-viscous damping that the damping force is proportional to the out-of-balance force, our damping force is calculated based on the relative motion between particles during the impact. For the active forces, dashpots are placed along the normal and tangential directions accompanied with contact springs. The relevant coefficients are given as C_n and C_t . Dashpots stop working when spring breaks or sliding happens. The damping forces in both directions are shown as

$$\begin{aligned} F_{dn} &= C_n \dot{\delta}_n \\ F_{dt} &= C_t \dot{\delta}_t \end{aligned} \tag{62}$$

F_{dn} and F_{dt} are the normal and tangential components of damping force, while $\dot{\delta}_n$ and $\dot{\delta}_t$ are calculated in the same format as mentioned before. Through our model, it shows that less energy is dissipated in the high velocity impact (Brilliantov et al., 1996; Delaney et al., 2007).

Mentioned by Cleary (2000), the damping coefficient is related to the restitution coefficient ε which describes the energy dissipated per cycle (O’Sullivan, 2011) or a percentage ratio measured by the velocity before and after a collision (Luding, 1998). Coefficients are shown as

$$C_n = 2\gamma\sqrt{\langle m \rangle K_n}, \quad C_t = 2\gamma\sqrt{\langle m \rangle K_t} \tag{63}$$

$\langle m \rangle$ is the effective mass of the system or also keeps the same name as the reduced mass in

Cleary's paper (2000) determined by $\frac{m_a m_b}{m_a + m_b}$ (Luding, 1998). Parameter γ is in a form of the restitution coefficient ε as follows:

$$\gamma = -\frac{\ln(\varepsilon)}{\sqrt{\pi^2 + \ln(\varepsilon)^2}} \quad (64)$$

After considering the damping force, the complete form of the normal and the tangential forces are illustrated as

$$\begin{aligned} F_n &= K_n \delta_n + C_n \dot{\delta}_n \\ F_t &= -\min\{\mu F_n, K_t \int \dot{\delta}_t dt + C_t \dot{\delta}_t\} \end{aligned} \quad (65)$$

Similar to forces, Ai et al. (2011) highlighted the necessary condition as adding a damper to the moment resistant model. Referred to Iwashita and Oda (1998), Ai et al. (2011), and Wensrich and Katterfeld (2012), the damping rate C_r is explored by

$$C_r = 2\gamma\sqrt{\langle I \rangle} K_r \quad (66)$$

$\langle I \rangle$ is the effective moment of inertia calculated through $\langle I \rangle = \frac{I_a I_b}{I_a + I_b}$. So the calculated moment becomes

$$M_r = -\min\{\eta F_n, K_r \int \dot{\theta}_r dt + C_r \dot{\theta}_r\} \quad (67)$$

3.4 Investigation of Tangential Force Response

In DEM simulations, forces acting between contacting particles are decomposed into the normal and tangential directions. Although the normal and tangential forces are sharing

the same contacting area and contacting time, the selected force-displacement models for describing the normal and tangential forces are decoupled. The basic assumption is that the normal force in the contact zone will not be influenced by the tangential force, but the acting time of the tangential force is determined by the normal force.

3.4.1 Alternative condition for checking the end of a collision

To investigate the tangential force response, the first step is to correctly determine the active time. Normally, when Hertzian theory is employed for detecting the normal force response, the end of a collision is determined by the magnitude of an overlap. In 1970, Timoshenko and Gooider proposed the equation for calculating the duration of contact time T respect to two identical spheres impact with velocities V_1 and V_2 .

$$T = 2.943 \left[\frac{5\sqrt{2}\pi\rho(1-\nu^2)}{4E} \right]^{\frac{2}{5}} \frac{R}{V_{rela}^{1/5}} \quad (68)$$

ρ , ν and E are particle density, Poisson's ratio and Young's modulus, respectively. r is the radius, while $V_{rela} = V_1 + V_2$ gives the relative velocity of these two spheres. V_1 and V_2 are the incoming velocities. Since there is no damping factors, their equation is only fit for the condition of elastic contacts.

In our DEM model, damping force is calculated by the relative motion. If particles are in high velocity contact, extremely high damping force will be encountered. Therefore, a "kicking problem" was experienced in our simulation. Some particles experienced energy increment and caused other particles to unnaturally exit the control volume. If the non-viscous damping model is employed, the damping force is set to be proportional to the

out-of-balance force. So, the related DEM models never experience such kind of problem.

By plotting the evolution of the normal force in arbitrary units as a function of damping ratios in **Fig. 3-1**, Luding (1998) highlighted that using the overlap to depict the end of a collision is insufficient for damped systems. t_c is the elastic contact time calculated by the above equation provided by Timoshenko and Gooider (1970). The figure shows that the contact normal force has a finite value at the beginning of the contact with $t = 0$. Luding clarified that this is caused by the application of the viscous damping term. However, as increasing the viscosity normal forces quickly go downward to the negative values even still in the duration. So, when this difference or the damping force is small, the condition can approximately provide the results for checking the ends. Otherwise, results become worse as encountering an over-damped system. To fix this condition, an alternative checking condition proposed by Luding (1998) is utilized to decide the ending state, $f^{(n)}(t_f^d) = 0$ where $f^{(n)}$ is the normal force and t_f^d is the duration of the contact respect to the damping systems.

3.4.2 Tangential force-displacement response

The general tangential friction force contacts two parts: the static friction force and the dynamic friction force. As we know, the dynamic friction force can be described by the Coulomb friction force law. However, no one clearly understands the basic principal of the static friction force, especially for the dynamic systems. This problem is easy to solve as using the Finite Element Method. By listing equilibrium equations of individual objects, the static friction force acting at the contact surface can be calculated. In DEM simulations, various publications are tried investigating the tangential force-displacement behavior. The complete version was original proposed by Mindlin and Deresiewicz (1953).

Due to its complicity which involves the loading history, Maw et al. (1976) posed another analytical expression in order to catching up the equivalent solution. They successfully recover the tangential force response in the stick regime without conducting a whole loading history analysis. They divided the contact area into a set of concentric annuli and gave the approximated function for the tangential displacements within each annuli. A figure demonstrating the tangential force-displacement response at intermediate angle is shown in **Fig. 3-2**. Since no damping force is considered, their solution can only be used for describing elastic systems.

Besides Maw et al.'s work, another early attempt is produced by Brilliantov et al. (1996). They list the dynamic equations and presented the initial averaging geometry conditions of the contacting surface. Their results displayed that the tangential force was transmitted between contacting particles as a factor of surface asperities. In the case of exceeding a crucial condition, which is known as the surface fracture, macroscopic shift happens. In their expression, the tangential force is illustrated as

$$F_t = -\mu F_n \left(\frac{\delta_t}{\delta_{t0}} - \left\lfloor \frac{\delta_t}{\delta_{t0}} \right\rfloor \right) \quad (69)$$

here $\lfloor x \rfloor$ is an operator calculating the integer value of x . The phenomenon behind their analysis is named as a saw-tooth condition and the correlated value is limited to the Coulomb friction force (Brilliantov et al, 1996; Kruggel-Emden et al., 2008). The corresponding expression of the sketched evolution of the tangential force during the impact is presented by Kruggel-Emden et al. (2008) in **Fig. 3-3**. From this figure, it is clear that when the impact angle is small, tangential force will flip signs and the magnitude is limited to the

value given by the Coulomb friction force law. Otherwise, there is no change in sign.

Mindlin and Deresiewicz (1953) built the foundation of the basic tangential force model applied in DEM simulations. The tangential force in upcoming time step F_t^{i+1} is calculated from the tangential force in the previous time step F_t^i , the change of the elongation of the spring $\Delta\delta_t^i$ and the related spring stiffness K_t^i .

$$F_t^{i+1} = F_t^i + K_t^i \Delta\delta_t^i \quad (70)$$

Starting from this opinion, based on the elongation configuration of the spring and its limitation, three models are commonly used in literature. Cundall and Strack (1979a) firstly proposed linear spring models for estimating the normal and tangential forces during the contact. The tangential force is given by the minimum value of the force stored in the spring and the Coulomb force.

$$F_t = -\min(|K_t \delta_t|, |\mu F_n|) \cdot \text{sign}(\delta_t), \text{ where } \delta_t = \int_{t_0}^t \dot{\delta}_t dt \quad (71)$$

Same as our proposed model, the elongation of the tangential spring or the relative displacement along the tangential direction is calculated by the integration of the relative velocity at the contact points. If the Cundall-Strach spring model is combined with the Tomas model (2003) which describes the normal force in visco-plastic behavior, the basic three tangential force-displacement modes according to the different incident angles are published by Kruggel-Emden et al. (2008) in **Fig. 3-4**.

Mentioned by Brendel and Dippel (1998), because the direction of the tangential force is related to the elongation, it does not allow the reversal of $\dot{\delta}_t$. Furthermore, an arbitrary

elongation of the spring during the sliding phase needs a long time for spring relaxation. As an improvement, a modification of the original Cundall and Strack model was posted by Brendel and Dippel (1998). They kept using original assumption of the tangential force. Alternatively, instead of cutting off the force, they froze the elongation of the spring at the threshold.

$$F_t = - | K_t \delta_t | \cdot \text{sign}(\delta_t), \text{ where } \delta_t = \int_{t_0}^t \dot{\delta}_t \Theta(\mu | F_n | / K_t - | \delta_t |) dt \quad (72)$$

where Θ is the Heaviside function. This model correctly presents the tangential force before reaching the Coulomb limit. However, pointed by Kruggel-Emden et al. (2008), since the elongation of the spring is not identical to the displacement experienced by the contact point this method fails to predict the tangential force as it goes back to the stick region. The corresponding response is demonstrated in **Fig. 3-5**.

To get rid of the frozen tangential force and the inconsistent displacement at the contacts, instead of changing the expression of the relative displacement Di Maio and Di Renzo (2004) limited the elongation of the spring to a specific value calculating based on the Coulomb friction force. The tangential force is given as

$$F_t = - | K_t \delta_t | \cdot \text{sign}(\delta_t), \text{ where } \delta_t = \min\left(\int_{t_0}^t \dot{\delta}_t dt, \frac{\mu | F_n |}{K_t}\right) \cdot \text{sign}(\delta_t) \quad (73)$$

The evolution of the tangential force with a constrained tangential spring at different impact angles is presented in **Fig. 3-6** (Kruggel-Emden et al., 2008). Pretty good performance is achieved in this case with little difference contained in the position of inflection points (Kruggel-Emden et al., 2008).

Since it's difficult to link the stiffness of a linear spring to material properties, non-linear tangential spring models are utilized. Vu-Quoc et al. (2000) firstly employed the piecewise linear spring stiffness to their model. The tangential stiffness K_t^i is given as a combination result of the normal force F_n^i , the tangential force at the current time step F_t^i , and the inflection point F_t^{i*} which is initially zero and records the inflection points as F_t^i reverses its direction, and the dynamic friction coefficient μ .

$$K_t^i = \begin{cases} K_t^0 \left(1 - \frac{F_t^i - F_t^{i*}}{\mu F_n^i - F_t^{i*}}\right)^{1/3} & \text{for } F_t \text{ increasing} \\ K_t^0 \left(1 - \frac{F_t^i - F_t^{i*}}{\mu F_n^i + F_t^{i*}}\right)^{1/3} & \text{for } F_t \text{ decreasing} \end{cases} \quad (74)$$

where K_t^0 is the initial tangential stiffness.

Otherwise, Tsuji et al. (1992) proposed a different approach the stiffness of the tangential spring is coupled to the normal displacement in a non-linear function. The benefit of this approach is that it easily connected to the non-linear model without adjusting any special parameters. This models is employed in EDEM (DEM Solutions, 2014). However, at first, this model is only valid for a fully elastic analysis. To extend this application to widely impact angles, a modified version is suggested by Di Renzo and Di Maio (2005). The tangential force is showing as

$$F_t = \frac{2}{3} \cdot K_t \cdot \delta_t = \frac{2}{3} \cdot 8G_{eff} \sqrt{R_{eff}} \cdot \delta_t \quad (75)$$

where δ_t keeps the same expression as Cundall and Strack's work. The effective shear modulus and the equivalent radius are given as $G_{eff} = \left(\frac{2-\nu_i}{G_i} + \frac{2-\nu_j}{G_j}\right)^{-1}$ and $R_{eff} = \left(\frac{1}{R_a} + \frac{1}{R_b}\right)^{-1}$.

The tangential displacement is limited by $\delta_t = \frac{\mu F_n}{K_t}$.

In practical applications, normal and tangential models are applied in arbitrary combinations. When the normal force is calculated using a linear visco-elastic damping model, combined with Cundall and Strack tangential spring six collision modes are provided in **Fig. 3-7** (Kruggel-Emden et al., 2008). However, in this case, due to the non-zero normal force the non-zero Coulomb friction force at the beginning and the end of the contact are caused. If the visco-elastic spring damping model is combined with a strained tangential spring the number of modes is reduced to five in **Fig. 3-8** (Kruggel-Emden et al., 2008). In our analysis, when a non-linear visco-elastic Hertzian contact model is coupled with our proposed tangential model, four basic modes are included for describing the evolution of tangential force (**Fig. 3-9**). Our results got good performance with previous results. It shows a pre-sliding at the beginning of the contact. Tangential force can flip signs during a collision. The difference at the end of a contact is due to the application of different conditions for checking the ends. Our results also show a perfect matching with Maw et al.'s (1976) analytical solution.

3.4.3 Transition between stick and sliding regions

Except for checking the force-displacement response, relation between the incident and reflection angles is another quantitative parameters for estimating the behavior of tangential force. In 1998, Luding provided a scheme of velocity ratio $\Psi_1 (= \frac{V_{st}}{V_{cn}})$ versus $\Psi_2 (= \frac{V'_{st}}{V'_{cn}})$ while applying different tangential force laws. The related response is presented in **Fig. 3-10**.

Comparing his results with one figure achieved from our DEM results in **Fig. 3-11**, a clear transition zone appears. With increasing the damping ratio, the calculation rule automatically moved from using the viscous tangential force law to the applied Coulomb

friction force law. Through our analysis, this is due to effect that whether the rotational velocity is taken into account or not since the relative velocity is calculated by using the following equations.

$$\dot{\delta}_i = \begin{cases} [v_i^b + e_{ijk}\omega_j^b(x_k^C - x_k^b)] - [v_i^a + e_{ijk}\omega_j^a(x_k^C - x_k^a)] & \text{in } \textit{stick} \\ v_i^b - v_i^a & \text{in } \textit{sliding} \end{cases} \quad (76)$$

Similar results obtained from Brilliantov et al. (1996). The friction coefficient is in a mutual coupling function between two contacting particles. Due to the fact that the friction force is only measured by using $v_i^b - v_i^a$, these equations help explain why the static friction coefficient μ_s is always higher than the dynamic friction coefficient μ_d . In the stick region, the relative velocity should be considered as $[v_i^b + e_{ijk}\omega_j^b(x_k^C - x_k^b)] - [v_i^a + e_{ijk}\omega_j^a(x_k^C - x_k^a)]$ instead of $v_i^b - v_i^a$. Hence, in order to unify the performance of friction coefficients (μ_s and μ_d), only if the pure sliding happens or the complete surface fracture occurs, the relative velocity is calculated by the second equation; otherwise, the normal velocity should be a value between these two, e.g. $[v_i^b + \mu_R e_{ijk}\omega_j^b(x_k^C - x_k^b)] - [v_i^a + \mu_R e_{ijk}\omega_j^a(x_k^C - x_k^a)]$ where μ_R is a reduction factor.

3.5 Numerical results for Benchmark Tests

Discrete element method is a numerical simulation approach that simulates the mechanical properties of soil and other granular materials by calculating the acceleration achieved by all acting forces. It is necessary to validate the correction of DEM codes at particle impact level to insure the proposed models are proper. A set of benchmark tests designed by Chung and Ooi (2011) were utilized for validating DEM codes and summarized in **Table**

3-1. All material properties and input variables are listed in **Table 3-2**. A sequence of results obtained by our DEM code is compared with the existing published results, simple analytical solutions, or the experimental data. Comparison listed here are not only limited to the verification of current code, but also enhance our understanding of forces behavior during an impact.

Before showing our results, some important variables are denominated in **Fig. 3-12** to help us understand the following results and consequently make judgments. c is the abbreviation of “center”. Lower letter “s” shows the contact point. n and t indicate the components of contact force, including the normal and tangential forces. Variables with prime imply the state of those variables. V_{cn} , V_{ct} , and ω are normal contact velocity, tangential contact velocity and angular velocity of the centroid before collision, respectively, V_{st} is the pre-collision tangential velocity at the contact point; whereas V'_{cn} , V'_{ct} , V'_{st} and ω' denote the corresponding post-collision values after the collision. In this section, numbers 1 and 2 mark the number of spheres. All positive direction of these variables are shown in this figure. Using the same parameters provided by Chung and Ooi (2011), the normal and tangential restitution coefficients at the mass center, and the tangential coefficient at the contact point are defined as the following forms.

$$e_n = -\frac{V'_{cn}}{V_{cn}}; e_t = -\frac{V'_{ct}}{V_{ct}}; \beta = -\frac{V'_{st}}{V_{st}} \quad (77)$$

These three coefficients measure the energy dissipated per cycle/contact. However, since the rolling coefficient is absent no rolling resistance is involved in their analysis.

Test 1: Elastic normal impact of two identical spheres

Test 1 considers the elastic normal impact of two identical spheres with the same magnitude velocity but in opposite directions. The objective is to correctly give the overlap and the contact stiffness at contacts based on the existing mechanical and geometry properties. The incoming velocity is setting as 10 m/s. Comparing with Chung and Ooi's work (2011) in **Figs. 3-13** and **3-14**, our DEM model results get exactly same results with the published ones. Since the restitution coefficient is set to unity, no energy is dissipated during a collision. The elasticity is also shown as a coincidence appeared between the loading and unloading paths for the force-displacement curve and the symmetric shape of the force evolution presented respect to the time.

Test 2: Elastic normal impact of a sphere with a rigid plane

Test 2 studies the elastic normal impact between a sphere and a rigid wall. This test aims at appropriately describing the normal force for wall contacts. Setting the normal restitution coefficient to be a unit representing no energy dissipation occurs. The force-displacement response and the force evolution are investigated in **Figs. 3-15** and **3-16**. Keeping the same assumption as Cundall and Strack (1979a) did, a contact in wall condition has the equivalent effect as a collision happened between two identical spheres. The normal contact stiffness for a wall contact is doubled since the overlap in this case is half smaller. Through the comparison, an excellent matching is shown between our DEM results and the published ones.

Test 3: Normal contact with different restitution coefficients

Test 3 verifies the normal impact of a sphere with a rigid wall but varying with different restitution coefficients (or different damping ratios). This test aims at investigating the damping effect. As a straight line appears in Chung and Ooi's (2011) results, it's confident to believe that local non-viscous damping model has been utilized for their testing. The damping coefficient is setting to be proportional to the energy loss ratio. Declared by Chung and Ooi, the restitution coefficient is assumed to be a constant in their mathematical analysis. In reality, the dissipated energy should be a function of the incoming velocities. Brilliantov et al. (1996) and Luding (1998) also explained that the damping effect should depend on not only the material properties but also the relative motion at the contact. For a single particle contact, the difference between these two definitions is small. However, when dealing with a group of particles, calculating respect to the energy loss ratio becomes an empirical method since without testing it's difficult for people to get the rid of the velocity effect. Even with same particles, after changing the incoming velocity the damping coefficient needs to be re-tested. In contrast, using the viscous damping model, for the contact with different materials, the restitution coefficient only needs to be tested once. Through these viewpoints, it's confident to say our results are more close to the realistic condition. Because different damping models are employed for analysis, slight discrepancies can be found between our numerical results and the published ones as shown in **Fig. 3-17** and **3-18**. As a side, after closing the damping force calculation, our DEM model can exactly hit the zero value meanwhile no energy has been dissipated.

Test 4: Oblique impact of a sphere with a rigid plane with a constant resultant velocity but at different incident angles

A sphere impacts a rigid wall with a constant resultant velocity but at different incident angles is conducted in Test 4. It is well known as oblique contact. The resultant velocity V was set as 3.9 m/s. θ is the incident angle varied from 5° to 85° . Results here are also compared with the experimental data achieved from Kharaz et al. (2001) in **Figs. 3-19 ~ 3-24**.

Comparing with the published results, the presented DEM code perform a great agreement with Chung and Ooi's work. The tiny different with the experiments at small angles impact is caused by the ignorance of applying moment resistance since the rolling friction parameter is not provided. An interesting thing. Although the tangential velocity at contact point has the contribution coming from the translational velocity and the rotational velocity (Cundall and Strack, 1979a; O'Sullivan, 2011), there is a perfect matching with the Coulomb friction force in sliding regimes. Meanwhile, when sliding happens, the tangential force is related to the translational velocity only. It might due to a reduction of irregular surface fitness happens in the sliding region.

Test 5: Oblique impact of a sphere with a rigid plane with a constant normal velocity but different tangential velocities

Test 5 validates the case where a sphere contacts a rigid plane with a constant normal velocity but at different tangential velocities. The normal velocity keeps as a constant of 5 m/s, while the tangential velocity varies between 0.1 and 70.0 m/s. Similar to the Test 4, the main purpose of Test 5 is studying the behavior of tangential force in the stick and slip

regions. To get rid of the damping effect, setting the restitution coefficient to a unit has simplified the studied problem. From **Figs. 3-25** and **3-26**, the current DEM results matches perfectly with the analytical solution demonstrated in Chung and Ooi's paper (2011) and the FEM results provided by Wu et al. (2003). Maw et al.'s (1976) method was an analytical solution, but it can only be referred for the elastic condition. As the FEM approach uses the equilibrium equation to solve the forces, it is able to restore the friction force behavior in the stick region. The lower ratio of $\frac{V'_{st}}{\mu V'_{cn}}$ appeared in their work before sliding is due to the Hertz-Mindlin no-slip simplified model is insufficient to describe the tangential force behavior in stick region. Same observation can be found in the figure with axis of $\frac{r\omega'_1}{\mu V_n}$.

Test 6: Impact of a sphere with a rigid plane with a constant normal velocity but at different angular velocities

Test 6 tests the condition when a sphere impacts a rigid wall with a constant normal velocity but varying with different velocities. The constant normal velocity is 0.2 m/s. Angular velocities are varied from 0.175 to 22.86 rad/s. More complicated than Test 5, the restitution coefficient is set to 0.5. Meanwhile, damping effect needs to be taken into account. Analyzing **Figs. 3-27** and **3-28**, good agreements are achieved in the sliding regime, but big differences are shown in the stuck state. Velocity directions go back and forth with varied values of $[3.5\mu(1 + e_n)\frac{V_n}{V_s}]$. Particles keep stuck according to the mass center. Additionally, the slope of inclined lines also show discrepancies in the sliding regions for **Figs. 3-29** and **3-30**. As better results are gained for our Tests 3 and 5, it is reasonable to believe the correction of the current applied damping and friction models.

To deeply understand the internal contact behaviors, advanced studies are conducted

through **Figs. 3-31 ~ 3-34**. Under the same wall conditions, parameters varied with different restitution coefficients respect to these two materials are plotted. Without damping, the tendency of these varying variables are similar to the published ones. When using the local non-viscous damping model and changing the damping ratio to 0.5, reductions in stick region is similar to the published one. However, in current DEM results, as continue reducing the restitution ratio, deduction appears in the magnitude of inflection points of the β plots. Increasing the damping force will accelerate the flip sign frequency of the velocity in the stick regime and consequently stop the moving spheres. The deduction in velocity is related to material properties. In our examples, results show that spheres made of Nylon stop faster than those made of Al. alloy. Those phenomenons are matching perfectly with the reality.

Test 7: Impact of two identical spheres with a constant normal velocity and varying angular velocities

Test 7 studies the situation when two identical spheres collide with a constant normal velocity but at different angular velocities. Directions of normal and angular velocities between these two spheres are on the opposition sides. The normal velocity is 0.2 m/s, while the angular velocity varies between 0.175 and 22.86 rad/s. **Figs. 3-35 ~ 3-36** show the velocities at the mass center regarding to various angular velocities. Since tangential force only prevents the relative tangential motion of contact particles, there is no influence in the normal direction. Tangential velocities for Sphere 1 and 2 are showing zero values before and after the impact. Results are perfectly matching with the previous results. Same behavior is also found for angular velocities in **Figs. 3-37** and **3-38**. The whole system is symmetric about the contact plane. Without moment resistant system, no energy will be dissipated

in rolling friction. So, same variables are achieved for the pre-collision and post-collision angular velocities.

Test 8: Impact of two differently sized spheres with a constant normal velocity and varying angular velocities

Test 8 studies the collision between a small sphere and a big sphere which is stationary at original. The smaller sphere maintains the same contact behavior as demonstrated in Test 6. The density of the big is 1000 times bigger than the smaller one and the radius is 5 times larger. Two situations are considered here: a) shear modulus of the big sphere is 1000 times than that for the smaller one; b) the big sphere has the same mechanical properties as the smaller one. The goal of Test 8 is to give the effective contact stiffness as a function of the individual ones. Provided results show a significantly different behavior as Test 6 did in the stick region (**Figs. 3-39 ~ 3-46**). However, the slope of recoil angle $\frac{V'_{st}}{V'_{cn}}$ in the sliding region also contains slightly difference, especially in **Figs. 3-42 and 3-44**. Advanced studies are carried out through **Figs. 3-47 ~ 3-54**. When the density and the stiffness are large for big sphere, results can be compared with the condition of rigid wall in Test 6. Comparing with the previous one, the fluctuation in β plots gets smaller as the tiny movement of the big sphere helps release energy. This phenomenon accelerates the stopping of the smaller sphere; while in Test 6 energy is only dissipated by the contacting sphere. Same reduction is more obvious as illustrated in Case B. Because of the increased accuracy provided by the present model for prior tests, the results from these models may prove useful in providing additional comparisons for other DEM models in the future.

3.6 Summary and Conclusions

A nonlinear viscoelastic damping model has been proposed in this paper for detecting noncohesive contacts and compared with published results for future use. A general Hertz model is used for describing the normal force, while an improved nonlinear spring tangential model has been introduced for simulating the tangential force response that captures the key mechanics while avoiding the entire loading history. The rolling friction force associated with surface asperities is included in this model. The damping force is calculated based on the relative velocity between contacting particles and an alternative condition for checking the end of a collision has been extended to fit over-damped systems. Through investigating the evolution of the tangential force and comparing with published results in literature, the present model is able to recover the tangential force response in both stick and sliding regimes.

Using the numbering scheme and benchmark tests of Chung and Ooi (2011), the following conclusions can be drawn:

1. Comparisons with the solutions identified by Chung and Ooi (2011) for Tests 1, 2, 4, and 7 yields virtually identical results.
2. For Test 3, the present model allows for a varying coefficient of restitution, yielding slightly different and quite possibly better results than those of Chung and Ooi (2011).
3. For Test 5, the present model provides better agreement with existing FE and analytical results than comparative models in Chung and Ooi (2011).
4. For both Test 6 and 8, the present model is in excellent agreement with the benchmark results for sliding regions. In sticking contact, the results are noticeably different.

Because of relative improvements of results for Test 3 and Test 5, results from the present model may be more accurate than those of the benchmark study.

5. Additional results are provided for Tests 6 and 8 that modify the level of damping. Results incorporate the change in sign of the velocity and the relative strength of the damping force and give results that appear physically realistic and new. These results could possibly serve as additional results for future DEM models.

Table 3-1: Summary of Benchmark test problems (Chung and Ooi, 2011)

Test	Title	Objective	Reference(s)
1	Elastic normal impact of two identical spheres	Check the elastic normal contact between two spheres	Timoshenko and Goodier (1970)
2	Elastic normal impact of a sphere with a rigid plane	Check the elastic normal contact between a sphere and a plane	Timoshenko and Goodier (1970), Zhang and Vu-Quoc (2002)
3	Normal contact with different restitution coefficients	Check the effect of damping ratio	Ning and Ghadiri (1996)
4	Oblique impact of a sphere with a rigid plane with a constant resultant velocity but at different incident angles	Check the tangential force calculation between a sphere and a plane	Foerster et al. (1994), Kharaz et al. (2001), Di Renzo and Di Maio (2004)
5	Oblique impact of a sphere with a rigid plane with a constant normal velocity but at different tangential velocities	Check the tangential force calculation between a sphere and a plane	Maw et al. (1976), Wu et al. (2003)
6	Impact of a sphere with a rigid plane with a constant normal velocity but at different angular velocities	Check the tangential force calculation between a sphere and a plane	Vu-Quoc and Zhang (1999)
7	Impact of two identical spheres with a constant normal velocity and varying angular velocities	Check the tangential force calculation between two spheres	Chung (2006)
8	Impact of two differently sized spheres with a constant normal velocity and varying angular velocities	Check the tangential force calculation between two spheres	Chung (2006)

Table 3-2: DEM input parameters of benchmark tests (Chung and Ooi, 2011)

Input parameters	Test No.1		Test No.2		Test No.3		Test No.4	
	Ex. 1	Ex. 2	Ex. 1	Ex. 2	Ex. 1	Ex. 2	Ex. 1	Ex. 2
	Glass	Limestone	Al.alloy	Mg. alloy	Al. oxide	Cast iron	Al. oxide	Al. alloy
Young's modulus E (N/m^2)	4.80E+10	2.00E+10	7.00E+10	4.00E+10	3.80E+11	1.00E+11	3.80E+11	7.00E+10
Poisson ratio ν	0.2	0.25	0.30	0.35	0.23	0.25	0.23	0.33
Friction coefficient	0.350	0.350	0.000	0.000	0.000	0.000	0.092	0.092
Restitution coefficient	1.00	1.00	1.00	1.00	different values		0.98	0.98
Density (kg/m^3)	2800	2500	2699	1800	4000	7000	4000	2700
Radius (m)	0.010	0.010	0.100	0.100	0.0025	0.0025	0.0025	0.0025
Velocity (m/s)	± 10	± 10	0.2	0.2	3.9	3.9	3.9	3.9
Input parameters	Test No.5		Test No.6		Test No.7		Test No.8	
	Ex. 1	Ex. 2	Ex. 1	Ex. 2	Ex. 1	Ex. 2	Ex. 1	Ex. 2
	Steel	Polyethylene	Al. alloy	Nylon	Al. alloy	Copper	Al. alloy	Nylon
Young's modulus E (N/m^2)	2.08E+11	1.00E+09	7.00E+10	2.05E+09	7.00E+10	1.20E+11	7.00E+10	2.50E+09
Poisson ratio ν	0.30	0.40	0.33	0.40	0.33	0.35	0.33	0.40
Friction coefficient	0.300	0.300	0.400	0.400	0.400	0.400	0.400	0.400
Restitution coefficient	1.00	1.00	0.50	0.50	0.50	0.50	0.50	0.50
Density (kg/m^3)	7850	1400	2700	1000	2700	8900	2700	1000
Radius (m)	1.00E-05	1.00E-05	0.100	0.100	0.100	0.100	0.100	0.100
Velocity (m/s)	5	5	0.2	0.2	0.2	0.2	0.2	0.2

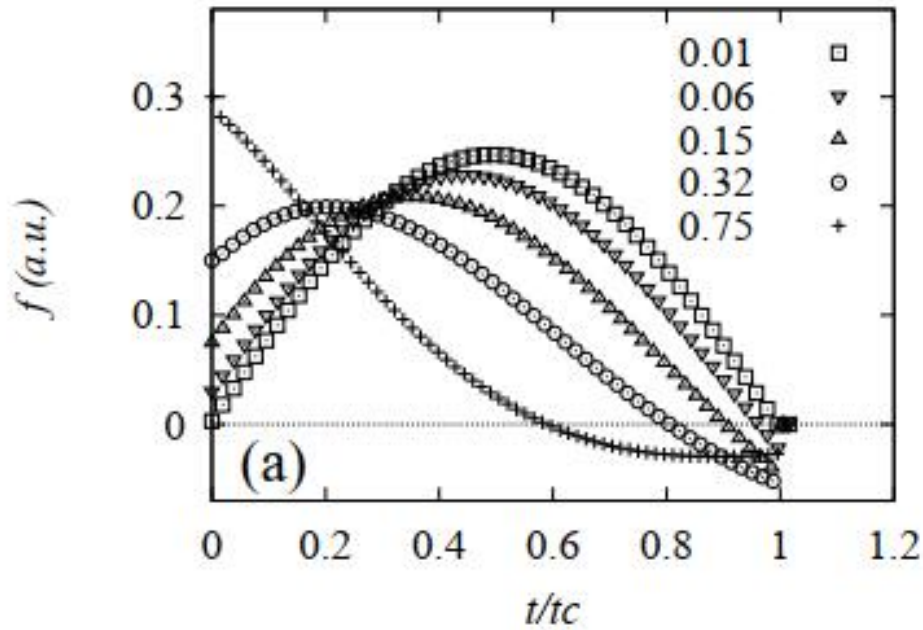


Figure 3-1: Normal force-time response in arbitrary units as a function of different damping ratios (Luding, 1998)

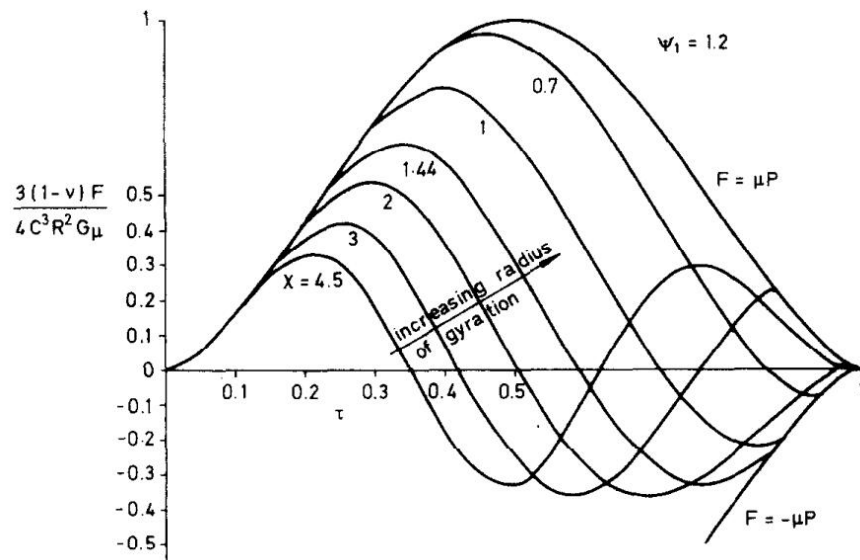


Figure 3-2: Evolution of tangential forces during the impact at intermediate angle of incidence $\psi_1 = 1.2$ for spheres of various radii of gyration χ (Maw et al., 1976)

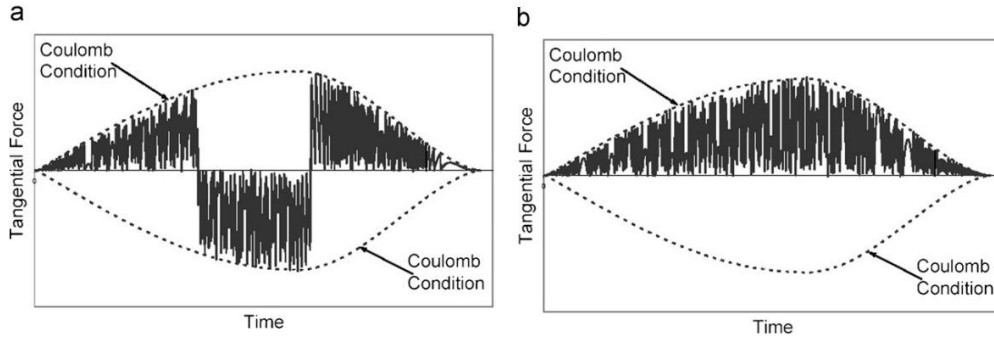


Figure 3-3: Evolution of tangential forces during different impact regimes for a combination of the normal model by Tomas and a tangential force calculated from the model by Brilliantov: (a) nearly frontal contact at a small impact angle and (b) grazing impact at larger impact angle. (Kruggel-Emden et al., 2008)

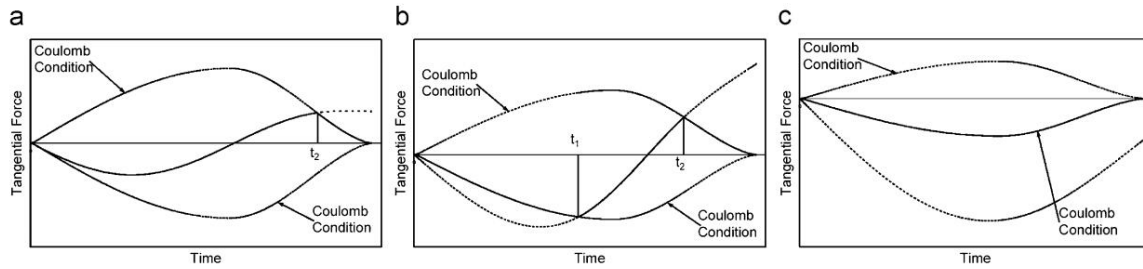


Figure 3-4: Evolution of tangential forces during different impact regimes for a combination of the normal model by Tomas and a tangential force calculated from an unconstrained spring limited by the Coulomb condition: (a) small impact angle, (b) intermediate impact angle, and (c) large impact angle. (Kruggel-Emden et al., 2008)

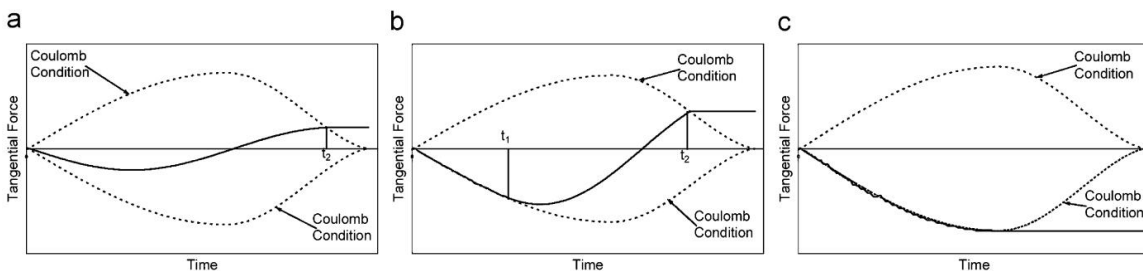


Figure 3-5: Evolution of tangential forces during different impact regimes for a combination of the normal model by Tomas and a tangential force calculated from a spring according to Brendel and Dippel (1998): (a) Small impact angle, (b) intermediate impact angle and (c) large impact angle. (Kruggel-Emden et al., 2008)

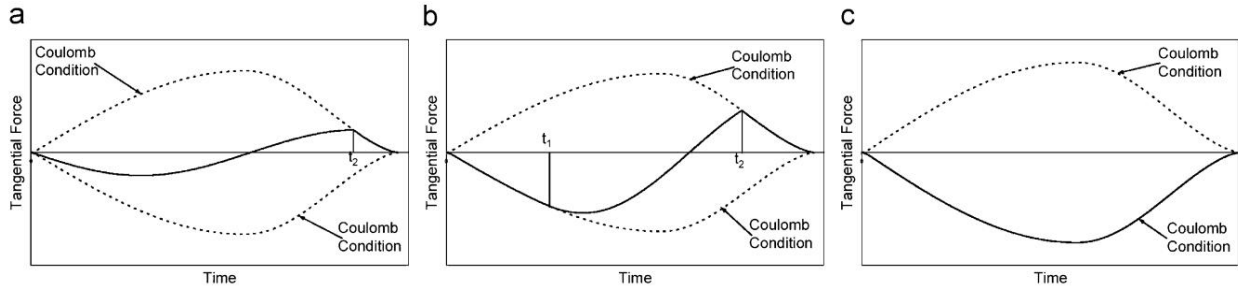


Figure 3-6: Evolution of tangential forces during different impact regimes for a combination of the normal model by Tomas and a tangential force calculated from a constrained spring limited by the Coulomb condition: (a) Small impact angle, (b) intermediate impact angle and (c) large impact angle. (Kruggel-Emden et al., 2008)

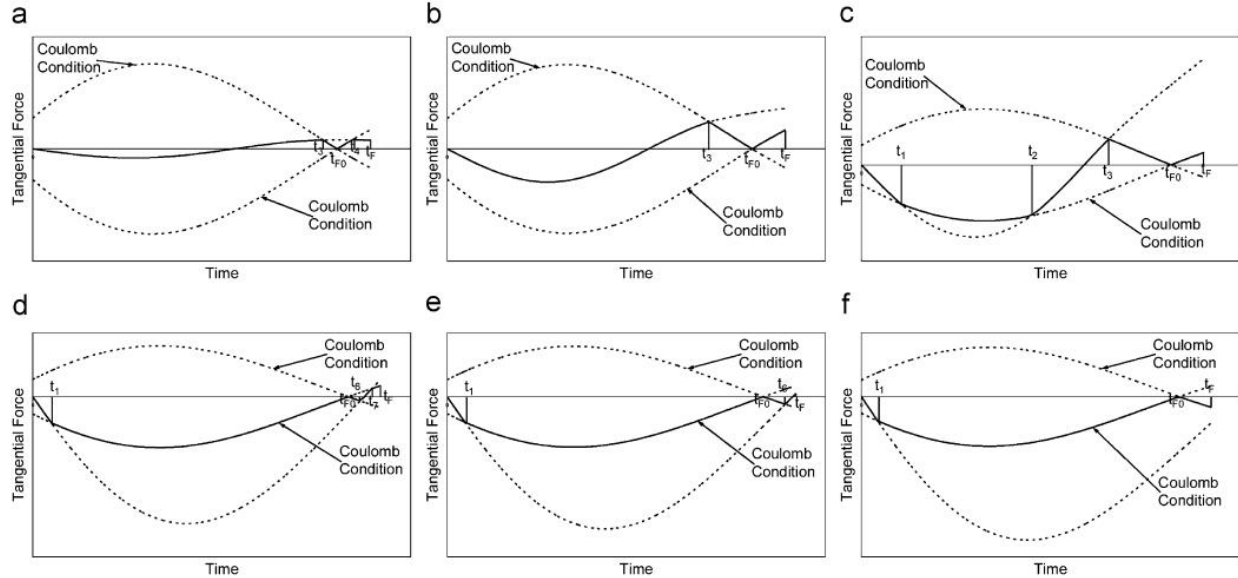


Figure 3-7: Evolution of tangential forces during different impact regimes for a combination of the extended linear spring damping normal model and a tangential force calculated from an unconstrained spring limited by the Coulomb condition. Impact angle increases from (a) to (f) (Kruggel-Emden et al., 2008)

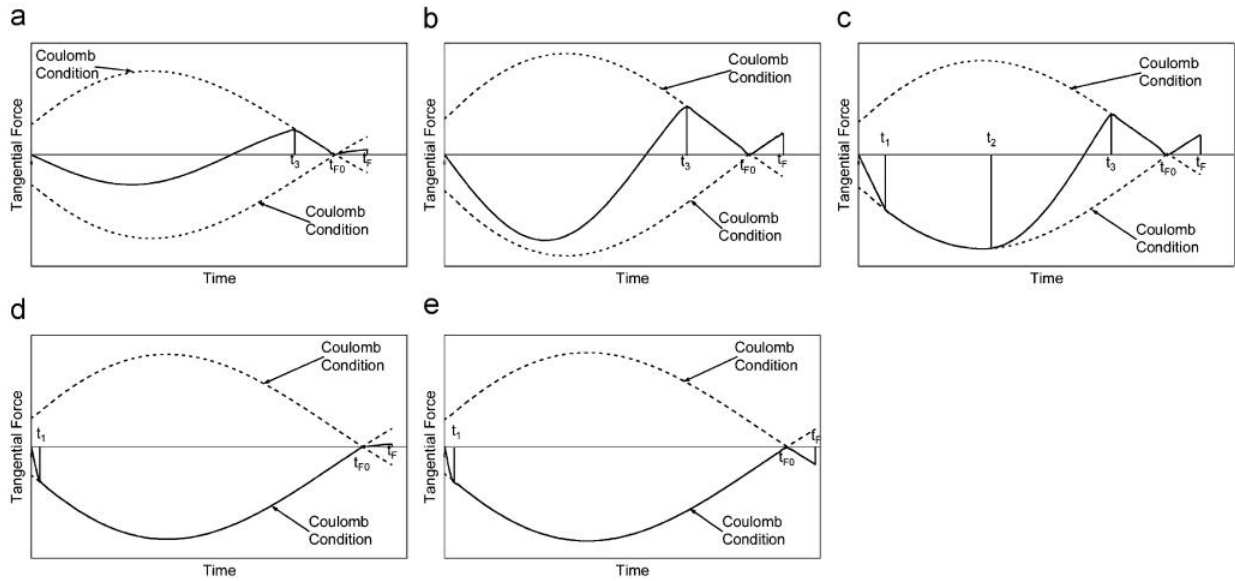


Figure 3-8: Evolution of tangential forces during different impact regimes for a combination of the extended linear spring damping normal model and a tangential force calculated from a constrained spring limited by the Coulomb condition. Impact angle increases from (a) to (e) (Kruggel-Emden et al., 2008)

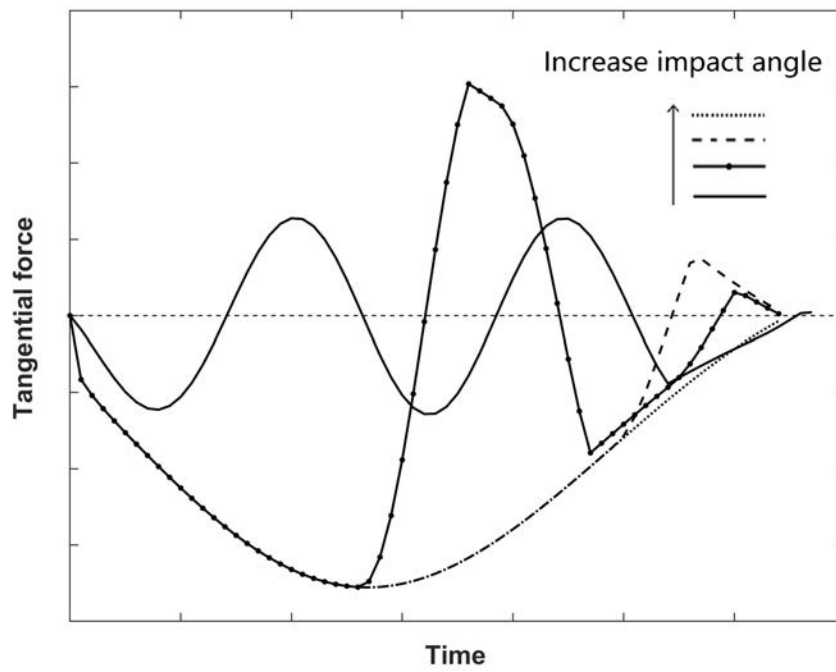


Figure 3-9: Evolution of tangential forces during the impact with different impact angles by using the proposed models and the input parameters from Benchmark Test 6. Results are checked at $\omega = 0.175, 2, 4,$ and 8 rad/s.

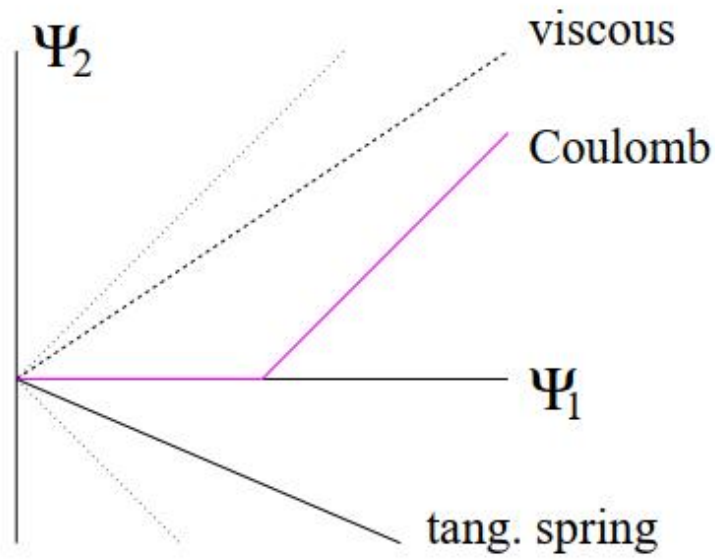


Figure 3-10: Schematic picture of the velocity ratio Ψ_1 versus Ψ_2 for the different force laws (Luding, 1998)

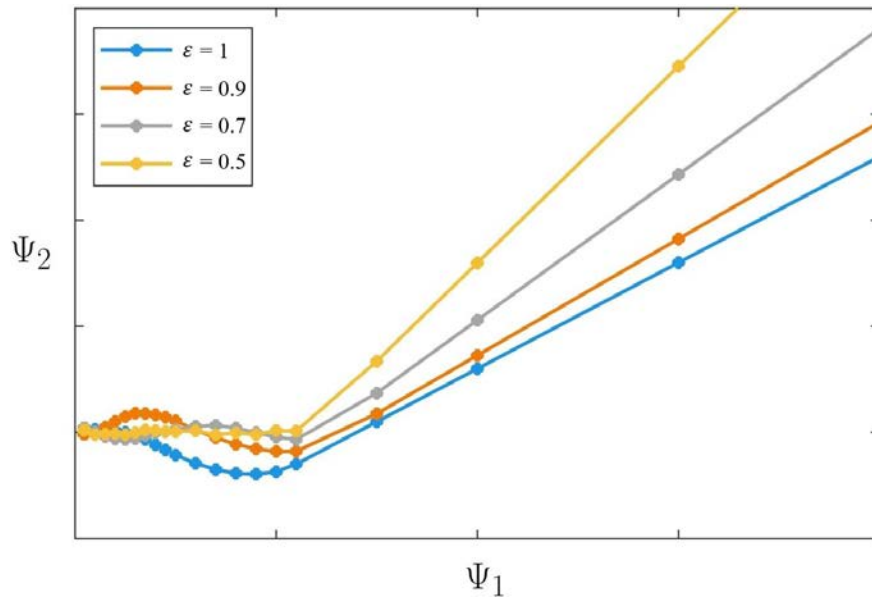


Figure 3-11: An example showing a schematic picture of the velocity ratio Ψ_1 versus Ψ_2 from the presented numerical model

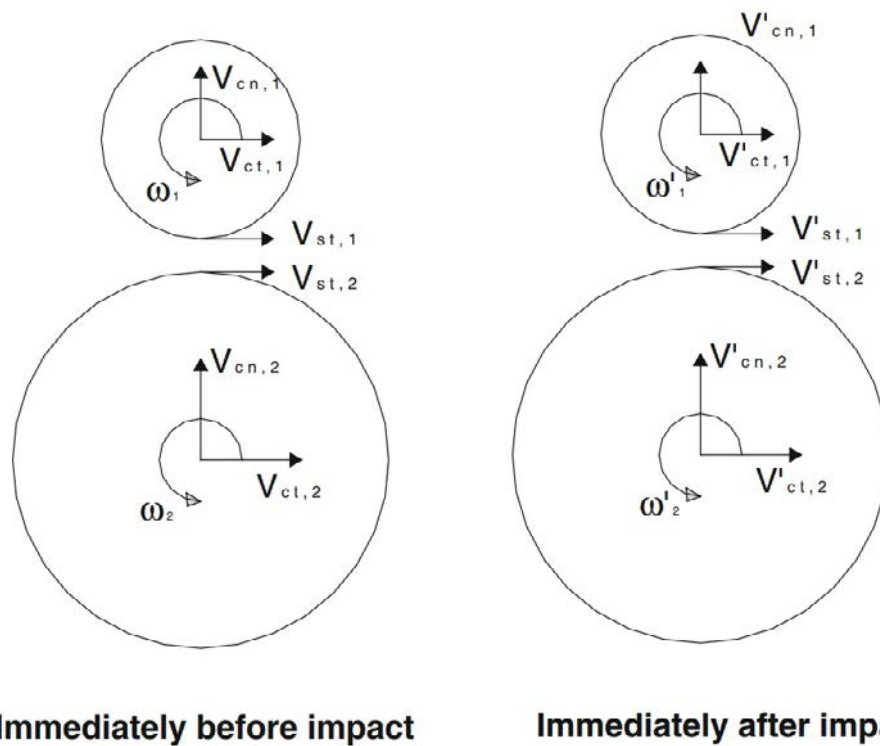


Figure 3-12: The definition of positive directions and symbols of linear and angular velocities before and after impact (Chung and Ooi, 2011)

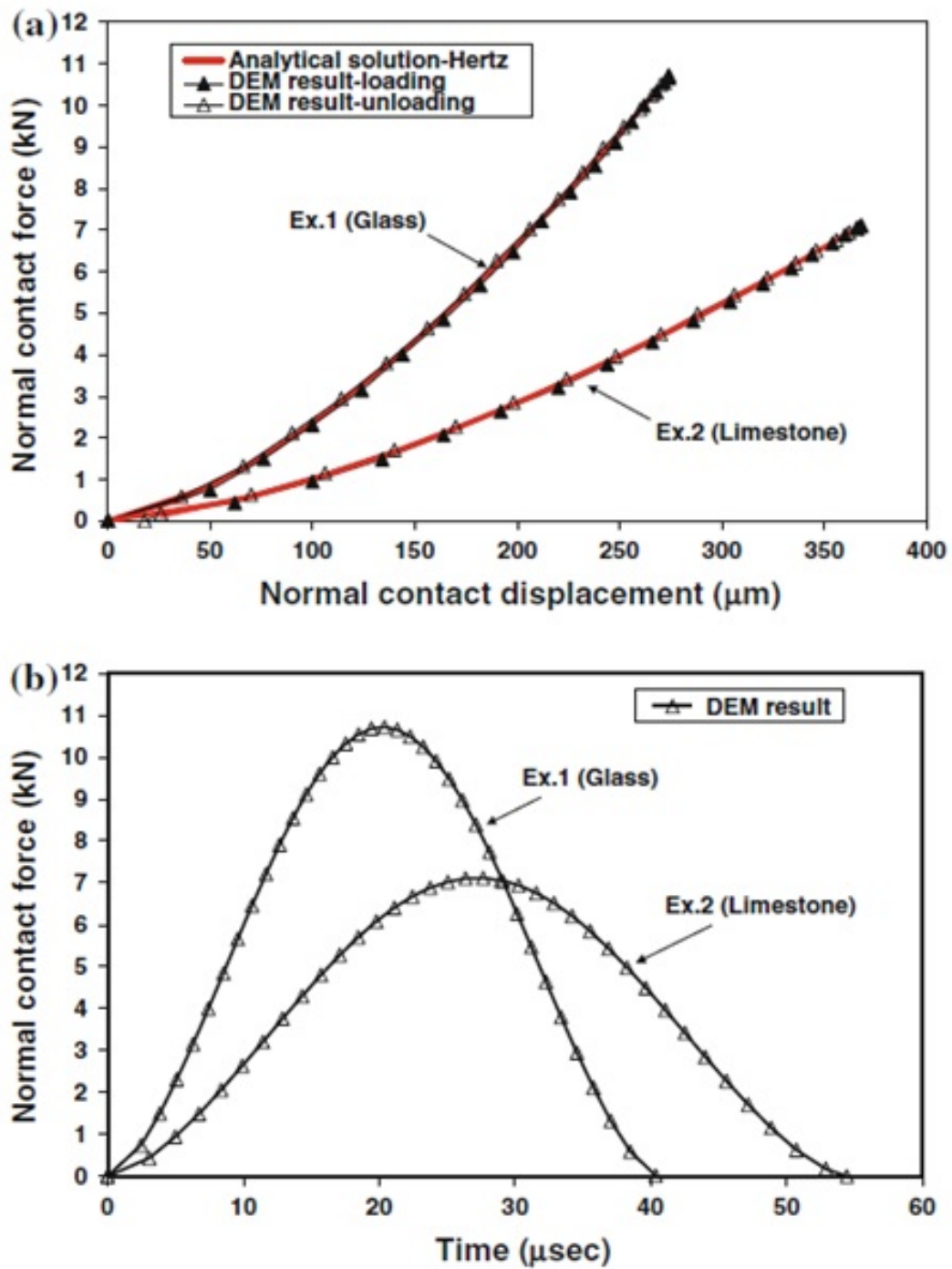


Figure 3-13: Test 1(Prior study): elastic normal impact of two identical spheres: (a) force-displacement curve; (b) force-time curve

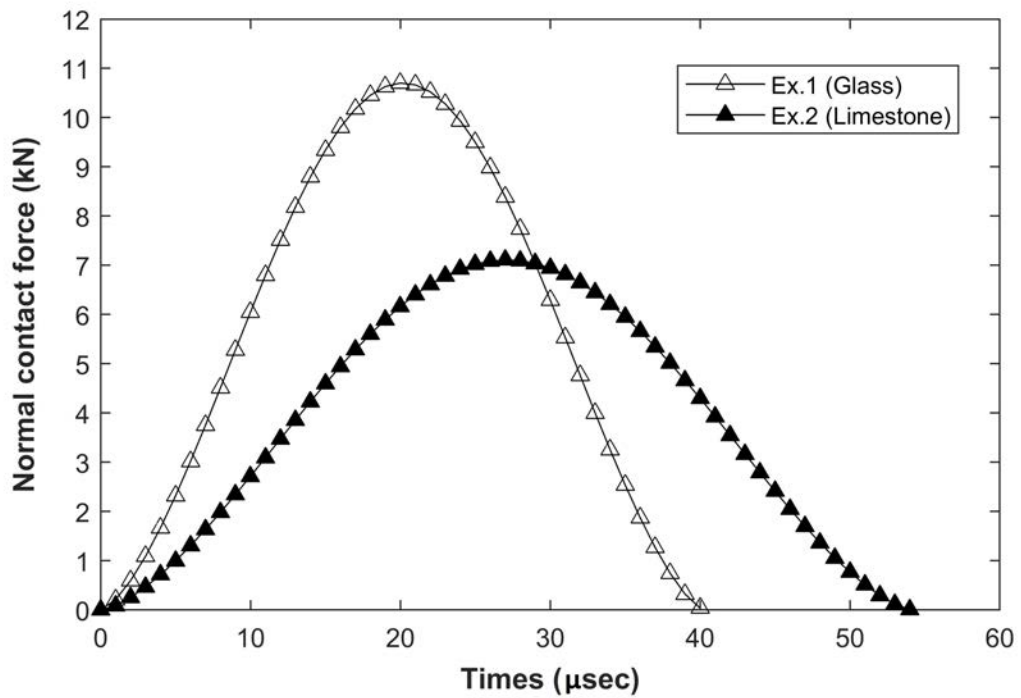
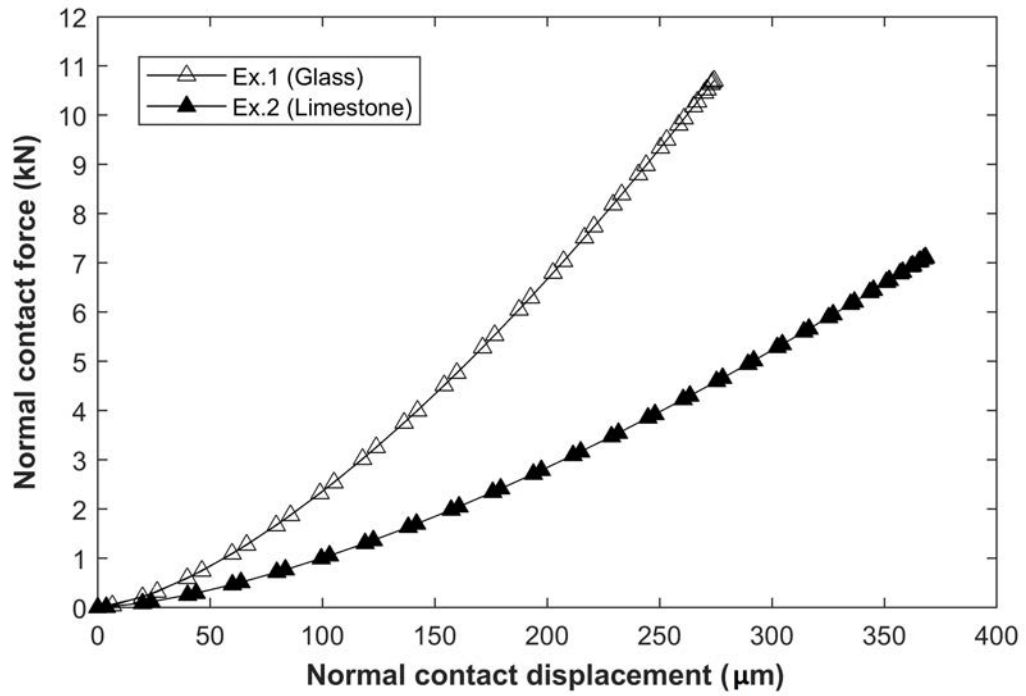


Figure 3-14: Test 1(Present DEM): elastic normal impact of two identical spheres: (a) force-displacement curve; (b) force-time curve

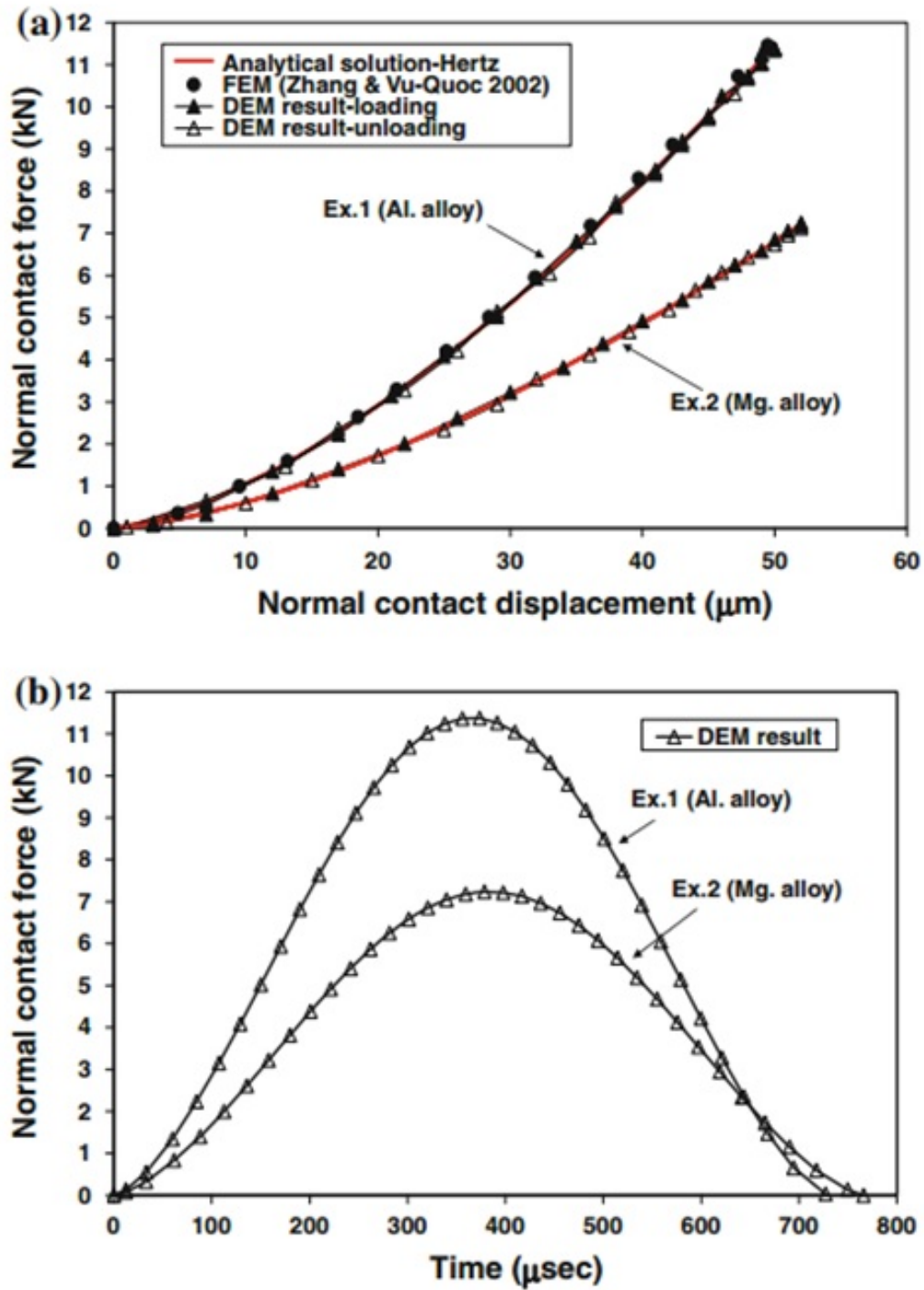


Figure 3-15: Test 2(Prior study): elastic normal impact of a sphere with a rigid plane: (a) force-displacement curve; (b) force-time curve

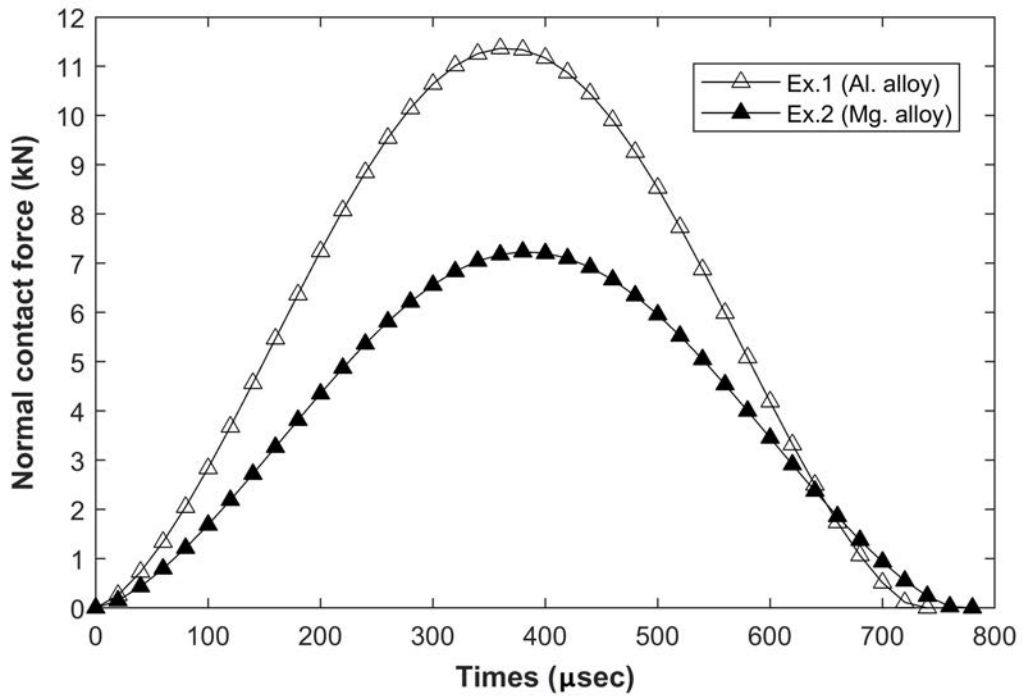
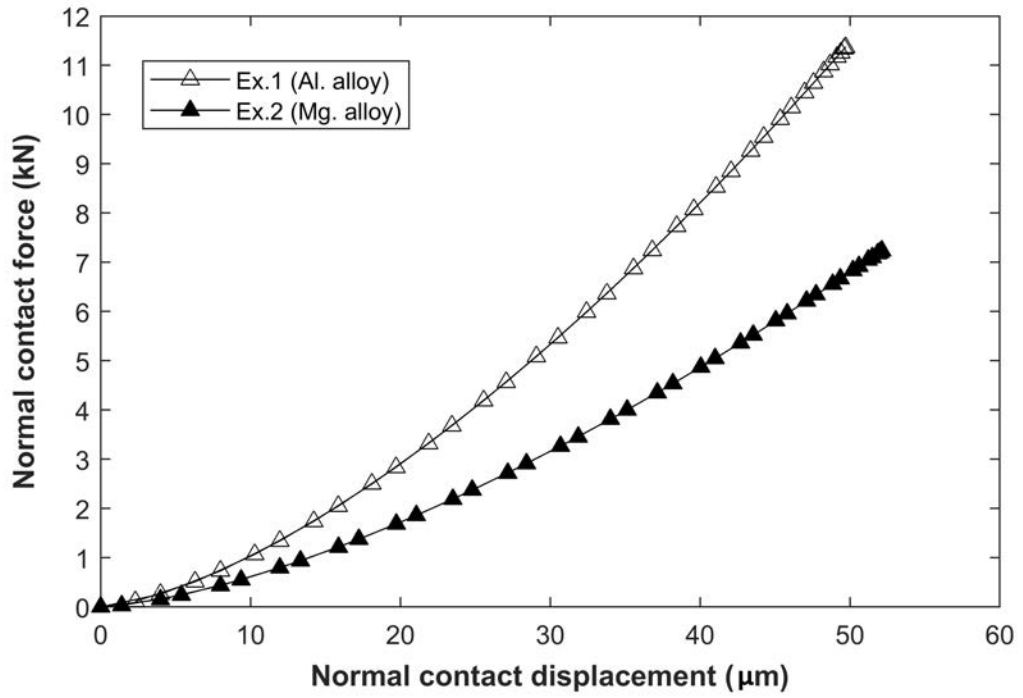


Figure 3-16: Test 2(Present DEM): elastic normal impact of a sphere with a rigid plane: (a) force-displacement curve; (b) force-time curve

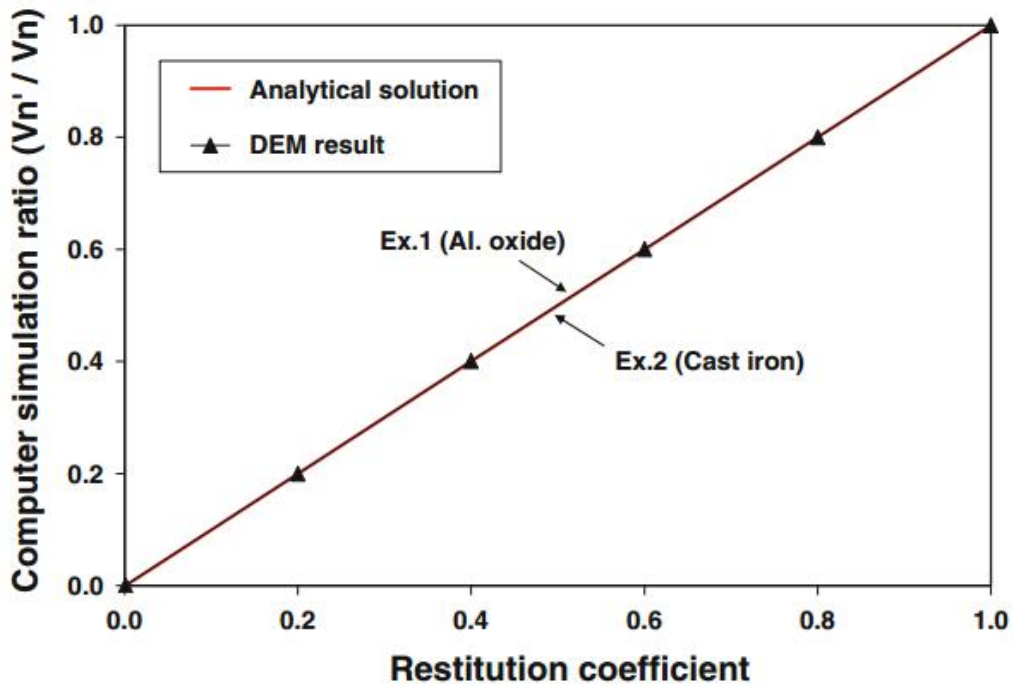


Figure 3-17: Test 3(Prior study): comparison between simulated velocity ratio and input value of the restitution coefficient

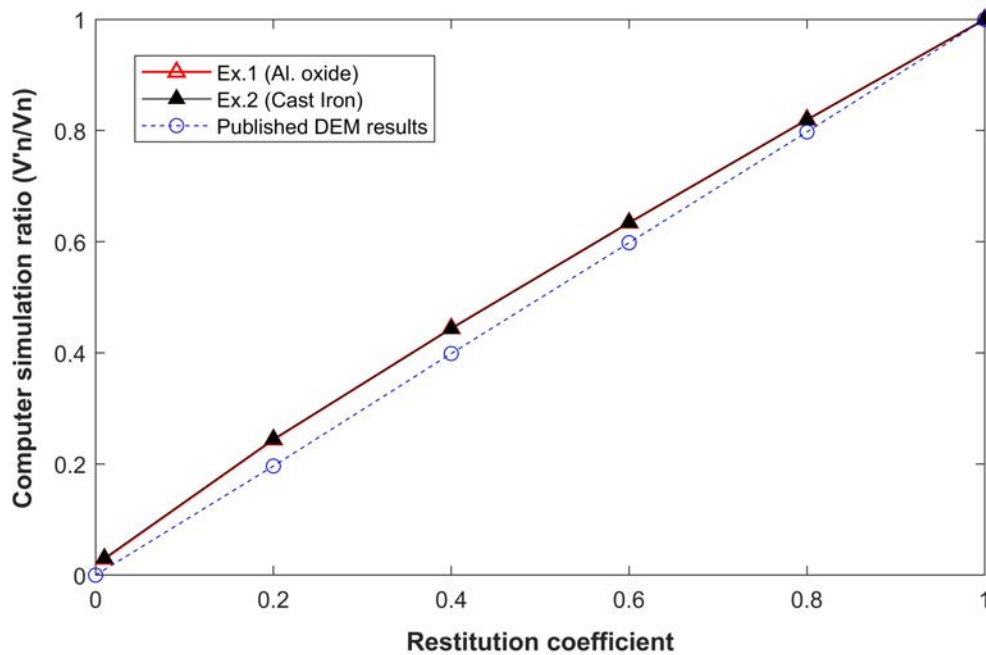


Figure 3-18: Test 3(Present DEM): comparison between simulated velocity ratio and input value of the restitution coefficient

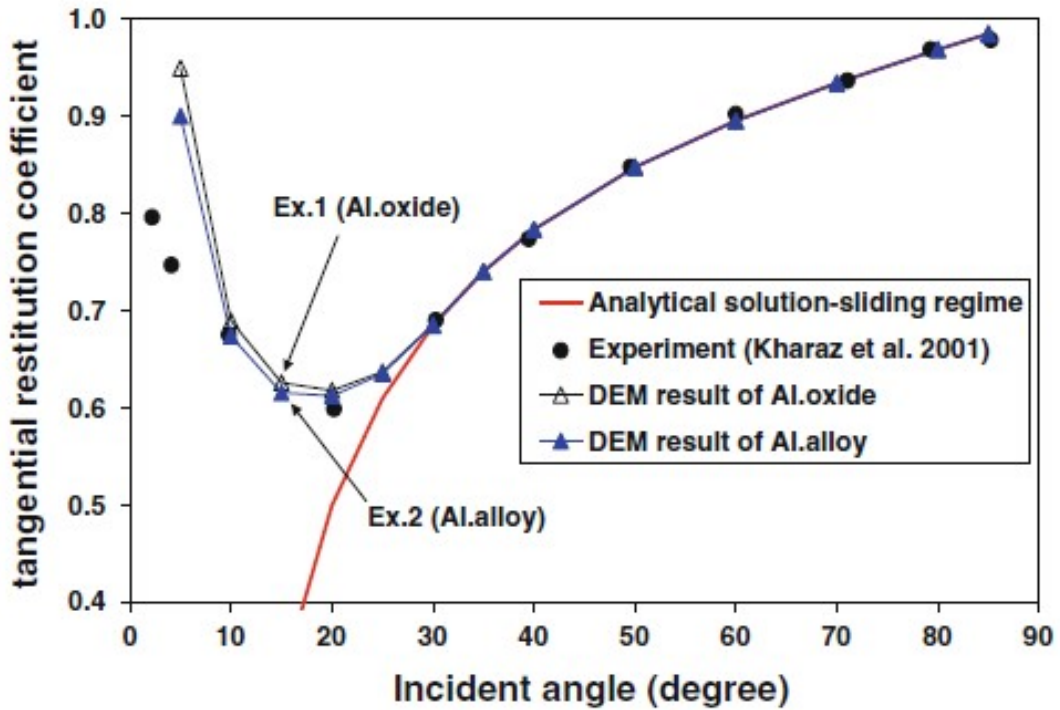


Figure 3-19: Test 4(Prior study): simulated, theoretical and experimental tangential restitution coefficient e for varying incident angles θ

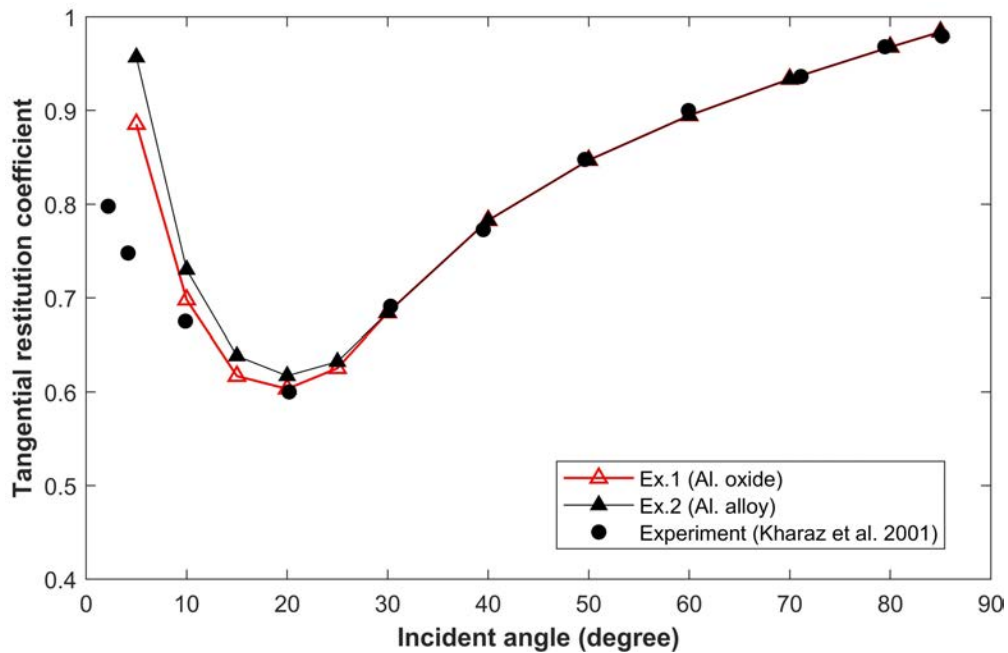


Figure 3-20: Test 4(Present DEM): simulated, theoretical and experimental tangential restitution coefficient e for varying incident angles θ

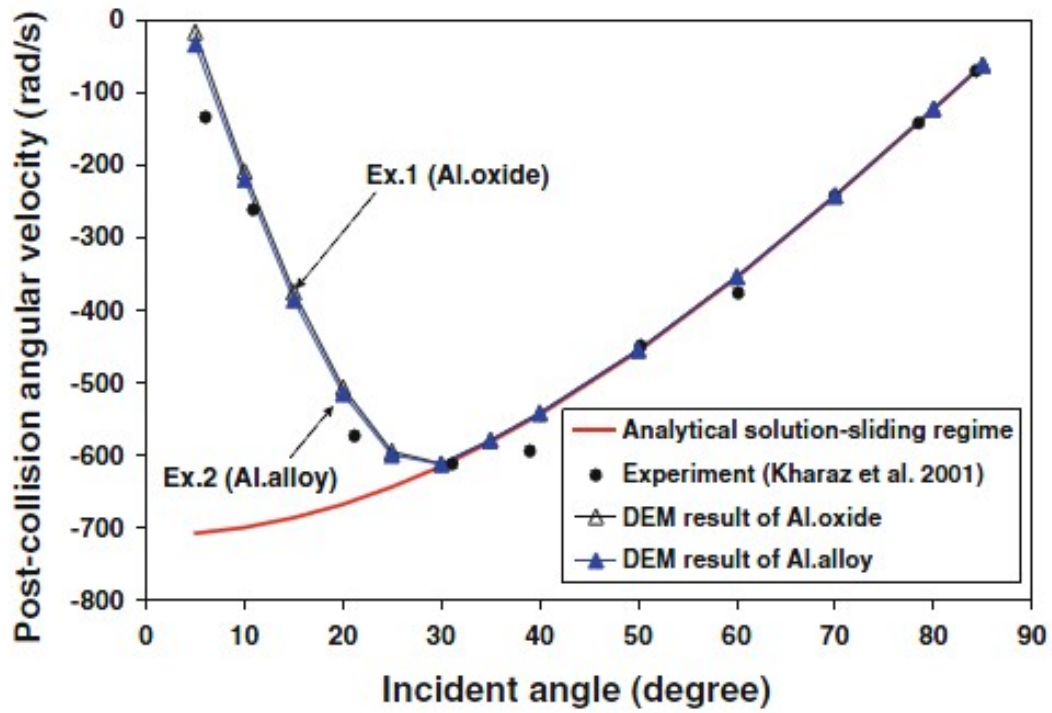


Figure 3-21: Test 4(Prior study): simulated, theoretical and experimental post-collision angular velocity ω'_1 for varying incident angles θ

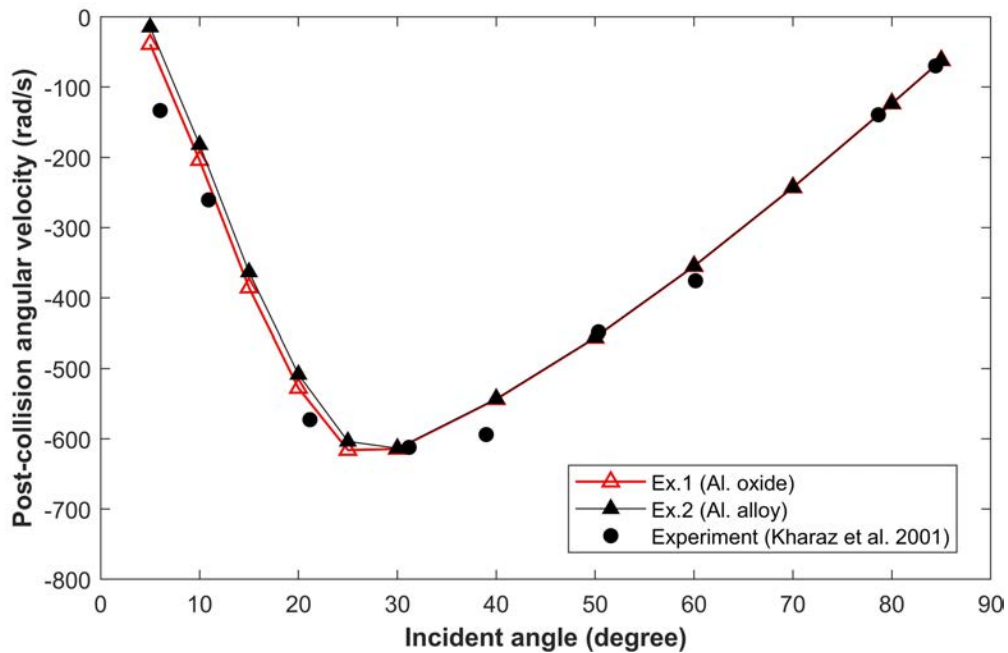


Figure 3-22: Test 4(Present DEM): simulated, theoretical and experimental post-collision angular velocity ω'_1 for varying incident angles θ

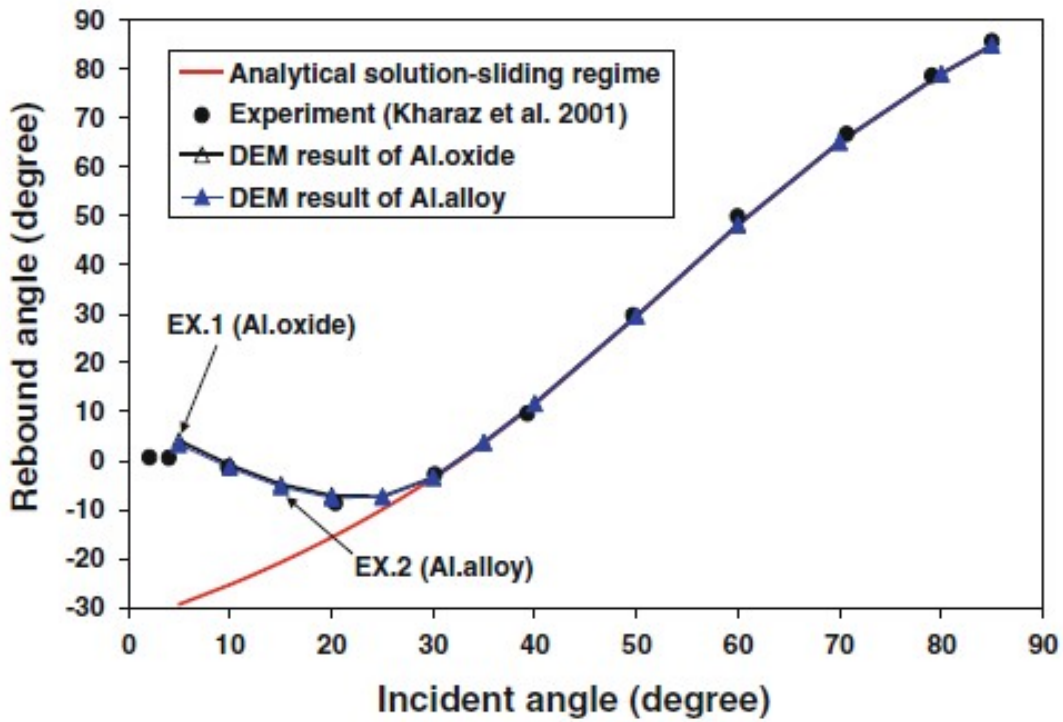


Figure 3-23: Test 4(Prior study): simulated, theoretical and experimental rebound angles φ for varying incident angles θ

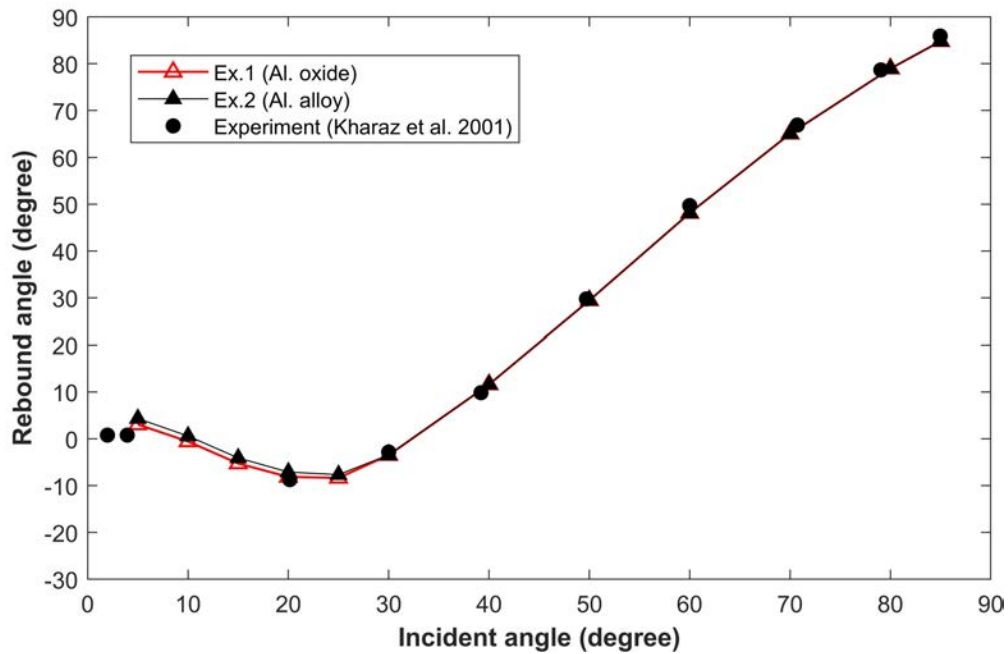


Figure 3-24: Test 4(Present DEM): simulated, theoretical and experimental rebound angles φ for varying incident angles θ

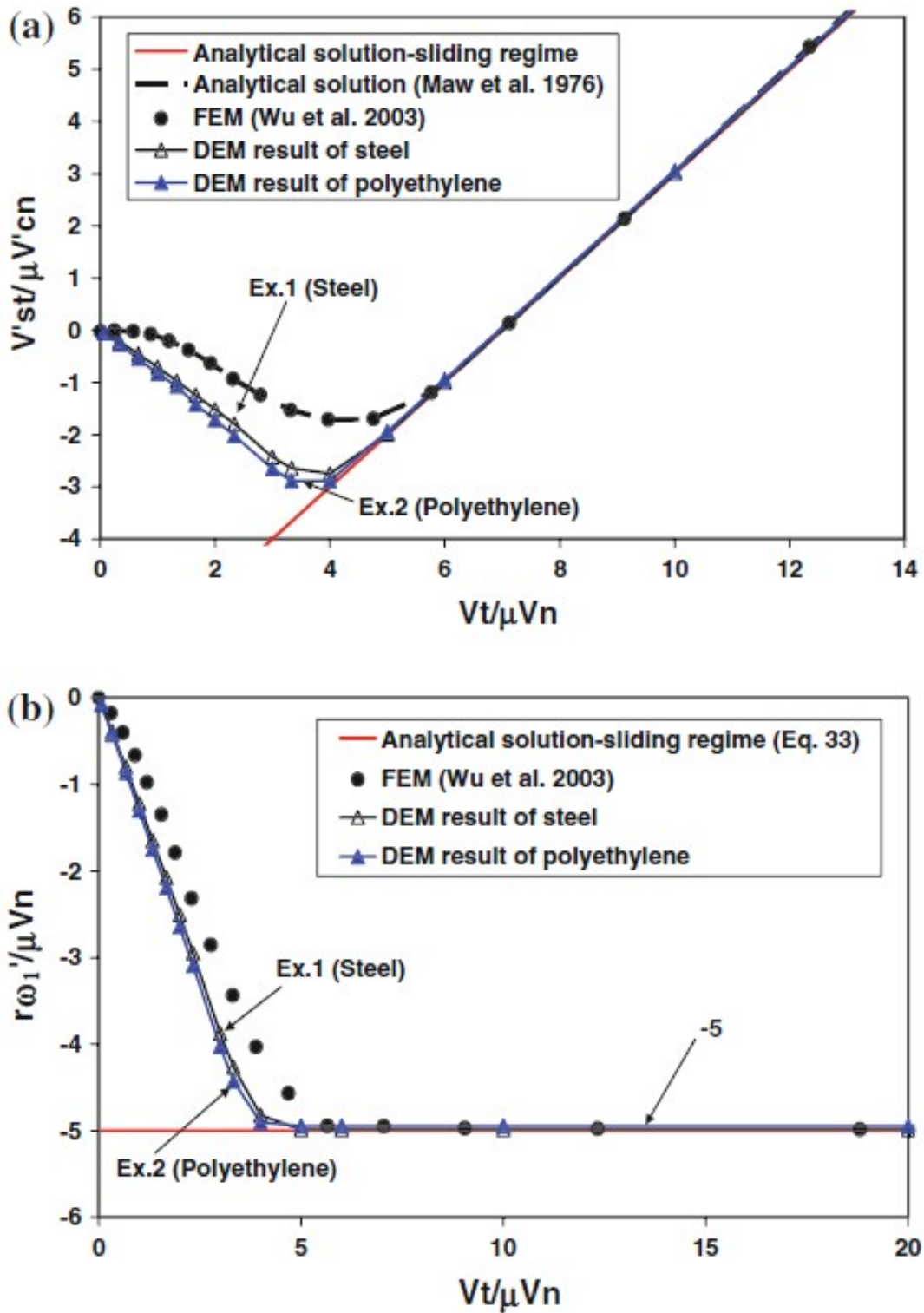


Figure 3-25: Test 5(Prior study): oblique impact for varying tangential velocities: (a) normalized recoil angle versus normalized incident angle; (b) normalized post-collision angular velocity versus normalized incident angle

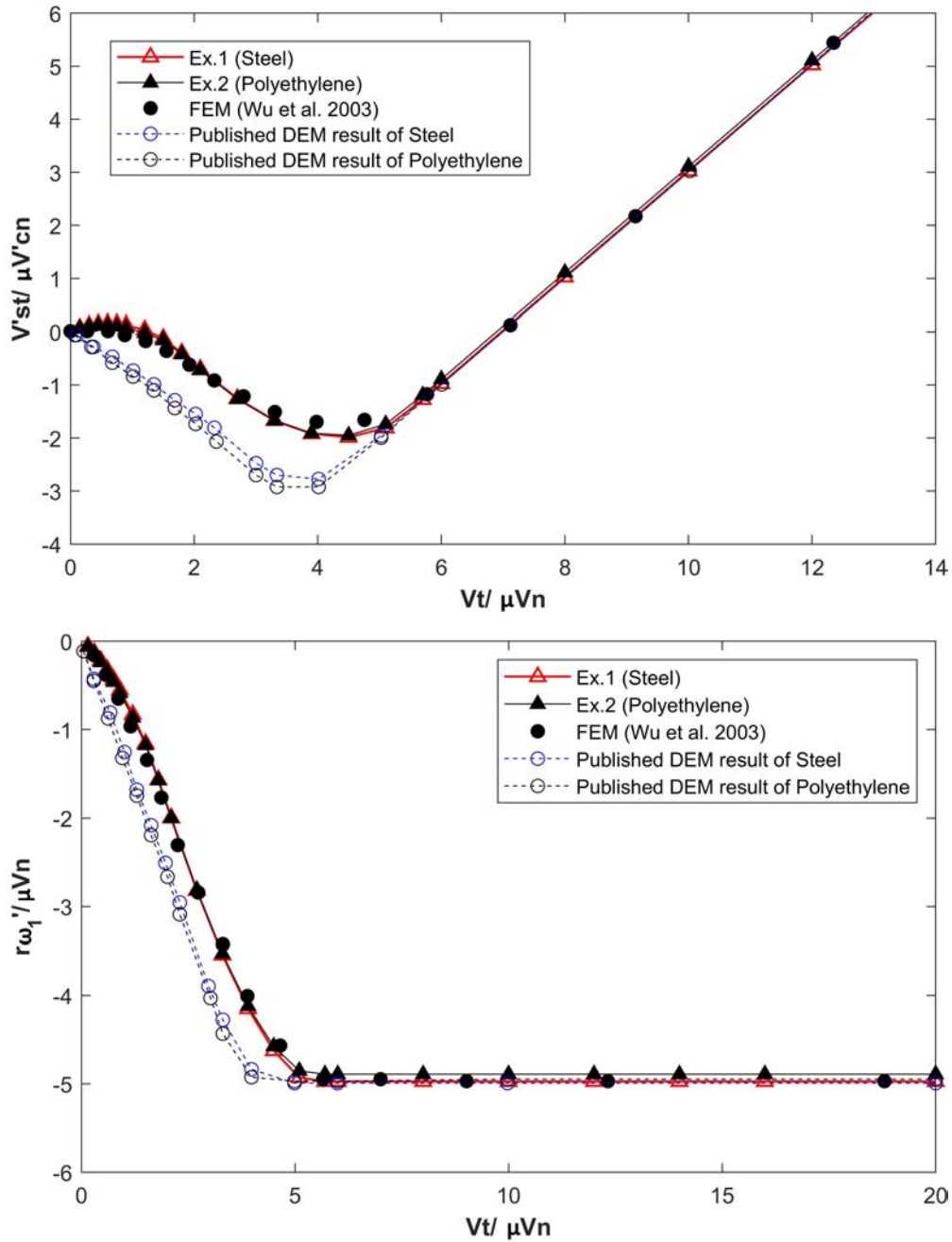


Figure 3-26: Test 5(Present DEM): oblique impact for varying tangential velocities: (a) normalized recoil angle versus normalized incident angle; (b) normalized post-collision angular velocity versus normalized incident angle

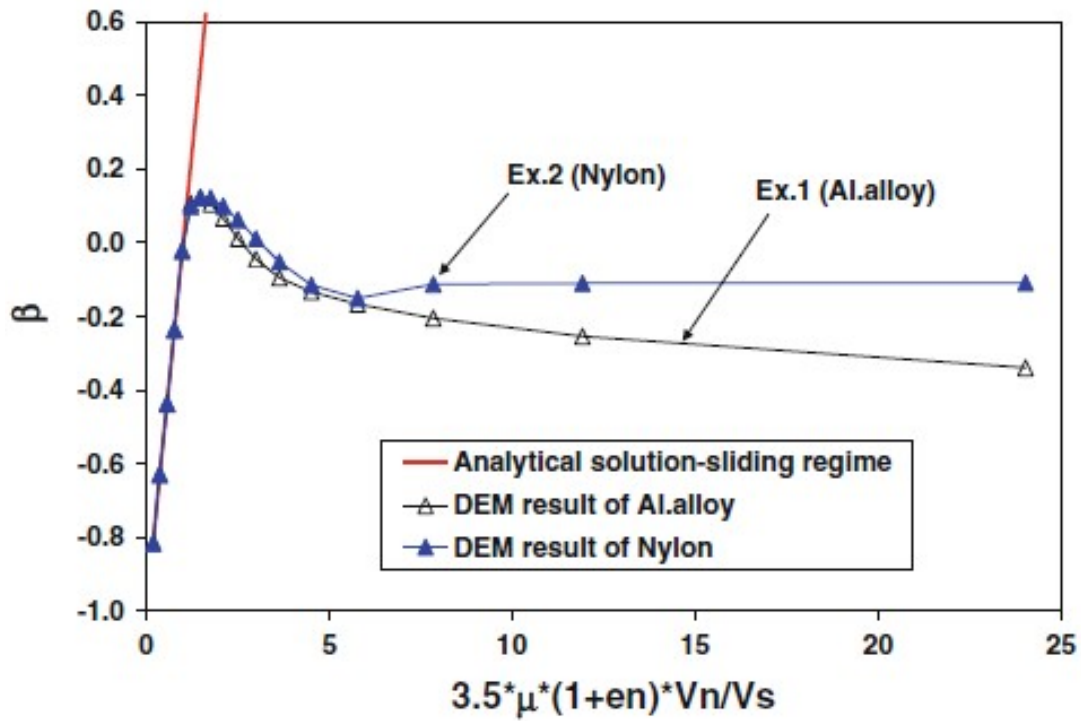


Figure 3-27: Test 6(Prior study): simulated and theoretical tangential restitution coefficient β versus the quantity $[3.5\mu(1 + e_n)\frac{V_n}{V_s}]$

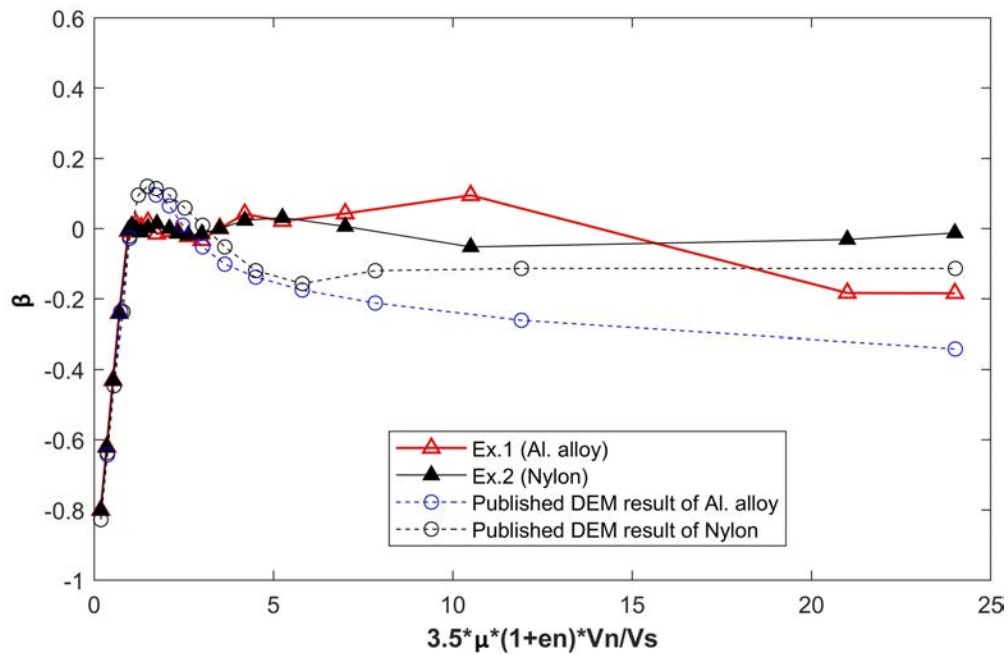


Figure 3-28: Test 6(Present DEM): simulated and theoretical tangential restitution coefficient β versus the quantity $[3.5\mu(1 + e_n)\frac{V_n}{V_s}]$

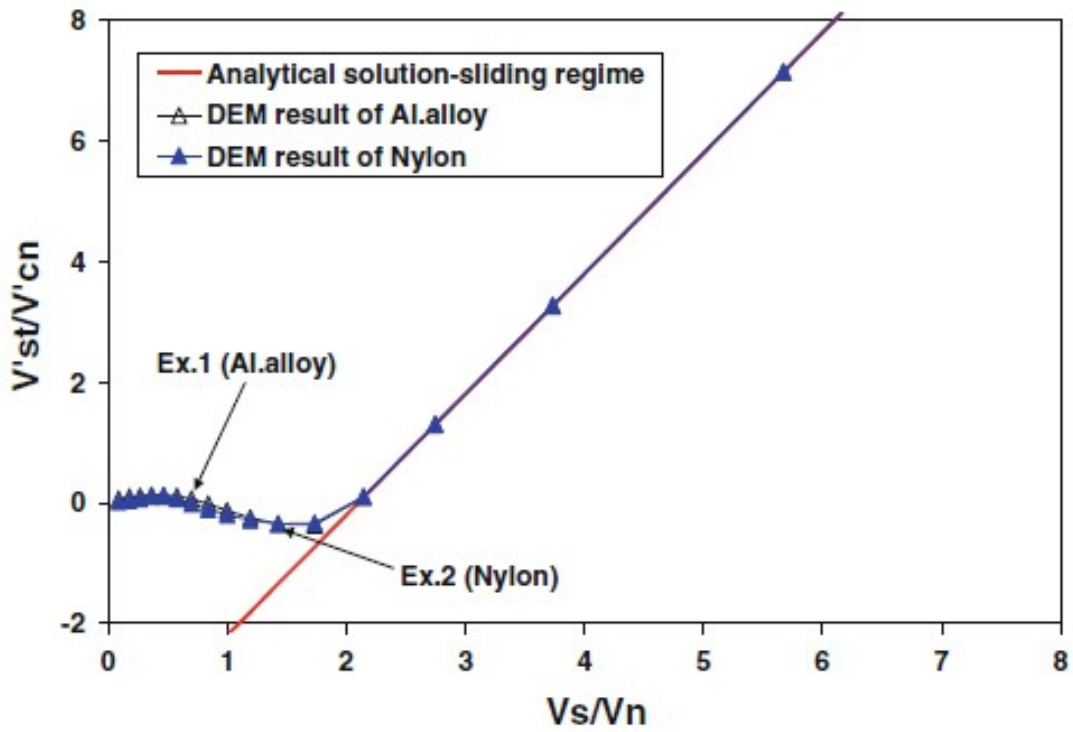


Figure 3-29: Test 6(Prior study): simulated and theoretical tangent of recoil angle $\frac{V'_{st}}{V'_{cn}}$ for varying tangent of incident angles $\frac{V_s}{V_n}$

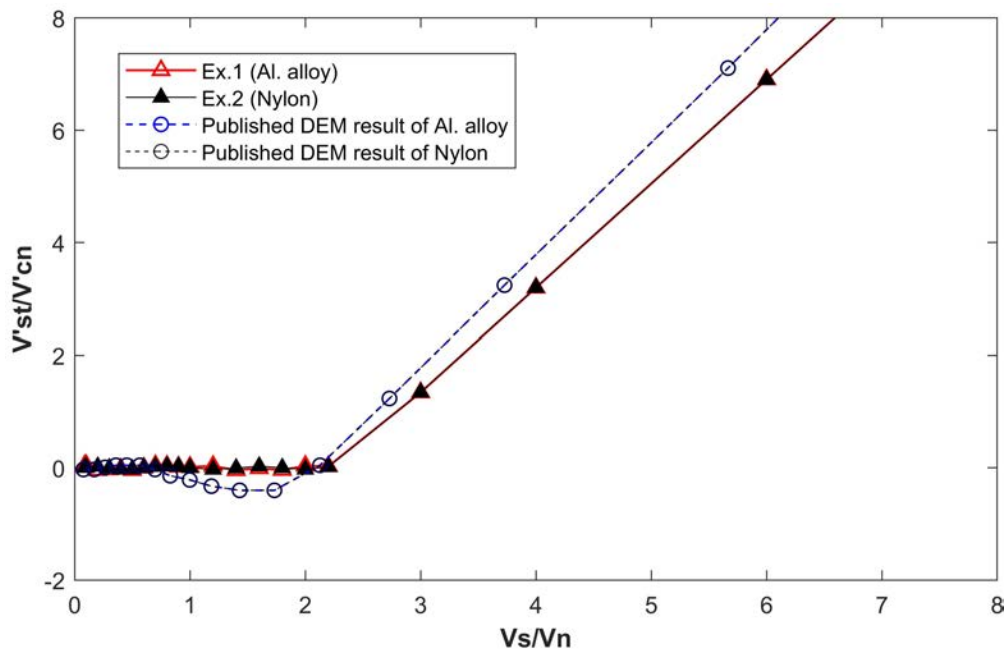


Figure 3-30: Test 6(Present DEM): simulated and theoretical tangent of recoil angle $\frac{V'_{st}}{V'_{cn}}$ for varying tangent of incident angles $\frac{V_s}{V_n}$

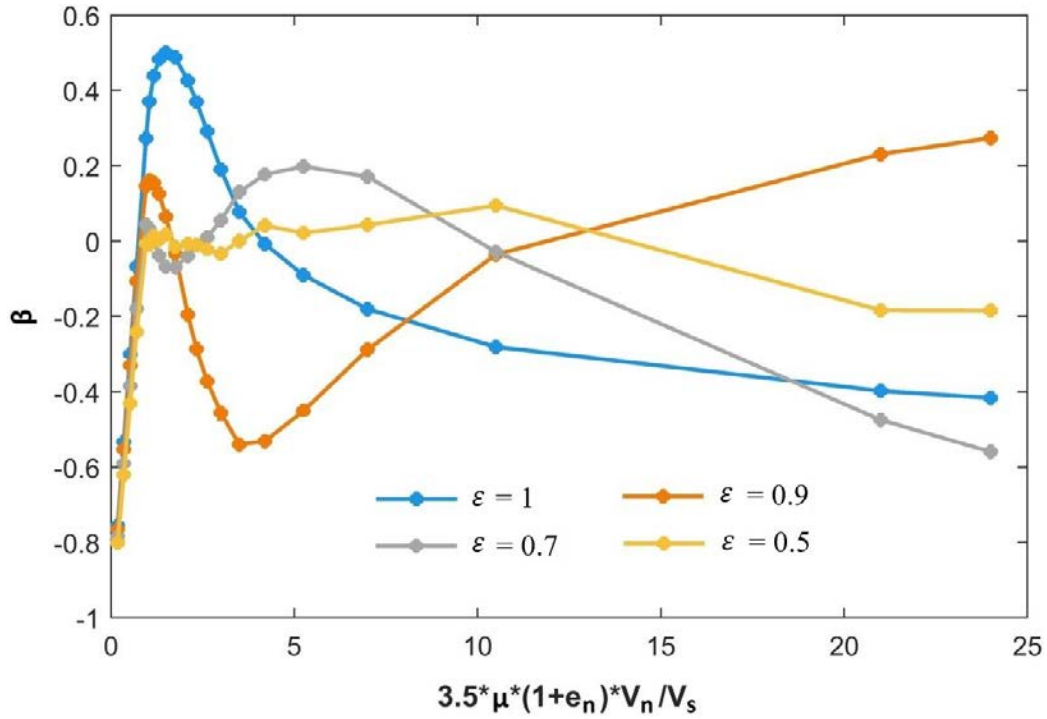


Figure 3-31: Test 6(Present DEM): simulated tangential restitution coefficient β varying as a function of the quantity $[3.5\mu(1 + e_n)\frac{V_n}{V_s}]$ with different restitution coefficients ε respect to Al. alloy

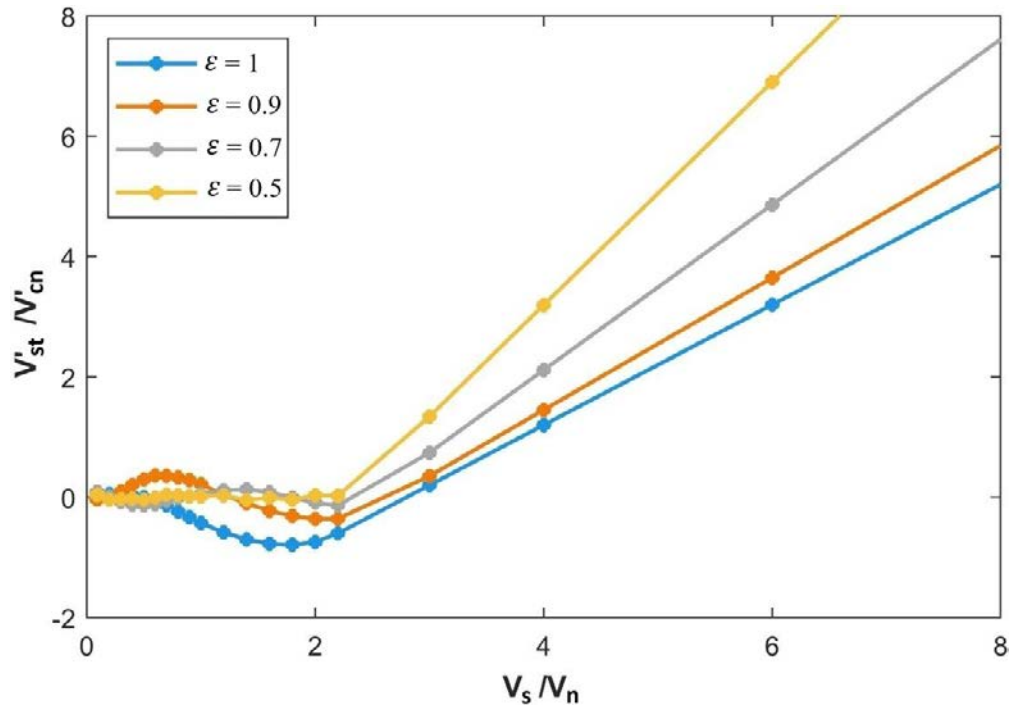


Figure 3-32: Test 6(Present DEM): simulated tangent of recoil angle $\frac{V'_{st}}{V'_{cn}}$ versus various tangent of incident angles $\frac{V_s}{V_n}$ with different restitution coefficients ε respect to Al. alloy

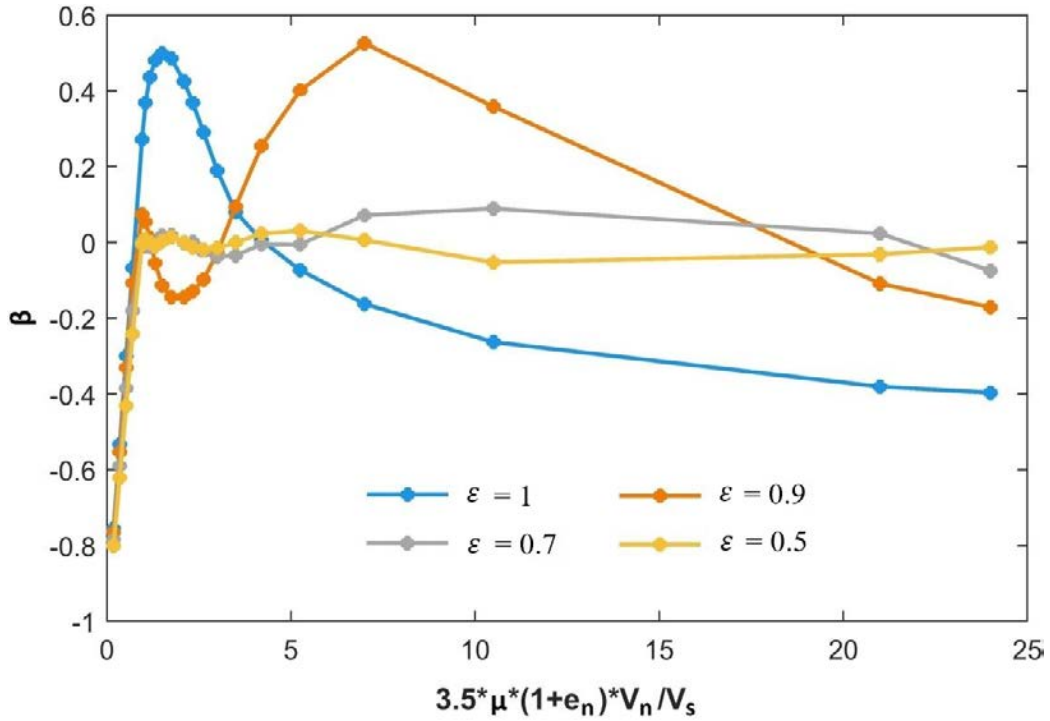


Figure 3-33: Test 6(Present DEM): simulated tangential restitution coefficient β varying as a function of the quantity $[3.5\mu(1+e_n)\frac{V_n}{V_s}]$ with different restitution coefficients ϵ respect to Nylon

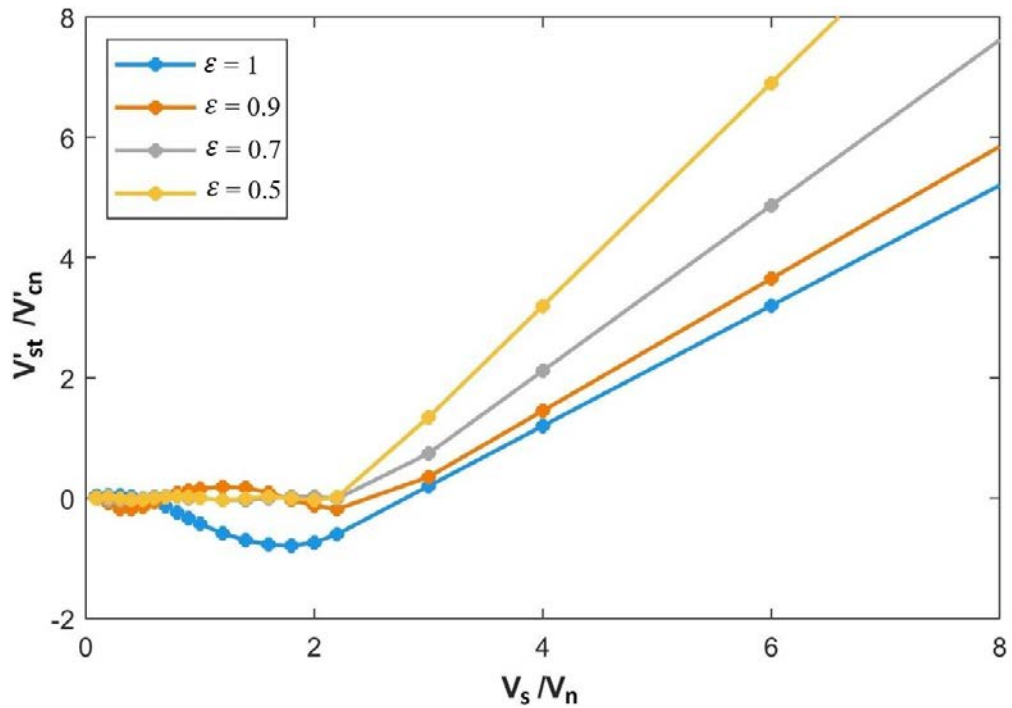


Figure 3-34: Test 6(Present DEM): simulated tangent of recoil angle $\frac{V'_{st}}{V'_{cn}}$ versus various tangent of incident angles $\frac{V_s}{V_n}$ with different restitution coefficients ϵ respect to Nylon

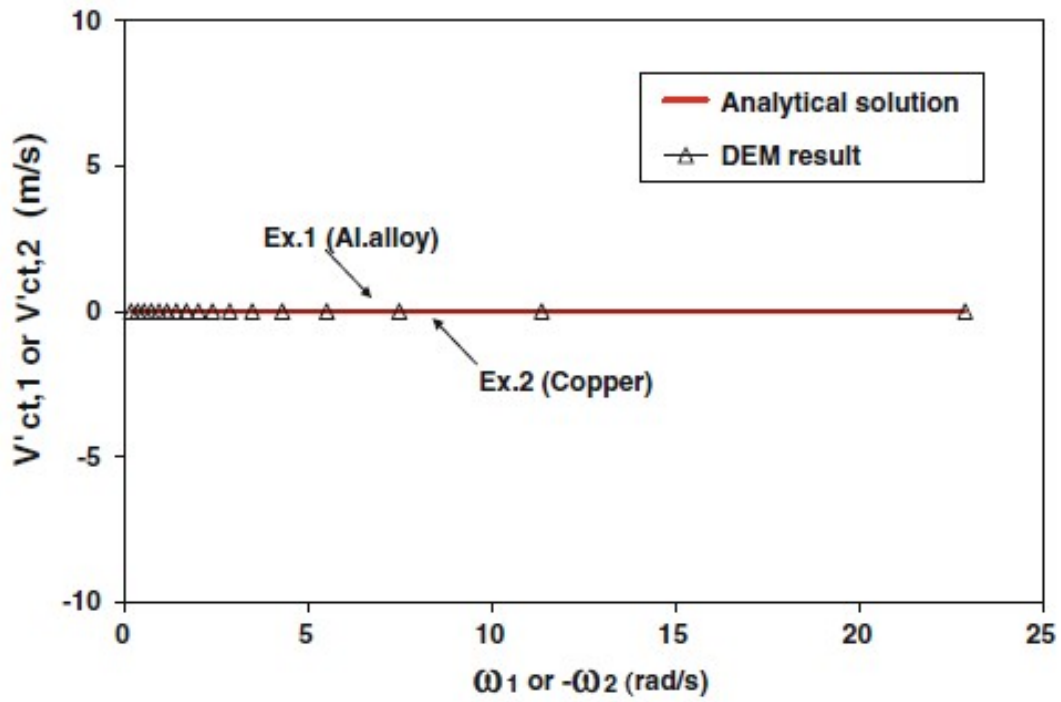


Figure 3-35: Test 7(Prior study): post-collision tangential velocity at the mass center for varying pre-collision angular velocities

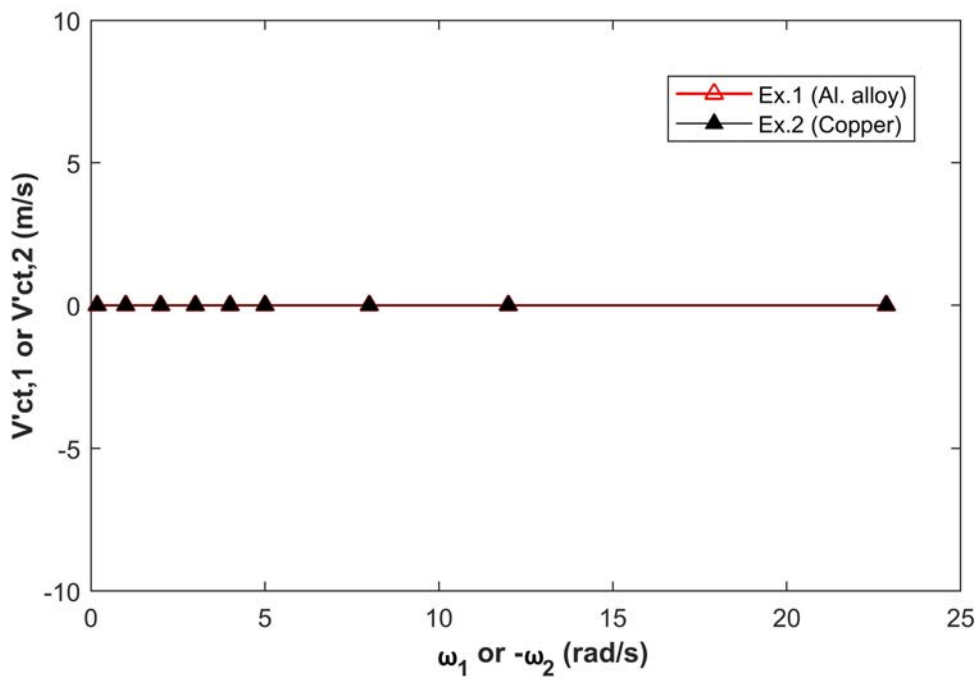


Figure 3-36: Test 7(Present DEM): post-collision tangential velocity at the mass center for varying pre-collision angular velocities

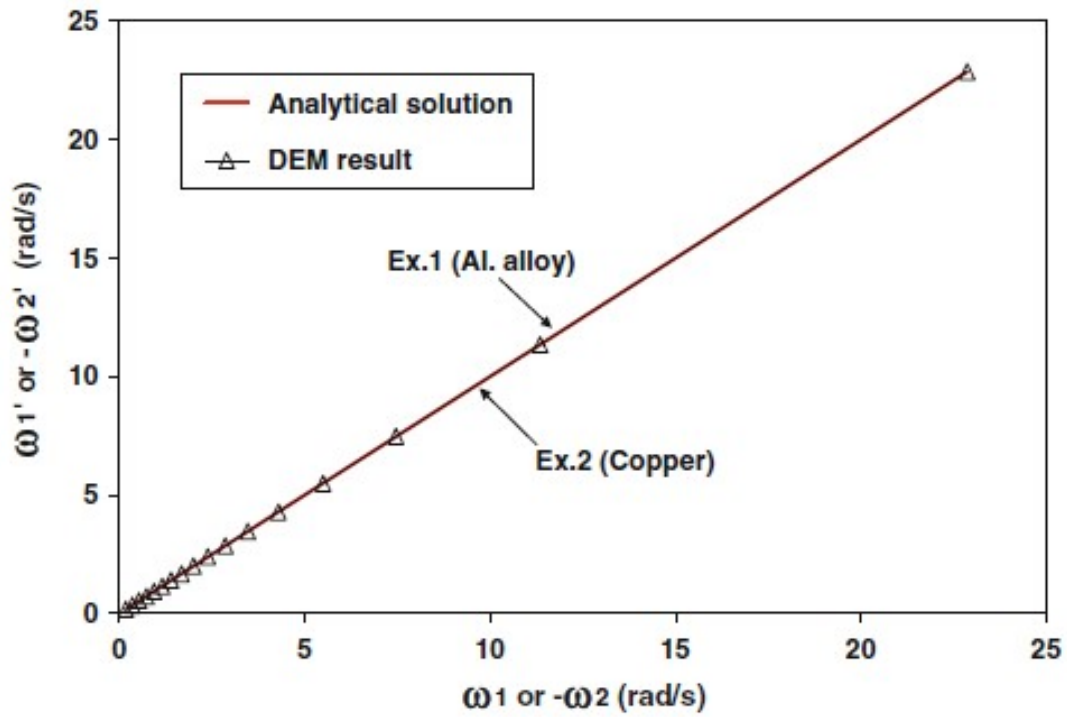


Figure 3-37: Test 7(Prior study): post-collision angular velocity for varying pre-collision angular velocities

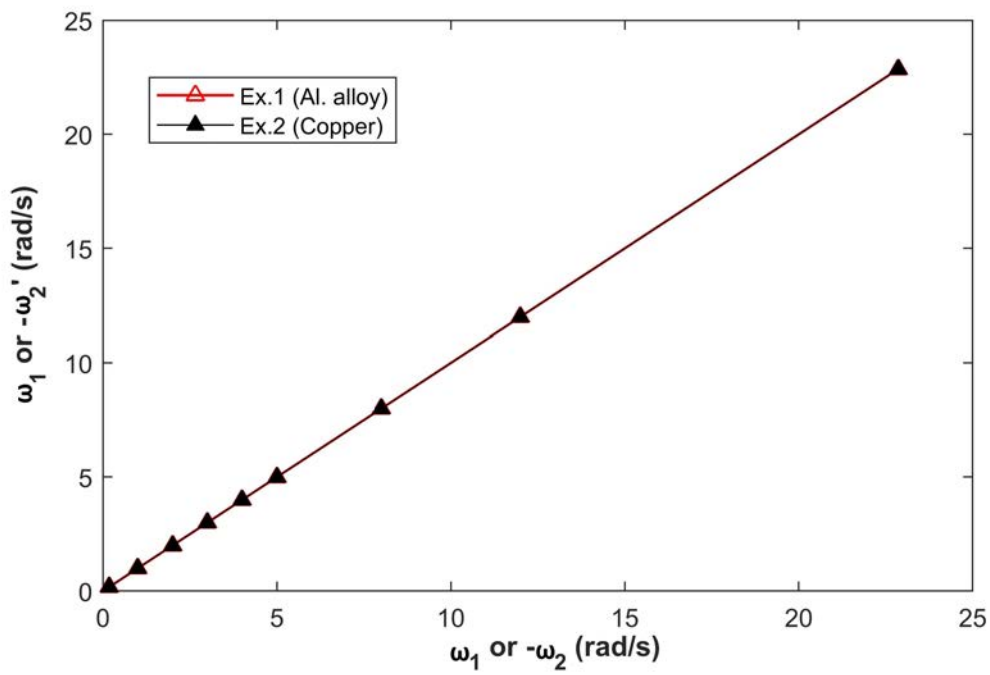


Figure 3-38: Test 7(Present DEM):post-collision angular velocity for varying pre-collision angular velocities

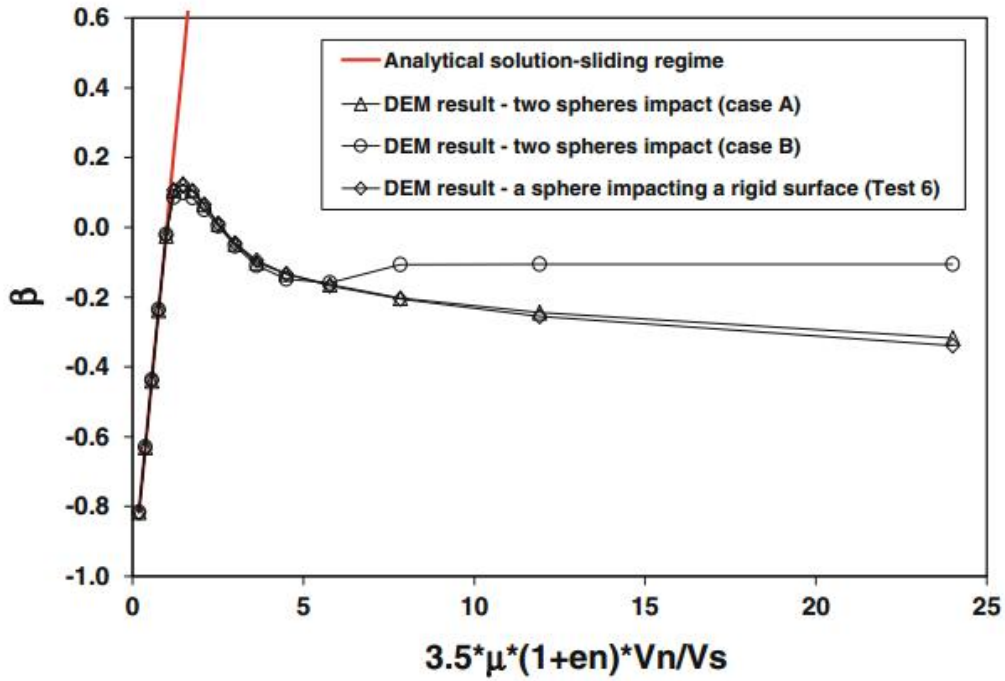


Figure 3-39: Test 8(Prior study): Al.alloy, simulated and theoretical tangential restitution coefficient β versus quantity $[3.5\mu(1 + e_n)\frac{V_n}{V_s}]$

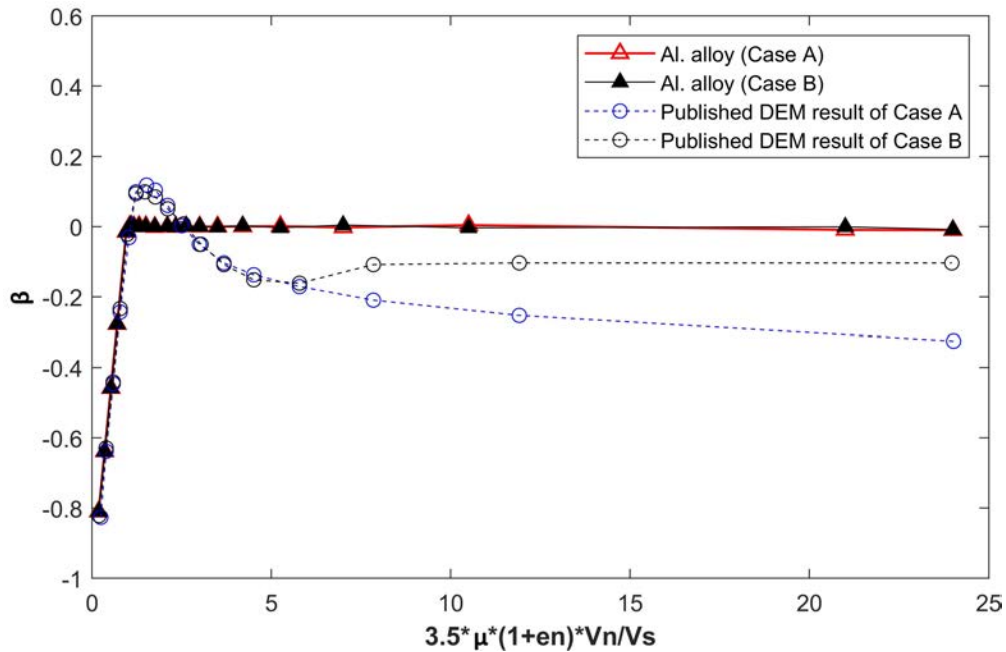


Figure 3-40: Test 8(Present DEM): Al.alloy, simulated and theoretical tangential restitution coefficient β versus quantity $[3.5\mu(1 + e_n)\frac{V_n}{V_s}]$

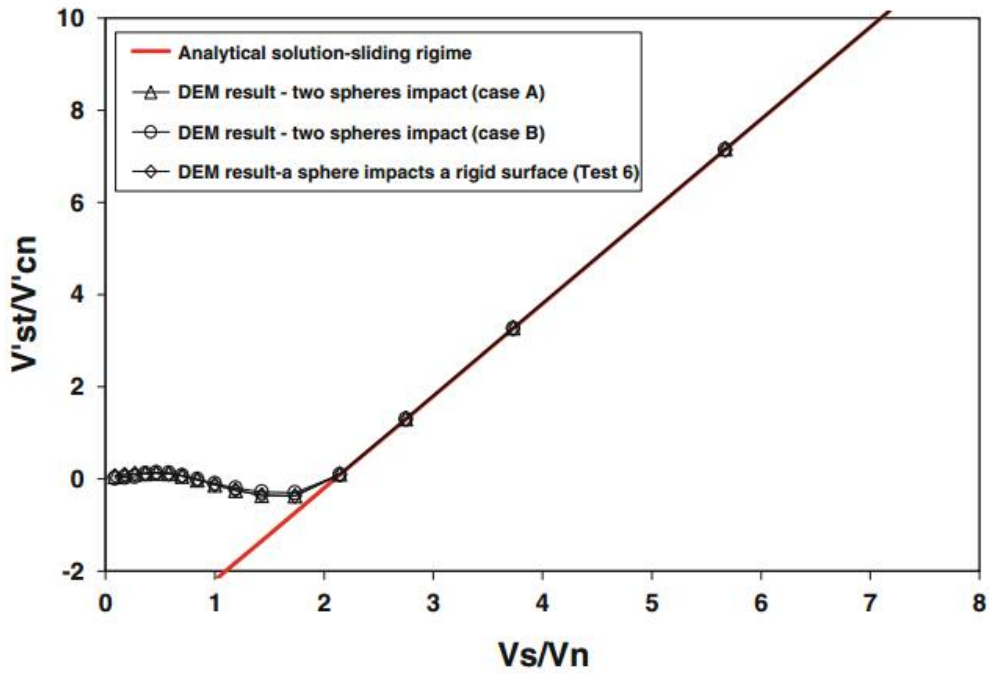


Figure 3-41: Test 8(Prior study): Al.alloy, simulated and theoretical tangent of recoil angle $\frac{V's_t}{V'_{cn}}$ versus tangent of incident angle $\frac{V_s}{V_n}$ for the small sphere

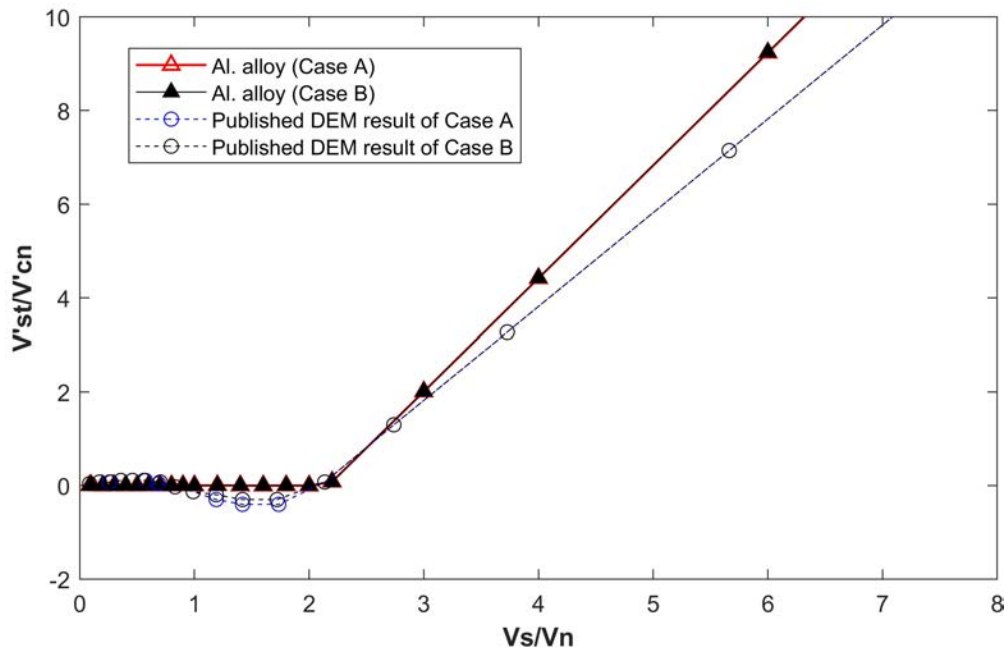


Figure 3-42: Test 8(Present DEM): Al.alloy, simulated and theoretical tangent of recoil angle $\frac{V's_t}{V'_{cn}}$ versus tangent of incident angle $\frac{V_s}{V_n}$ for the small sphere

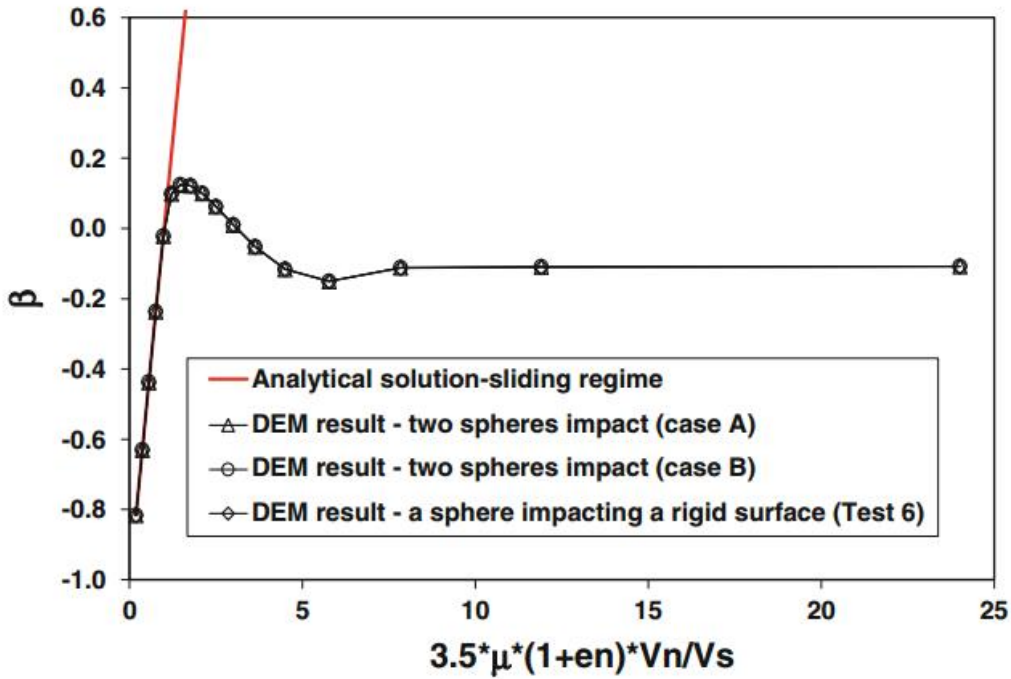


Figure 3-43: Test 8(Prior study): Nylon, simulated and theoretical tangential restitution coefficient β versus quantity $[3.5\mu(1 + e_n)\frac{V_n}{V_s}]$

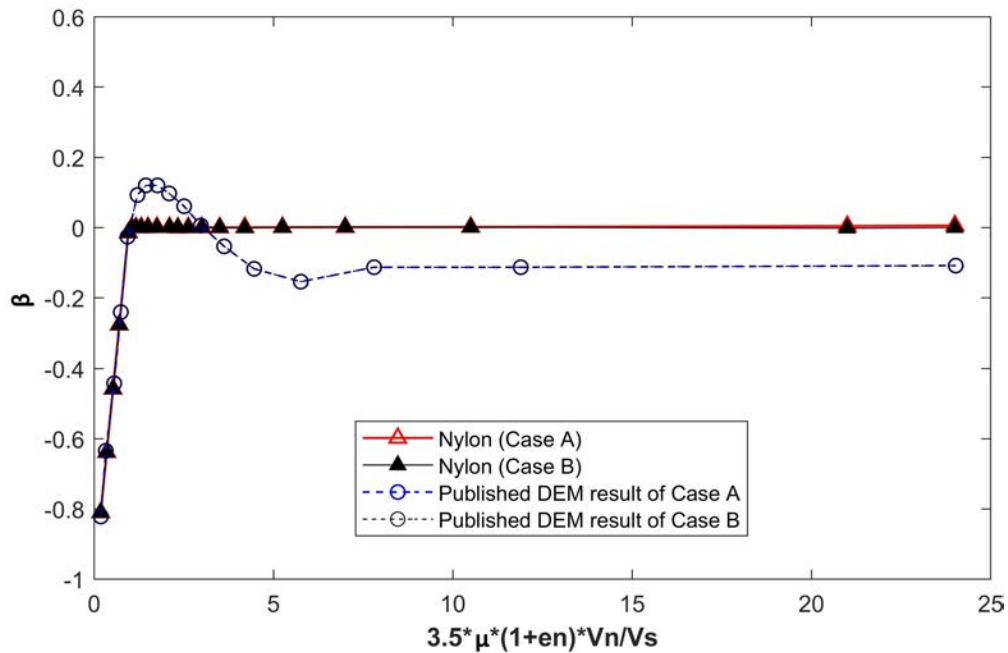


Figure 3-44: Test 8(Present DEM): Nylon, simulated and theoretical tangential restitution coefficient β versus quantity $[3.5\mu(1 + e_n)\frac{V_n}{V_s}]$

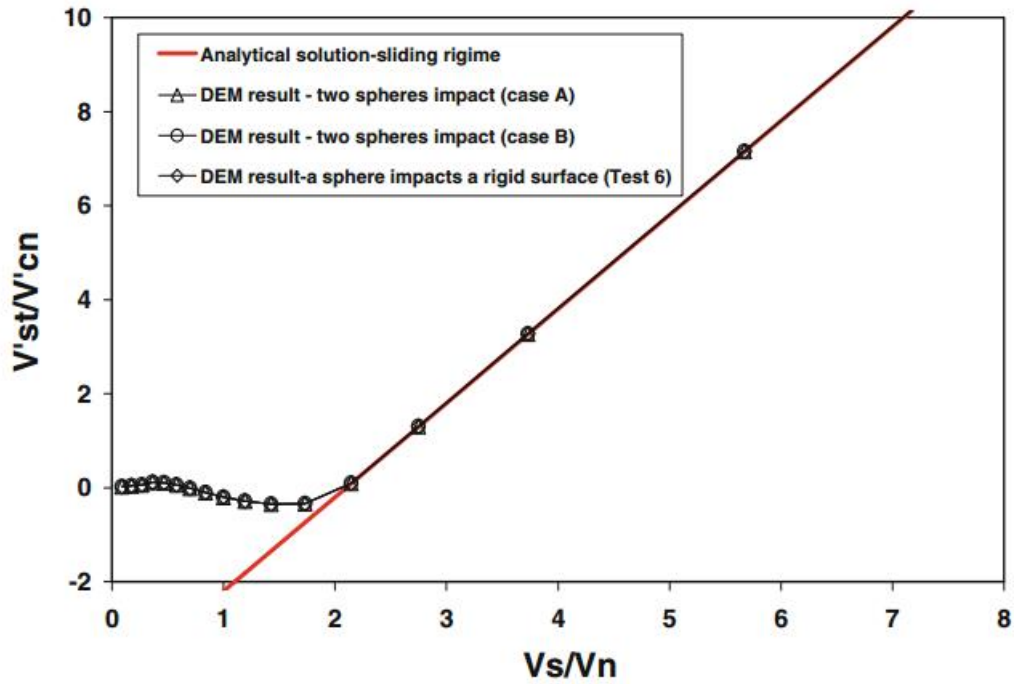


Figure 3-45: Test 8(Prior study): Nylon, simulated and theoretical tangent of recoil angle $\frac{V's_t}{V'c_n}$ versus tangent of incident angle $\frac{V_s}{V_n}$ for the small sphere

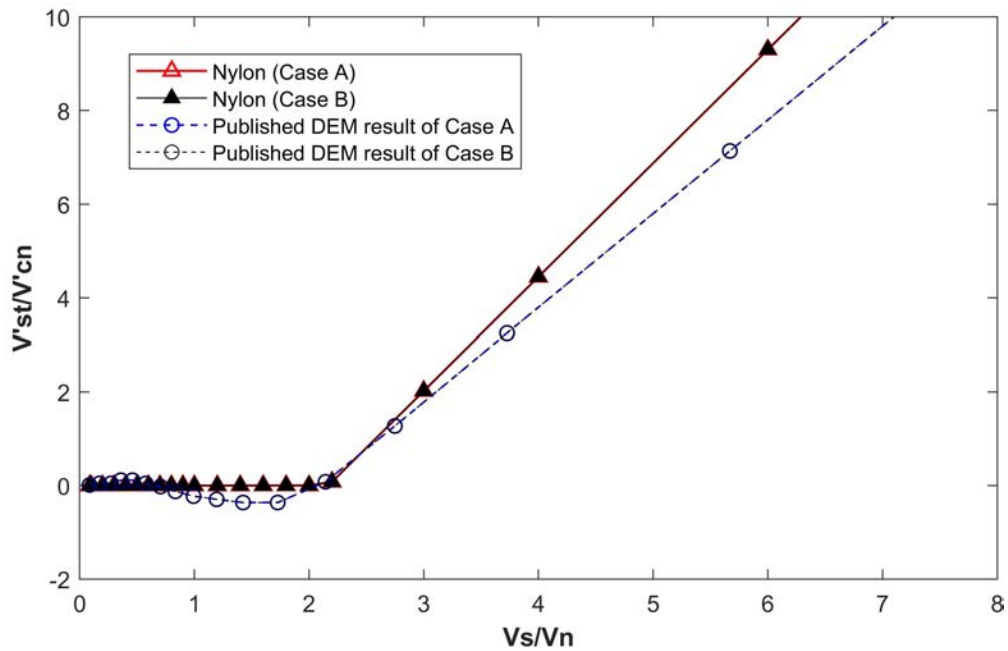


Figure 3-46: Test 8(Present DEM): Nylon, simulated and theoretical tangent of recoil angle $\frac{V's_t}{V'c_n}$ versus tangent of incident angle $\frac{V_s}{V_n}$ for the small sphere

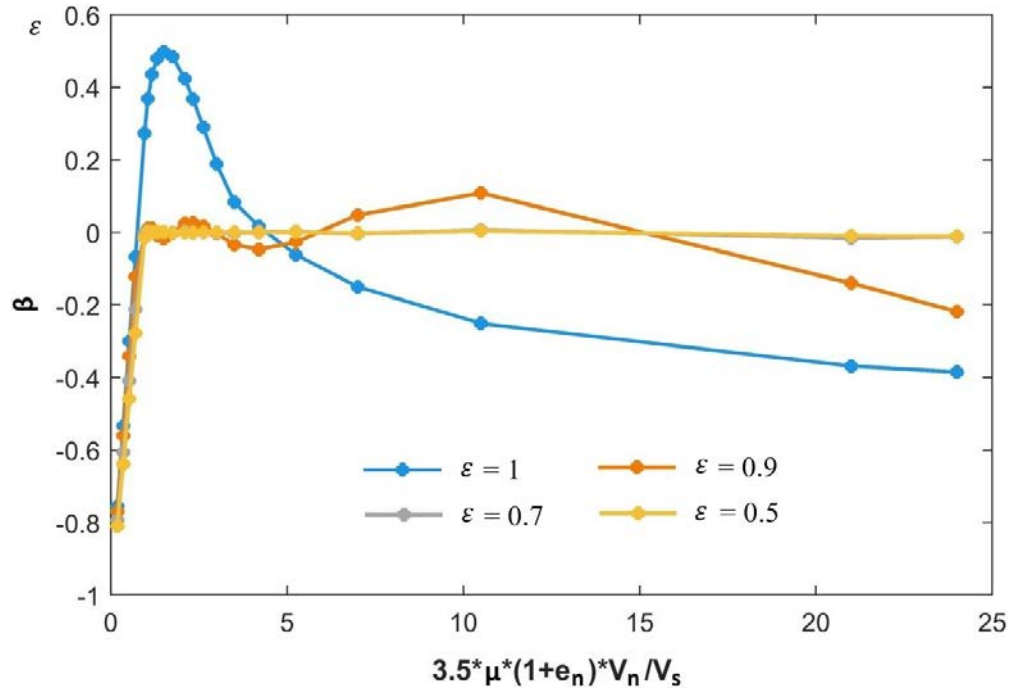


Figure 3-47: Test 8(Present DEM): simulated tangential restitution coefficient β varying as a function of the quantity $[3.5\mu(1 + e_n)\frac{V_n}{V_s}]$ with different restitution coefficients ε respect to Al. alloy for Case A

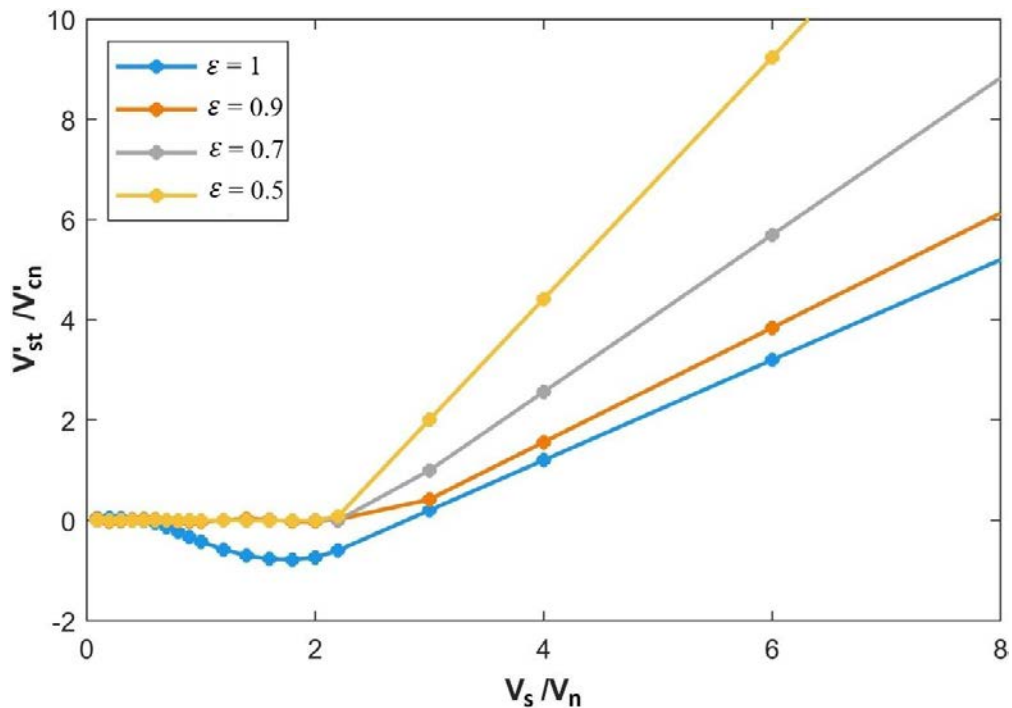


Figure 3-48: Test 8(Present DEM): simulated tangent of recoil angle $\frac{V'_{st}}{V'_{cn}}$ versus various tangent of incident angles $\frac{V_s}{V_n}$ with different restitution coefficients ε respect to Al. alloy for Case A

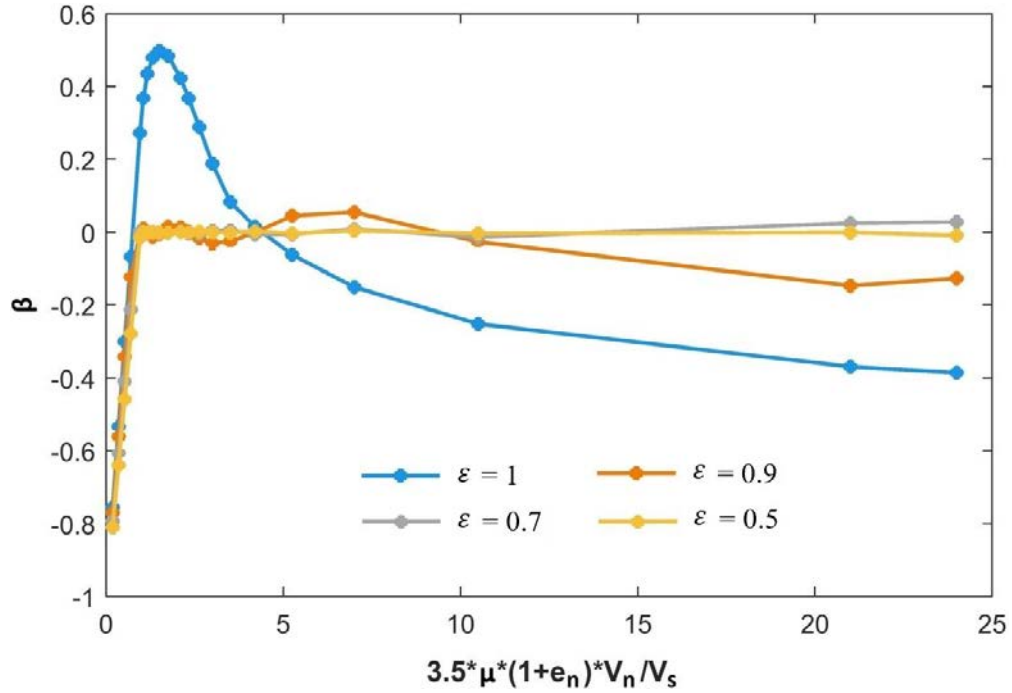


Figure 3-49: Test 8(Present DEM): simulated tangential restitution coefficient β varying as a function of the quantity $[3.5\mu(1 + e_n)\frac{V_n}{V_s}]$ with different restitution coefficients ε respect to Al. alloy for Case B

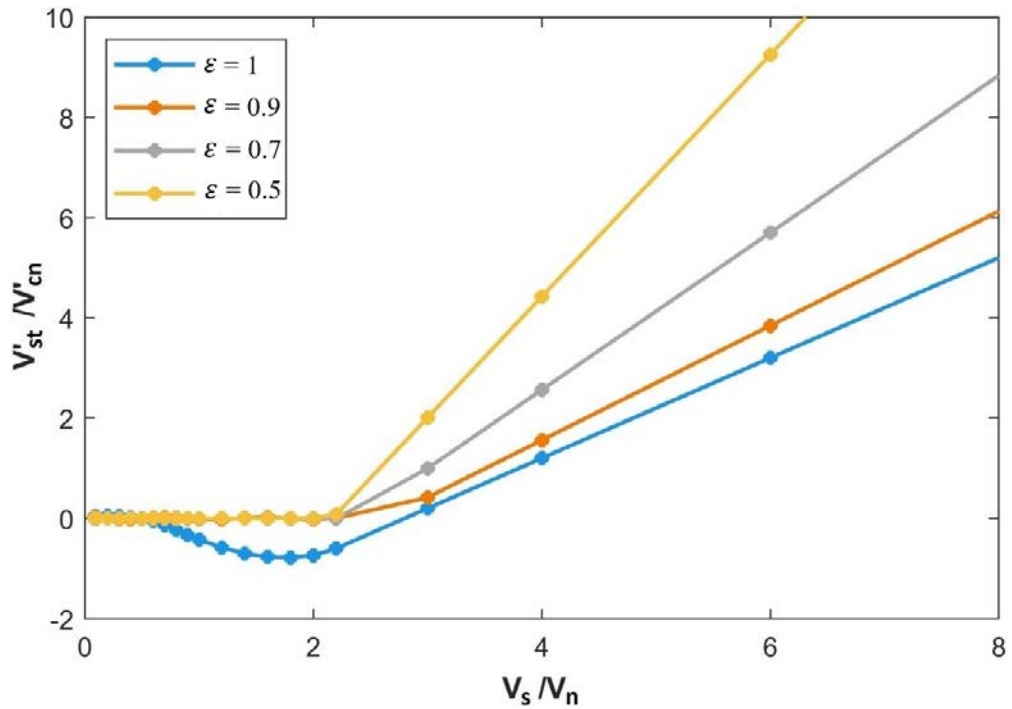


Figure 3-50: Test 8(Present DEM): simulated tangent of recoil angle $\frac{V'_{st}}{V'_{cn}}$ versus various tangent of incident angles $\frac{V_s}{V_n}$ with different restitution coefficients ε respect to Al. alloy for Case B

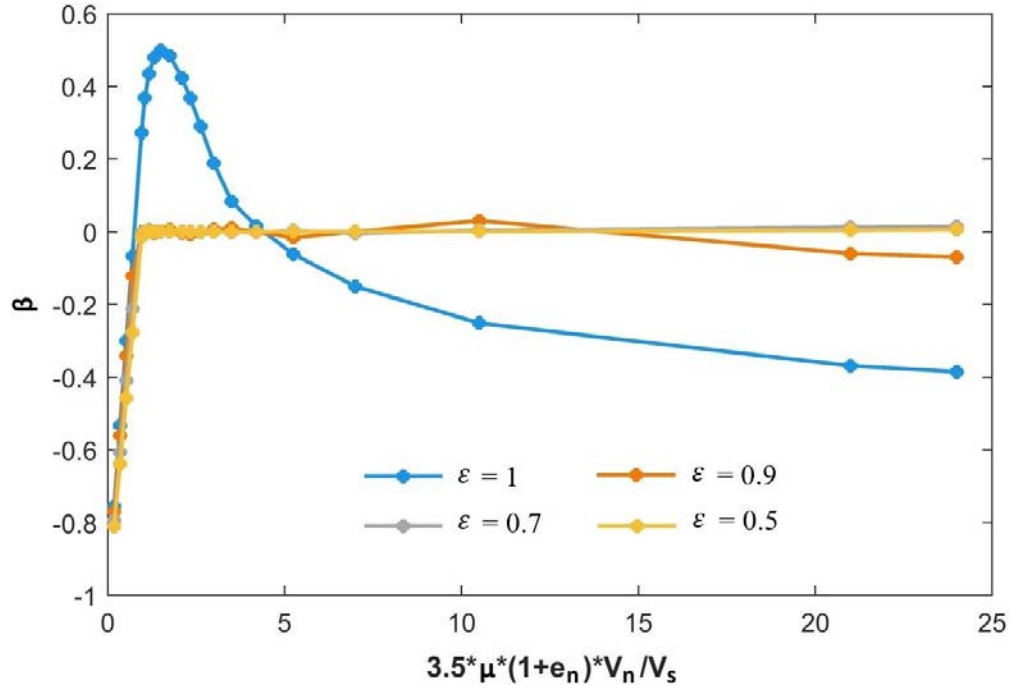


Figure 3-51: Test 8(Present DEM): simulated tangential restitution coefficient β varying as a function of the quantity $[3.5\mu(1 + e_n)\frac{V_n}{V_s}]$ with different restitution coefficients ε respect to Nylon for Case A

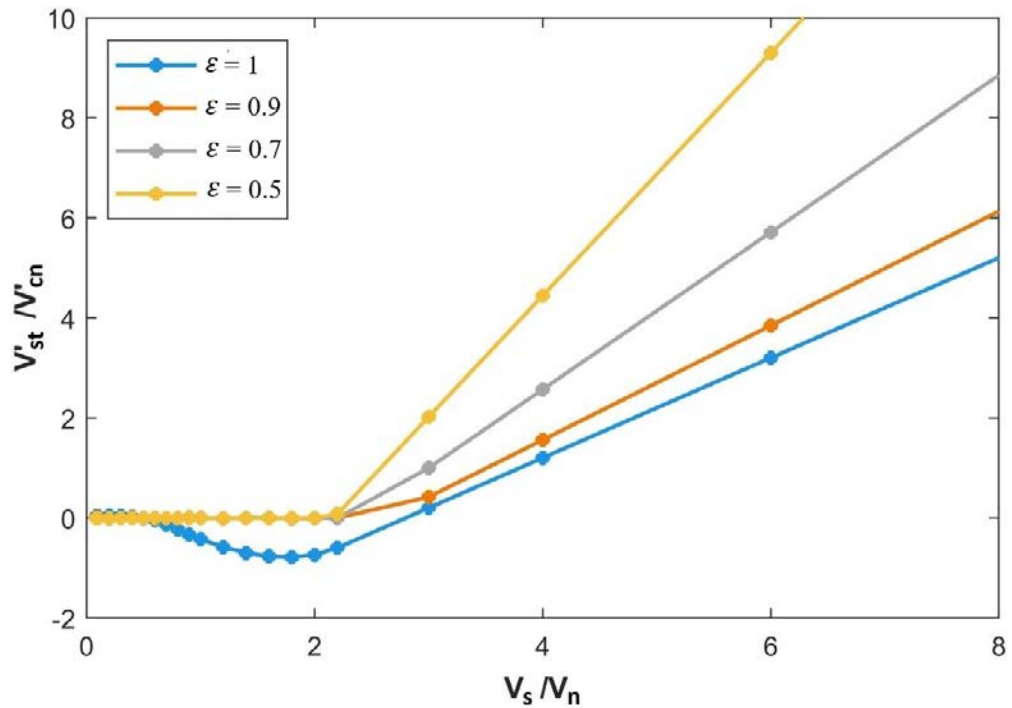


Figure 3-52: Test 8(Present DEM): simulated tangent of recoil angle $\frac{V'_{st}}{V'_{cn}}$ versus various tangent of incident angles $\frac{V_s}{V_n}$ with different restitution coefficients ε respect to Nylon for Case A

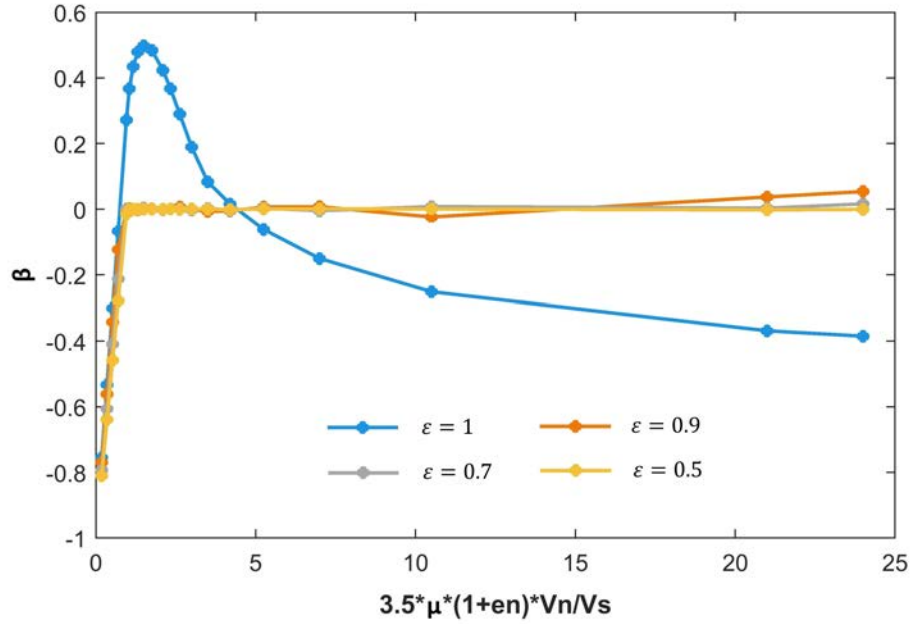


Figure 3-53: Test 8(Present DEM): simulated tangential restitution coefficient β varying as a function of the quantity $[3.5\mu(1 + e_n)\frac{V_n}{V_s}]$ with different restitution coefficients ε respect to Nylon for Case B

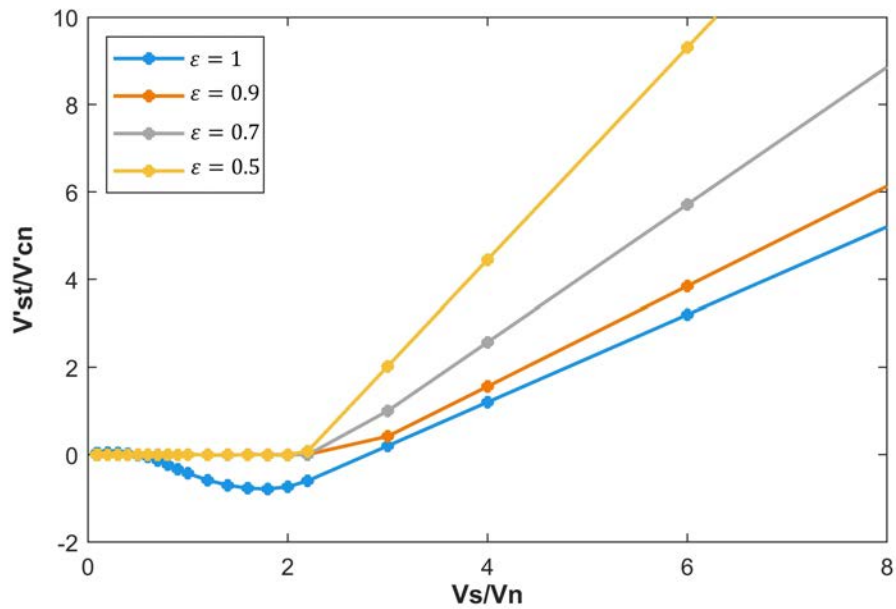


Figure 3-54: Test 8(Present DEM): simulated tangent of recoil angle $\frac{V'_{st}}{V'_{cn}}$ versus various tangent of incident angles $\frac{V_s}{V_n}$ with different restitution coefficients ε respect to Nylon for Case B

CHAPTER 4: MIXING PROPERTIES OF BINARY GRANULAR MIXTURES UNDER GRAVITY DEPOSITION

4.1 Overview

Binary granular mixtures are widely used in geotechnics and construction. The complex composite nature of these mixtures can bring unpredictable influences to its overall performance because of large local variability of the effective bulk properties. A number of physical tests have been completed to explore the properties of binary mixtures and it has been found that the bulk properties of these aggregates are highly dependent on the degree of mixing. Even during the same mixing process, a significant difference in effective properties is shown as a result of the mixing. A complete study of the nature of the mixing process awaits completion, and the empirical evidence and laboratory results contain both uncertainty and non-reproducibility because of the complexity of the mixing process. In addition, few methods are available to determine the mixing properties of the final aggregate packing. Hence the full application of synthetic mixtures has been somewhat restricted. To deeply understand the mixing behavior, a comprehensive investigation on the process at the particle scale is required. This study is aimed at using a proven comprehensive discrete element method (DEM) model to evaluate the existing mixing procedures and see how much influence they can have over the homogeneity of the final packing. Through this analysis, a sequence of effective recommendations are suggested for future mixing designs.

4.2 Introduction

Binary granular mixtures that contain two different sizes of particles are commonly used in geotechnical engineering and construction applications, including roads, railways, and dams. The idea of mixing different particles into a new aggregate and then using the final product for purposes that possibly take advantage of the properties of the individual particles is attractive. Using this sort of composite packing has potential advantages over uniform mixes but also poses numerous challenges in terms of both the mixing process and evaluating the properties of the final mixed aggregate.

Numerous physical tests have been conducted to explore the mixing behavior of binary mixtures. Early studies included the collection of empirical experience to find effective mixing methods to improve mixing properties (Wilson, 2001; Fines et al., 2003; Williams et al., 2003). Additional techniques were developed to evaluate strength properties of mixed materials (Wilson et al., 2000; Wilson et al., 2003). Extensive laboratory column tests were completed to gain a fundamental understanding of the mixture response (Wickland et al., 2003; Wickland and Wilson, 2005; Wickland et al., 2006). However, more extensive testing has shown that the binary mixture behavior is highly determined by the variability in the parameters typical used to evaluate how well the composite is mixed. Additional effort has focused on evaluating the mechanical properties of binary mixes as a function of the mixing ratios (Vallejo and Mawby, 2000; Vallejo, 2001; Zhao and Zhang, 2013).

Since the complex composite nature of binary mixtures brings unpredictable influences on its overall performance, the optimal mixed aggregate would limit any large variations in mixing and mechanical properties. An aggregate with these properties is known as being well-distributed and homogeneous. Yet few studies have appeared that have shown effective

methods to determine the mixing characteristics of engineered mixtures and there is no specification that can be used to quantify mixing properties to meet engineering requirements. Field-scale experimental methods can be combined with laboratory tests to obtain empirical data (Khalili et al., 2010; Leduc et al., 2004; Wickland et al., 2010; Jehring and Bareither, 2016) but these methods can contain both uncertainty and non-reproducibility simply because of the nature of the problem. Both stiffness and strength properties commonly remain unknown until it is possible to test the final product in its equilibrium configuration, and it is a challenge to determine the effects of different variables on these final metrics.

Present challenges in the study of binary mixtures include being able to evaluate existing mixing procedures and determine how much influence these methods, and their variants, can have on mixing properties. The discrete element method (DEM) is a numerical modeling approach that can greatly assist in this analysis. The method represents the behavior of individual particles and their interactions both during the mixing process and afterwards when all particles are in their static equilibrium positions. Compared with physical experiments, this method has numerous advantages. First, this methodology is at least in some sense reproducible in that the same mixing process can be repeated for various samples. Second, by eliminating unexpected variables that can exist in physical experiments, the input parameters generated by this method can be controlled. Finally, as the DEM solves the dynamic equations of motion at the mass center of individual particles, it can provide a new viewpoint by introducing a mechanism to study micro-mechanical interactions producing qualitative results at the particle level such as shear bands. In the past several decades, many studies have demonstrated the feasibility and effectiveness of using the DEM to replicate geotechnical engineering tests. DEM simulations have also been well-developed and proficiently applied

in industry. Feng and et al. (2015) used this approach to explore the viscoelastic behavior of asphalt mixtures and investigate the density of internal stress distribution. Rahman et al. (2011) conducted DEM simulations to investigate the segregation patterns of binary particle mixtures. By comparing with a tube-sampling experiment, their results showed excellent agreement with experiments and demonstrated that DEM simulations are useful tools for dealing with industrial design. Xu et al. (2019) carried out three dimensional (3D) DEM models to study the effects of gravel content on the shear behavior of particle mixtures and their results were in good agreement with the experimental data. A gravity consolidation method proposed by Dabeet et al. (2014) was used to create 3D samples, but this study was somewhat simplified and provided an idealized analysis of the true physical phenomenon.

The main objective of this research is to use a validated DEM model to study the binary particle mixing simulation from sample generation to the subsequent testing. The mixing and mechanical properties of the final aggregate were studied, and effective methods are introduced to improve the mixing process to meet final engineering requirements on the aggregate. This research is aimed at providing significant knowledge that will supplement and expand upon important results from full-scale field test data.

4.3 DEM model Description

The DEM considers the uncoupled equations of motion for the individual particles instead of solving a system of equations for the entire system. All forces acting on particles are used to update the particle positions in moving over a discrete increment of time. Spheres are employed to simulate these particles in the present study. The translational and rotational motions are described by the following equations.

$$\begin{aligned}
m\ddot{x}_i &= \sum_{c=1}^{N_c} F_{ic}^{con} + F_i^g \\
I \frac{d\omega_i}{dt} &= \sum_{j=1}^{N_{mom}} M_{ij}
\end{aligned} \tag{78}$$

Here \ddot{x} and $\frac{d\omega_i}{dt}$ are global accelerations and F_{ic}^{con} are the contact forces including the normal and tangential components from the c th contact. Rather than explicitly considering damping forces, those terms are typically included in the calculation of the contact forces. There are total of N_c contacts, caused either by adjacent particles or neighboring boundaries, F_i^g are gravitational forces, M_{ij} are moments transmitted through the j th normal or tangential contact force, N_{mom} are the total number of applied moments, and the variable i varies from 1 to 3 denoting the x, y and z directions, respectively.

4.3.1 Contact models

Contact forces are typically introduced by the amount of overlap at the point of contact. Simplified Hertzian contact models are usually applied to describe the normal force behavior between two contacting particles. A series of non-linear formulations are then formed in terms of the particle shear modulus, radius, and Poisson ratio to replicate the behavior of the contact spring. The normal force F_n is calculated using

$$F_n = K_n \delta_n \tag{79}$$

Here K_n is an effective stiffness and δ_n represents the overlap length along the line joining the centers of two contacting particles. For a particle-particle contact, the effective stiffness is given as $K_n = \frac{2K_a K_b}{K_a + K_b}$, where K_a and K_b are spring stiffnesses associated with each particle.

For contacts between a rigid wall and the particle, the stiffness is doubled since the overlap length is half the value of a particle-particle contact.

Fiction resistance is an inherent property caused by relative particle motion at the contacts. A simplified Mindlin-Deresiewicz contact model is used to simulate the tangential force response without having to introduce the loading history. Rather than using the overlap length, the cumulative incremental displacement is employed for the tangential force calculation. This displacement exists at the contact point and is summed over every time increment initiating from the moment when the contact is first formed. This quantity is calculated by integrating the relative tangential velocities $\dot{\delta}_t$ at the contacts. Assuming that the particle has the same properties in every direction, the initial tangential contact stiffness is assumed to be $K_t = K_n$. However, the maximum value is bounded by the Coulomb friction force. Before this point, particle sliding occurs. Hence the general form for calculating the tangential friction force is

$$F_t = -\min(|\mu F_n|, K_t \int_{t_0}^t \dot{\delta}_t dt) \frac{\dot{\delta}_t}{|\dot{\delta}_t|} \quad (80)$$

During the contact, moments are transmitted either by surface asperity or by an unbalanced stress distribution. To imitate moment resistance, the Iwashita-Oda (1998) model is used supplemented with normal and tangential springs. When a relative rotational motion is generated between two particles, a moment M_r is transmitted from one particle to the other. In a fashion similar to the definition of the cumulative incremental displacement for the tangential force calculation, an incremental relative rotational displacement is used to calculate the moment resistance. This quantity is a function of the relative rotational ve-

locities between two contacting particles. Iwashita and Oda (1998) proposed the expression of rolling stiffness as $K_r = K_t r^2$. With an upper bound ηF_n , the transmitted moment is written as

$$M_r = -\min(|\eta F_n|, K_r \int_{t_0}^t \dot{\theta}_r dt) \frac{\dot{\theta}_r}{|\dot{\theta}_r|} \quad (81)$$

Here η is a rolling friction parameter related to the particle surface asperities or the eccentricity of the particle centroid (Ai et al., 2011) and $\dot{\theta}_r$ is the angular velocity which keeps the same meaning of ω in the present study.

A viscous damping model is used to damp out non-physical phenomena (Munjiza, 2004). The damping force is proportional to the relative motion at the contacts, while the damping coefficients are calculated to match a specified restitution coefficient ε , which is a commonly used parameter for describing energy dissipated per cycle (O’Sullivan, 2011) or a percentage ratio represented by the reduction of the velocity before and after a collision (Luding, 1998). As used by Cleary (2000), Iwashita and Oda (1998), Ai et al. (2011), and Wensrich and Katterfelf (2012), the damping coefficients with respect to the normal, tangential, and rotational directions are calculated by

$$C_n = 2\gamma\sqrt{\langle m \rangle K_n}, \quad C_t = \gamma\sqrt{\langle m \rangle K_t}, \quad \text{and} \quad C_r = \gamma\sqrt{\langle I \rangle K_r} \quad (82)$$

where γ is expressed as $-\frac{\ln(\varepsilon)}{\sqrt{\pi^2 + \ln(\varepsilon)^2}}$. The quantities $\langle m \rangle$ and $\langle I \rangle$ are the effective mass and moment of inertia. As a consequence, the updated forces and moment become

$$\begin{aligned}
F_n &= K_n \delta_n + C_n \dot{\delta}_n, & F_t &= -\min(|\mu F_n|, K_t \int_{t_0}^t \dot{\delta}_t dt + C_t \dot{\delta}_t) \frac{\dot{\delta}_t}{|\dot{\delta}_t|} \\
M_r &= -\min(|\eta F_n|, K_r \int_{t_0}^t \dot{\theta}_r dt + C_r \dot{\theta}_r) \frac{\dot{\theta}_r}{|\dot{\theta}_r|}
\end{aligned} \tag{83}$$

4.3.2 Boundary conditions

In the simulations that follow, collections of particles are poured into a control volume bounded by fixed rigid walls. To focus the study on the mixing process and save on computational time, two types of boundary conditions were applied to simulate these conditions: the periodic inlet boundary and finite rigid walls. These are briefly described below.

Periodic inlet boundary conditions

A periodic condition was constructed to simulate the behavior of a belt/ramp inlet that might be used in large-scale field studies to drop particles via gravity deposition into a bounding control volume. In practice, the control volume may not be bounded but rather a slowly growing pile of the particle aggregate. In this study, a repeated collection of incoming particles was specified that included two cohorts of particles, each with their own geometry and material properties. When particles are detected to move across a geometric location defining the periodic wall or the belt/ramp inlet, new particles with the same properties were introduced on the opposite side of this repeated section to represent the nature of particle transport and subsequent deposition into the control volume. This operation was designed to keep the number and initial position and velocity of the incoming particles identical but then vary the way the particles are subsequently mixed and deposited into the control volume depending on what is placed below the inlet position.

Finite rigid wall/mixer boundary conditions

Surfaces of the bounding volume are defined by using the finite rigid wall boundary condition. The contact points between the particles and these bounding walls must first be detected. For particles that satisfy with this condition, the normal particle-wall force relationships are then imposed.

A more difficult application of a rigid surface is introduced by placing cylindrical obstacles at varying locations under the particle point of entry into the control volume to represent physical disrupters that redirect particle flow behavior during the mixing process. In this case, the curved surface is identified by its origin at specified planar Cartesian coordinates and a fixed radius that identifies the impenetrable rigid curved wall. Contact conditions are applied in a fashion similar to those of the bounding walls to determine if the projected points are within the contacting area of these rigid cylinders. All other contacts during the mixing process follow the rules outlined for sphere-sphere contacts.

4.3.3 Post-mixing analysis

One of the benefits of DEM simulations is that it is possible to obtain detailed information of the internal structure of the final particle packing at any point within the mixtures (O’Sullivan, 2011). For all final binary composite packings that are at equilibrium following the mixing process, two sets of analyses were completed. These are described below.

Mixing parameters

The mixing parameters of a granular material, which can provide levels of homogeneity in the final particle aggregate, can be quantified by the volume ratio (ϕ_v), mass ratio (ϕ_m), void ratio (e), porosity (n), dry bulk density (ρ_b), and coordination number (Z). These are

all conventional parameters utilized in measurements and other applications, and have been adopted in this work to provide estimates on comparative levels of mixing effectiveness using different mixing obstacles used to direct and disrupt particle flow after it enters the control volume.

Bardet and Proubet (1991) evaluated the void ratio of 2D virtual samples using a unique geometric methodology. In the present study this idea has been extended for three-dimensional packings using a spherical sub-volume with a radius r and a origin located at a specific point within the final particle aggregate. A view of a planar cut of this situation is given in Figure **Fig. 4-1**. The occupied volume V_i of the i th particle in this case is given as

$$V_i = \begin{cases} 0, & d_i \geq R_i + r \\ \frac{4}{3}\pi R_i^3, & d_i \leq r - R_i \\ \frac{1}{3}\pi(3r - h_1)h_1^2 + \frac{1}{3}\pi(3R_i - h_2)h_2^2, & r - R_i < d_i < R_i + r \end{cases} \quad (84)$$

Here R_i is the radius of the particle of interest, d_i is the distance from the detected point to the centroid of the i th particle, and h_1 and h_2 are the heights of the relevant crown distance that allows measurement of the part of the particle volume that is contained within the control sphere volume used to measure the mixing parameters. These geometric measures can be computed as

$$\begin{aligned} \theta_2 &= 2 \arccos \left\{ \frac{d_i^2 + R_i^2 - r^2}{2d_i R_i} \right\} & \text{and} & & h_2 &= R_i - R_i \cos\left(\frac{\theta_2}{2}\right) \\ \theta_1 &= 2 \arcsin \left\{ \frac{R_i}{r} \sin \frac{\theta_2}{2} \right\} & & & h_1 &= r - r \cos\left(\frac{\theta_1}{2}\right) \end{aligned} \quad (85)$$

The volume ratio is then calculated as $\phi_v = \frac{V_{big}}{V_{small}}$, where the subscripts are the relative

particle sizes and for each material are calculated as $\sum V_i$ where the subscript i indicates either the large or small particles. When these volumes are multiplied by the relevant mass densities, the mass ratio can be calculated as $\phi_m = \frac{m_{big}}{m_{small}}$. The void ratio e is provided by $e = \frac{V_v}{V_s}$, where V_s represents the total solid volume of the large and small particles and $V_v = \frac{4}{3}\pi r^3 - V_s$ is the volume of voids. The porosity is given by $n = \frac{V_v}{\frac{4}{3}\pi r^3}$. In geotechnics, the void ratio and the porosity are linked via $n = \frac{e}{1+e}$. However, this function is difficult to be satisfied in DEM simulations as the total volume occupied by the particles is a challenge to calculate. However, through the proposed algorithm described earlier, the measured variables are in fairly good agreement with the above equation. The dry bulk density is given as $\rho_b = \frac{M_s}{V_t}$, where V_t is the total control volume and M_s is the total mass of the solids, which is given as $\sum \rho_i V_i$, where ρ_i is the corresponding density associated with either the large or small particles. The coordination number that quantifies the number of contacts per particle is written as $Z = 2\frac{N_c}{N_p}$, where N_c indicates the total number of contacts and N_p is the total number of particles within the subdomain. The scalar multiplier 2 signifies that each contact is shared by two contacting particles.

The effective elastic properties

In addition to the mixing ratio, the parameters that characterize the mechanical behavior of the final packing in terms of the relationship between aggregate stress and strain is also of interest. Simulated confined compression tests were employed for this investigation in an attempt to estimate the bulk elastic response between the normal stresses and normal strains within the particle aggregate and its variation over the entire control volume. Inside the full sample, a specific set of cubic sub-regions were used for this analysis. The subdomain

was confined by five rigid walls, and was compressed with a horizontal plane at the top of this cubic sub-region lowered onto the remaining particles. When the top plane moves downward, the particles near the walls experience translational and rotational movements. Under this compression, forces within the particles will be generated within the subdomain which generate forces on the remaining five walls. Assuming that the total aggregate acts in an isotropic fashion, these can be used to generate the effective elastic modulus E and Poisson ratio ν .

For a closed continuous domain with volume V , as noted by Bagi (1999b) and O’Sullivan (2011), the average stress $\bar{\sigma}_{ij}$ can be written as

$$\bar{\sigma}_{ij} = \frac{1}{V} \sum_{k=1}^{N_{BF}} x_i^k f_j^k \quad (86)$$

where f_j^k is the boundary force applied at location x_i^k and there are a total of N_{BF} forces acting along the boundary surfaces. The strain for a measured domain is calculated by considering boundary positions of the edge particles. The distance between the top and bottom planes is used for updating the overall axial strain, which assuming the compressive boundary is aligned with the z -axis, is given as $\bar{\epsilon}_{zz} = \frac{\Delta H_{zz}}{H_{zz}}$ where H_{zz} is the original height and ΔH_{zz} is the change in height of the subdomain in the z -direction. Since there is no extension along x and y axes, the two other normal strains are zero. Although it would not be unreasonable to assume isotropic bulk properties of the final aggregate, there are actually three independent elastic constants that result from this procedure. In the simulations that follow, we invoke the assumption that the elastic modulus in all three directions is the same, but allow the Poisson ratio to vary for the horizontal versus vertical directions. This allows

at least an initial attempt to estimate the levels of anisotropy resulting in this type of gravity deposition. Hence the three independent elastic constants are the elastic modulus E and the two Poisson ratios ν_{xy} and $\nu_{xz} = \nu_{yz}$. The final constitutive relation therefore takes the form

$$\begin{Bmatrix} \bar{\epsilon}_{xx} \\ \bar{\epsilon}_{yy} \\ \bar{\epsilon}_{zz} \end{Bmatrix} = \begin{bmatrix} \frac{1}{E} & -\frac{\nu_{xy}}{E} & -\frac{\nu_{xz}}{E} \\ -\frac{\nu_{xy}}{E} & \frac{1}{E} & -\frac{\nu_{xz}}{E} \\ -\frac{\nu_{xz}}{E} & -\frac{\nu_{xz}}{E} & \frac{1}{E} \end{bmatrix} \begin{Bmatrix} \bar{\sigma}_{xx} \\ \bar{\sigma}_{yy} \\ \bar{\sigma}_{zz} \end{Bmatrix} \quad (87)$$

4.4 Sample Generation

To study the effect of adding geometric mixers within the large-scale control volume for the entire aggregate, six different configurations were generated in addition to the simple case of pure gravity deposition without any disruptors whatsoever. The particles enter an uncovered cubic box with dimensions $1 \times 1 \times 2 \text{ m}^3$. The periodic inlet is employed to simulate the behavior of a converter belt that might be used in a practical physical field mixing technique. **Table 4-1** lists the required input parameters for both sets of particles assumed for these simulations and gives the initial front- and side-view configurations for the repeated section. These particle cohorts are assumed to enter the control volume as stacked layers similar to what might be encountered in a physical mixing process as two different types of materials are first poured on top of each other. The layer of 4 larger spheres is placed on the top and the smaller spheres are distributed in eight layers with 64 spheres per layer. So, a total of 516 particles are included for the repeated section.

One objective of this study is to compare different mixing methods in terms of how effective they are to improve the degree of mixing in the new deposit. This is achieved by

evaluating the existing mixing procedures by quantifying the mixing parameters and seeing how much influence the addition of geometric mixers can have over the homogeneity of the final packing. In the present analysis, cylindrical obstacles are introduced at varying locations within the control volume under the point of entry of the particles. The boundary condition at the surface is relatively simple to enforce as a no-penetration boundary conditions as the particles impact the mixer. In addition, and perhaps more importantly, the well-known oblique benchmark tests demonstrate that particles change their trajectory with different incident angles. Through the introduction of these cylindrical mixers, a wide range of reflection angles can be generated during one collision and result in far more particle interacting collisions as illustrated in **Fig. 4-2**. This phenomenon helps particle dispersion in space. In this work, different mixing systems are examined based on obstacle positions or the number of applied obstacles. To make direct comparisons reasonable, the maximum number of cylindrical mixers was limited to two for this relatively small control volume.

A total of six different mixing barrier scenarios were explored using DEM simulations. These are labeled Models 1-6, and indicate no cylindrical barriers (Model 1), a single cylindrical barrier at three geometric positions (Models 2-4), and two cylindrical barriers at varying vertical and horizontal positions (Models 5-6). There are an infinite number of combinations and positions that could be investigated, and these were selected as being representative of what might be encountered during a field mixing event. The mixing process for these six models is shown in **Figs. 4-3 ~ 4-8**, where the filling status is shown at specific time intervals. Even a cursory glance at the particle positions indicates the large influence that the mixing barriers can have in directing the flow of the stacked particles entering the control volume. After the packing volume reaches a specific depth, no more particles are allowed and

the mixing parameters of the aggregate packing under static equilibrium can be measured at specific locations within the control volume.

In addition to the number and position of the mixing barriers, it is also possible to mix the particles together multiple times. This practice has been used in industrial applications and consists of simply scooping up the collecting aggregate pile and running it through gravity mixing a second time. The results are promising enough to consider here, but it is the modeling of the second mixing iteration that is more challenging than accomplishing what is relatively easy to do in the field. To do this using the DEM model, the following steps were used: a smaller volume from the final aggregate packing in the control volume achieved from the 1st mixing is taken with a depth of 1 *m*. This is then discretized into subdomains with dimensions $1 \times 0.5 \times 0.25 \text{ m}^3$. These smaller domains were then ordered in a line where they are allowed to enter through the inlet in sequence to simulate cells of particles on a conveyor belt. By re-filling the control volume using the same mixing process, the packing should in theory be even more homogeneous than that resulting from a single mixing iteration. Partial representative packings after the 2nd mixing showing the internal packing state for the six models are given in **Fig. 4-9**.

In the subsections that follow, the influence of the primary variables used to mix the particles are qualitatively explored and discussed using direct observations of the final particle positions. In a later section, the various mixing schemes are quantitatively evaluated using the direct measurement of the mixing parameters.

4.4.1 Number of obstacles

Observing the final configuration of Model 1 after mixing with the 1st iteration given in **Fig. 4-3**, it is clear that without the application of obstacles, significant heterogeneity occurs. Large particles frequently appear to be floating during simulation animations and have been gradually pushed to an external wall. Gowan et al. (2010) have emphasized that it is not typically a viable option in a mining facility to mix materials under purely mechanical behavior. Hence, the mixing obstacles may need to be added to improve mixing conditions.

Through **Figs. 4-4 ~ 4-6**, visual results and direct observation on the final positions of the particles show that obstacles promote mixing compared with the Model 1 case of no obstacles. However, the nature of this improvement is qualified and depends on the role and positioning of the obstacles during mixing. For example, comparing the single barrier of Model 3 with the two mixers in Model 5, a slight improvement for the mixing degree is given in **Fig. 4-7** of Model 5. In fact, comparing the single obstacle results of Model 2 with those of Model 1 indicate that for this specific experiment the benefit of adding more cylindrical obstacles is not at all obvious.

One possible explanation for the limits of obstacle mixing can be generated by observing the upper right and the lower left corners in our Model 5, it seems that associated with each obstacle, there is an area of influence. This area is around $0.1\text{ m} \sim 0.9\text{ m}$ in height away from the bottom of the container for Model 3. This specific area for the upper left obstacle is marked with the blue area sector as illustrated in **Fig. 4-10**, while same area for obstacles on the right is drawn in red. Because the curved surface amplifies the range of angles at which the particles can move after impact, the dimensions of the regions in which the particles will travel will be a function of their incoming velocities and their relevant mechanical properties.

For multiple obstacles, particle distributions post-impact will be a function of the combined effect of the individual obstacles. But the positioning of these obstacles is critical. For example, for the results from Model 6 in **Fig. 4-8**, the second obstacle generates a second area of influence that reduces the level of particle mixing rather than enhancing it as shown in **Fig. 4-10 (c)**. The results of these simulations visually show that in general the use of obstacles for a single mixing iteration can provide some benefits. However, in the case of a finite control volume, the applied number of obstacles will be limited by space, which further complicates optimizing barrier design.

4.4.2 Obstacle position

Through **Figs. 4-4 ~ 4-6**, it is also visually apparent that the geometric positioning of the obstacles can play a large role during the mixing. In Model 2, the obstacle is positioned in such a way as to make the mixing even worse than in the case of no barriers of Model 1. It does this by essentially dividing the flow of the particles into two directions from the impact, where the larger particles move right and the smaller particles move left. Hence this positioning acts to separate rather than mix. By shifting the barrier slightly to the left in Models 3 and 4, more of the smaller particles are directed towards the right, impacting the larger spheres and providing a better mixing.

The same sort of behavior can be observed by visual comparisons of Models 5 and 6. In Model 6, the lower of the two barriers appears to be too far to the right, and once again acts to separate the particle flow and limit interactions between the small and larger particles. By moving the lower barrier only 0.1 meters to the left, the final particle positions appear to be far better mixed by forcing more particle interactions just after barrier impact.

4.4.3 Affect of mixing iterations in filling

The results from a second mixing through each of the barrier models are shown as a cross-sectional view from each case in **Fig. 4-9**. Even a cursory view of these mixed packings demonstrates that the second mixing provides a far better result than a single run through the mixing process, regardless of barrier presence, type, or position. Even the circumstances of Model 1, where there are no barriers placed but the assembly is simply gathered and re-poured, are promising in terms of the overall result.

Hence, there are two different cases to consider and quantify: a) the case of a single pour through the mixing configuration, and b) the case of two iterations of the same mixing process using the scoop-and-pour simulation process described above. Below, these methods are discussed in the context of mixing parameters generally used to identify the level of homogeneity of a mixed particle packing.

4.5 Results and Discussion

To better understand the role of the mixing process, quantifying the variation in the mixing and mechanical properties of the final particle aggregate is necessary to supplement the qualified observations of the previous section. Marketos and Bolton (2010) have highlighted the fact that the final packing state will be influenced by the presence of flat boundaries. In this section, the subdomains that are analyzed for evaluation are removed from the bounding surfaces of the control volume as is the region near the top equilibrium surface of the final packing. By measuring the parameters in multiple domains away from these regions, a more consistent set of values can be expected for the six barrier/mixing models.

4.5.1 Mixing parameters

For measuring the mixing parameters, spherical regions with radii of 0.05 m , 0.1 m , and 0.2 m were originally used where the center locations of these measurement control volumes are listed in **Table 4-2**. Through a number of simulated evaluations, it was found that when smaller dimensions of the control sphere are applied, specifically the radius 0.05 m , local mixing differences become obvious. However, for the larger radius, there were so many particles that differentiating between the measured values of the mixing parameters was somewhat blurred. Because of these reasons, the mixing parameters were measured only using the control volume radius of 0.1 m . After the 1st mixing iteration, the six common mixing parameters were calculated and are plotted in **Fig. 4-11** for the six different mixing models. On the vertical lines of each sub-figure, the data points are marked by different dark symbols. The average values are given as red squares and their standard deviations are indicated by gray bars.

In Figures **Fig. 4-3** and **Fig. 4-4**, it appears that most of the larger particles are eventually located in the right side of the control volume. In the case of Model 1 this is primarily because the larger particles are stacked on top of the smaller particles and their tendency during pouring impact is to travel to the right. This behavior is somewhat exacerbated by the placement of the single mixer in Model 2, which also directs the larger particles towards the right. These visually poor levels of mixing are reflected in the measured values of the volume ratio ϕ_v shown in **Fig. 4-11 (a)**. There are a large number of very small or even zero values for this parameter for Models 1 and 2 with a very low mean value. As the obstacles are introduced at locations that increase impacts between the differently sized particles, the levels of mixing as reflected by the volume ratio tends to improve, with

mean values closer to 0.25 than to zero. Model 4 has by far the largest variation that is also reflected in visual evidence, while models 3, 5, and 6 having somewhat smaller variations. Similar behavior is found for the mass ratio ϕ_m as illustrated in **Fig. 4-11 (b)**, which effectively replicates the behavior in the volume ratio but includes particle density, and is shown here for completeness.

O’Sullivan (2011) has stated that in the three-dimensional case with uniform spheres, the minimum void ratio is 0.4. For the mixes in this study, with two differently sized particle groups, the void ratio can be less than this number when there are particles of larger size within the smaller control volume. The results from Model 2 in **Fig. 4-11 (c)**, which is dominated by regions occupied by smaller spheres, the minimum e value is around 0.4, which partially validates the methodology used here. The void ratio e helps explain how smaller spheres can partially fill the voids formed by large particles. For well-mixed deposits, the variation of void ratios over the nine measured regions should be small. In our analysis, important information is given when e is below the value of 0.4. With an increment of large spheres falling into the subdomain, the measured values drop below 0.4. A relatively low e presented in Model 4 corresponds to the highest volume ratio ϕ_v shown in **Fig. 4-11 (a)**. Through the proposed particle volume algorithm, combining the volume ratio ϕ_v with the void ratio e , the numbers of occupied particles in the controlled volume can be exactly calculated. For example, the solid volume V_s is computed by $\frac{4}{3}\pi r^3$ and the number of big spheres can be quantified by using the equation of $\frac{V_s\phi_v}{\frac{4}{3}\pi R_{big}^3}$, where R_{big} represents the radius of large spheres. However, 0.4 is only for the dense (hexagonal close or face-centered-cubic) packing. In reality, the particles may pack in loose form. Hence rather than determining the degree of mixing, the void ratio e is instead a good parameter to assist in the determination

of internal structure. The void ratio e and the porosity n are not independent and are automatically correlated with each other and in the function of $n = \frac{e}{1+e}$. Therefore, similar results are obtained for the porosity as illustrated in **Fig. 4-11 (d)**.

The dry bulk density ρ_b , which represents the proportion of weight occupied by solids, is given as $\rho_b = \frac{M_s}{V_t}$. The solid mass M_s is calculated by $\sum \rho_s V_s$, so this parameter automatically loses any ability to describe how well two different materials are mixed. The same lack of ability is clear in examining the coordination number Z in **Fig. 4-11(f)**. This parameter is normally used for assessing force transmission and determining local failure. Since the particles are in relatively dense packing following the mixing procedure, there relatively little variation of this parameter in the investigated models.

Fig. 4-12 gives the measured mixing parameters for the presented models following a second iteration of mixing. Except for the dry bulk density and coordination number, the results illustrate that a 2nd mixing reduces the variation in all parameters and results in mean values of the specific parameter that are far more consistent despite the nature of the mixing scheme. For a well-mixed particle aggregate, the volume ratio should approach the value calculated using the input quantities. In the present analysis, and based on the particle percentage in repeated sections, the ideal average volume ratio is 0.0625. However, because the obstacles are added only in the direction of gravity, the measured values are slightly larger than this quantity.

Overall, for the analysis of binary mixtures, the volume ratio can be used to quantify the level of mixing by measuring this parameter at various locations within the final aggregate. For well-mixed deposits, the measured data points are consistent with only small fluctuations. There are few extreme values, including zeros and relatively large values, and depending on

the general mixing the average volume ratio is getting close to the input. It is also clear that regardless of the mixing method used, a second iteration of mixing is far more important than the nature of number of the mixing barriers.

4.5.2 Effective elastic properties

The effective elastic properties are measured using simulated uniaxial compression tests. The same geometric center locations as those of the mixing parameters were selected for doing these measurements except that the studying domain was replaced by nine cubic regions with side lengths of 0.2 m . The imposed axial compressive stress for the top moving wall was specified as 1000 Pa as computed by the methods described above and the measured stress tolerance was within 10 Pa.

After the 1st mixing, the equivalent elastic modulus E for each of the six mixing models are presented in **Fig. 4-13**. The same notation is used as that applied for plotting the mixing parameters. With respect to the individual models, detailed information including the Poisson ratios is given in **Fig. 4-14**. A dual y-axis chart is applied to show both the elastic modulus and the two values of the Poisson ratio: ν_{xy} and then $\nu_{xz} = \nu_{yz}$. The results generally confirm several features observed when evaluating the mixing parameters, with Model 5 giving the smallest variation of elastic modulus. To avoid the effect introduced by extreme values, each average is calculated by removing the highest and the lowest values. The six models provide mean values of the elastic modulus that range from 1817 to 3211 Pa after this first mixing (in **Table 4-3**). The in-plane (by this we mean the horizontal plane) Poisson ratio values shown in **Table 4-4** range from 0.63 to 0.86, while the out-of-plane (this includes the vertical direction) Poisson ratios range from 0.10 to 0.32 as given in **Table 4-5**.

Following the 2nd mixing iteration, the computed equivalent elastic properties are plotted in **Figs. 4-15** and **4-16**. It is again observed that the effective mechanical properties are also sensitive to the number of mixing iterations and that a repeated mixing is more important than the type and nature of the geometric mixers. The range of elastic modulus over all models is now from 1812 to 2564 Pa. The corresponding mean values for the elastic modulus and their standard deviations are listed in **Table 4-3**. The two Poisson ratios now range from 0.57 to 0.77 for ν_{xy} and from 0.22 to 0.35 for ν_{xz} . Hence the second mixing tends to reduce the range found in effective properties using various types of geometric mixers. It is also clear that there is very strong anisotropy in the final particle mixing, indicated by the measured values of Poisson ratio that are over twice as large in the horizontal plane versus the same parameter that contains the vertical direction. Although a more extensive exploration of the nature of the effective stiffnesses is outside the scope of this study, these results indicate that using the assumption of bulk isotropy for gravitationally deposited binary packings may not be justified.

4.6 Summary and Conclusions

In this paper, numerical simulations were used to determine the internal mixing degree and mechanical properties of binary particle mixtures based on various geometric mixers positioned below the particle entry point into a control volume. A well-developed DEM model, which is capable of recovering basic mechanical behaviors, was employed to simulate the mixing process. The number and position of obstacles and the number of mixing iterations were used to study the effects on mixing properties. A sub-volume algorithm was proposed and simulated compression tests were applied to numerically evaluate mixing properties of

the final particle aggregate.

The most significant conclusions of this work are as follows:

1. The mixing degree of the final aggregate is best quantified by the volume ratio ϕ_v .
2. For a single mixing iteration, fixed geometric mixers can improve the degree of mixing if the mixer acts to direct particle interaction rather than separate the particle cohorts.
3. A second mixing iteration, with or without geometric mixers, is just as effective as any other system to mix the particles together.
4. Preliminary numerical experiments indicate a strong level of anisotropy in gravitationally deposited binary mixtures.

Table 4-1: Summary of input parameters

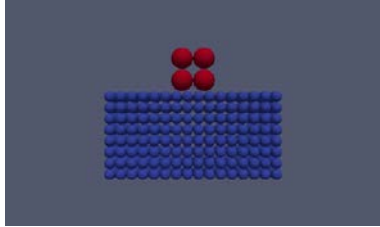
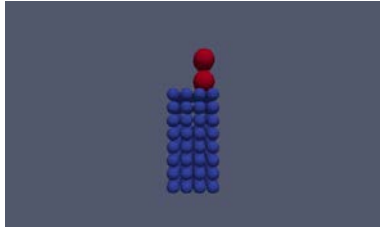
Particle types	Parameters	Values	Figures
Big	Young's modulus $E(N/m^2)$	5.0E5	 
	Poisson ratio ν	0.28	
	Density (kg/m^3)	3600	
	Radius (m)	0.03	
Small	Young's modulus $E(N/m^2)$	8.0E6	
	Poisson ratio ν	0.33	
	Density (kg/m^3)	4000	
	Radius (m)	0.015	
General	Friction coefficient	0.2	
	Restitution coefficient	0.3	
	Rolling coefficient	0.1	
	Velocity (m/s)	1	
	Time increment $dt(sec)$	1.0E-4	
			Front and Side views

Table 4-2: Point locations for measuring mixing parameters and the equivalent elastic properties

	x	y	z
1	0.25	0.5	0.2
2	0.5	0.5	0.2
3	0.75	0.5	0.2
4	0.25	0.5	0.5
5	0.5	0.5	0.5
6	0.75	0.5	0.5
7	0.25	0.5	0.7
8	0.5	0.5	0.7
9	0.75	0.5	0.7

Table 4-3: The mean value and related standard deviation of the effective elastic modulus E (N/m^2) for each model after different mixing iterations

Models	1 st mixing iteration		2 nd mixing iteration	
	mean	std	mean	std
1	1954	841	2249	782
2	2230	992	1812	189
3	2842	1255	1776	445
4	3211	1731	2564	577
5	1817	367	2171	830
6	2105	1046	1736	662

Table 4-4: The mean value and related standard deviation of the effective Poisson ratio ν_{xy} for each model after different mixing iterations

Models	1 st mixing iteration		2 nd mixing iteration	
	mean	std	mean	std
1	0.631	0.158	0.690	0.075
2	0.710	0.136	0.633	0.064
3	0.842	0.224	0.608	0.058
4	0.861	0.323	0.767	0.077
5	0.651	0.099	0.688	0.122
6	0.666	0.204	0.573	0.124

Table 4-5: The mean value and related standard deviation of the effective Poisson ratio ν_{xz} or ν_{yz} for each model after different mixing iterations

Models	1 st mixing iteration		2 nd mixing iteration	
	mean	std	mean	std
1	0.320	0.134	0.281	0.079
2	0.269	0.126	0.328	0.046
3	0.127	0.210	0.340	0.046
4	0.095	0.312	0.221	0.077
5	0.302	0.070	0.272	0.101
6	0.285	0.182	0.351	0.093

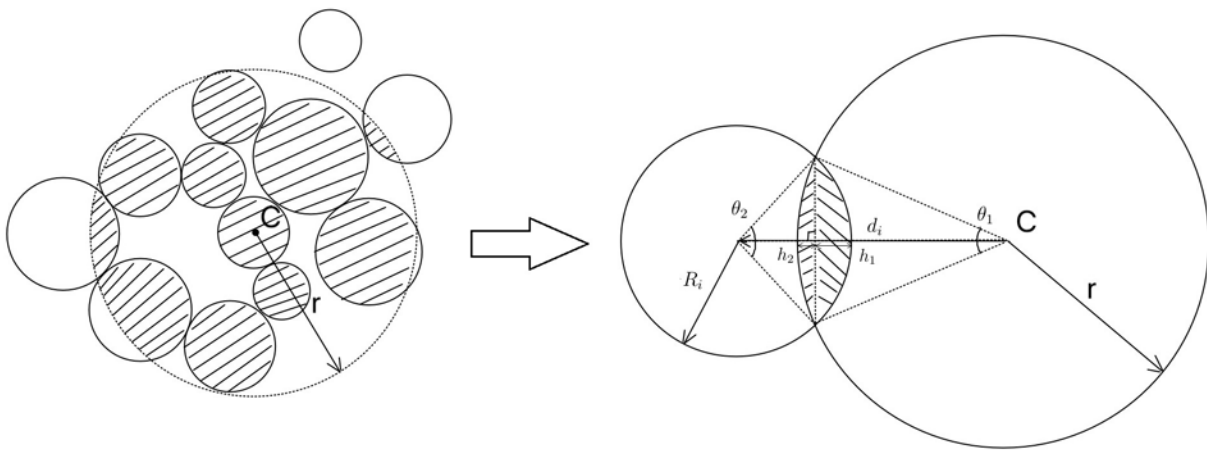


Figure 4-1: A scheme illustrating the algorithm of area calculation for 2D virtual samples

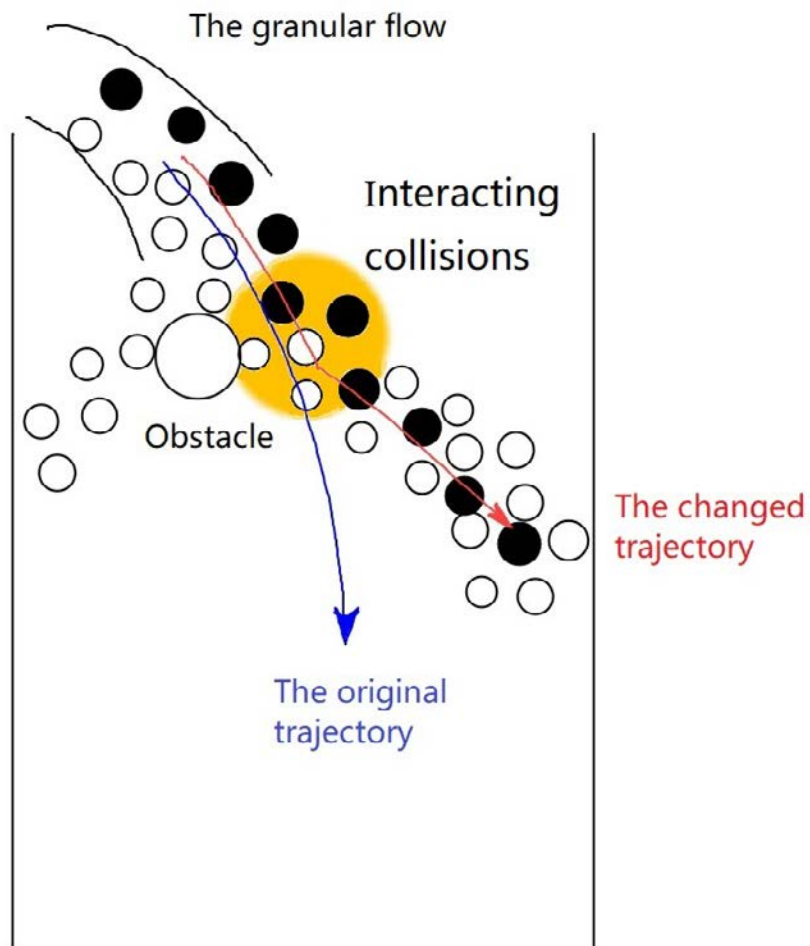


Figure 4-2: The application of cylindrical mixers helps particle dispersion in space. By changing the trajectory of the granular flow, different particles have more chance to interact with each other and promote interacting collisions in particles.

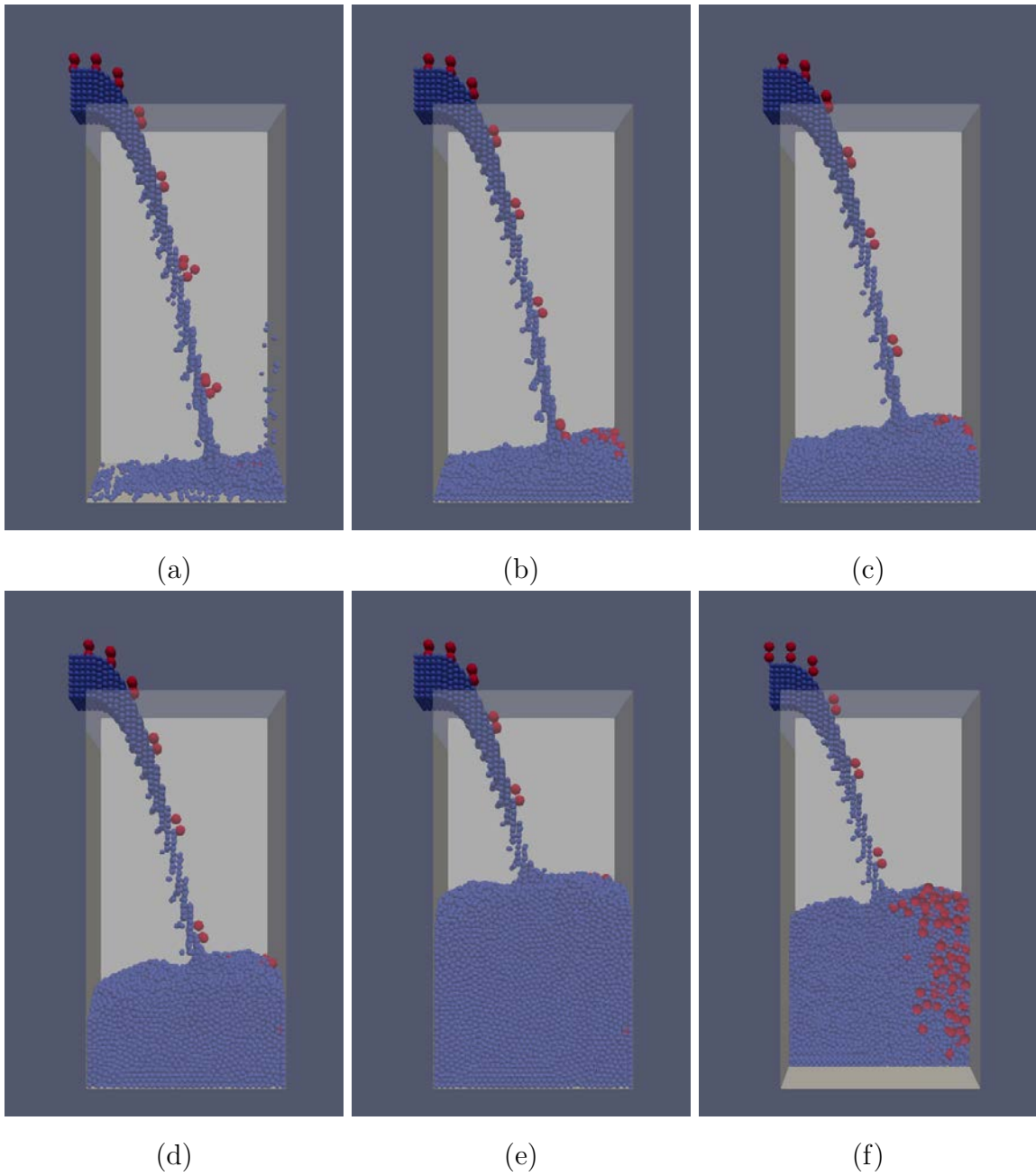


Figure 4-3: Model 1: A filling under pure gravity deposition was investigated at specific times: (a) $t=1$ s, (b) $t=2$ s, (c) $t=3$ s, (d) $t=6$ s, and (e) $t=11$ s; and (f) a middle clip showing the final stacking state after mixed with the 1st iteration.

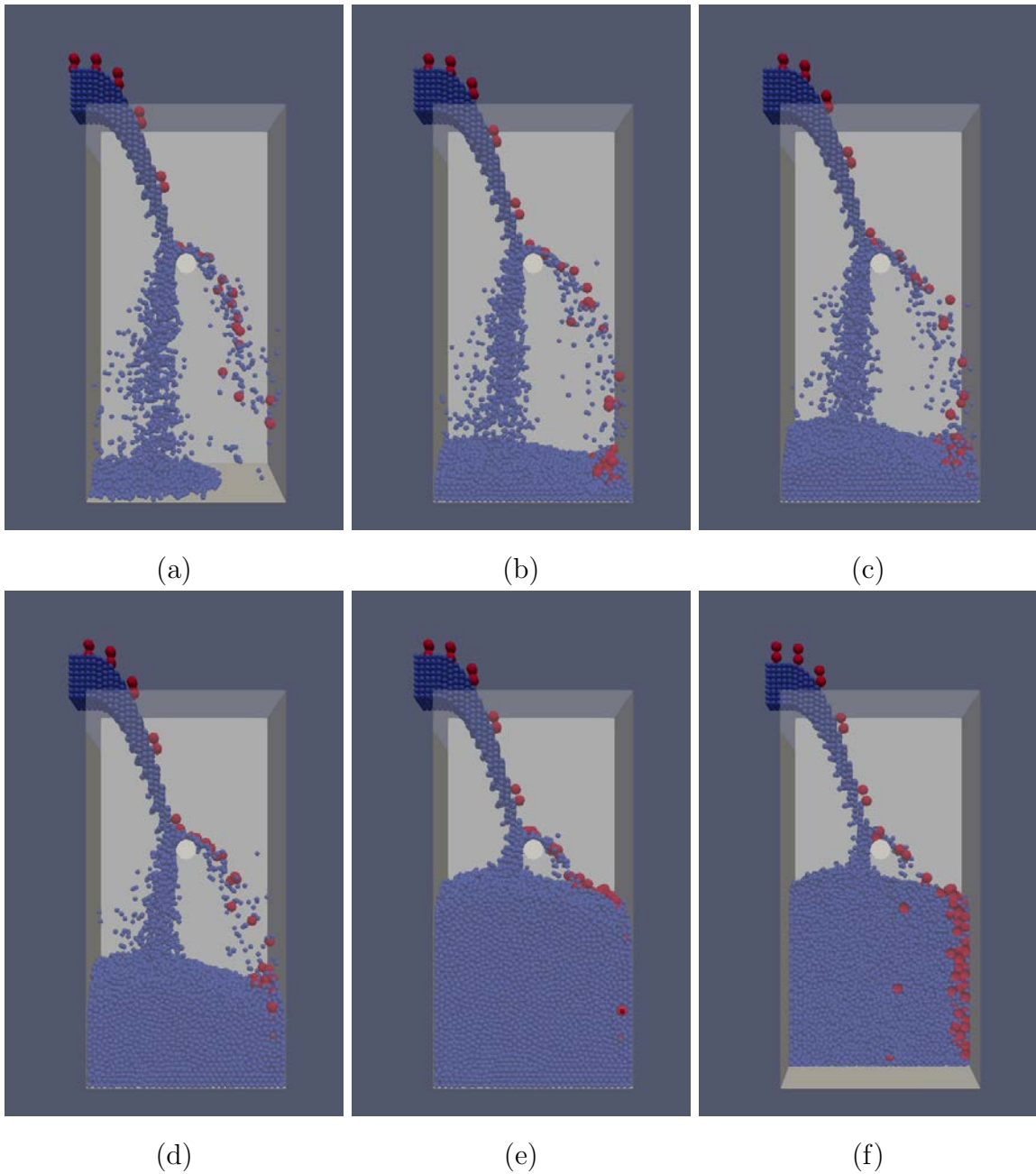


Figure 4-4: Model 2: A filling under gravity deposition with one obstacle placed at locations $x=0.5$ m and $z=1.2$ m was investigated at specific times: (a) $t=1$ s, (b) $t=2$ s, (c) $t=3$ s, (d) $t=6$ s, and (e) $t=11$ s; and (f) a middle clip showing the final stacking state after mixed with the 1st iteration.

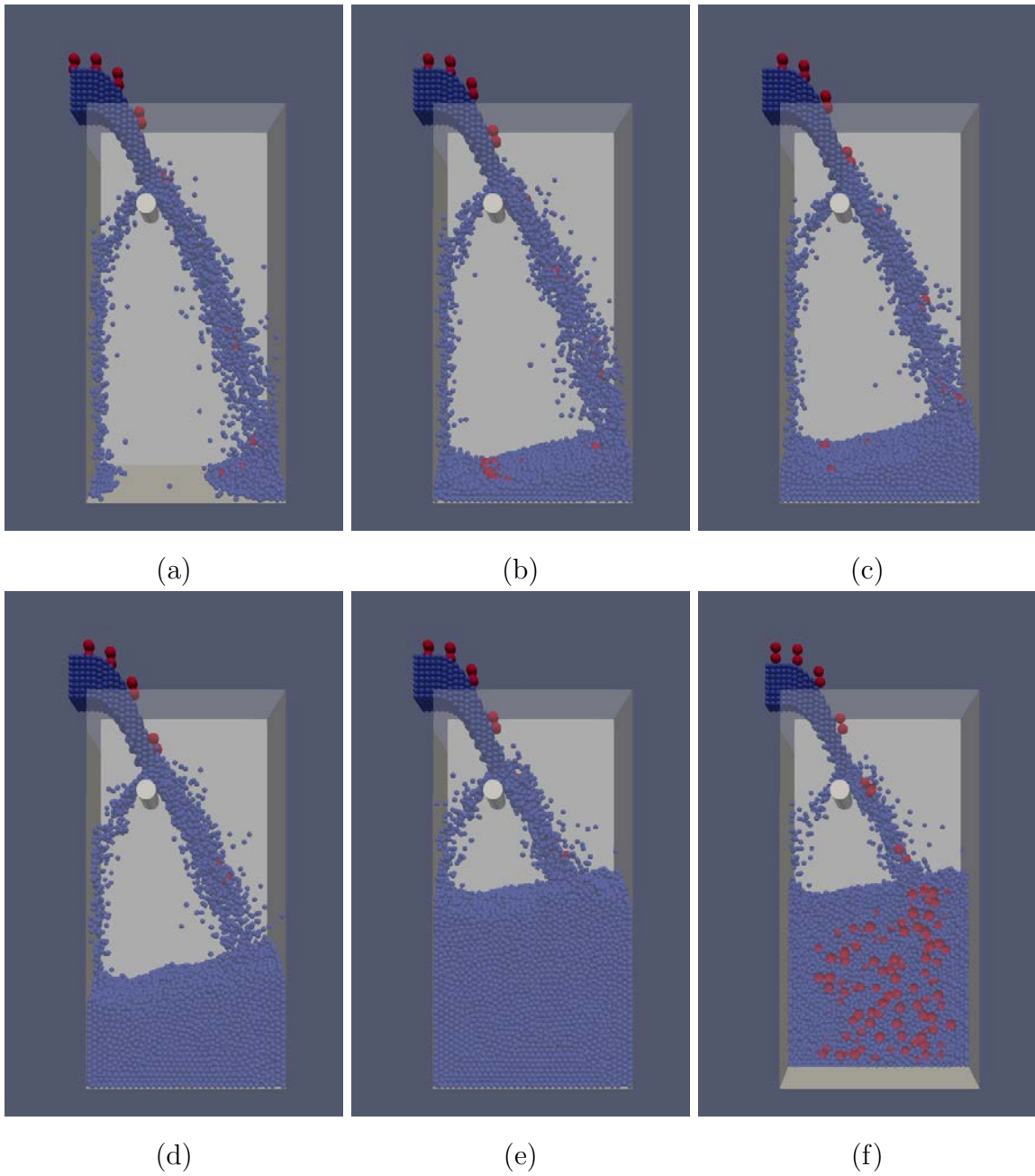


Figure 4-5: Model 3: A filling under gravity deposition with one obstacle placed at locations $x=0.3$ m and $z=1.5$ m was investigated at specific times: (a) $t=1$ s, (b) $t=2$ s, (c) $t=3$ s, (d) $t=6$ s, and (e) $t=11$ s; and (f) a middle clip showing the final stacking state after mixed with the 1st iteration.

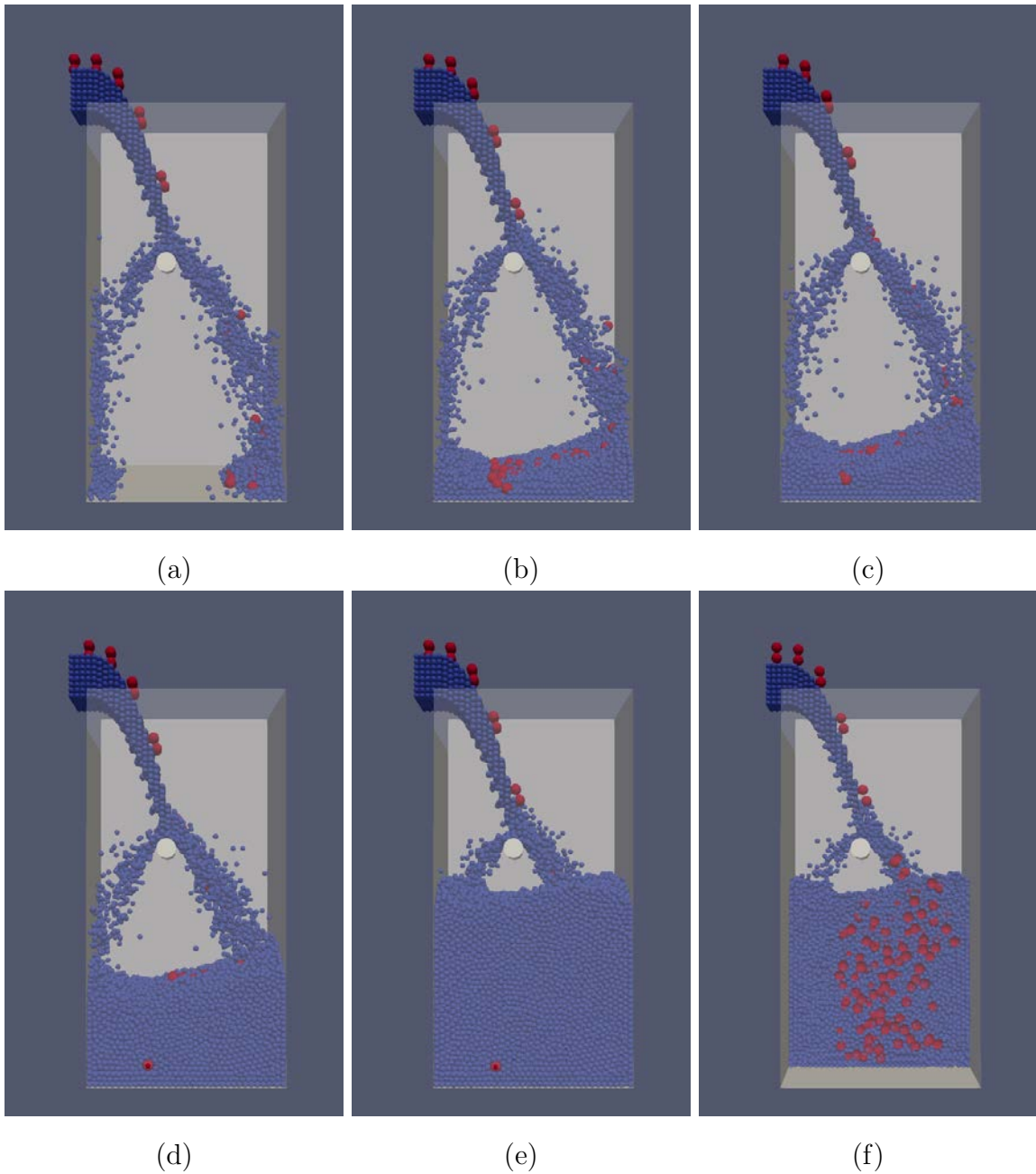


Figure 4-6: Model 4: A filling under gravity deposition with one obstacle placed at locations $x=0.4$ m and $z=1.2$ m was investigated at specific times: (a) $t=1$ s, (b) $t=2$ s, (c) $t=3$ s, (d) $t=6$ s, and (e) $t=11$ s; and (f) a middle clip showing the final stacking state after mixed with the 1st iteration.

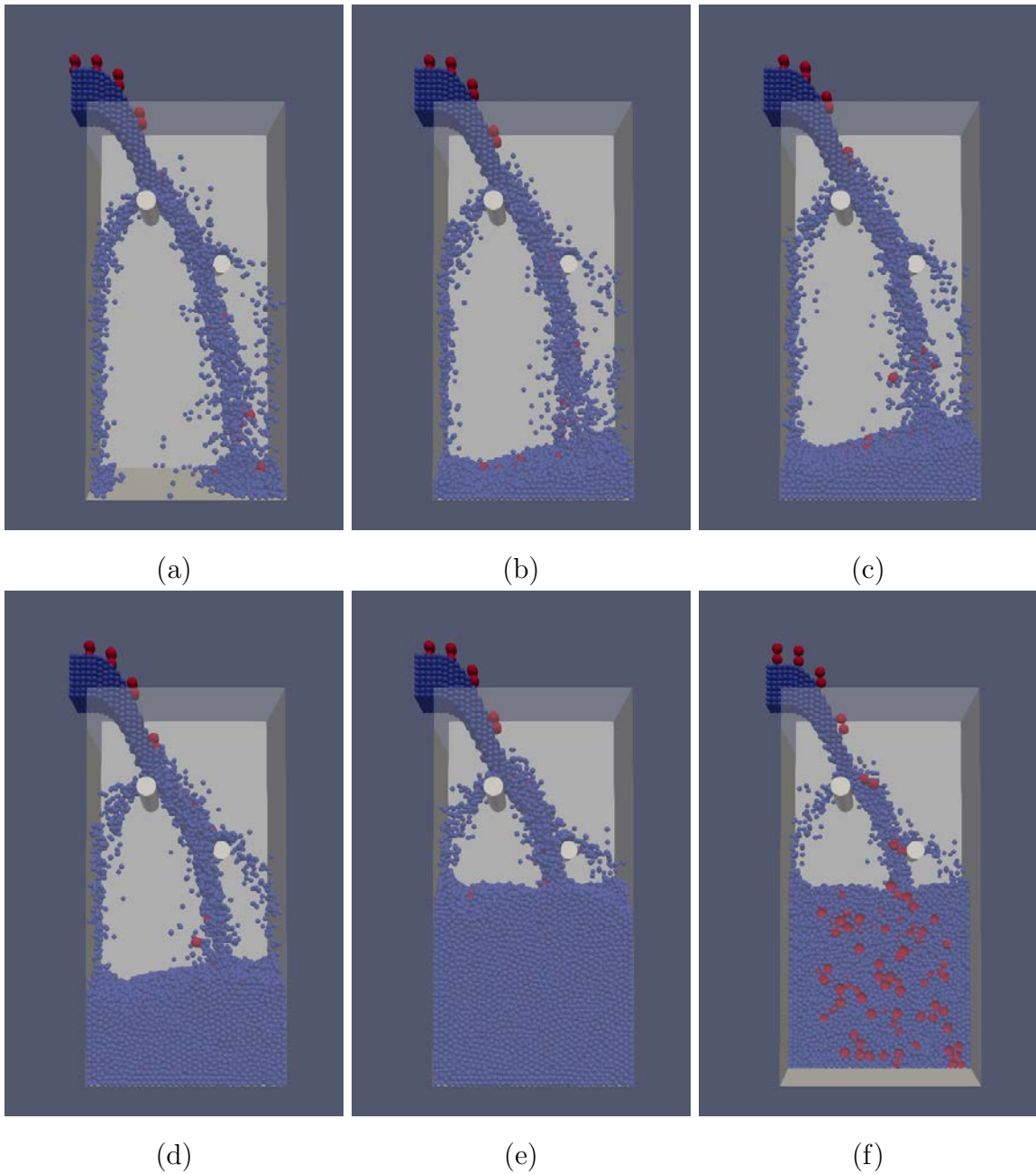


Figure 4-7: Model 5: A filling under gravity deposition with two obstacles placed at locations $x=0.3$ m & $z=1.5$ m and $x=0.7$ m & $z=1.2$ m was investigated at specific times: (a) $t=1$ s, (b) $t=2$ s, (c) $t=3$ s, (d) $t=6$ s, and (e) $t=11$ s; and (f) a middle clip showing the final stacking state after mixed with the 1st iteration.

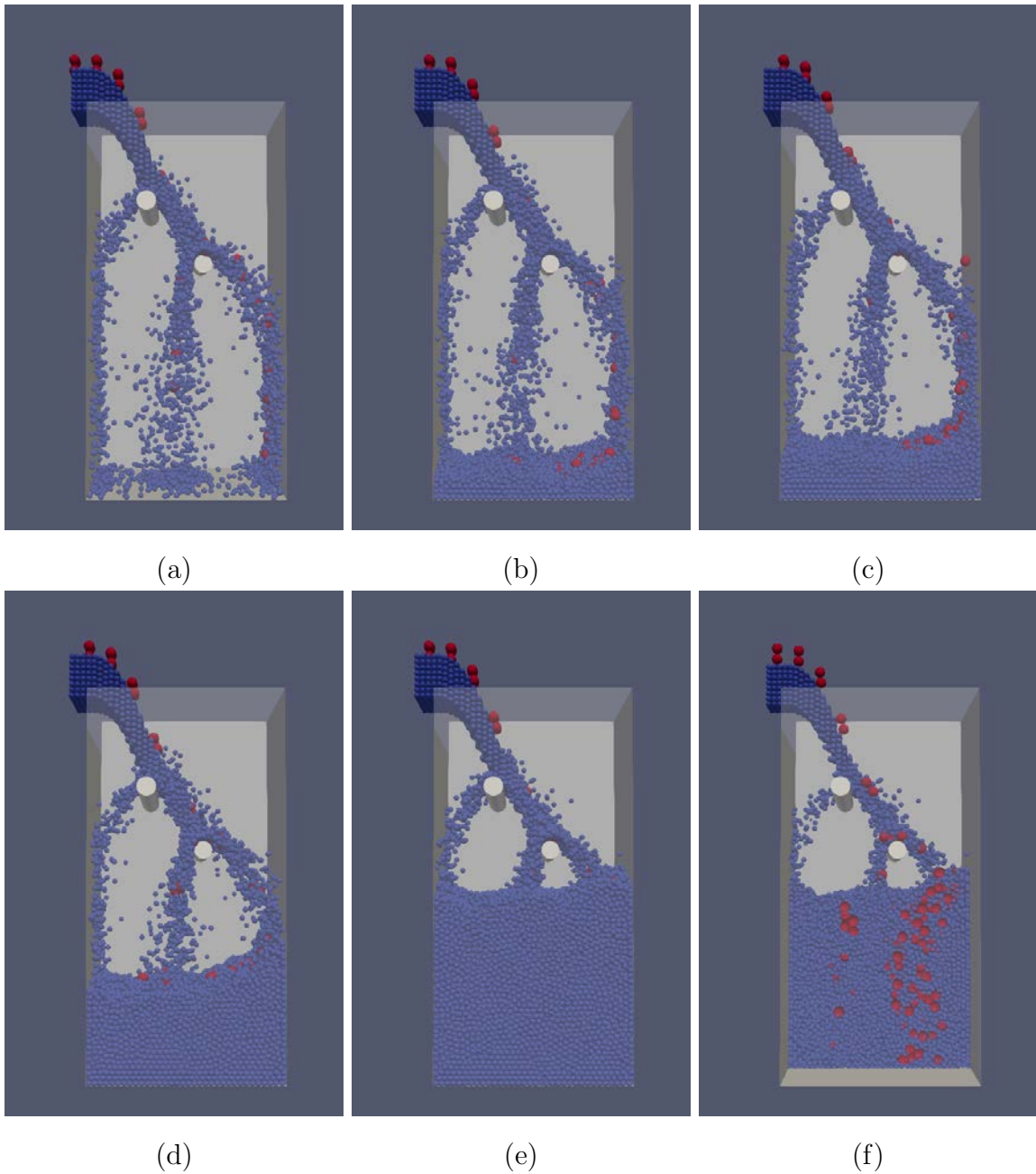


Figure 4-8: Model 6: A filling under gravity deposition with two obstacles placed at locations $x=0.3$ m & $z=1.5$ m and $x=0.6$ m & $z=1.2$ m was investigated at specific times: (a) $t=1$ s, (b) $t=2$ s, (c) $t=3$ s, (d) $t=6$ s, and (e) $t=11$ s; and (f) a middle clip showing the final stacking state after mixed with the 1st iteration.

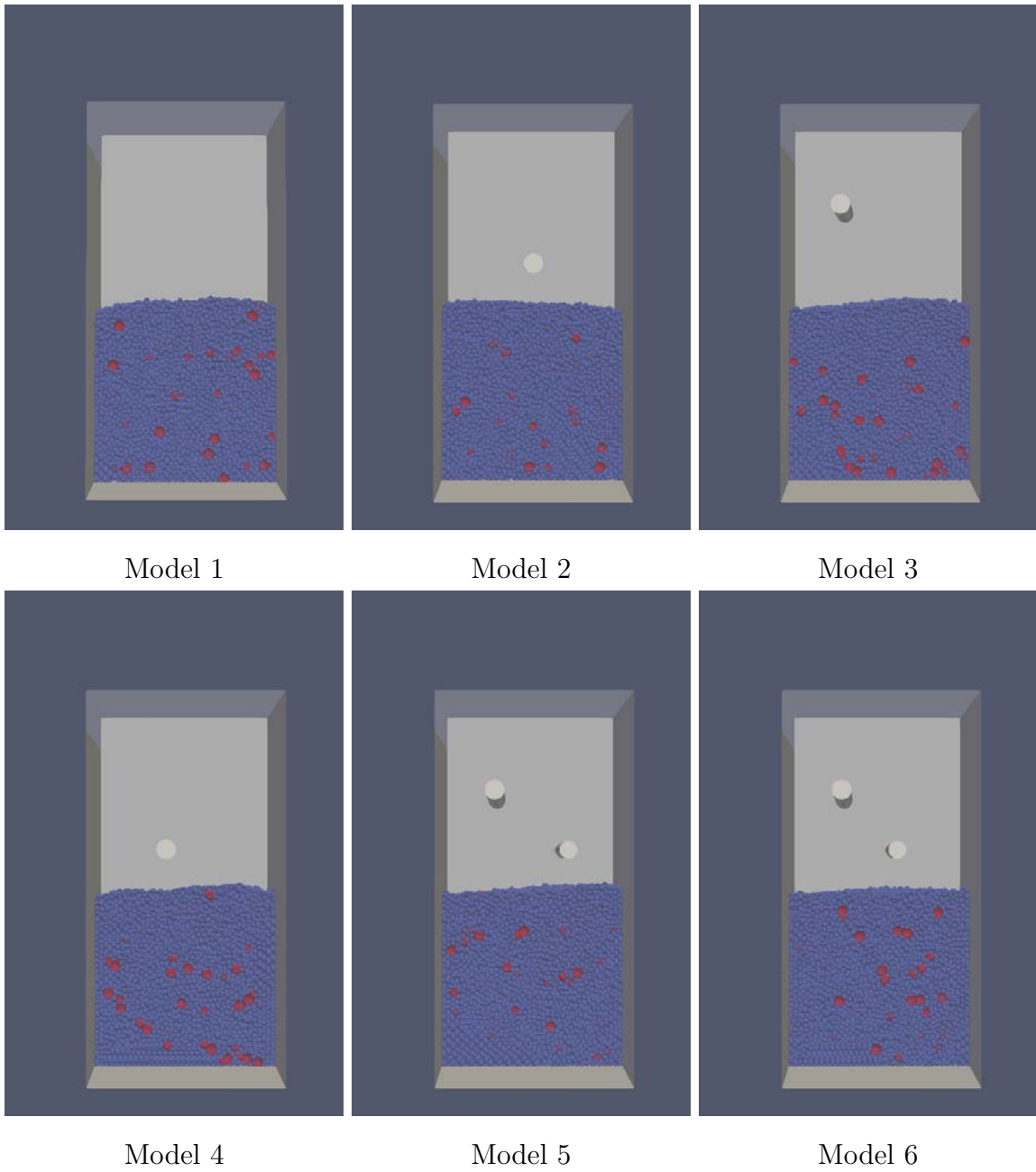
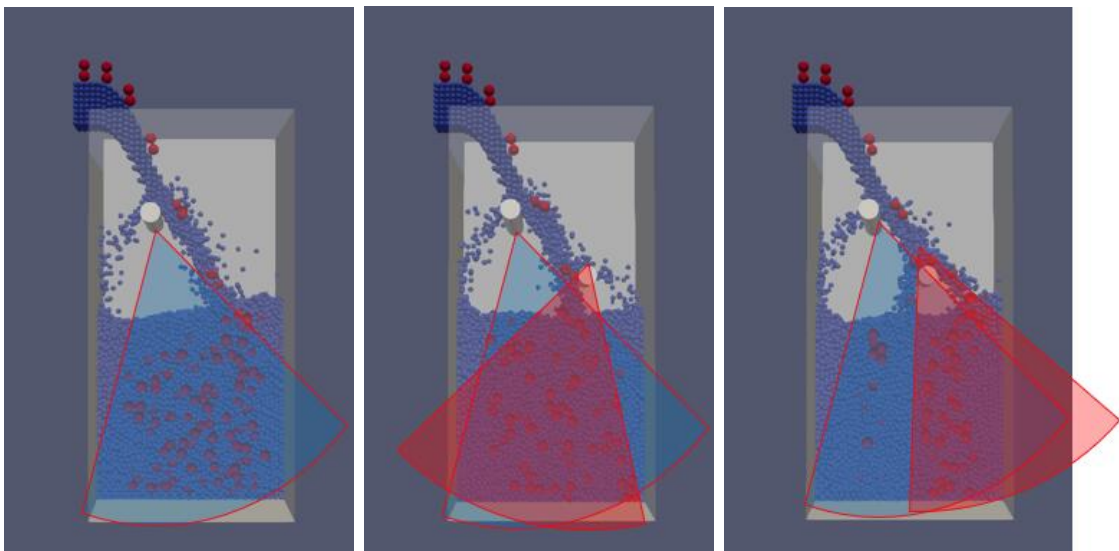
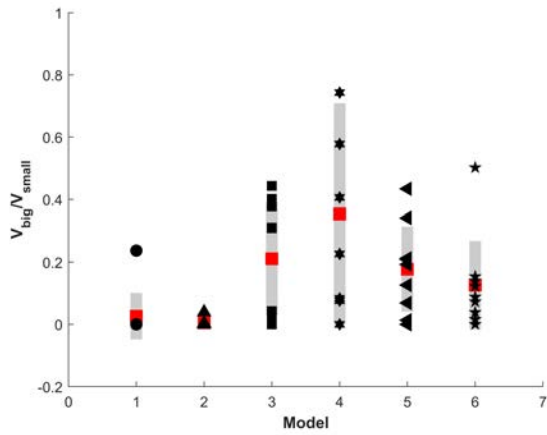


Figure 4-9: Middle clips showing the final stacking states of the previously studied 6 models after re-filling with the 2nd iteration.

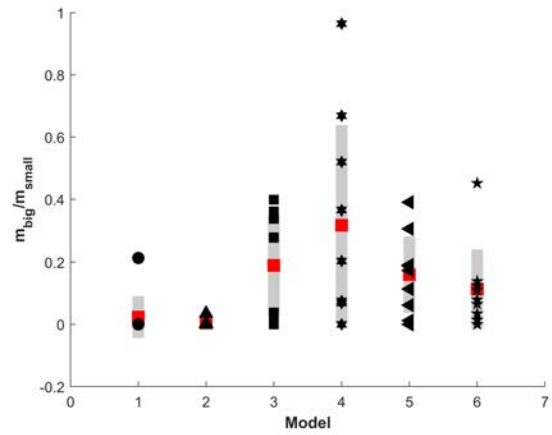


(a) The area of influence (b) Overlapped influence area (c) Interfered influence area

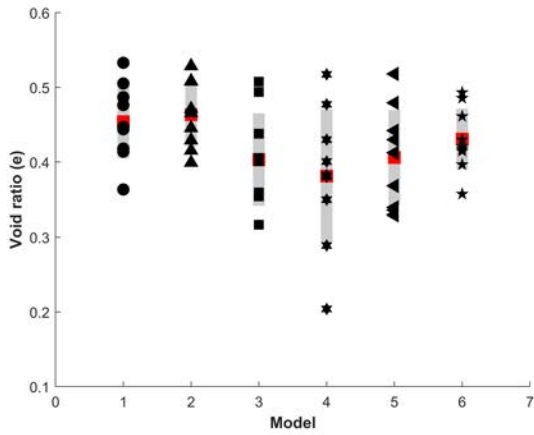
Figure 4-10: Different types of influence area



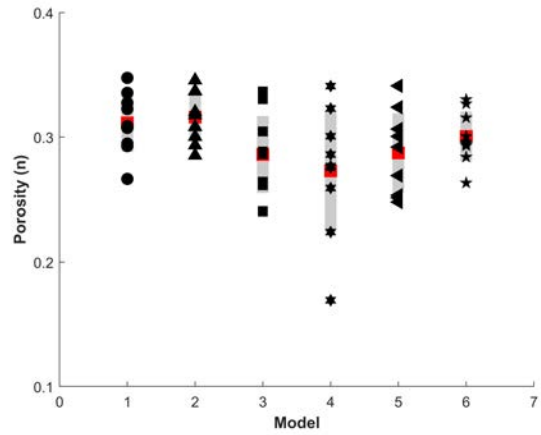
(a) Volume ratio ϕ_v



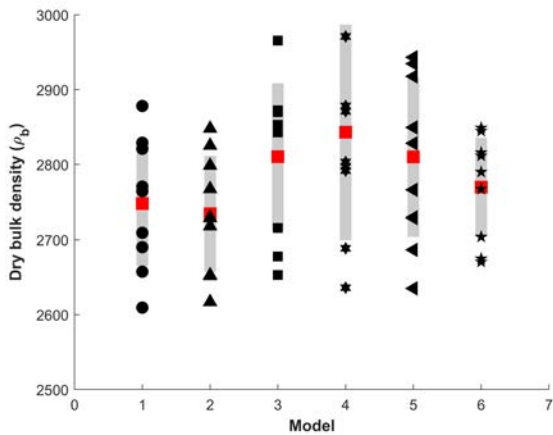
(b) Mass ratio ϕ_m



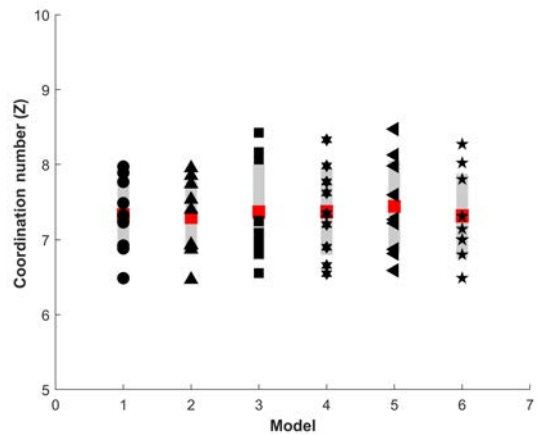
(c) Void ratio e



(d) Porosity n

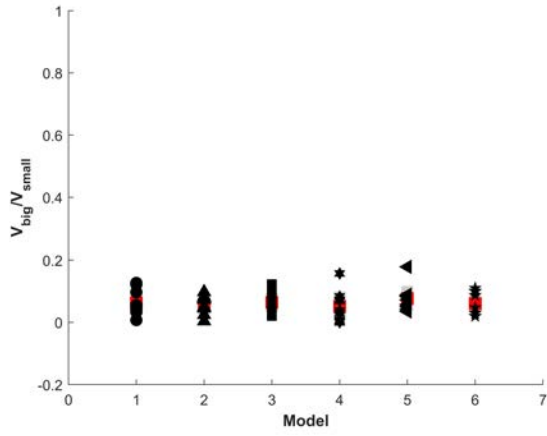


(e) Dry bulk density ρ_b

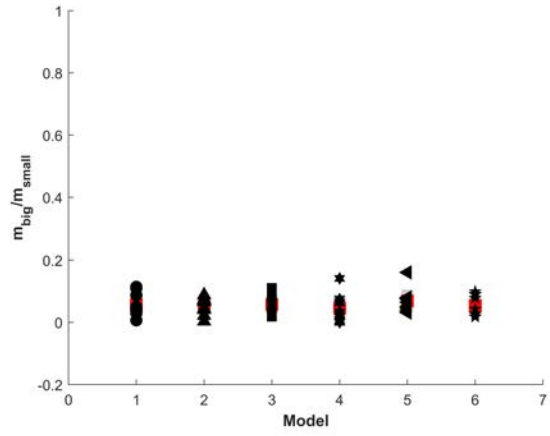


(f) Coordination number Z

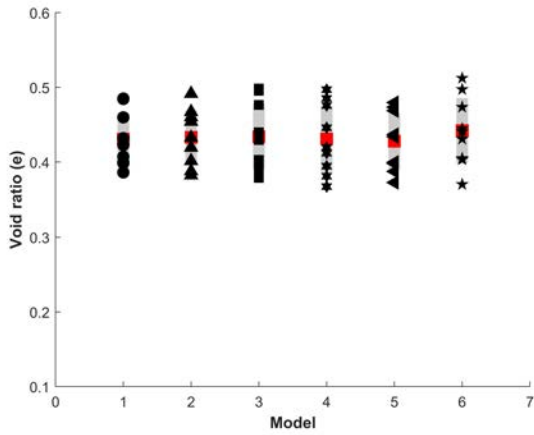
Figure 4-11: Mixing parameters measured in nine spherical regions for the presented six models after filling with the 1st iteration



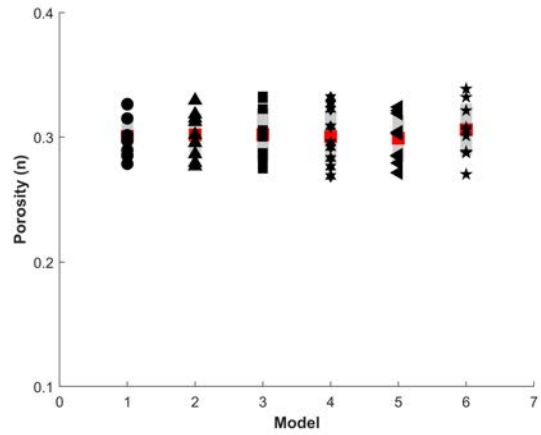
(a) Volume ratio ϕ_v



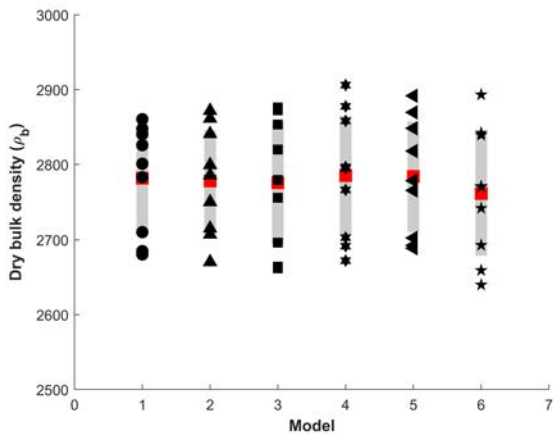
(b) Mass ratio ϕ_m



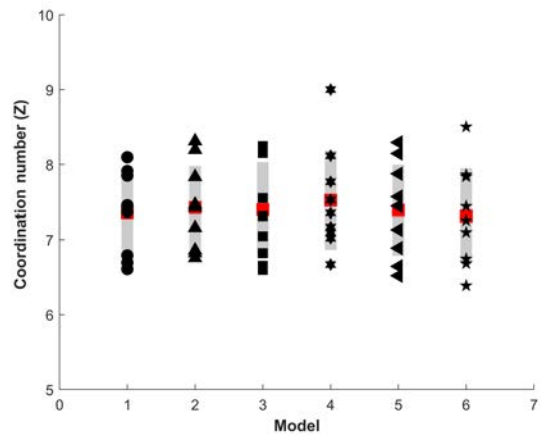
(c) Void ratio e



(d) Porosity n



(e) Dry bulk density ρ_b



(f) Coordination number Z

Figure 4-12: Mixing parameters measured in nine spherical regions for the presented six models after re-filling with the 2^{nd} iteration

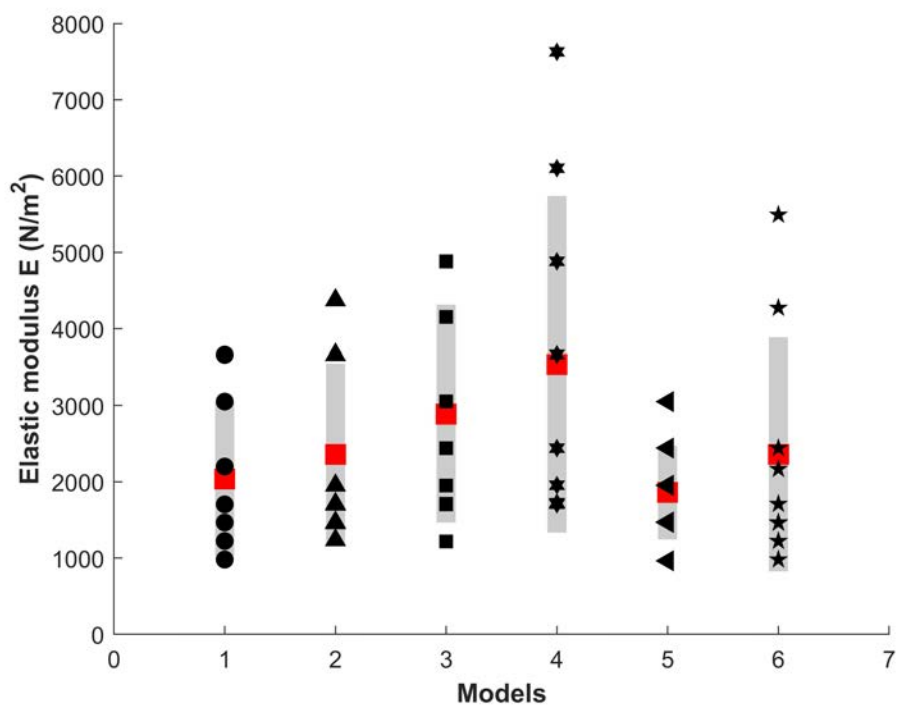


Figure 4-13: The effective elastic modulus E measured in nine cubic regions for the presented six models after mixing with the 1st iteration

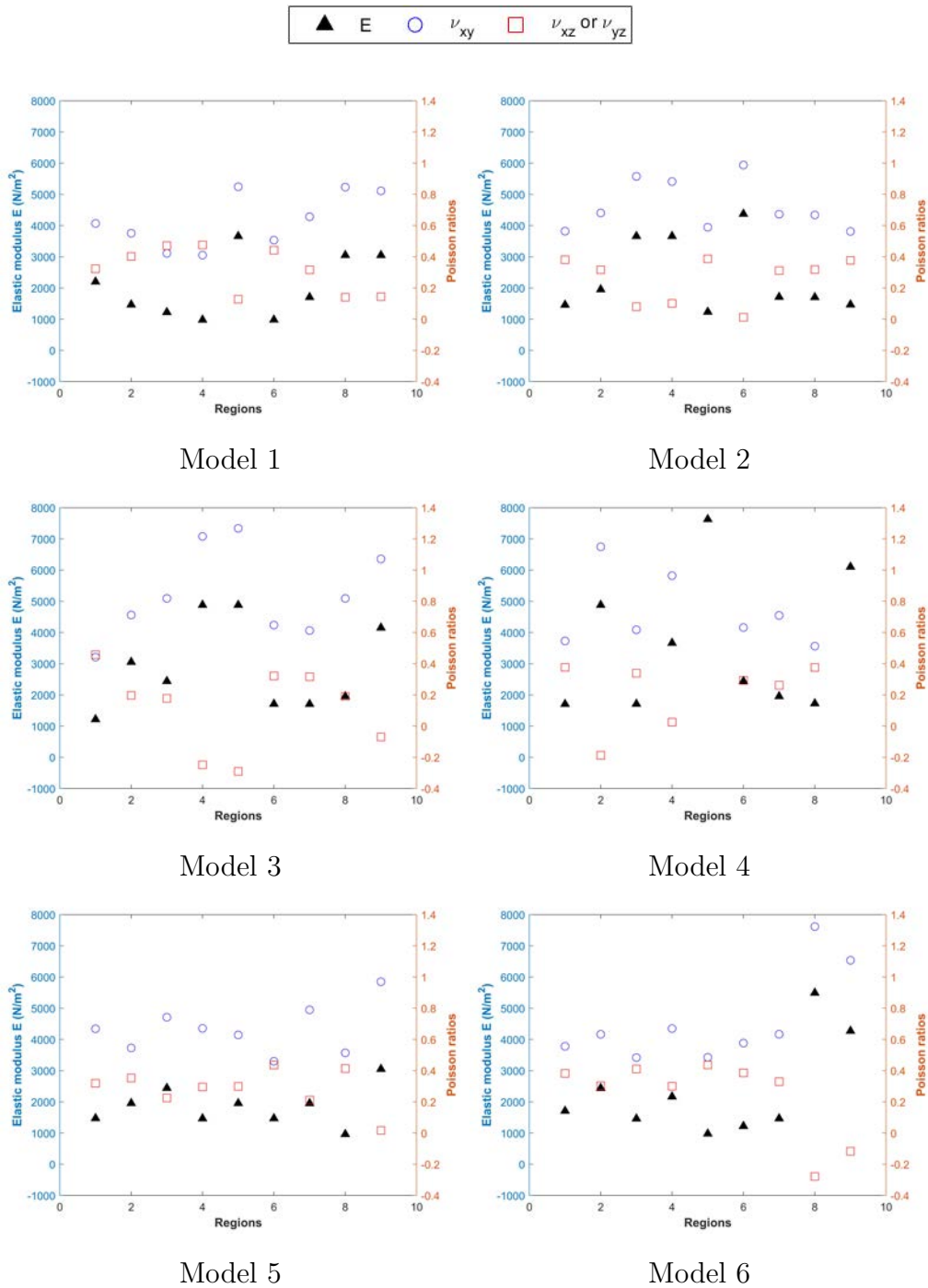


Figure 4-14: The distribution of the calculated effective elastic properties E and ν for each model as mixing with the 1st iteration

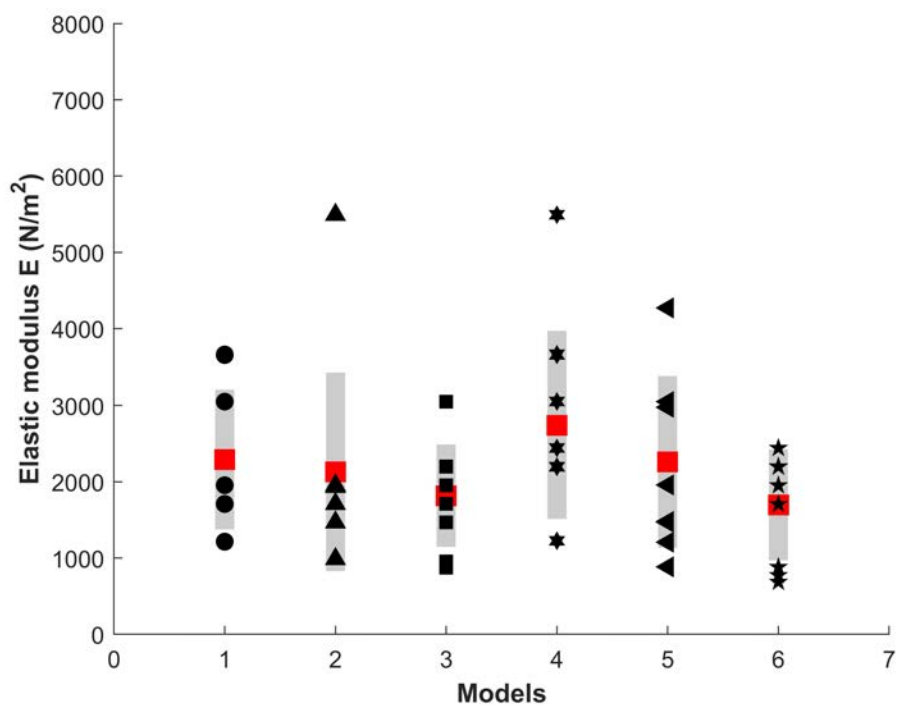


Figure 4-15: The effective elastic modulus E measured in nine cubic regions for the presented six models after mixing with the 2^{nd} iteration

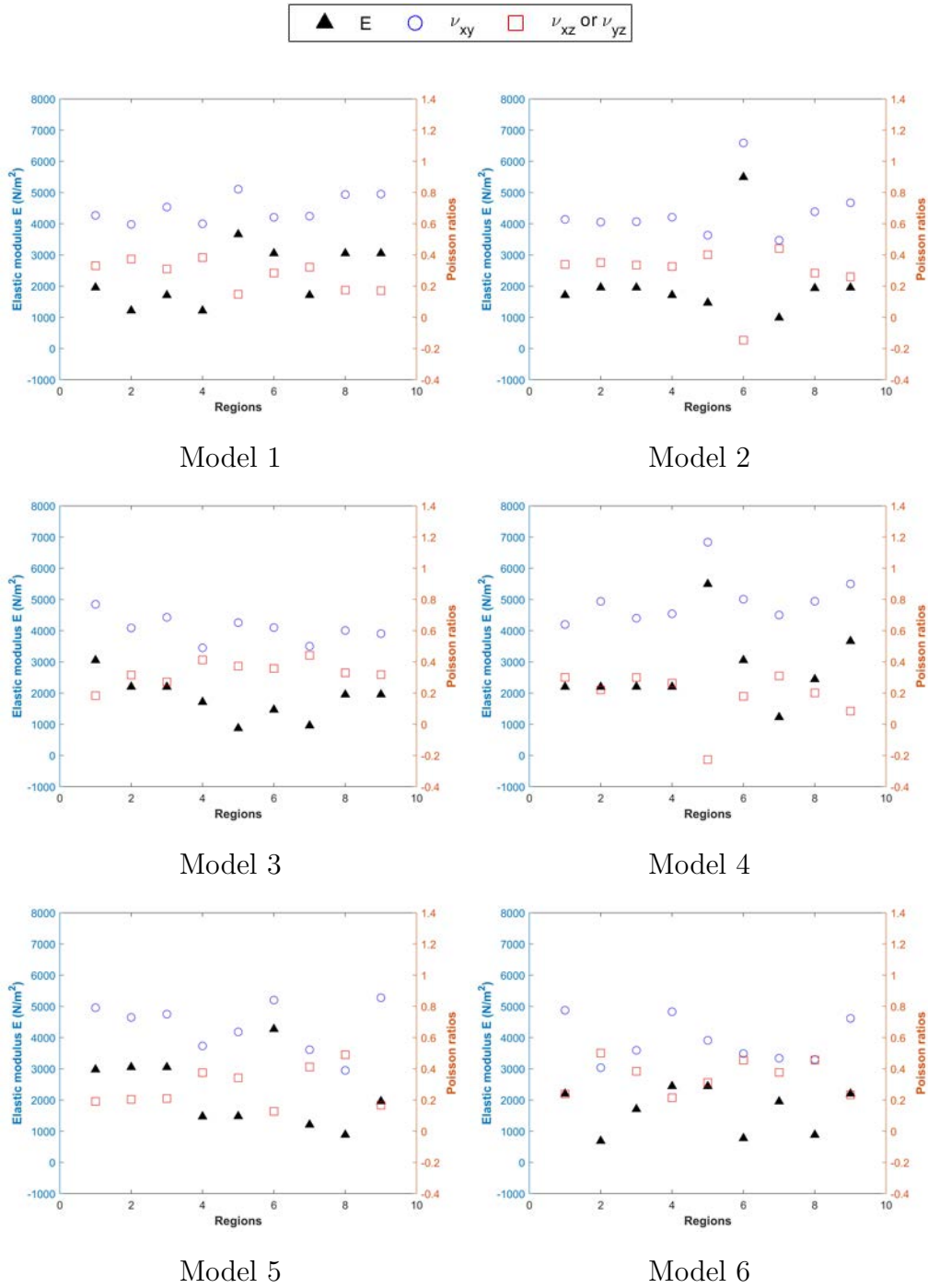


Figure 4-16: The distribution of the calculated effective elastic properties E and ν for each model as mixing with the 2nd iteration

CHAPTER 5: MIXING PROPERTIES OF BINARY GRANULAR MIXTURES WITH BONDED PARTICLES

5.1 Overview

Binary mixtures of dissimilar particles are frequently found in many engineering applications. Frequently, particles can be bonded together either at the individual particle level or within a larger representative volume that can be modeled as a collection of particles. The role of the strength of the bond between particles can be a critical parameter and can serve to characterize the the behavior of many granular materials that can influence their mechanical behavior. Because of the relative complexity of these physical systems, studies have been largely limited to laboratory tests. However, the parallel bonded model proposed by Potyondy and Cundall (2004) has made the analysis of bonded particle aggregates much more feasible and has promoted the application of the Discrete Element Method (DEM) to assist in the analysis of this type of behavior.

In this chapter, a DEM model was used to evaluate the mixing properties of the mixtures of particle assemblies where one of two types of particles are originally bonded together. Various mixing properties and relevant effective mechanical properties were quantified at various locations within the mixtures. Through this analysis, results show the performance of these aggregates is highly determined by the inter-particle bond strength. An change in this parameter can generate a wider range of reflection angles as the particles interact with geometric mixers and simultaneously change the parameters used to quantify mixing. The effective mechanical properties of the final combined aggregate were determined as a function of the bond strength and the degree of mixing.

5.2 Introduction

The research on bonded particles has penetrated many fields including powder technology, mining operations, geophysics, and geomechanics (Choi et al., 2013; Lim et al., 2012; Shahnazari and Rezvani, 2013; Russell and Einav, 2013). Bonded particle mechanics, which is a typical characteristic of granular materials, frequently occurs in structural and geotechnical engineering processes such as high rockfill dam construction (Tapias et al., 2015; Jia et al., 2017; Xiao et al., 2020), compaction of coastal foundations (Xiao et al., 2016), and pile penetration (Jardine et al. 2013; Mao et al. 2019). Particle interactions during construction and operating processes may result in particle breakage when their allowable strength has been exceeded. When subjected to large stresses, significant breakage can occur with originally strong materials (Yasufuku and Hyde, 1995). Potyondy and Cundall (2004) have clarified that particle breakage can be induced even by relatively low values of confining stresses. Particle breakage and the resulting changes in the aggregate can result in large changes in the physical and mechanical properties of the granular mixture. Changes in the original engineering properties of the bonded particles can result in large deformation or stability issues to the aggregate and jeopardize its service life. Therefore, understanding the nature of particle bonds and especially their interaction during mixing processes is of much interest.

Experimental studies have resulted in the identification of several key factors associated with the occurrence of particle breakage. Okada et al. (2004) explained that construction with crushable particles lowered the soil permeability in the shear zone and was responsible for the motion of landslides. Zeghal (2009) found that the effect of particle crushing in road construction has a great impact on overall road behavior. Through laboratory-testing of

field samples, this influence was quantified. Casini et al. (2013) highlighted that particle crushing gave a modification to the particle size distribution; consequently, this influenced the frictional properties of the final deposits and their critical states. Lade et al. (1996) affirmed the necessity of studying particle crushing on the stress-strain curve and strength properties of the aggregate. Other related effects have been investigated including changes in plastic yielding and hardening (McDowell et al, 1996; McDowell and Bolton, 1998), dilatancy (Bolton, 1986), and energy dissipation (Tarantino and Hyde, 2005). Although the significant influence of particle crushing has been well known for some time, research into this topic remains in early stages, and thus far and laboratory testing has been the primary method of analysis.

In the past two decades, to supplement the data collected from laboratory tests, the Discrete Element Method (DEM) has been employed in the analysis of particle mixtures that can break or fracture, and significant new results have been obtained. This numerical method can not only provide a quantitative prediction for material properties of a granular material but it can also help in gaining a better understanding of the mechanisms of particle behavior at the micro-scale. Through this method, particles are usually treated as rigid bodies and the dynamic equations of motion are enforced at the center of the particle. As proposed by Potyondy and Cundall (2004), particle fracture is simulated using what they termed the parallel bond model, which makes the study of particle crushing and the simulation of irregular particles much more feasible. In this model, crushable particles are introduced as initially bonded aggregates that contain multiple sub-spheres. By calibrating the strength of the bonded contacts between sub-spheres, this model is capable of simulating targeted material properties at the macro-scale (Potyondy and Cundall, 2004; Cho et al.,

2007; Manso et al., 2018). Since particle breakage is an inherent characteristic of granular materials, the DEM has provided a useful tool for the study of these types of bonded particle aggregates.

Because of the complex nature of particle crushing, DEM studies have been somewhat confined to specific types of behavior. By using simulated uniaxial compression tests with crushable particles, Cho et al. (2007) successfully predicted the stress-strain behavior and the complete nonlinear failure envelope of certain granular materials. Bono and McDowell (2014) simulated high-pressure triaxial shear tests and studied material critical states as a result of particle crushing. When performing tests on single particles, Sun et al. (2018) found that particle crushing can induce a large change in porosity. Recently, Desu et al. (2021) analyzed the macroscopic stress-strain response of a polydisperse crushable spherical granular assembly.

Overall, studies on crushable particles have been limited to relatively small-scale simulation in an attempt to determine aggregate porosity, strength and the stress-strain curve. As particle crushing is a significant characteristic of granular materials and can influence overall behavior, this paper is aimed at studying variations in the mixing and mechanical properties of binary aggregates made of crushable particles. The study includes simulations that range from dynamic sample generation to subsequent quasi-static testing under uniaxial compression. Detailed steps of the analysis include estimating the effectiveness of the existing mixing processes on mixtures, giving suggestions to meet engineering requirements, and providing a useful method to supply full-scale tests are all provided.

5.3 DEM model Description

A three-dimensional DEM model was developed for all simulations contained in this study using rigid spheres of arbitrary diameter, density, and mechanical properties. The dynamic equations of motion are enforced at the center of each sphere. Contact overlaps between particles and bounding surfaces are allowable to introduce external forces. Although the evolution of the mixing systems used in this study are continuous, simulations over a period of time are examined at specific time intervals. The primary mechanism studied in this work is the mixing process between two different cohorts of particles as they enter a control volume and interact through particle and geometric mixing boundaries introduced in the control volume. For mixing with crushable particles, external forces are induced both through contacts between the spheres and the bond behavior between connected spheres. Those models are both demonstrated in **Fig. 5-1**. Each are described separately below.

5.3.1 Contact behavior

Since unbonded spherical particle motions are decoupled, the components of both the contact force F_i and the moment M_i can be divided into two components:

$$F_i = F_n \cdot n_i + F_t \cdot t_i \tag{88}$$

$$M_i = M_n \cdot n_i + M_t \cdot t_i + M_r$$

Here n_i and t_i are unit vectors that define the normal and the tangential contact planes. An additional term M_r is added to the moment to incorporate particle surface asperities.

The contact model gives a linear relation between the relative displacements and contact forces, whereas the stiffness is in non-linear form. The normal force F_n between two

contacting spheres a and b is calculated using

$$F_n = K_n \delta_n, \text{ and } K_n = \frac{2K_n^a K_n^b}{K_n^a + K_n^b} \quad (89)$$

Here K_n^a and K_n^b are the normal spring stiffnesses associated with each sphere. The tangential force is computed in cumulative form where the relative displacement is recorded based on the relative tangential velocity $\dot{\delta}_t$ at the contacts. Assuming that the spheres have the same stiffness and strength properties in every direction, the tangential stiffness is given as $K_t = K_n$. But this force is limited to the value provided by the Coulomb friction force law. Hence, with a friction coefficient of μ , the general form for calculating the tangential force is shown as

$$F_t = -\min(|\mu F_n|, K_t \int_{t_0}^t \dot{\delta}_t dt) \frac{\dot{\delta}_t}{|\dot{\delta}_t|} \quad (90)$$

In a fashion similar to that used to compute the tangential force, the transmitted moment is given as a function of the relative rotational velocities between the two contacting spheres. The rolling stiffness is set equal to $K_r = K_t r^2$ and the maximum allowable moment before sliding is limited to the value of ηF_n . Hence the moment can be written as

$$M_r = -\min(|\eta F_n|, K_r \int_{t_0}^t \dot{\theta}_r dt) \frac{\dot{\theta}_r}{|\dot{\theta}_r|} \quad (91)$$

Here η is a rolling friction coefficient related to the particle surface asperities or the eccentricity of the particle centroid, and $\dot{\theta}_r$ is the angular velocity. A viscous damping model is applied to damp out non-physical phenomenon. The damping force calculation is related to

the relative velocity at the contacts. The associated coefficients are in the compound function of the energy dissipated per cycle, the effective stiffness, and the effective mass/moment of inertia.

5.3.2 Bond behavior

Crushable particles in this study are simulated using spheres that are bonded together with an adjustable bond strength. This model was proposed by Potyondy and Cundall (2004) and is frequently used in the commercial DEM codes PFC2D and PFC3D. Since these bonds are located parallel to previously used contact springs, this model has become known as the “parallel bonds” method. The bonds connecting adjacent spheres are playing the role of one-dimensional beam elements that possess both axial and shear stiffness and strength and transmit forces and moments. The simulated crushable particles can also be termed as bonded aggregates. The action of bonds in the 3D case can be imagined as an elastic beam with circular cross-section or composed of a series of elastic springs that are uniformly distributed over the acting area. The latter description is more appropriate for the condition of distributed stresses. The force and moment carried by a bond are presented as \bar{F}_i and \bar{M}_i , respectively. These actions can also be decomposed into normal and tangential directions, which are expressed as

$$\begin{aligned}\bar{F}_i &= \bar{F}_n \cdot n_i + \bar{F}_t \cdot t_i \\ \bar{M}_i &= \bar{M}_n \cdot n_i + \bar{M}_t \cdot t_i\end{aligned}\tag{92}$$

The capacity of each bond is determined by five parameters: the normal and shear stiffness given in force per unit area (\bar{k}_n and \bar{k}_t), the tensile and shear strengths carried by

bonds ($\bar{\sigma}_c$ and $\bar{\tau}_c$), and the bond-radius multiplier used for describing the acting area ($\bar{\lambda}$). This latter quantity gives the connection capacity or the percentage ratio of a bond acting area. Therefore, the acting radius between spheres a and b is calculated by

$$\bar{R} = \bar{\lambda} \min(R_a, R_b) \quad (93)$$

Consequently, the effective geometric properties of a single bond are given as

$$A = \pi \bar{R}^2, \quad I = \frac{1}{4} \pi \bar{R}^4, \quad \text{and} \quad J = \frac{1}{2} \pi \bar{R}^4 \quad (94)$$

When the bonds are initially formed, \bar{F}_i and \bar{M}_i are set to zero. Subsequently, each relative movement ($\Delta\delta_n, \Delta\delta_t, \Delta\theta_n$ and $\Delta\theta_t$) will create increments to each of the current variables.

Since elastic behavior is assumed, the increments are given with the following forms:

$$\begin{aligned} \Delta\bar{F}_n &= -\bar{k}_n A \Delta\delta_n \\ \Delta\bar{F}_t &= -\bar{k}_t A \Delta\delta_t \\ \Delta\bar{M}_n &= -\bar{k}_t J \Delta\theta_n \\ \Delta\bar{M}_t &= -\bar{k}_n J \Delta\theta_t \end{aligned} \quad (95)$$

The maximum capacity of a bond is computed using a combination of beam theory, axial bar theory, and circular torsion theory. The stresses computed at the bond are written as:

$$\begin{aligned} \bar{\sigma}^{max} &= \frac{-\bar{F}_n}{A} + \frac{|\bar{M}_t| \bar{R}}{I} \\ \bar{\tau}^{max} &= \frac{\bar{F}_t}{A} + \frac{|\bar{M}_n| \bar{R}}{J} \end{aligned} \quad (96)$$

If either the maximum normal stress or the maximum shear stress exceeds the allowable

strength or the critical states, for example $\bar{\sigma}^{max} \geq \bar{\sigma}_c$ or $\bar{\tau}^{max} \geq \bar{\tau}_c$, the bond breaks and is removed from the analysis. The contact between the spheres returns to the conditions of the unbonded case.

5.3.3 Post-analysis

To assess the quality of the generated mixtures, mixing parameters were checked at various locations within the final control volume. The investigation of each measured subdomain was quantified through two physical measures: the internal degree of mixing and the equivalent elastic properties.

Internal mixing degree

In Chapter 4, it has been concluded that the internal mixing degree of binary mixtures can be best quantified by measuring the volume ratio ϕ_v using the extended Bardet and Proubet's method (1991). A sphere with a radius of r and the measured point C located at the center is considered as a control volume. Therefore, for each sub-domain as indicated by such a sphere, the total volume V_t is computed as $\frac{4}{3}\pi r^3$. Through this particle volume algorithm, the volume of spheres falling into this region is then measured. To show this more clearly, a 2D sketch has been illustrated in **Fig. 5-2**. The occupied volume V_i of the i th particle is calculated through any of the following conditions:

$$V_i = \begin{cases} 0, & d_i \geq R_i + r \\ \frac{4}{3}\pi R_i^3, & d_i \leq r - R_i \\ \frac{1}{3}\pi(3r - h_1)h_1^2 + \frac{1}{3}\pi(3R_i - h_2)h_2^2, & r - R_i < d_i < R_i + r \end{cases} \quad (97)$$

Here R_i is the radius of the i th particle, d_i is the distance between the region center C and

the centroid of the i th particle, h_1 and h_2 are the heights of the relevant crown distance calculated using

$$\begin{aligned} \theta_2 &= 2 \arccos \left\{ \frac{d_i^2 + R_i^2 - r^2}{2d_i R_i} \right\} & \text{and} & & h_2 &= R_i - R_i \cos\left(\frac{\theta_2}{2}\right) \\ \theta_1 &= 2 \arcsin \left\{ \frac{R_i}{r} \sin \frac{\theta_2}{2} \right\} & & & h_1 &= r - r \cos\left(\frac{\theta_1}{2}\right) \end{aligned} \quad (98)$$

By accounting for all of the covered volume within this sub-domain, the occupied volume of each material can be exactly computed as $\sum V_i$. As a consequence, the mixing volume ratio ϕ_v for binary mixtures is given as $\frac{V_{big}}{V_{small}}$, where the subscripts denote the relative particle dimensions. This value will vary over the entire collection space of the particles, but for aggregates that are well mixed, the value should be relatively uniform across this domain in regions away from the top surface and bounding walls.

The equivalent elastic properties

The mechanical properties of the produced mixtures following mixing are examined by performing simulated compression tests as illustrated in **Fig. 5-3**. Detected points are distributed within the final aggregates which are now motionless and in static equilibrium. Cubic regions with the detected points at the center are used for performing these measurements. Each cubic region is surrounded by five fixed rigid walls with the top horizontal plane moving downward utilized for applying the uniaxial force. A representative stress for the sample is measured on the top plane to obtain the required stress. As the top plane moves downward, particles near the rigid walls experience translational and rotational movements. Under the compression, expansion forces are generated at the center and push the surrounding particles moving outward. Consequently, the uniaxial force has been transmitted to other

directions and large boundary forces are generated through walls in the vertical direction and the two perpendicular directions in the horizontal plane.

The average stress $\bar{\sigma}_{ij}$ components are calculated by summing all contacting forces along the boundary surface using

$$\bar{\sigma}_{ij} = \frac{1}{V} \sum_{k=1}^{N_{BF}} x_i^k f_j^k \quad (99)$$

Here V is the controlled volume and f_j^k is the boundary force applied at location x_i^k . A total of N_{BF} forces are applied. As the sample is surrounded by rigid walls, there is no extension of the control volume along the x and y axes. The only non-zero strain is the axial vertical compressional strain which is calculated by considering boundary positions using the equation of $\bar{\epsilon}_{zz} = \frac{\Delta H_{zz}}{H_{zz}}$, where H_{zz} is the original length along z axis and ΔH_{zz} is the change in length. After applying an assumed Hooke's law and assuming $\nu_{xz} = \nu_{yz}$, the equivalent elastic properties E and two independent values of Poisson ratio ν_{xy} and ν_{xz} can be solved using

$$\begin{Bmatrix} \bar{\epsilon}_{xx} \\ \bar{\epsilon}_{yy} \\ \bar{\epsilon}_{zz} \end{Bmatrix} = \begin{bmatrix} \frac{1}{E} & -\frac{\nu_{xy}}{E} & -\frac{\nu_{xz}}{E} \\ -\frac{\nu_{xy}}{E} & \frac{1}{E} & -\frac{\nu_{yz}}{E} \\ -\frac{\nu_{xz}}{E} & -\frac{\nu_{yz}}{E} & \frac{1}{E} \end{bmatrix} \begin{Bmatrix} \bar{\sigma}_{xx} \\ \bar{\sigma}_{yy} \\ \bar{\sigma}_{zz} \end{Bmatrix} \quad (100)$$

5.4 Sample Generation

To study mixtures made of crushable particles, two groups of bonded spheres were generated and compared to a third control aggregate that consisted of completely unbonded spheres. In all cases, the particles are simulated to enter a cubic uncovered box with dimen-

sions $1 \times 1 \times 2 m^3$. A periodic boundary condition was used to imitate the inlet behavior consistent with entry via a conveyor belt and to save on computational time. The summarized input parameters for these cases are listed in **Table 5-1**, while the relevant front-view, side-view and 3D view of particles in the repeated section are shown in **Fig. 5-4**. Particles are denoted using different colors, with the larger unbonded spheres placed on top and shown in red. The smaller spheres are arranged in blocks of blue particles that appear as blocks of $2 \times 2 \times 8$ spheres that are connected with bonds of varying strength. This system is meant to represent a breakable cake of material along the conveyor belt with larger unconnected particles that collect on the top surface. This is by no means a comprehensive representation of all possibly mixing scenarios, and was chosen to be representative of the process in which there is the most interest. Including the larger spheres, which appear as a $2 \times 2 \times 2$ unbonded block, there are a total of 516 spheres are used in each periodic aggregate. The connecting pattern that illustrates the arrangement of the introduced bonds is shown in **Fig. 5-4**, where these bonds appear as short white line segments. Two ultimate stresses were used to describe the ultimate bond capacity. The words “weak” and “strong” are adopted for distinction in the discussions that follow. The bond strength was the primary variable of interest in this study, and all other variables and conditions were kept constant in the simulations to isolate this effect.

In Chapter 4, which focused on the mixing of two cohorts of unbonded spheres, the introduction of obstacles improved single-iteration mixing. By guiding the granular flow and promoting the interacting collision between different particles, a higher level of mixing can be achieved when compared to mixing without obstacles. It is reasonable to hypothesize that when particle crushing occurs, further improvements may appear as a result of the mixing

barrier generating impact forces during flight of the bonded particles and the increased interacting surfaces between particles. The mixing simulations were conducted with six geometric mixing arrangements while pure gravitational pouring was used as a basis for comparison. Cylindrical obstacles were applied due to the fact that in practice they are simple and inexpensive to introduce into the control volume. From the well-known oblique benchmark tests, particles change their trajectory with different incident angles. Hence a wide range of reflection angles can be generated during collision with a single barrier. The mixing systems used here were designed on rudimentary systems that have been reported in field tests and were conducted based on obstacle positions or the number of applied obstacles. Because of the relatively small control volume used to capture the dispersed particles, the maximum number of obstacles was limited to two. The geometric placement of the obstacles was somewhat strategic in that they were designed to either separate the particle flow or induce inter-particle collisions. After the poured particles have reached a specific depth, subdomains of the overall deposits were identified for testing the numerical values of various mixing and elastic parameters. Simulations of the filling process for each type of mixing model at various points in time are shown for the bounding face and the middle of the domain to show the primary differences in the various mixing qualities in **Figs. 5-5 ~ 5-22**.

General behavior of bonded particles

Group 1 is labeled as the reference grouping of particles that contain perfectly unbonded spheres (or bonds with zero original strength/stiffness). Under gravity deposition, the layered particles in repeated sections are continuously passing through the periodic inlet, traveling through the mixing system, interacting with each other, and finally accumulating into a

new deposit. Subjected to six different boundary conditions as denoted by the number and position of the geometric mixers, the filling processes with respect to each system are displayed through **Figs. 5-5 ~ 5-10**. At the early state of each model, e.g. **Fig. 5-5(a)** and **Fig. 5-6(a)**, low surface roughness allows the spheres to freely roll and eventually spherical particles are distributed everywhere on the bottom surface of the control volume. As clarified by O’Sullivan (2011), when spheres are used for DEM simulations, to stop their movements contact per particle experienced are higher than the real ones. Therefore, well mobilization is presented for unbonded spheres. Theoretically, dense internal structures tend to be formed.

In Chapter 4, we summarized that the level of interacting collisions between different particles works as the primary rule for determining the mixing of the final aggregate. The introduction of interior obstacles/mixers can effectively guide the granular flow, but the real function on mixing is decided by either the obstacles directing particle interactions or acting to separate the particle cohorts. These phenomena are particularly prominent in Model 2 of Group 1. Adding a single obstacle at the center works to divide the original granular flow into two parts, each of which are dominated by either large or small particles. Following this division, the flow of the right stream divides further into two smaller groups with little interaction between particles of varying size. This particle separation almost automatically prohibits the interacting collisions. Hence compared with the pure pouring condition, a lower level of mixing is achieved despite the placement of a geometric obstacle for which the intent is to increase mixing. Model 3 provides a good example on how adding obstacles can improve the mixing. By guiding the trajectory of the smaller granular flow into the larger particles, more of the larger spheres have chance to participate in the main incoming flow and

promote the interacting collisions in particles. Therefore, the mixing degree for Model 3 has been significantly improved, at least visually, when compared to Model 2. Comparing Model 3 with Model 4, it is obvious that by adjusting obstacle positions particle distribution between the center and the periphery can be controlled. The influence area that bounds the geometric region where particles appear after impact with the internal obstacles has been adjusted and subsequently there are far more particle collisions. Comparing Models 5 and 6, results indicate that to increase the interacting collisions, the geometric position of the mixers is more important than the number of obstacles. Overall, the degree of mixing in these binary aggregates when mixing obstacles are used is highly dependent on the direction and the related mixing level of the primary granular flow. In addition, in a behavioral feature that will be contrasted later with bonded particles, the final upper surface of the final mixtures tend to be relatively flat with only slight curvature.

Crushable particles containing weak bonds between the smaller particles are labeled as Group 2. The same six mixing processes were used with visual results presented in **Figs. 5-11 ~ 5-16**. The rectangular cross-section showing the early stage of free fall without impact/interaction illustrates that the smaller spheres are successfully bonded together until they interact with either the mixing barriers or impact with other particle blocks. This is in contrast to the case of zero bonds, where the particles separate during free-fall. By observing the final stacking states of Models 1 and 2, the easily crushed particles somewhat surprisingly attain a better mixing state than the completely unbonded particles. The impact with the obstacles not only breaks the bonded aggregates into smaller pieces but the release of the bonds results in a far more scattered and dispersed flow of the resulting particles. This behavior can be seen by comparing the particle positions at 1 second for the three different

Groups. The unbonded particles possess a much more uniform flow pattern compared to the initially bonded aggregate blocks that tend to scatter this ordered dispersion. The particle crushing associated with the release of these internal bonds has expanded the reflection angle range for smaller spheres and simultaneously increases the interacting surface of different particles. Either caused by particle impact velocities or the obstacle position, particle crushing has also been enhanced for Model 4 and is reflected by the increased reflection angle range on the left. Overall, it appears that in mixing with bonded particles, the earlier in the flow path that the obstacles are added, the better the mixing may be. It also appears that a better final particle distribution is provided by Model 5. Since particle breakage can promote the interacting collisions when mixing easily crushed particles, additional obstacles play a more important role to improve single-iteration mixing.

Figs. 5-17 ~ 5-22 provides the results from the six mixing models for Group 3, which contain crushable particles with strong bonds. One immediate observation of the final particle positions is related to the fact that because particles with unbroken bonds normally have angular surfaces with irregular shapes, piecewise-linear or lightly inclined slopes tend to be formed for the final stacking free surface. The results also indicate that far more voids tend to be created within the final aggregate near boundaries of the control volume. This is shown in **Fig. 5-23**, obtained by Model 1 of Group 3. By observing the initial stacking state of Model 1 in **Fig. 5-17(a)**, it appears that particle crushing is far less likely under pure pouring without obstacles. The mixing condition improves with the introduction of obstacles but unlike the case of particles with weak bonds, the mixing decreases for the case of strong bonds. In this case, the geometric obstacles have a different role than the one they played in the case of unbonded particles. In the unbonded case, the obstacles act to guide

the flow and force particle interaction between the differently sized cohorts. In the bonded case, the obstacles primary purpose is the grind/fracture the aggregate blocks. When the bonds are weak, the mixing can improve. When the bonds are strong, the mixing appears to be worse.

5.5 Results and Discussion

Up to this point, the observations on the degree of mixing that was observed for the various cases was qualitative based on visual evidence. To more directly quantify the degree of mixing, a series of virtual experiments were conducted to checking the mixing properties of the final composite aggregate. The investigation was conducted through measurement of two physical quantities: the degree of mixing as quantified by the volume ratio, and the equivalent mechanical properties that relate applied stress to induced strain.

5.5.1 Internal mixing degree

In Chapter 4, mixing parameters that are widely used in geotechnics were computed and the volume ratio was found to be most capable in depicting the level of mixing in the final composite aggregate. This parameter is measured using scattered spherical regions within the final control volume. If the volume ratio is relatively consistent across all regions, the aggregate is well-mixed. Control volumes with a radius of $0.1 m$ were used for calculating these parameters. A total number of 27 spherical regions were used with the geometric centers listed in **Table 5-2**. By investigating mixing ratios distributed at the middle plane located at $y = 0.5 m$, the results can be compared with previous observations. The volume ratios ϕ_v of the six different models are plotted in **Fig. 5-24 ~ 5-26**. Each figure contains

two parts. The sub-figures at the top illustrate the ratios of the entire domain including all 27 sub-regions. Each of the segmented rectangular widths correspond to data points taken in one of the three y-planes. The bottom sub-figures represent the volume ratios at the middle of the domain ($y=0.5m$). The data points are classified according to the six different mixing models. The mean values are given by red squares and the related standard deviations are illustrated by gray bars. The detailed values for these two parameters are listed in **Table 5-3**. Well-mixed deposits without loss of mass possess an average volume ratio that is close to the input value of 0.0625. For reference, this value is indicated by horizontal red dashed lines in each of these figures. Hence an ideal mixed packing would have a mean value of 0.0625 without deviation.

The results for Group 1 are shown in **Fig. 5-24**. The volume ratios are relatively low with numerous zero values appearing for Model 1. This is due to the fact that big spheres appear to float during the mixing and are pushed towards the bounding walls of the control volume. The central area is primarily occupied by the smaller unbonded spheres. By placing a single obstacle near the control volume center, the mixing worsens because the obstacle acts to divide the flow rather than mix it. The large spheres again move to the right wall as illustrated in **Fig. 5-6(d)**, with a large number of zero values of volume ratio appearing and in fact the average volume ratio is near zero. A significant improvement appears for Model 3, where the obstacle now forces particle interaction with a mean value of volume ratio about 0.47, with overall better mixing compared with Model 4. Model 5 appears both visually and numerically to provide the overall best level of mixing. In Model 6, the lower right obstacle drives the prime flow to the sides, resulting in enormous increases in standard deviation.

In **Fig. 5-25**, which represents the results from Group 2, it is clear that particle crushing with weak bonds promotes the homogeneity of the mixtures over unbonded aggregates. This change is illustrated through the following aspects: 1) Extreme values, including zeros and relatively high values of volume ratio, are more limited. In Models 1 and 2, small increases are found in the measured volume ratios and the number of zero ϕ_v values has been reduced. The extreme value in Model 3 as shown in **Fig. 5-24(b)** has also vanished. 2) The range of variation is smaller over the different regions. For example, in Model 3, there is a drop of over 50 percent from unbonded to weakly bonded. 3) There are increases in the volume ratio in the regions near the boundary as shown in **Fig. 5-25(a)**. 4) With consistent values, small fluctuations, and lower mean values close to the input, better levels of mixing are provided by Model 3 and Model 5. In Model 6, the 2nd obstacle has changed the direction of the prime flow to the side and the deviation becomes much higher than that in Model 3.

The results for strongly bonded particles are shown in **Fig. 5-26**. In general, the same sort of trend occurs when compared to the unbonded particles: the impact of the initially bonded particles tends to scatter the resulting particles after collision and the mixing process tends to improve. Because of the limited results, it is difficult to draw broad conclusions between the strong and weak bonded particle assemblies. Clearly, for particles with extremely high bond strength the mixing properties would eventually decline since the smaller particles cannot mix with the larger particles if they stay together as a single volume. This sort of limit will await future studies.

5.5.2 Effective elastic properties

Simulated element compression tests were used to measure the effective elastic properties. Although numerous studies have assumed that particle aggregates possess isotropic bulk properties, in this study we allow for two independent Poisson ratios for the horizontal plane directions and then the horizontal-vertical plane directions. The same center locations placed at middle zones as were used for the mixing parameters were used but in this case cubic regions with the side length of 0.2 m were used with a friction coefficient of the bounding walls of 0.2. The applied axial stress in the vertical direction was specified as 5000 Pa with the other two normal stresses in the horizontal plane calculated from the bounding forces. The equivalent isotropic elastic modulus E was measured for the six barrier models for the three groups and are plotted in **Fig. 5-27**. The same notation is used here as was used for plotting the mixing parameters. With respect to each model, detailed information including the two independent Poisson ratios is plotted through **Figs. 5-28 ~ 5-30**. A dual y-axis chart is used to show the computed elastic properties where $\nu_{xz} = \nu_{yz}$. To avoid the differences caused by the specified criterion and the slight differences in the nature of the different control volumes, the mean values were calculated after eliminating the highest and lowest values. The results are shown in **Table 5-4** and **Table 5-5**.

From **Fig. 5-27(a)**, the results are generally consistent with the evaluation of the mixing parameters. For the completely unbonded particles, the data points are widely distributed at the extremes with relatively large variations shown by Models 1 and 2. With a slightly increased level of mixing, for example Models 4 and 6, the measured values of elastic modulus are more evenly distributed over the variation range. With further improvements in mixing, the fluctuations become smaller. With the exception of Model 4, the mean values for the

elastic modulus range from 4483 to 5970 N/m^2 and the Poisson ratio values range from 0.513 to 0.559 for ν_{xy} and from 0.386 to 0.441 for ν_{xz} . Vallejo (2001) has concluded that if the concentration by weight of the larger spheres is greater than 70%, the shear strength of the mixtures is controlled by the frictional resistance of large spheres. If the concentration of large spheres is smaller than 40%, the shear strength is determined by smaller spheres. Otherwise, the shear strength is controlled by both sizes of sphere. Although in this study it is the stiffness rather than the strength that is being estimated, it is possible that similar metrics can be developed for both bonded and unbonded spheres. In any case, with an increased number of larger spheres in the measured regions, a strong anisotropy is shown in the final aggregates as evidenced by the differences in the Poisson ratios.

There are several clear trends that emerge from the results for the elastic module and the two values of Poisson ratio as the smaller particles are bonded together with increasing strength. First, the effective elastic modulus decreases in value with an increase in particle bond strength. Part of the reason for this is that the bonded particles tend to form smaller pockets or voids within the total control volume that are particle-free (see **Fig. 5-23**, and hence force chains within those regions may not be able to form and contribute to the overall stiffness. Second, the range of predicted values tends to decrease somewhat with increasing bond strength, indicating that the bonded particle blocks provide less variability over the separate control volumes. Third, the values of the in-plane Poisson ratio ν_{xy} are significantly higher than the out-of-plane values of $\nu_{xz} = \nu_{yz}$, indicating that the mixing process results in at least some level of anisotropy in the final aggregate. However, this behavior is slightly more complex in that the anisotropy tends to decrease as the particle bond strength increases. This is because the unbonded particles possess the largest in-plane

Poisson ratio and the lowest out-of-plane Poisson ratio. As the bond strength increases, ν_{xy} decreases but ν_{xz} increases. The decreases in elastic modulus are in the range of 25 percent, while the changes in the values for Poisson ratio the shifts are in the range of about ten percent. Regardless, the mechanical elastic constants are measurably influenced by the bond strength between particles.

5.6 Summary and Conclusions

This Chapter proposed a new method for determining the effects of crushable particles on mixing properties. Three groups of spheres were generated for numerical simulations. For each group, six mixing systems are created for studying the effects of adding obstacles to both separate and direct the resulting particle flow. Studies were conducted to determine the influence of bond strength on the mixing volume ratio and the effective elastic constants of the final composite aggregate. The primary conclusions of this work are as follows:

- Particles that are originally bonded together with either weak or strong bonds result in better mixing than particle cohorts that are originally unbonded. The interaction of the connected particles results in far more particle collisions and a larger range of reflection angles and interactions than the relatively ordered particle flow that occurs for the unbonded spheres.
- The introduction of mixing obstacles within the control volume improves the mixing properties of the final aggregate.
- The final composite aggregate exhibits significant anisotropy as measured by the two independent values of Poisson ratio.

- An increase in bond strength results in a decline in the effective elastic modulus.
- An increase in bond strength reduces the level of anisotropy in the final particle aggregate.

Table 5-1: Summary of input parameters

Particle types	Parameters	Values
Big	Young's modulus $E(N/m^2)$	5.0E5
	Poisson ratio ν	0.33
	Density (kg/m^3)	3200
	Radius (m)	0.03
Small	Young's modulus $E(N/m^2)$	1.0E6
	Poisson ratio ν	0.28
	Density (kg/m^3)	4000
	Radius (m)	0.015
Bond		
<i>weak</i>	Bond-radius multiplier $\bar{\lambda}$	1.0
	Normal and shear stiffness $\bar{k}_n = \bar{k}_t (N/m^2)$	1.0E6
	Allowable strength $\bar{\sigma}_c = \bar{\tau}_c (N/m^2)$	5.0E3
<i>strong</i>	Bond-radius multiplier $\bar{\lambda}$	1.0
	Normal and shear stiffness $\bar{k}_n = \bar{k}_t (N/m^2)$	1.0E6
	Allowable strength $\bar{\sigma}_c = \bar{\tau}_c$	2.0E4
General	Friction coefficient	0.2
	Restitution coefficient	0.3
	Rolling coefficient	0.1
	Velocity (m/s)	1
	Time increment $dt(sec)$	1.0E-4

Table 5-2: Point locations for measuring mixing parameters and the equivalent elastic properties

Points	x	y	z	Points	x	y	z	Points	x	y	z
1	0.25	0.25	0.2	10	0.25	0.5	0.2	19	0.25	0.75	0.2
2	0.5	0.25	0.2	11	0.5	0.5	0.2	20	0.5	0.75	0.2
3	0.75	0.25	0.2	12	0.75	0.5	0.2	21	0.75	0.75	0.2
4	0.25	0.25	0.3	13	0.25	0.5	0.3	22	0.25	0.75	0.3
5	0.5	0.25	0.3	14	0.5	0.5	0.3	23	0.5	0.75	0.3
6	0.75	0.25	0.3	15	0.75	0.5	0.3	24	0.75	0.75	0.3
7	0.25	0.25	0.4	16	0.25	0.5	0.4	25	0.25	0.75	0.4
8	0.5	0.25	0.4	17	0.5	0.5	0.4	26	0.5	0.75	0.4
9	0.75	0.25	0.4	18	0.75	0.5	0.4	27	0.75	0.75	0.4

Table 5-3: The mean values and the related standard deviations of mixing ratios measured at the middle clips for the present six models in each group

Group 1	Models	1	2	3	4	5	6
	Avg.	0.0575	0.0186	0.4658	0.4507	0.3197	0.3214
	Std.	0.0933	0.0319	0.2712	0.2039	0.1548	0.3750
Group 2	Models	1	2	3	4	5	6
	Avg.	0.1210	0.1203	0.3643	0.4724	0.3771	0.3225
	Std.	0.1876	0.0469	0.1180	0.1695	0.1441	0.3449
Group 3	Models	1	2	3	4	5	6
	Avg.	0.0434	0.0501	0.2417	0.2846	0.1331	0.3163
	Std.	0.0663	0.0671	0.1927	0.1744	0.0540	0.4352

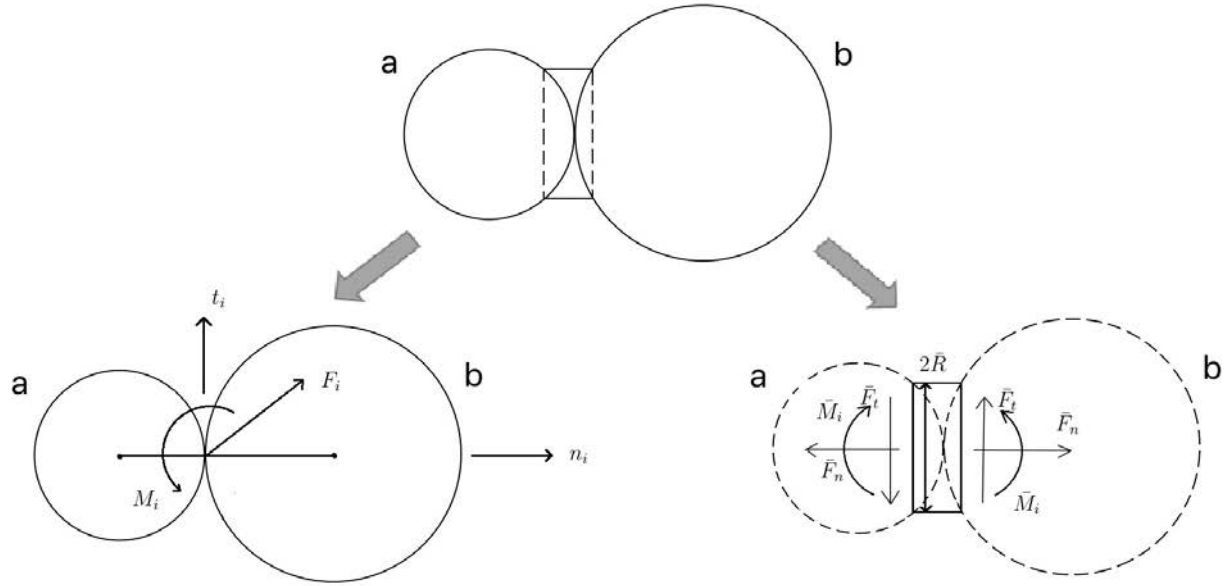
Table 5-4: The mean values and the related standard deviations of equivalent elastic modulus E (N/m^2) measured at the middle clips for the present six models in each group

Group 1	Models	1	2	3	4	5	6
	Avg.	4483	5702	4753	8195	5970	5427
	Std.	2860	3050	1317	3396	2801	2893
Group 2	Models	1	2	3	4	5	6
	Avg.	6522	4189	3157	3072	6759	4618
	Std.	1781	742	697	1081	2122	857
Group 3	Models	1	2	3	4	5	6
	Avg.	5838	4764	4880	5136	4803	4827
	Std.	1350	1317	1415	1959	820	1394

Table 5-5: The mean values and the related standard deviations of equivalent Poisson ratios measured at the middle clips for the present six models in each group

Poisson ratio ν_{xy}							
	Models	1	2	3	4	5	6
Group 1	Avg.	0.513	0.549	0.519	0.661	0.554	0.559
	Std.	0.074	0.076	0.122	0.117	0.080	0.118
	Models	1	2	3	4	5	6
Group 2	Avg.	0.578	0.470	0.451	0.495	0.554	0.509
	Std.	0.085	0.061	0.079	0.061	0.081	0.056
	Models	1	2	3	4	5	6
Group 3	Avg.	0.515	0.484	0.505	0.582	0.485	0.523
	Std.	0.066	0.055	0.091	0.071	0.049	0.084
	Models	1	2	3	4	5	6

Poisson ratio ν_{xz} or ν_{yz}							
	Models	1	2	3	4	5	6
Group 1	Avg.	0.441	0.412	0.411	0.298	0.386	0.387
	Std.	0.068	0.067	0.071	0.113	0.068	0.088
	Models	1	2	3	4	5	6
Group 2	Avg.	0.371	0.460	0.465	0.454	0.374	0.418
	Std.	0.063	0.034	0.045	0.029	0.060	0.029
	Models	1	2	3	4	5	6
Group 3	Avg.	0.426	0.452	0.428	0.386	0.442	0.419
	Std.	0.043	0.041	0.058	0.058	0.032	0.058
	Models	1	2	3	4	5	6



$$F_n = K_n \delta_n, \text{ and } K_n = \frac{2K_n^a K_n^b}{K_n^a + K_n^b}$$

$$F_t = -K_t \int_{t_0}^t \dot{\delta}_t dt \frac{\dot{\delta}_t}{|\dot{\delta}_t|}$$

$$M_r = -K_r \int_{t_0}^t \dot{\theta}_r dt \frac{\dot{\theta}_r}{|\dot{\theta}_r|}$$

$$\Delta \bar{F}_n = -\bar{k}_n A \Delta \delta_n$$

$$\Delta \bar{F}_t = -\bar{k}_t A \Delta \delta_t$$

$$\Delta \bar{M}_n = -\bar{k}_t J \Delta \theta_n$$

$$\Delta \bar{M}_t = -\bar{k}_n J \Delta \theta_t$$

$$A = \pi \bar{R}^2, \quad I = \frac{1}{4} \pi \bar{R}^4, \text{ and } J = \frac{1}{2} \pi \bar{R}^4$$

$$F_t \leq \mu F_n$$

$$M_r \leq \eta F_n$$

strength

$$\bar{\sigma}^{max} = \frac{-\bar{F}_n}{A} + \frac{|\bar{M}_t| \bar{R}}{I}$$

$$\bar{\tau}^{max} = \frac{\bar{F}_t}{A} + \frac{|\bar{M}_n| \bar{R}}{J}$$

Figure 5-1: Force-displacement behavior of the presented DEM model for simulating crushable aggregates

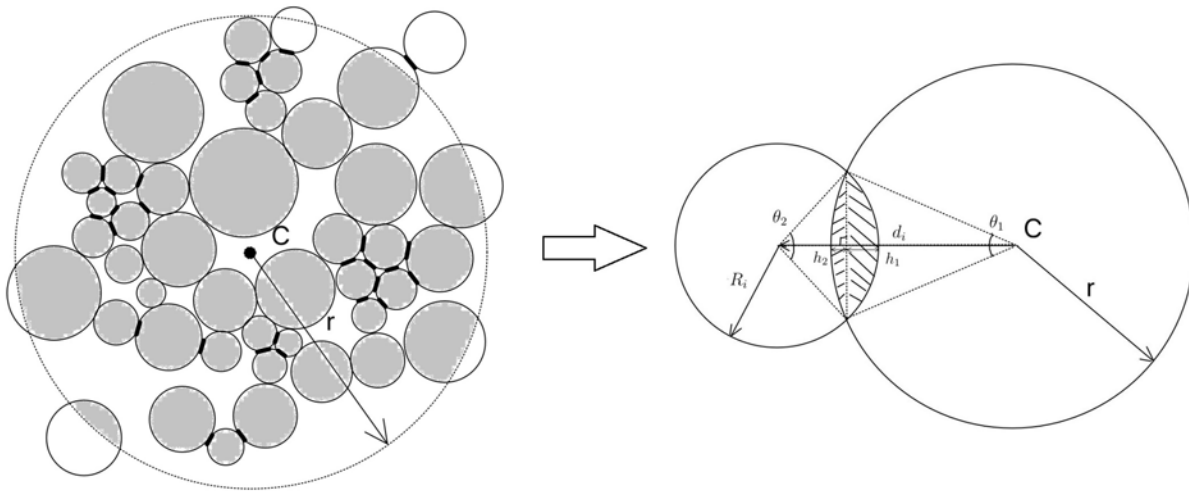


Figure 5-2: A planar cut showing the extended version of using Bardet and Proubet (1991) algorithm to calculate the volume ratio ϕ_v in 3D samples

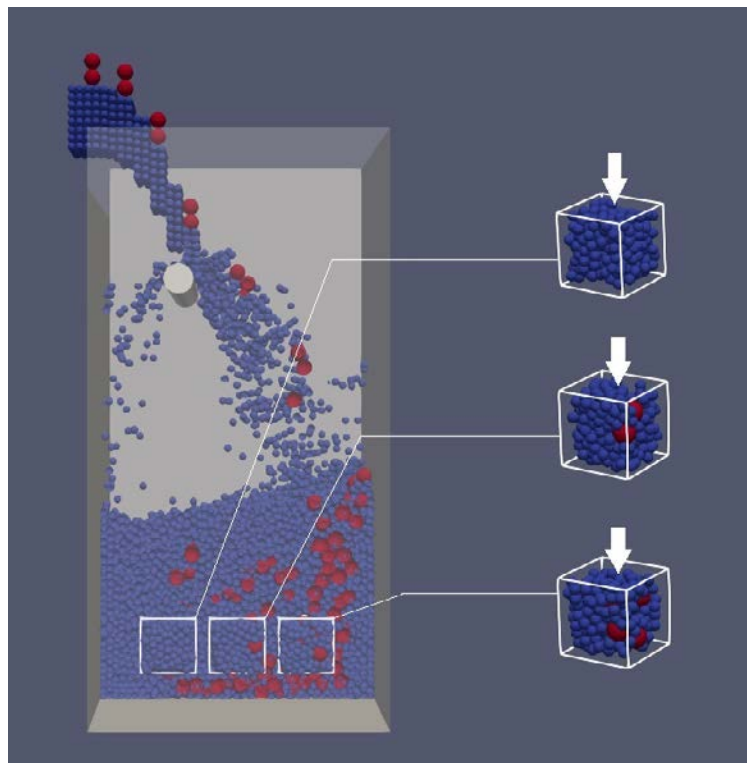
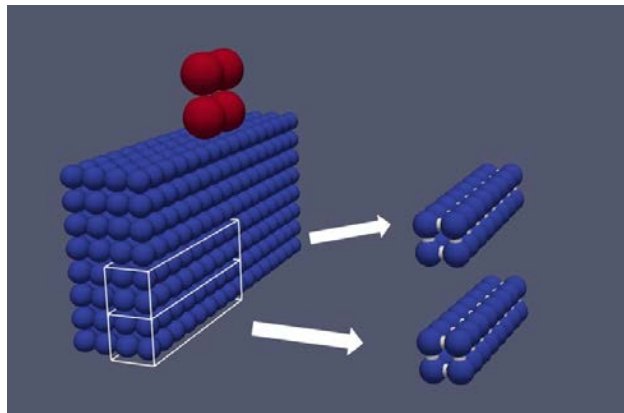


Figure 5-3: A planar cut showing our strategy for doing element compression tests. Detected points are distributed within the final aggregates. Cubic regions with the detected points placed at the center are used for measuring. Each cubic region is surrounded by five rigid walls, while the top one is movable. The white arrows illustrate the location for applied the uniaxial stress.



(a) The front-view

(b) The side-view



(c) A 3D view of bonded spheres

Figure 5-4: The front-view, side-view and a 3D view of particles in the repeated section. Crushable particles are bonded with 32 basic spheres where white short lines indicate the pattern of connecting bonds

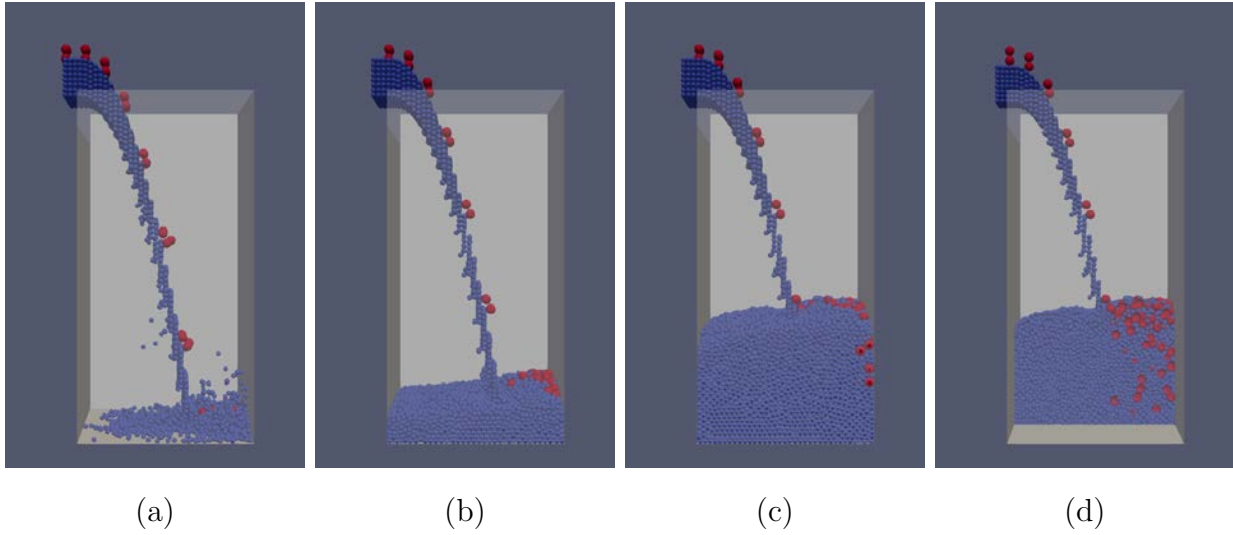


Figure 5-5: Group 1 (Model 1): A filling without applying crushable particles was simulated with unbonded spheres and under pure gravity deposition. The mixing process was investigated at specific times: (a) $t=1$ s, (b) $t=3$ s, (c) $t=9$ s; and (d) a middle clip showing the final stacking state.

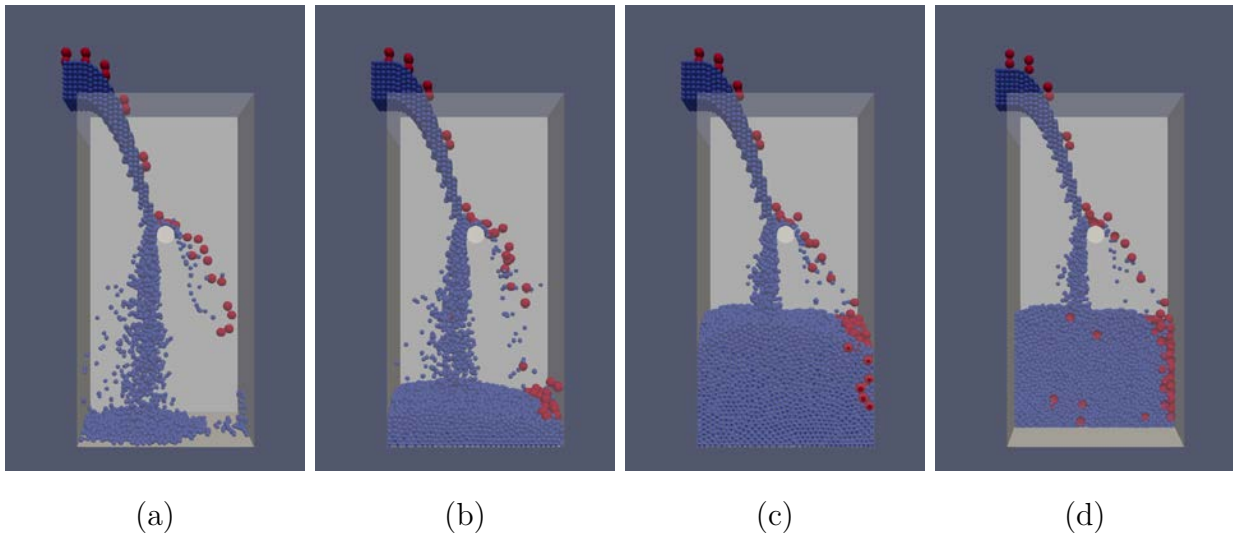


Figure 5-6: Group 1 (Model 2): A filling without applying crushable particles was simulated with unbonded spheres and under gravity deposition with one obstacle placed at locations $x=0.5$ m and $z=1.2$ m. The mixing process was investigated at specific times: (a) $t=1$ s, (b) $t=3$ s, (c) $t=9$ s; and (d) a middle clip showing the final stacking state.

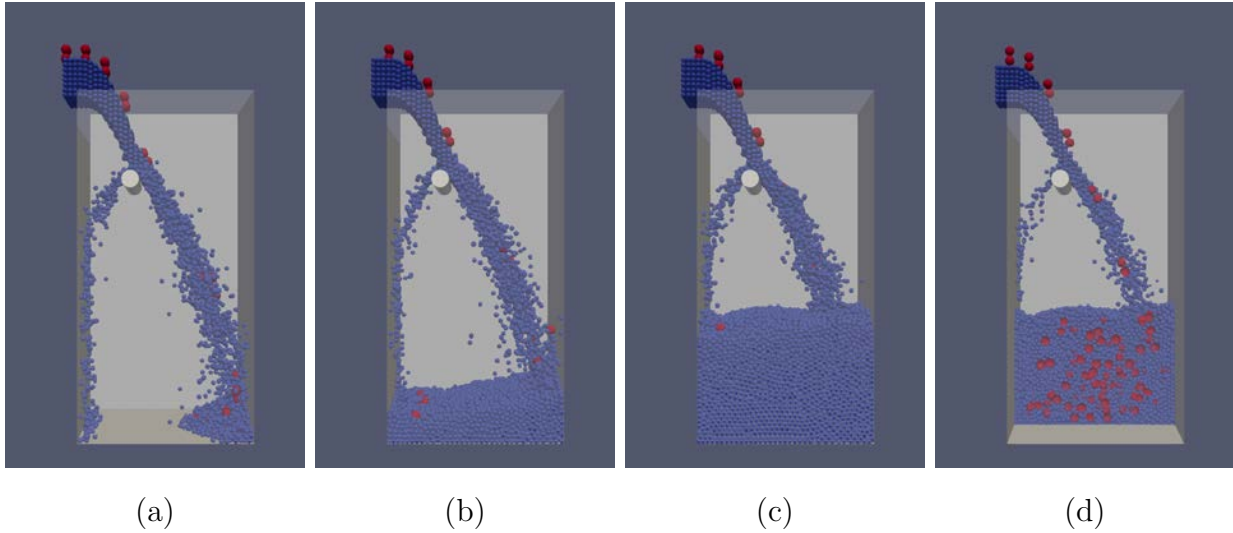


Figure 5-7: Group 1 (Model 3): A filling without applying crushable particles was simulated with unbonded spheres and under gravity deposition with one obstacle placed at locations $x=0.3$ m and $z=1.5$ m. The mixing process was investigated at specific times: (a) $t=1$ s, (b) $t=3$ s, (c) $t=9$ s; and (d) a middle clip showing the final stacking state.

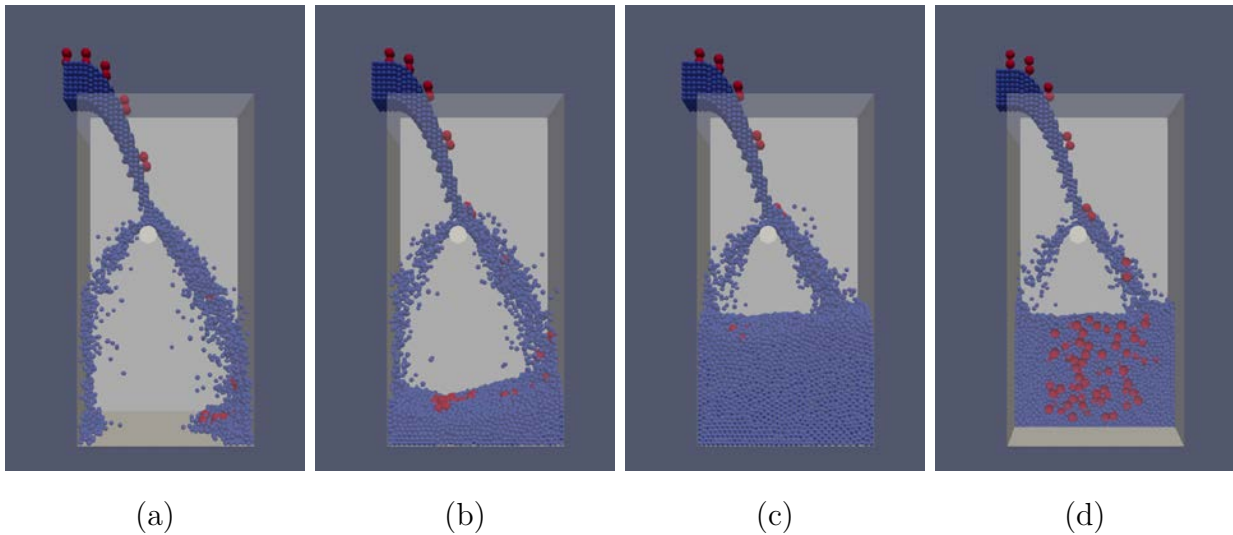


Figure 5-8: Group 1 (Model 4): A filling without applying crushable particles was simulated with unbonded spheres and under gravity deposition with one obstacle placed at locations $x=0.4$ m and $z=1.2$ m. The mixing process was investigated at specific times: (a) $t=1$ s, (b) $t=3$ s, (c) $t=9$ s; and (d) a middle clip showing the final stacking state.

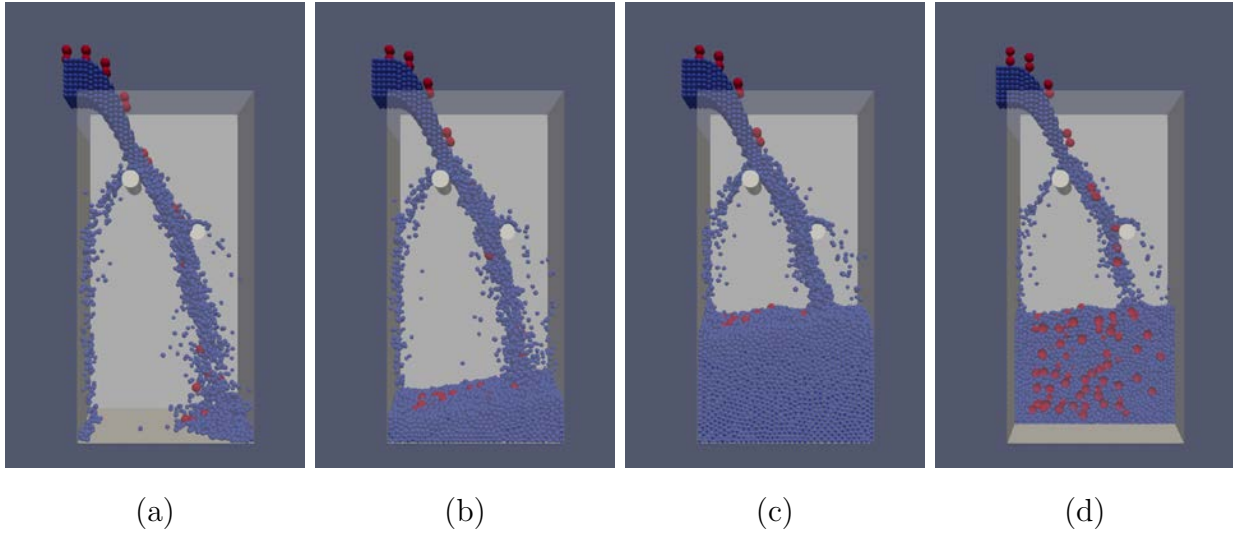


Figure 5-9: Group 1 (Model 5): A filling without applying crushable particles was simulated with unbonded spheres and under gravity deposition with two obstacles placed at locations $x=0.3$ m & $z=1.5$ m and $x=0.7$ m & $z=1.2$ m, respectively. The mixing process was investigated at specific times: (a) $t=1$ s, (b) $t=3$ s, (c) $t=9$ s; and (d) a middle clip showing the final stacking state.

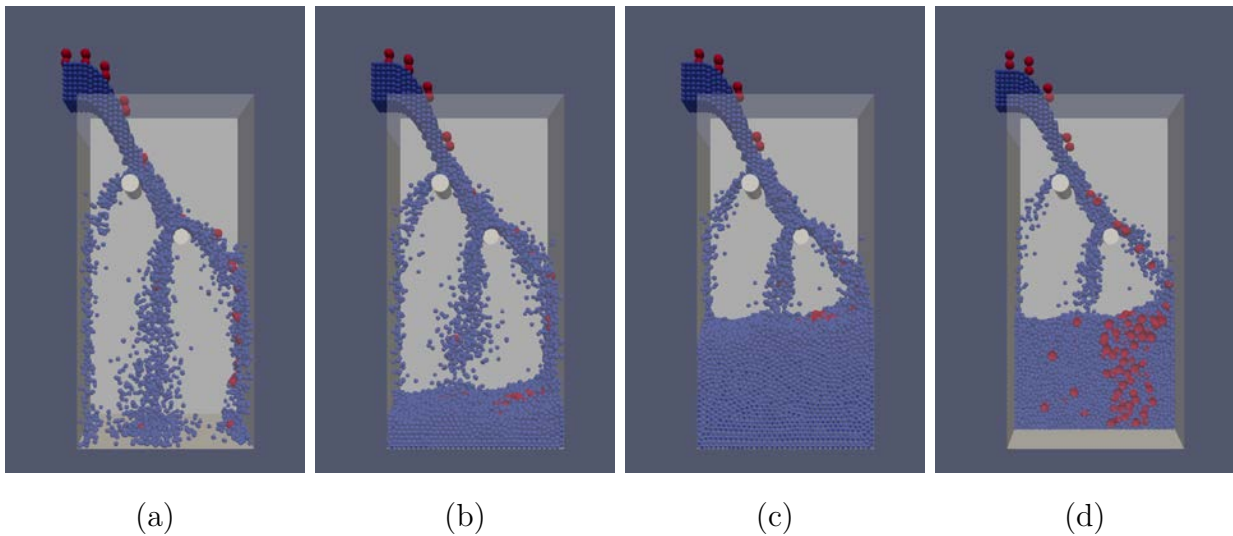


Figure 5-10: Group 1 (Model 6): A filling without applying crushable particles was simulated with unbonded spheres and under gravity deposition with two obstacles placed at locations $x=0.3$ m & $z=1.5$ m and $x=0.6$ m & $z=1.2$ m, respectively. The mixing process was investigated at specific times: (a) $t=1$ s, (b) $t=3$ s, (c) $t=9$ s; and (d) a middle clip showing the final stacking state.

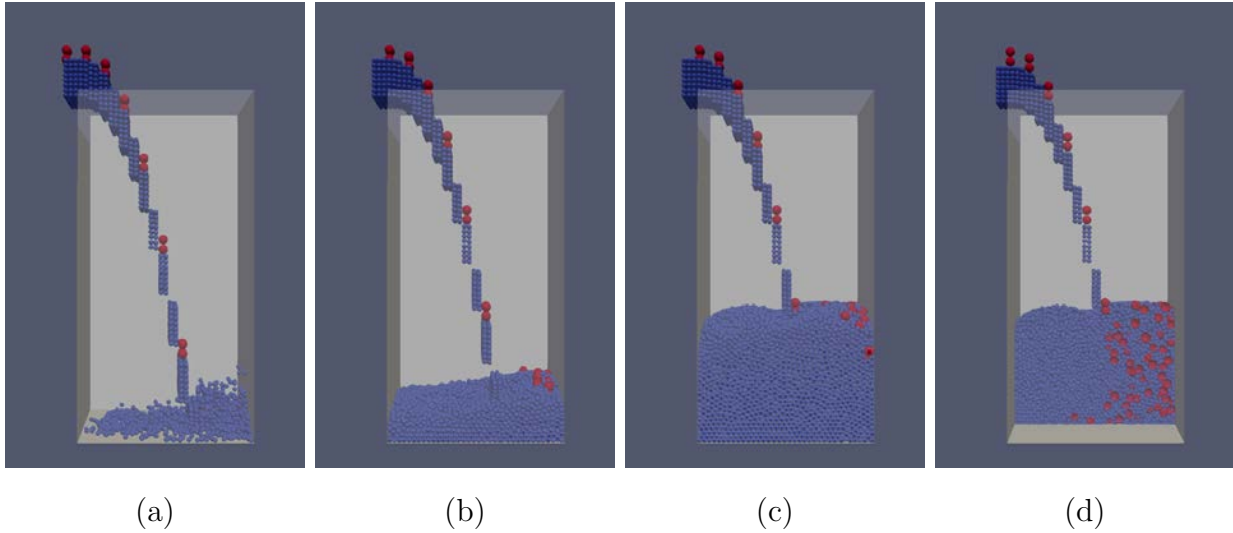


Figure 5-11: Group 2 (Model 1): A filling with crushable particles which was simulated with bonded aggregates using weak bonds and under pure gravity deposition. The mixing process was investigated at specific times: (a) $t=1$ s, (b) $t=3$ s, (c) $t=9$ s; and (d) a middle clip showing the final stacking state.

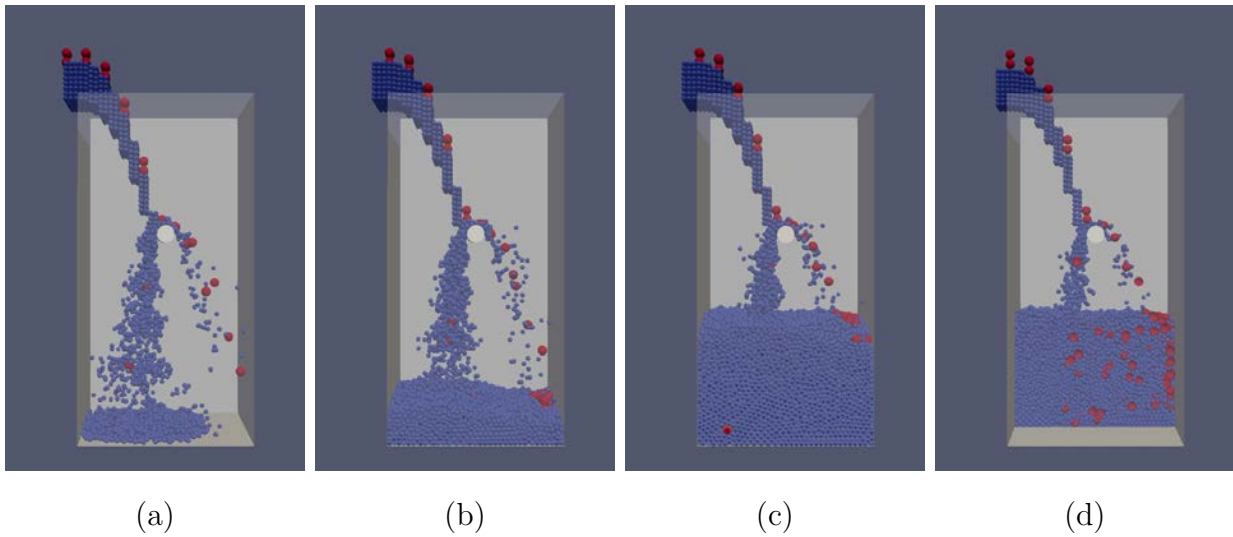


Figure 5-12: Group 2 (Model 2): A filling with crushable particles which was simulated with bonded aggregates using weak bonds and under gravity deposition with one obstacle placed at locations $x=0.5$ m and $z=1.2$ m. The mixing process was investigated at specific times: (a) $t=1$ s, (b) $t=3$ s, (c) $t=9$ s; and (d) a middle clip showing the final stacking state.

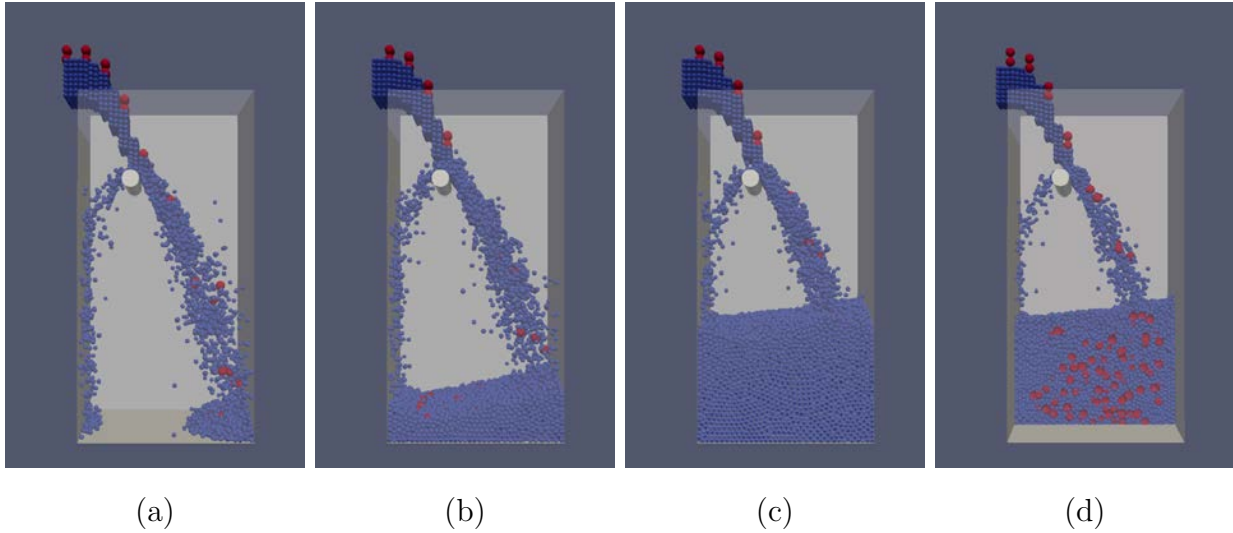


Figure 5-13: Group 2 (Model 3): A filling with crushable particles which was simulated with bonded aggregates using weak bonds and under gravity deposition with one obstacle placed at locations $x=0.3$ m and $z=1.5$ m. The mixing process was investigated at specific times: (a) $t=1$ s, (b) $t=3$ s, (c) $t=9$ s; and (d) a middle clip showing the final stacking state.

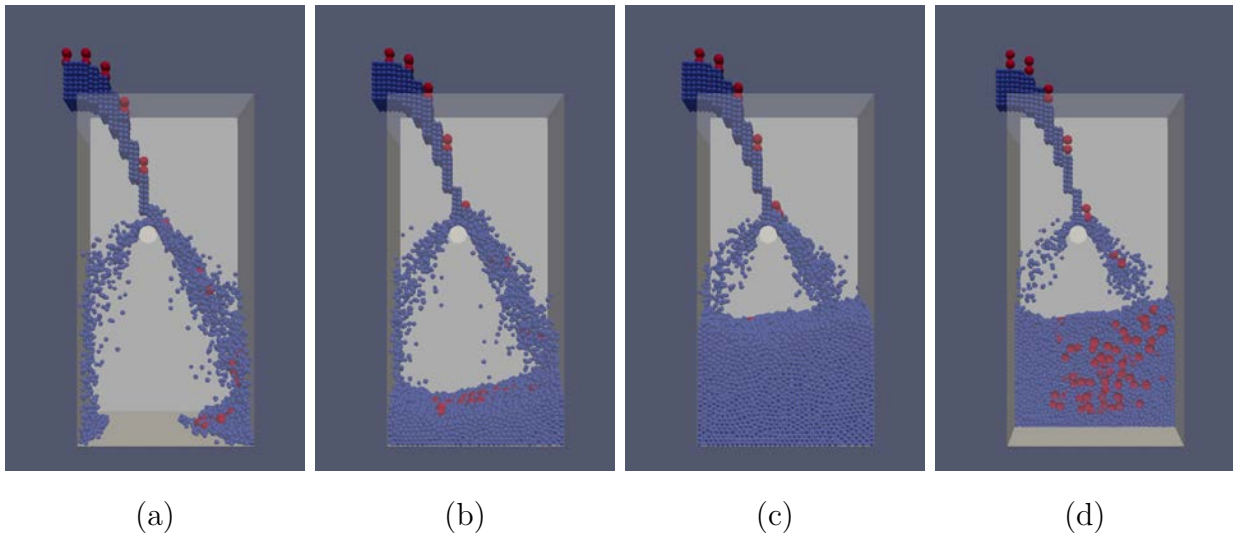


Figure 5-14: Group 2 (Model 4): A filling with crushable particles which was simulated with bonded aggregates using weak bonds and under gravity deposition with one obstacle placed at locations $x=0.4$ m and $z=1.2$ m. The mixing process was investigated at specific times: (a) $t=1$ s, (b) $t=3$ s, (c) $t=9$ s; and (d) a middle clip showing the final stacking state.

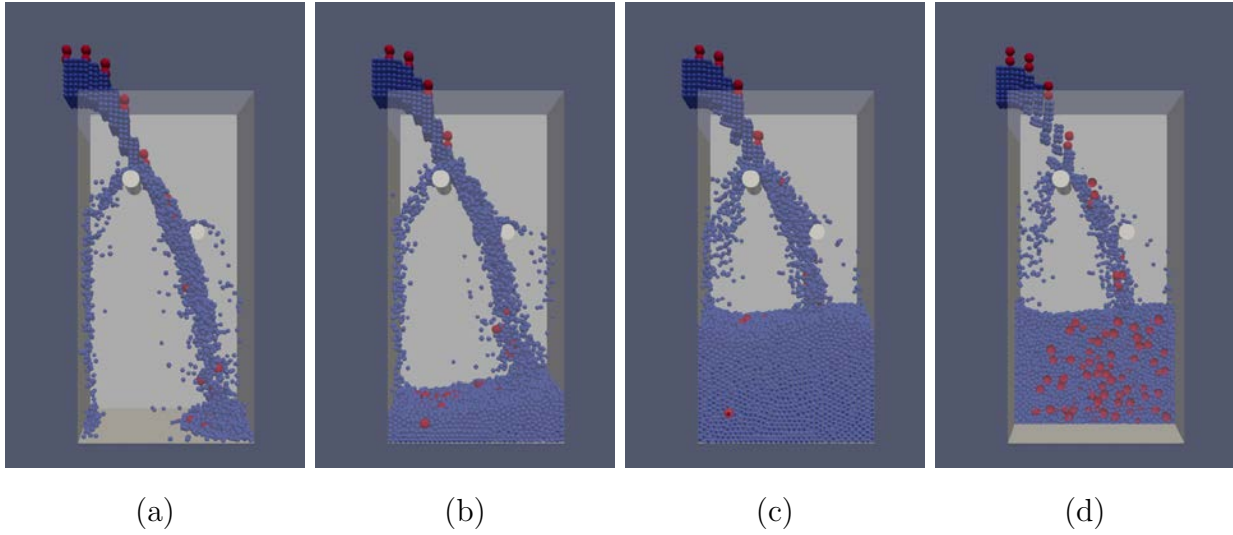


Figure 5-15: Group 2 (Model 5): A filling with crushable particles which was simulated with bonded aggregates using weak bonds and under gravity deposition with two obstacles placed at locations $x=0.3$ m & $z=1.5$ m and $x=0.7$ m & $z=1.2$ m, respectively. The mixing process was investigated at specific times: (a) $t=1$ s, (b) $t=3$ s, (c) $t=9$ s; and (d) a middle clip showing the final stacking state.

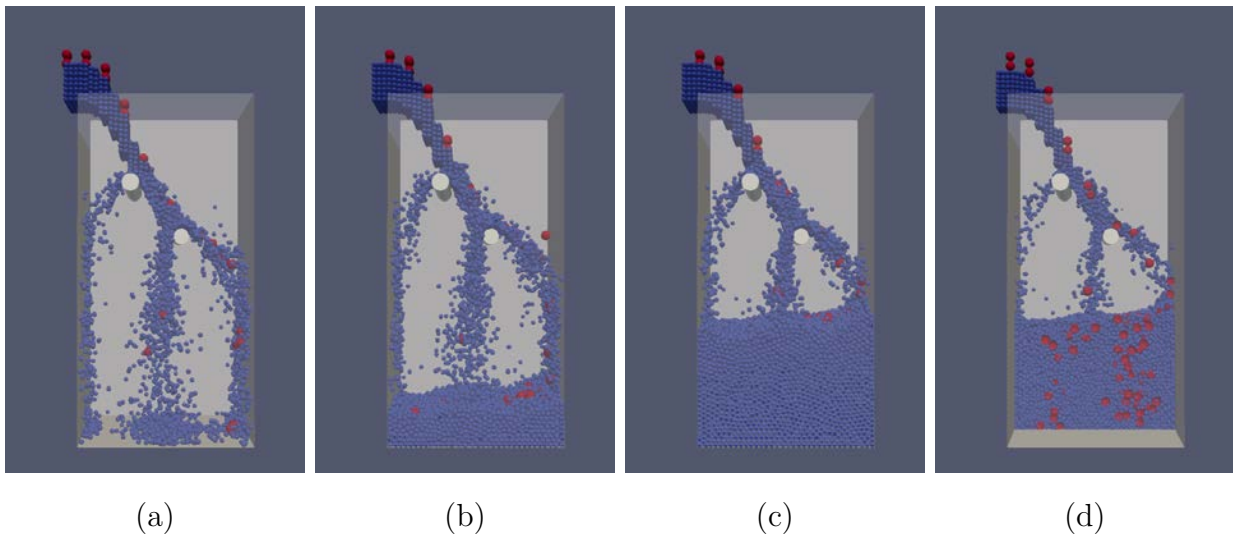


Figure 5-16: Group 2 (Model 6): A filling with crushable particles which was simulated with bonded aggregates using weak bonds and under gravity deposition with two obstacles placed at locations $x=0.3$ m & $z=1.5$ m and $x=0.6$ m & $z=1.2$ m, respectively. The mixing process was investigated at specific times: (a) $t=1$ s, (b) $t=3$ s, (c) $t=9$ s; and (d) a middle clip showing the final stacking state.

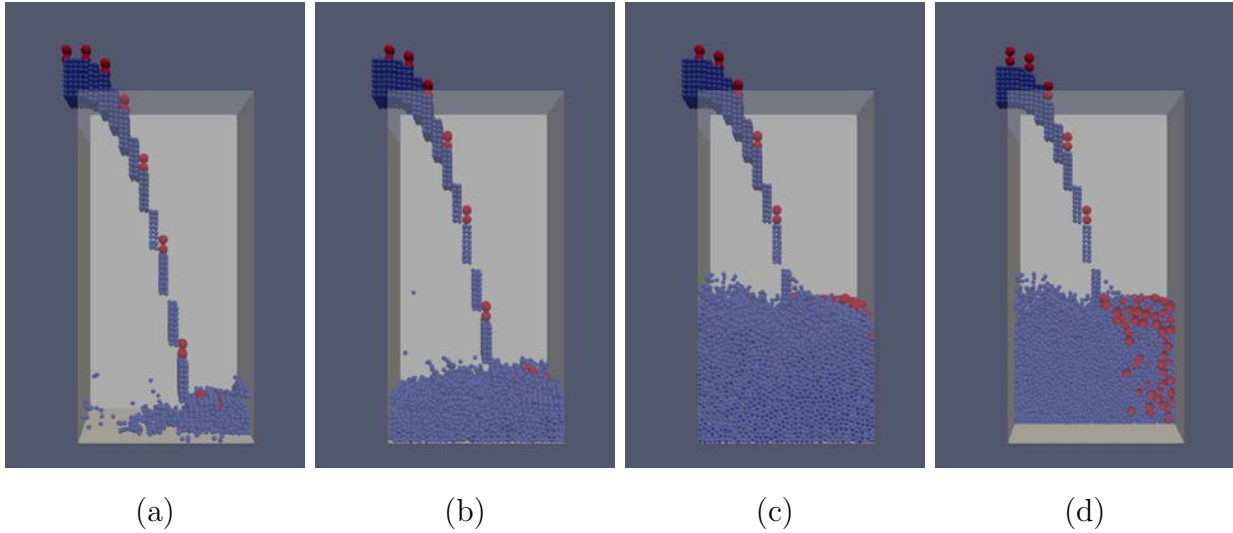


Figure 5-17: Group 3 (Model 1): A filling with crushable particles which was simulated with bonded aggregates using strong bonds and under pure gravity deposition. The mixing process was investigated at specific times: (a) $t=1$ s, (b) $t=3$ s, (c) $t=9$ s; and (d) a middle clip showing the final stacking state.

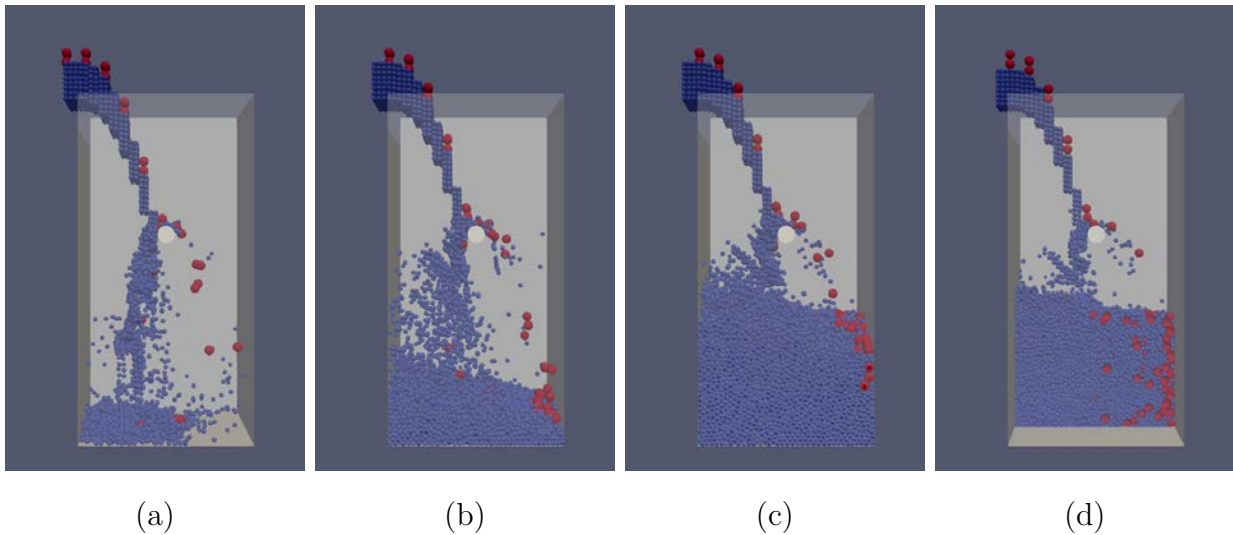


Figure 5-18: Group 3 (Model 2): A filling with crushable particles which was simulated with bonded aggregates using strong bonds and under gravity deposition with one obstacle placed at locations $x=0.5$ m and $z=1.2$ m. The mixing process was investigated at specific times: (a) $t=1$ s, (b) $t=3$ s, (c) $t=9$ s; and (d) a middle clip showing the final stacking state.

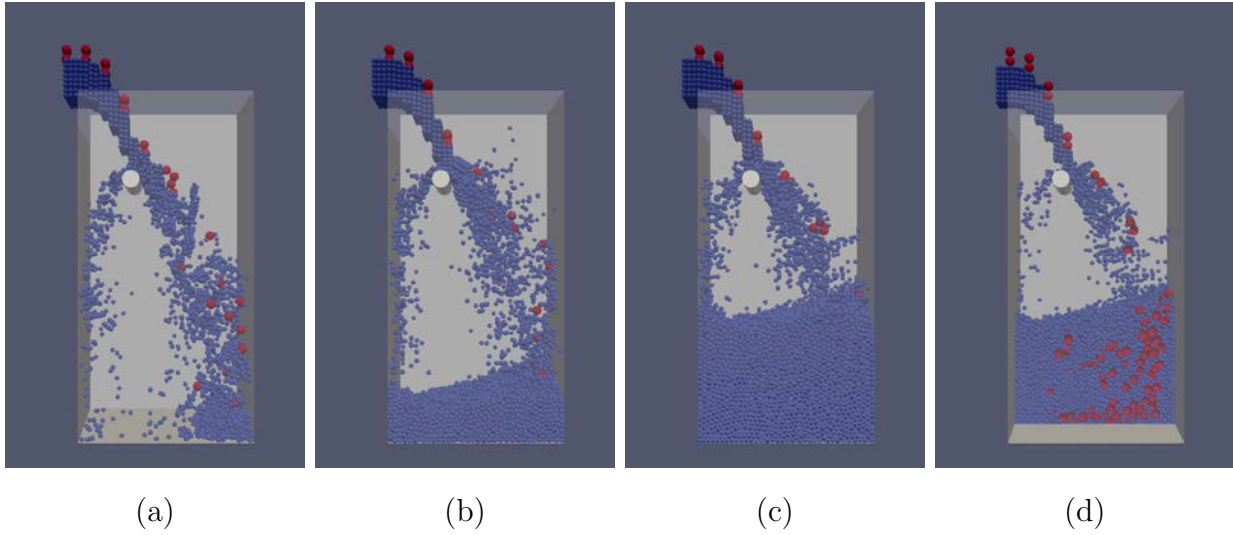


Figure 5-19: Group 3 (Model 3): A filling with crushable particles which was simulated with bonded aggregates using strong bonds and under gravity deposition with one obstacle placed at locations $x=0.3$ m and $z=1.5$ m. The mixing process was investigated at specific times: (a) $t=1$ s, (b) $t=3$ s, (c) $t=9$ s; and (d) a middle clip showing the final stacking state.

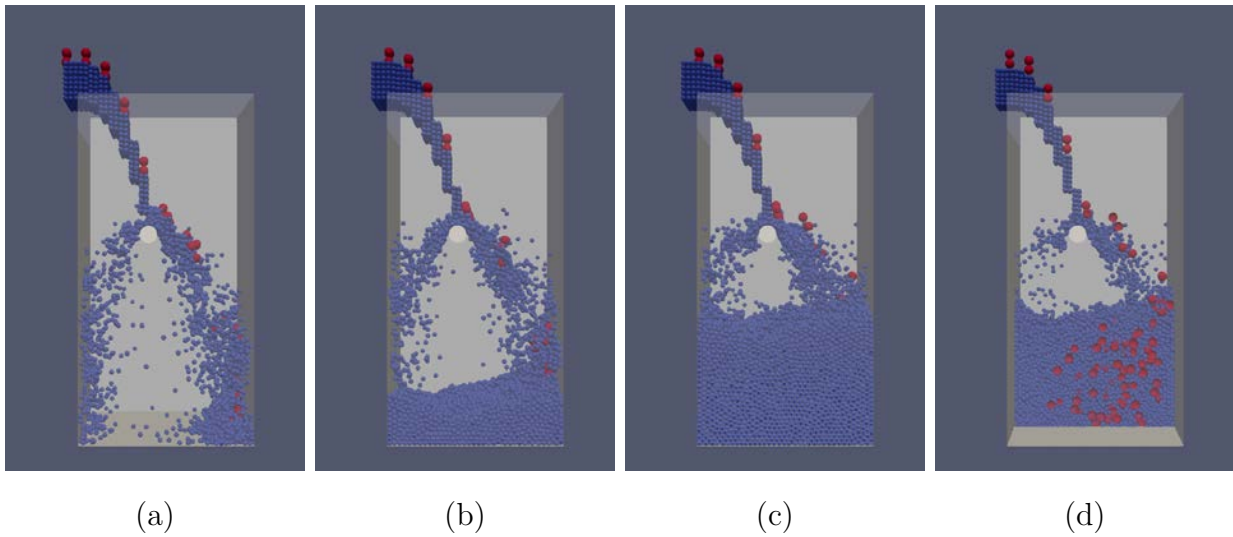


Figure 5-20: Group 3 (Model 4): A filling with crushable particles which was simulated with bonded aggregates using strong bonds and under gravity deposition with one obstacle placed at locations $x=0.4$ m and $z=1.2$ m. The mixing process was investigated at specific times: (a) $t=1$ s, (b) $t=3$ s, (c) $t=9$ s; and (d) a middle clip showing the final stacking state.

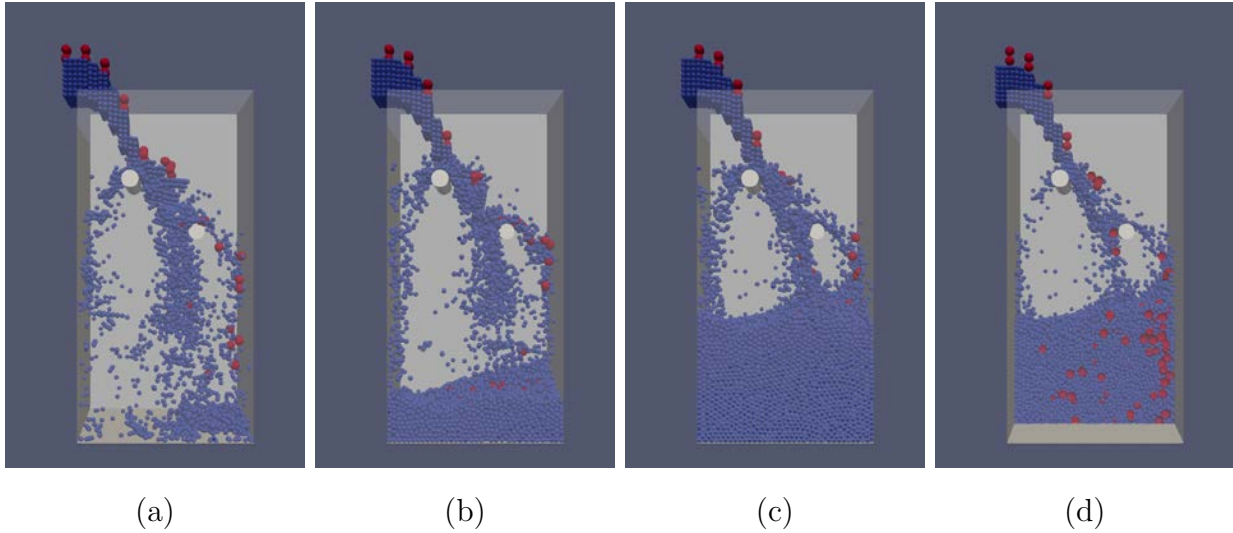


Figure 5-21: Group 3 (Model 5): A filling with crushable particles which was simulated with bonded aggregates using strong bonds and under gravity deposition with two obstacles placed at locations $x=0.3$ m & $z=1.5$ m and $x=0.7$ m & $z=1.2$ m, respectively. The mixing process was investigated at specific times: (a) $t=1$ s, (b) $t=3$ s, (c) $t=9$ s; and (d) a middle clip showing the final stacking state.

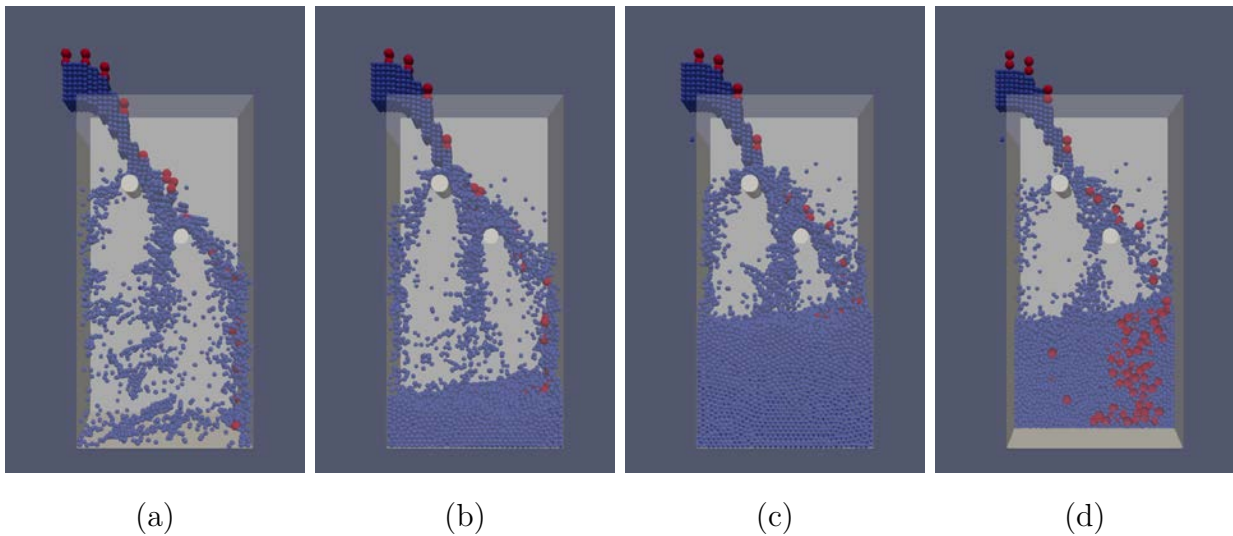


Figure 5-22: Group 3 (Model 6): A filling with crushable particles which was simulated with bonded aggregates using strong bonds and under gravity deposition with two obstacles placed at locations $x=0.3$ m & $z=1.5$ m and $x=0.6$ m & $z=1.2$ m, respectively. The mixing process was investigated at specific times: (a) $t=1$ s, (b) $t=3$ s, (c) $t=9$ s; and (d) a middle clip showing the final stacking state.

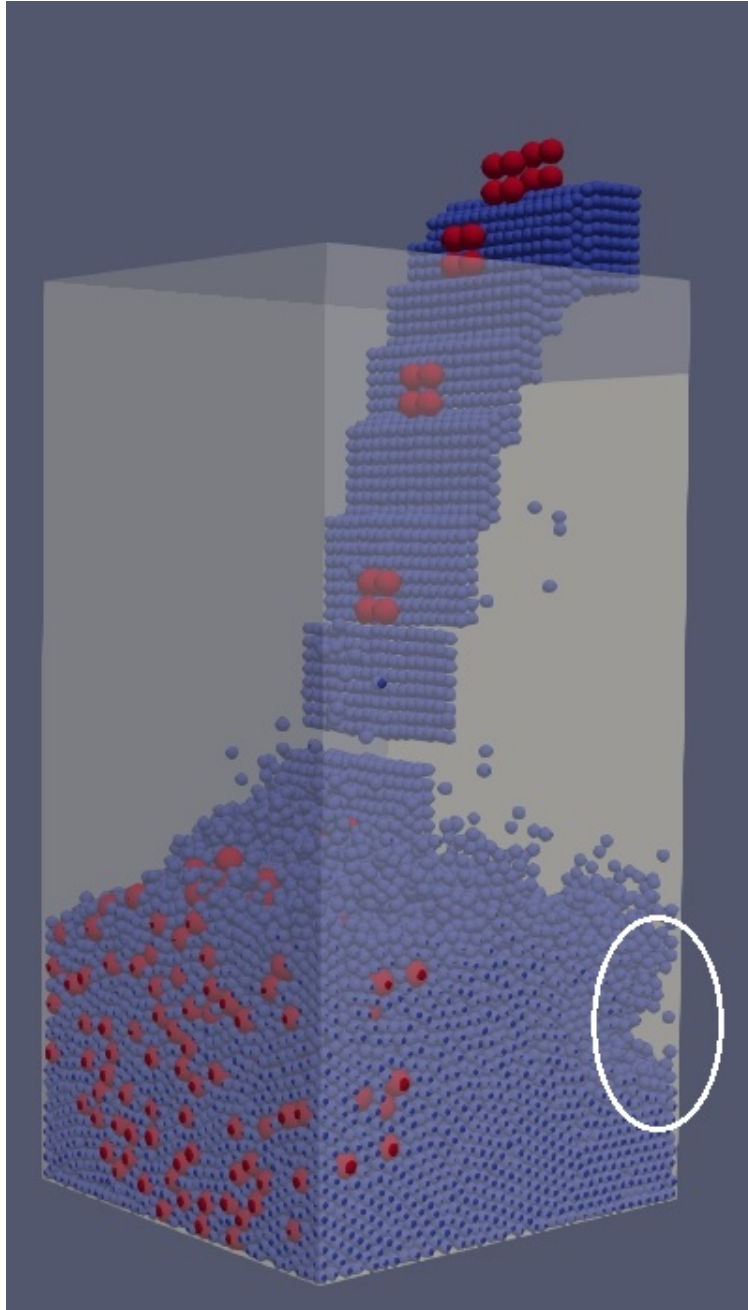
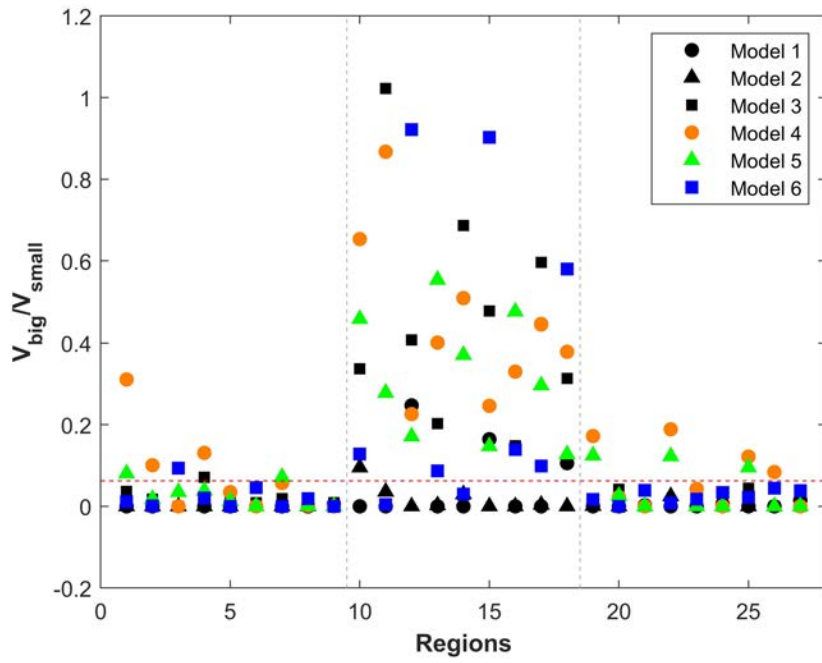
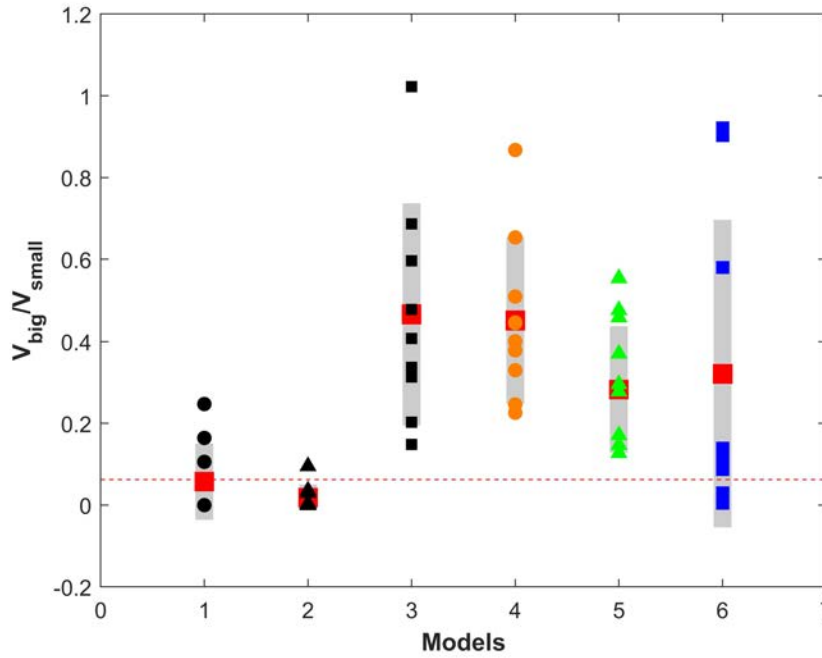


Figure 5-23: An example showing the created void coming from our Model 1 in Group 3

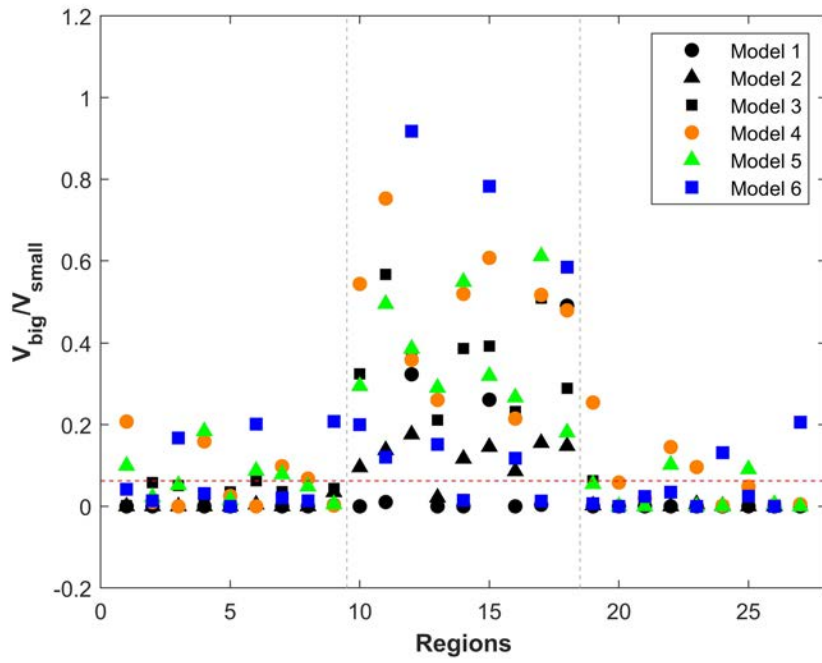


(a) Volume ratios ϕ_v measured in the provided 27 regions

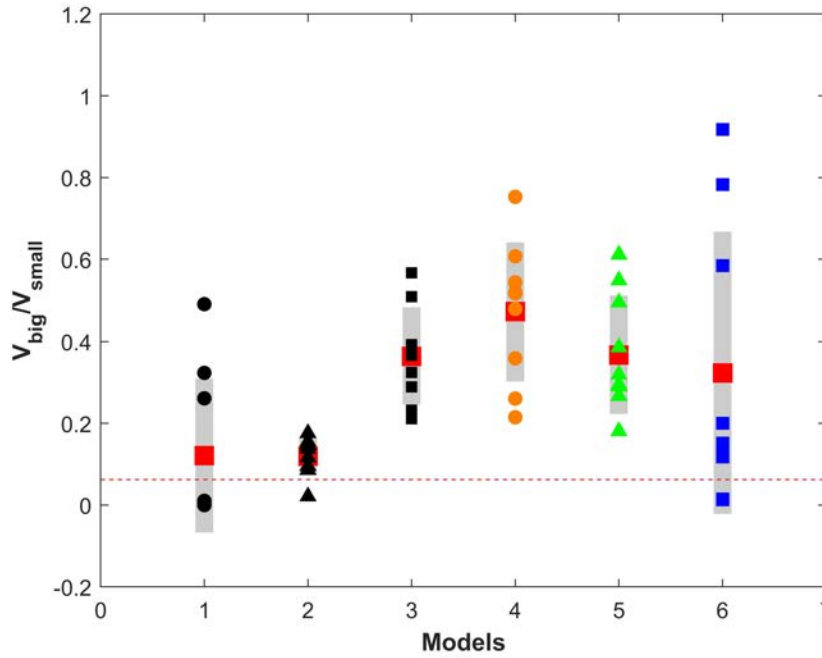


(b) Volume ratios ϕ_v measured at the middle clip

Figure 5-24: The distribution of volume ratio ϕ_v in measured regions for Group 1 mixed with unbonded particles

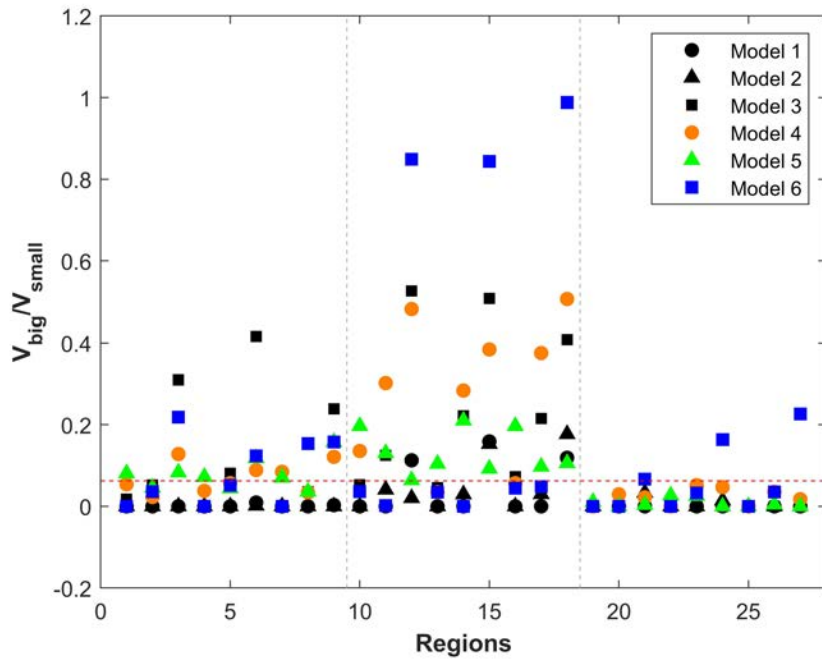


(a) Volume ratios ϕ_v measured in the provided 27 regions

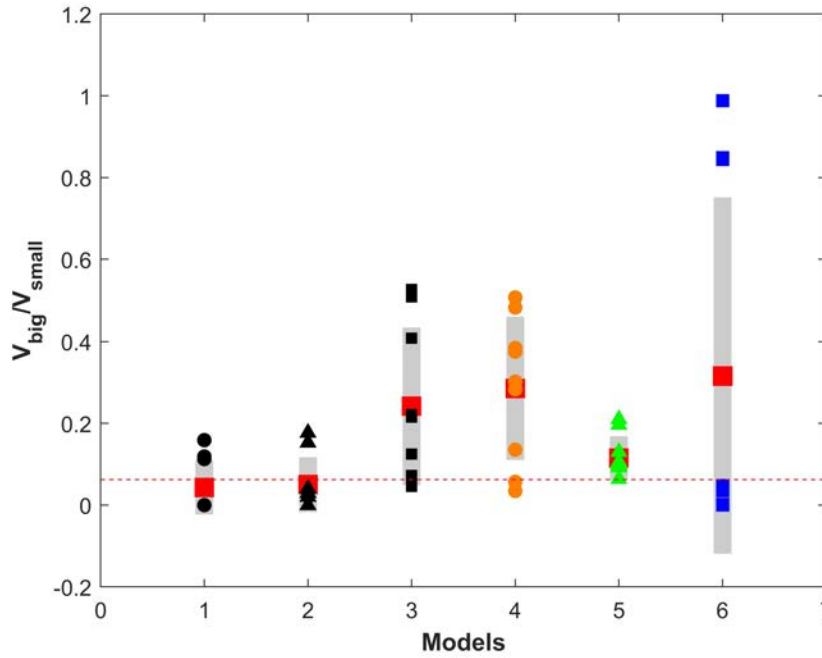


(b) Volume ratio ϕ_v measured at the middle clip

Figure 5-25: The distribution of volume ratio ϕ_v in measured regions for Group 2 mixing with crushable particle simulated using weak bonds

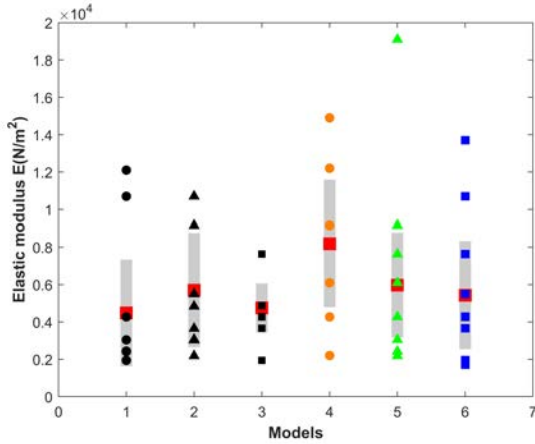


(a) Volume ratios ϕ_v measured in the provided 27 regions

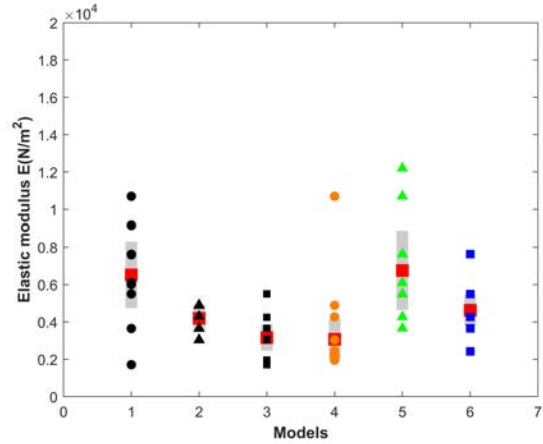


(b) Volume ratios ϕ_v measured at the middle clip

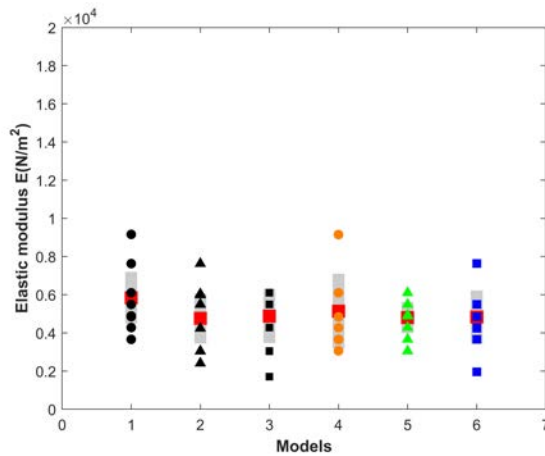
Figure 5-26: The distribution of volume ratio ϕ_v in measured regions for Group 3 mixing with crushable particle simulated using strong bonds



(a) The effective elastic modulus E of six mixing systems in Group 1 which is mixed with crushable particles



(b) The effective elastic modulus E of six mixing systems in Group 2 which is mixed with crushable particles simulated using weak bonds



(c) The effective elastic modulus E of six mixing systems in Group 3 which is mixed with crushable particles simulated using strong bonds

Figure 5-27: The distribution of the effective elastic modulus E measured at the middle clip for the presented three groups

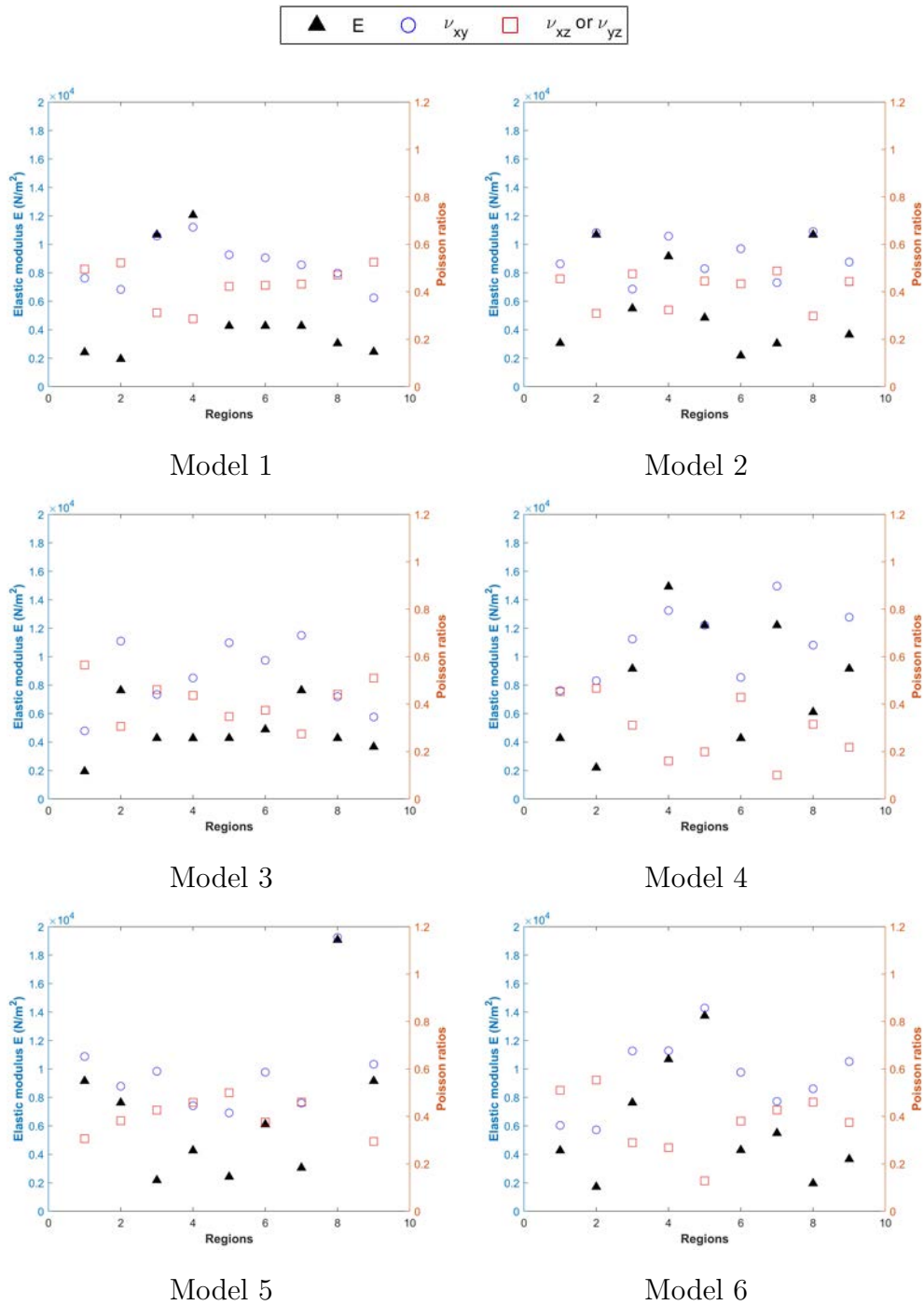


Figure 5-28: The distribution of the calculated effective elastic modulus E and two Poisson ratios ν_{xy} and ν_{xz} for six mixing models in Group 1 as mixed with non-crushable particles

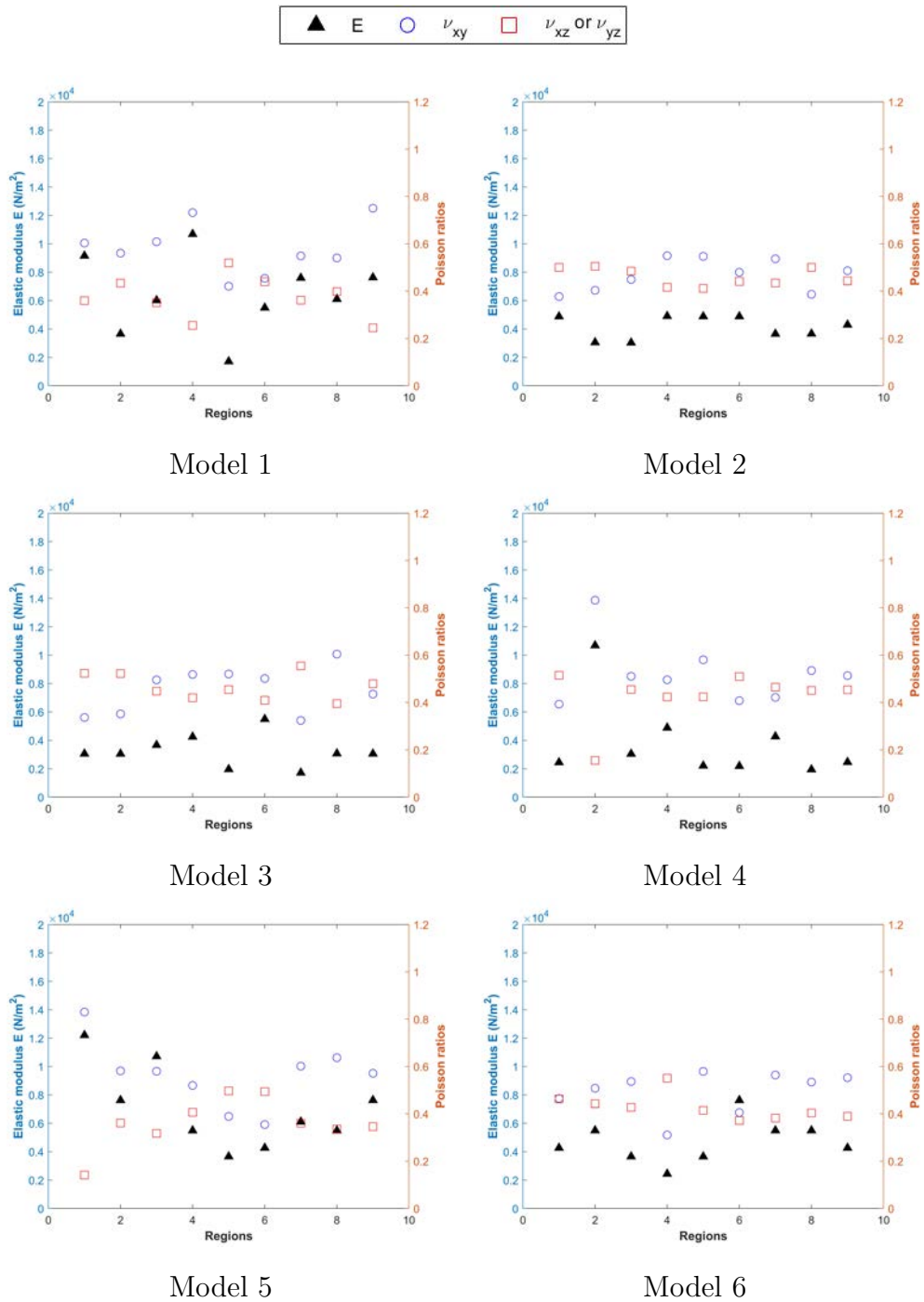


Figure 5-29: The distribution of the calculated effective elastic modulus E and two Poisson ratios ν_{xy} and ν_{xz} for six mixing models in Group 2 as mixed with crushable particles containing weak bonds

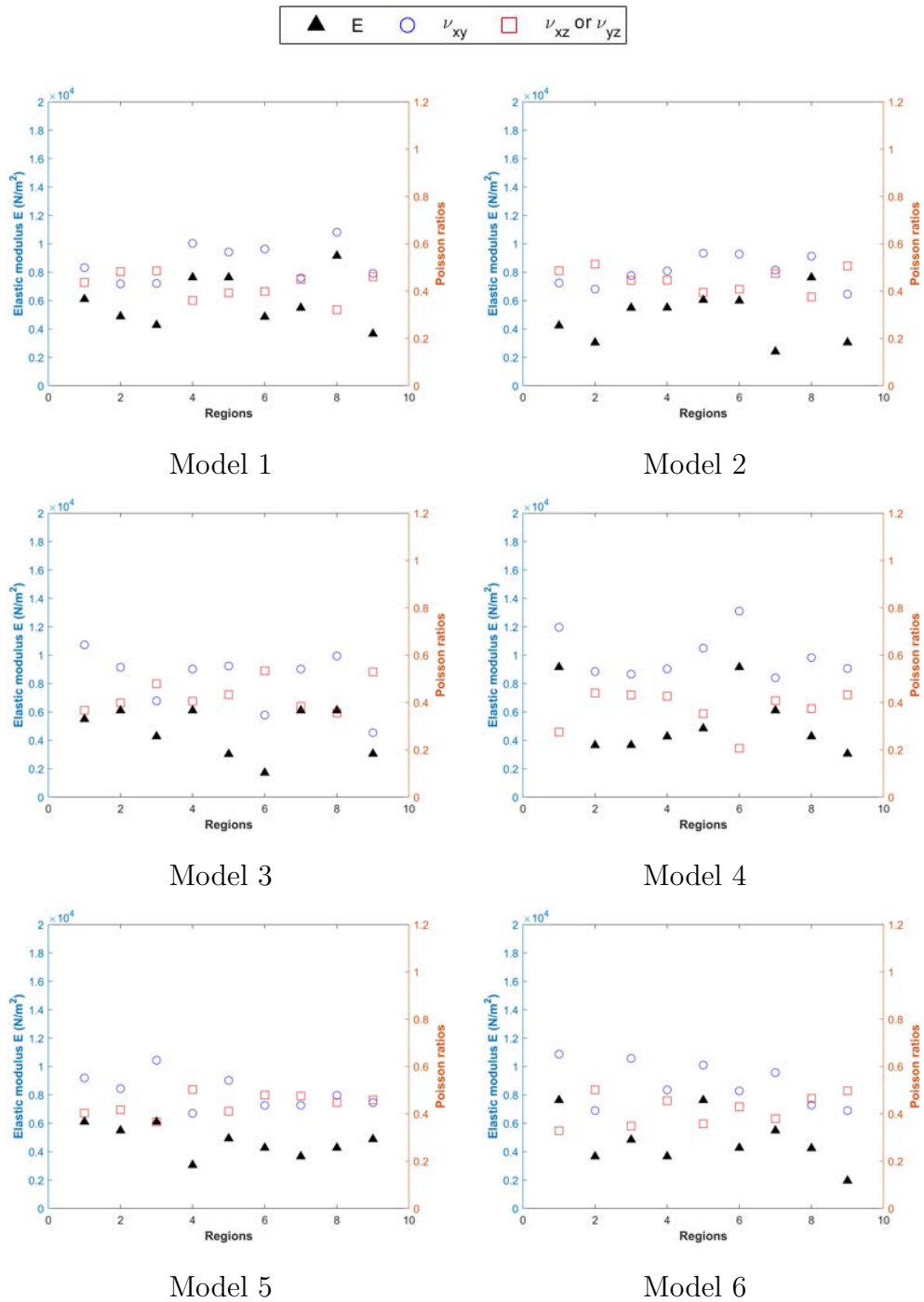


Figure 5-30: The distribution of the calculated effective elastic modulus E and two Poisson ratios ν_{xy} and ν_{xz} for six mixing models in Group 3 as mixed with crushable particles containing strong bonds

CHAPTER 6: SUMMARY OF THE DISSERTATION AND FUTURE STUDIES

6.1 Summary and Conclusions

The goal of this research is to develop a new program to study mixing and mechanical properties of man-made mixtures, quantify the difference within the final aggregates, and propose effective ways to improve the mixing properties to meet engineering requirements for special uses. Consequently, a numerical simulation program built by the Discrete Element Method (DEM) has been given to assist the future studies of binary granular mixtures. This project was completed in three parts.

In Chapter 3, a systematically non-linear visco-elastic damping model has been proposed for detecting non-cohesive contacts and validated with the published results. The analytical solution includes solving particle-particle contacts and a sphere with rigid wall contacts. A general used Hertz model is applied for describing the normal contact force, while an improved non-linear spring tangential model has been introduced for simulating the tangential force response which avoids considering the whole loading history. The rolling friction force caused by surface asperities is considered in this model. The damping force is calculated based on the relative velocity between contact products. In this study, an alternative condition is used for checking the end of a collision that has extended the application of the proposed model to fit the over-damped system. Our numerical results show that the proposed model can successfully recover the tangential force response between the stick and the slip regions. Our DEM results were compared with the authoritative benchmark tests for validation, good performance was achieved. Excellent agreements were achieved for Tests 1,

2, 4, 5 and 7. Slightly difference is contained in Test 3 because different damping models were applied. Since our model can capture the tangential force behavior in the stick region, updated numerical results are provided for Tests 6 and 8.

In Chapter 4, numerical simulations were used to investigate the internal mixing and mechanical properties of binary granular mixtures based on various applied obstacles. The well-developed DEM model which is capable to capture basic mechanical behaviors between particle contacts was employed to simulate the mixing process. The number and position of obstacles and the number of mixing iterations were used to study the effects on mixing properties. A sub-volume algorithm was proposed for calculating the internal mixing parameters and simulated element compression tests were applied for evaluating mixing properties of the final aggregates. In our analysis, we found that the mixing degree of the final deposits can be quantified by measuring the volume ratio ϕ_v . Finally, several useful suggestions were provided to assist full-scale tests, e.g. for a single mixing iteration, the application of fixed geometric mixers can improve the level of mixing by guiding the granular flow. But, the real function of the mixers was determined by whether the mixer acts to direct particle interactions or not. And results show that no matter with or without applying geometric mixers, a well mixing can be achieved after two mixing iterations.

In our Chapter 5, an updated DEM model was applied for determining the effects of using crushable particles on mixing properties. Three groups were generated while the mixing with unbonded spheres was setting as a referenced one for comparison. For each group, six mixing systems were created for studying the effect of applying obstacles. Studies were conducted to investigate the influence of bond strength on mixing ratios and the effective elastic properties of the final composite aggregate. Through the analysis, the study shows

that bond strength is an important parameter for describing the performance of crushable particles. The mixing with crushable particles can effectively improve the mixing by increasing the range of reflection angles, while the increment is associated with the strength in bonds. An increase in bond strength will give a decrease to the effective elastic modulus and simultaneously reduce the level of anisotropy in the final product.

6.2 Future Research

The outcome of this research is limited to the current understanding of binary mixtures, a thorough understanding requires comparing current results with empirical data, refining our DEM model, considering other effects and quantifying their influence. Following research projects are proposed as examples of potential future research.

6.2.1 An advanced study of the proposed Discrete Element Model

In Chapter 3, we validated our DEM model with the published benchmark tests. Good agreement was achieved. We successfully recovered the response of the static friction force, got matching with plenty of experimental results, and proposed the updated results for the tests to assist future studies. However, compared with the empirical data, slightly higher values are obtained in our numerical results in Test 4 with lower incident angles. We hypothesize this is given as a result of the ignored moment resistance. Due to the lack value of the rolling friction coefficient in Chung and Ooi's paper (2011), the relevant comparison cannot be executed through these tests. Otherwise, as the transition zone between the stick and slip regions has been shown, we suppose that for the limited condition, we should have $\mu F_n = \eta F_n$ since sliding is appeared at the same point. The sliding is given as a function

of the surface roughness and the matching velocity at the contact. To address our concerns, we can either measure the dynamic friction coefficient and the rolling friction coefficient to see whether they are co-linear with each other, or redrawn this figure to see after accounting the moment resistance how much influence can have over the plotting.

6.2.2 Effect of particle rearrangement on mixing properties

In our Chapter 4, studies were conducted through the effects of the number and position of obstacles and the number of mixing iterations. In real, studied factors are not limited to these. For example, currently, in our repeated section, particles were layered with big spheres on top. Whereas, in the industry field, rock waste composed of coarse-grained particles in normally placed at the bottom and keep fine-grained particles on the top. Therefore, during the pulling process, smaller particles can travel through the rock surface and consequently promote interacting collisions between them. Perhaps, this is another useful method to improve the mixing. An example illustrates the effect of particle rearrangement on mixing is illustrated in **Figs. 6-1** and **6-2**. In other words, through the proposed DEM program, we can query for any factors we are interested in.

6.2.3 A modification of the parallel bond model

In Chapter 5, the parallel bond model was utilized to study the mixing with crushable particles. Assumed parameters were utilized for bonds to imitate particle crushing. The exact force in bonds are not experimentally checked or quantified here. As clarified by Potyondy and Cundall (2004), their model is more fit for the simulation made of brittle materials. Currently, a connecting bond is described by five parameters as an elastic beam.

To extend the application of their model, a refined version will be provided. Here is our hypothesis. Force in bonds is similar to the capillary forces in unsaturated soil. A sketch of the modified version is given in **Fig. 6-3**.

A bond is still described by currently five parameters ($\bar{\lambda}$, \bar{k}_n , \bar{k}_t , $\bar{\sigma}_c$ and $\bar{\tau}_c$). For previous, we imaged the connecting bond as a beam with the same cross-section. This time, we suppose it looks like a bridge with varied cross-sections. The cohesive capacity $\bar{\lambda}$ is equal to 1 at the ends. There is no change for forces calculated at the ends of this beam. However, when calculating the maximum capacity of a bond, we need to consider the location with the minimum cross-section. In this case, $\bar{\lambda}_c$ is in a function of particles radii and the distance percentage according to each end, where the subscript c is an abbreviation of “critical”. To verify the correction of our model, we can compare our simulated results with a sequence of published single-particle crushing tests.

6.2.4 The quantitative analysis of bond strength on mixing properties of binary mixtures

Through our Chapter 5, we found that the performance of the final composite aggregates is highly determined by the inter-particle bond strength. An increase in this parameter can generate a wider range of reflection angles as particles encountered with geometric mixers and promote the level of mixing in the mixtures. A change in strength can also give an influence to particle crushing percentage. The higher in strength, the lower amount of particle crushing occurs. So, the analysis of the effect of bonded particles on mixing properties is not a univariate problem. With the development of Artificial Intelligence (AI), machines can think like humans and mimic their actions. The application of this technique has pene-

trated into every fields. Machine learning (ML) is a subset of artificial intelligence, that can automatically learn from the trained data and adapt to new data without being assisted by humans. In advance, deep learning (DL) techniques, which is a subset of machine learning, can extract low-level features from testes data, and use deep neural networks (DNN) to form high-level features for doing quantitative analysis and data prediction. In the future, we hope to combine this new technique with the DEM program to quantify the influence of bond strength on mixing properties.

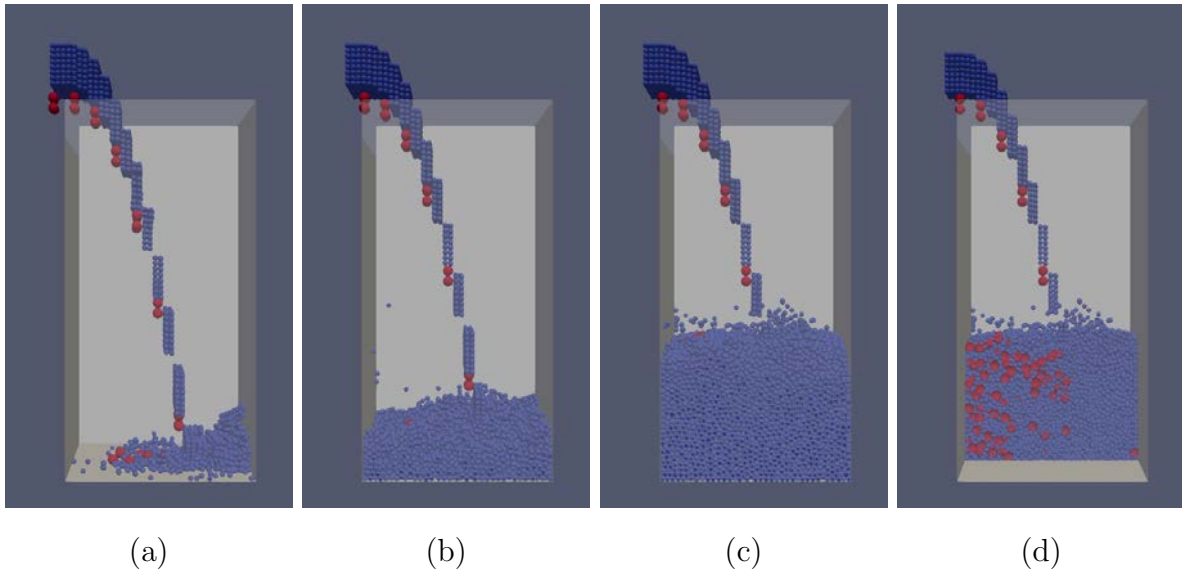


Figure 6-1: A filling under pure gravity deposition bonded with 32 basic spheres using rigid cements is investigated at specific times: (a) $t=1$ s, (b) $t=3$ s, (c) $t=9$ s, and (d) a middle clip showing the final packing state

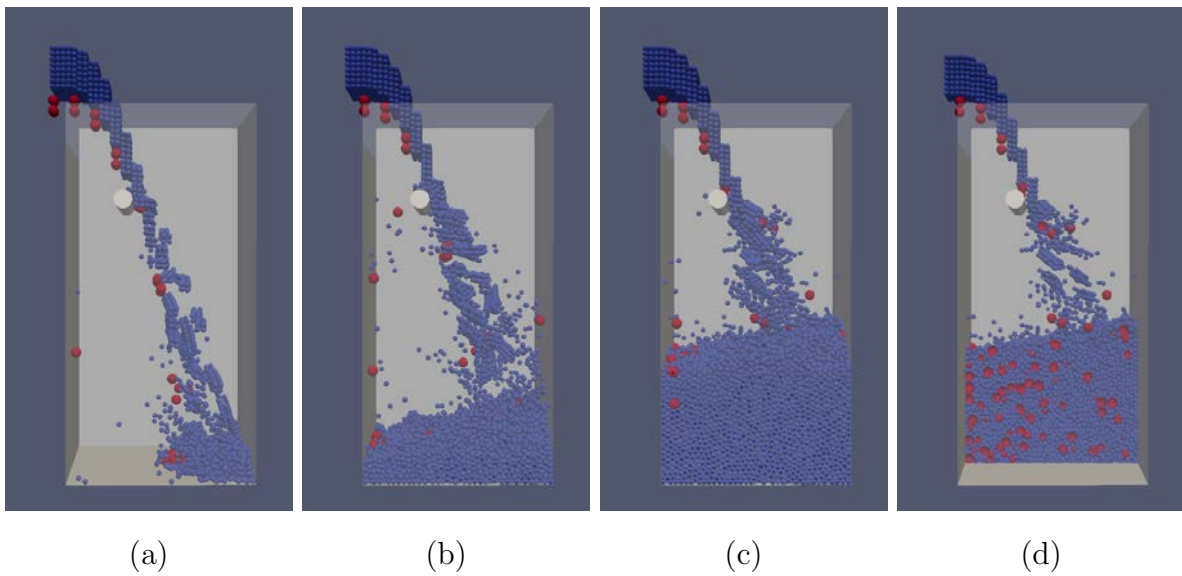
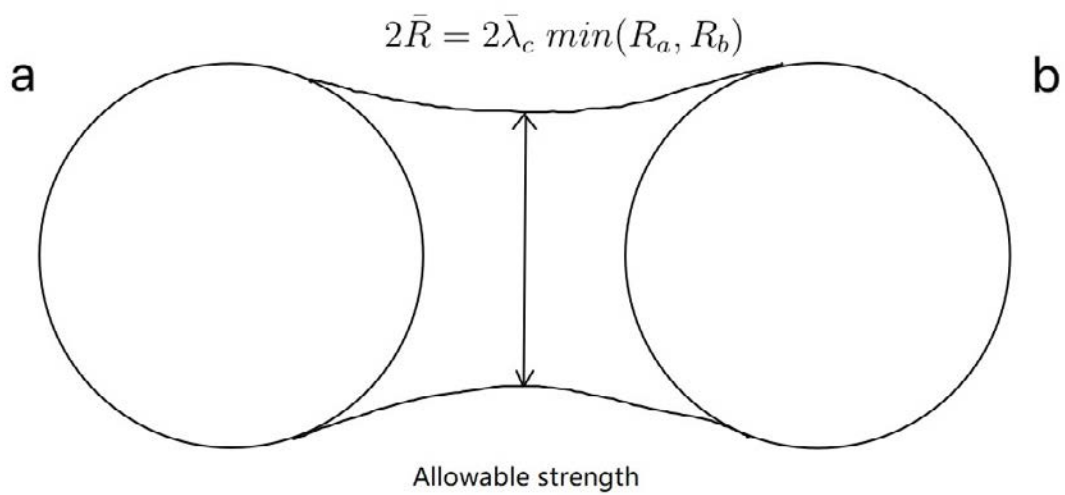


Figure 6-2: A filling under gravity deposition bonded with 32 basic spheres using rigid cements and a obstacle located at $x=0.3$ m & $z=1.5$ m is investigated at specific times: (a) $t=1$ s, (b) $t=3$ s, (c) $t=9$ s, and (d) a middle clip showing the final packing state



$$\bar{\sigma}^{max} = \frac{-\bar{F}_n}{A} + \frac{|\bar{M}_t|\bar{R}}{I}$$

$$\bar{\tau}^{max} = \frac{\bar{F}_t}{A} + \frac{|\bar{M}_n|\bar{R}}{J}$$

Figure 6-3: A modified version for simulating bond behaviors

REFERENCES

- Ai, J., Chen, J.-F., Rotter, J.M., and Ooi, J.Y. (2011). Assessment of rolling resistance models in discrete element simulations. *Powder Technology*, 206, 269-282.
- Bagi, K. (1999b). Stress and strain for granular materials. In M. Oda and K. Iwashita (Eds.), *Introduction to mechanics of granular materials*, A.A. Balkema.
- Bardet, J., and Proubet, J. (1991). A numerical investigation of the structure of persistent shear bands in idealized granular material. *Géotechnique*, 41, 599-613.
- Bagi, K., and Bojtar, I. (2001). Different microstructural strain tensors for granular materials. In N. Bicanic (Ed.), *Proceedings of the Fourth International Conference on Analysis of Discontinuous Deformation, 111-133*. University of Glasgow.
- Bolton, M. D. (1986). The Strength and Dilatancy of Sands, *Géotechnique*, 36(1), 65-78.
- Bono, J.P.D., and McDowell, G.R. (2014). DEM of triaxial tests on crushable sand. *Granular Matter*, 16(4), 551-562.
- Bossy, C., and Safuryn, P. (2016). *What is DEM: Theoretical background behind the Discrete Element Method (DEM)*. Edinburgh, United Kingdom.
- Brendel, L., and Dippel, S. (1998). Lasting contacts in molecular dynamics simulations. In: Hermann, H.J., Hovi, J.-P., Luding, S. (Eds.), *Physics of Dry Granular Media*. Kluwer Academic Publishers, Dordrecht, 313-318.
- Brilliantov, N.V., Spahn, F., Hertzsch, J.-M., and Pöschel, T. (1996). Model for collisions in granular gases. *Physical Review E*, 53(5), 5382-5392.
- Cambou, B., Chaze, M., and Dedecker, F. (2000). Change of scale in granular materials. *European Journal of Mechanics*. Vol. A (Solids), 19, 999-1014.
- Campbell, C. (2006). Granular material flows an overview. *Powder Technology*, 162, 280-229.
- Carolan, A. (2005). *Discrete element modelling of direct shear box tests*. Master's thesis, Imperial College London.
- Casini, F., Viggiani, G.M.B., and Springman, S.M. (2013). Breakage of an artificial crushable material under loading. *Granular Matter*, 15(5), 661-673.
- Cavarretta, I. (2009). *The influence of particle characteristics on the engineering behaviour of sands*. Ph.D. thesis.
- Cavarretta, I., Coop, M., and O'Sullivan, C. (2010). The influence of particle characteristics on the behaviour of coarse grained soils. *Géotechnique*, 60(5), 413-424.
- Cheng, Y., Nakata, Y., and Bolton, M. (2003). Discrete element simulation of crushable soil. *Géotechnique*, 53(7), 633-641.

- Cho, N., Martin, C.D., and Segou, D.C. (2007). A clumped particle model for rock. *Int. J. Rock. Mech. Min. Sci.*, 44(7), 997-1010.
- Choi, W., Son, Y., Park, J., Noh, S. and Bong, T. (2013), An Investigation on Crushing and Particle Size Distribution Characterizes of Bottom Ash as Compaction Energy. *2013 World of Coal Ash (WOCA) Conference*, Lexington, 22-25.
- Chung, Y.C. (2006). Discrete element modelling and experimental validation of a granular solid subject to different loading conditions. *PhD Thesis*, University of Edinburgh, Edinburgh, UK.
- Chung, Y.C., and Ooi, J.Y. (2011). Benchmark tests for verifying discrete element modelling codes at particle impact level. *Granular Matter*, 13, 643-656.
- Cleary, P. (2000). DEM simulation of industrial particle flows: case studies of dragline excavators, mixing in tumblers and centrifugal mills. *Powder Technology*, 109(1-2), 83-104.
- Cundall, P. (1987). Distinct element models of rock and soil structure. In E. Brown (Ed.). *Analytical and Computational Methods in Engineering Rock Mechanics*. Allen and Unwin.
- Cundall, P., and Strack, O. (1979a). A discrete numerical model for granular assemblies. *Géotechnique*, 29(1), 47-65.
- Dabeet, A., Wijewickreme, D., and Byrne, P. (2014). Application of discrete element modeling for simulation of the cyclic direct simple shear response of granular materials. *In: Proceedings of the 10th National Conference in Earthquake Engineering, Earthquake Engineering Research Institute*, Anchorage, AK.
- Delaney, G., Inagaki, S., and Aste, T. (2007). Fine tuning DEM simulations to perform virtual experiments with three dimensional granular packings. In Y. Aste, T. Di Matteo, and A. Tordesillas (Eds.). *Granular and Complex Materials*, 169-185. World Scientific.
- Desu, R.K., Gan, Y.X., Kamlah, M., and Annabattula, R.K. (2021). Compaction mechanics of a polydisperse crushable spherical granular assembly using discrete element method. *International Journal of Advances in Engineering Sciences and Applied Mathematics*, 13(1), 114-121.
- Di Maio, F.P., and Di Renzo, A. (2004). Analytical solution for the problem of frictional-elastic collisions of spherical particles using the linear model. *Chemical Engineering Science*, 59(16), 3461-3475.
- Di Renzo, A., and Di Maio, F.P. (2004). Comparison of contact-force models for the simulation of collisions in DEM-based granular flow codes. *Chemical Engineering Science*, 59, 525-541.
- Di Renzo, A., and Di Maio, F.P. (2005). An improved integral non-linear model for the contact of particles in distinct element simulations. *Chemical Engineering Science*, 60(5), 1303-1312.

- DEM Solutions (2014), *EDEM 2.6 theory reference guide*, Edinburgh, U. K.
- Feng, Hu., Pettinari, M., Hofko, B., and Stang, H. (2015). Study of the internal mechanical response of an asphalt mixture by 3-D discrete element modeling. *Construction and Building Materials*, 77, 187-196.
- Fines, P., Wilson, G.W., Landreault, D., Langetine, L., and Hulett, L. (2003). Co-mixing of tailings, waste rock and slag to produce barrier cover systems. *In Application of Sustainability of Technologies: Proceedings of the 6th International Conference on Acid Rock Drainage (ICARD)*, Cairns, Queensland, Australia, 14-17 July 2003. The AusIMM, Carlton South, Victoria, Australia, 1019-1022.
- Foerster, S.F., Louge, M.Y., Chang, H., and Allia, K. (1994). Measurements of the collision properties of small spheres. *Phys. Fluids*, 6, 1108-1115.
- Gowan, M., Lee, M., and Williams, D.J. (2010). Co-disposal techniques that may mitigate risks associated with storage and management of potentially acid generating wastes. In R.J. Jewell & A.B. Fourie (Eds), *Proceedings of the First International Seminar on the Reduction of Risk in the Management of Tailings and Mine Waste*, Australian Centre for Geomechanics, Perth, 389-404.
- Hertz, H. (1882). Ueber die Berührung fester elastischer Koerper. *Journal für die reine und angewandte Mathematik*, 92, 156-171.
- Itasca (2008). *PFC3D 4.0 Particle Flow Code in Three dimensions*. Theory and Implementation Volume. Minneapolis, Minnesota.
- Iwashita, K. and Oda, M. (1998). Rolling resistance at contacts in simulation of shear band development by DEM. *ASCE Journal of Engineering Mechanics*, 124, 285-292.
- Jardine, R.J., Zhu, B.T., Foray, P., and Yang, Z. X. (2013). Interpretation of stress measurements made around closed-ended displacement piles in sand. *Géotechnique*, 63(8), 613-627.
- Jehring, M.M., and Bareither, C.A. (2016). Tailings composition effects on shear strength behavior of co-mixed mine waste rock and tailings. *Acta Geotechnica*, 11, 1147-1166.
- Jiang, M., Yu, H.S., and Harris, D. (2005). A novel discrete model for granular material incorporating rolling resistance. *Computers and Geotechnics*, 32, 340-357.
- Jia, Y., Xu, B., Chi, S., Xiang, B., and Zhou, Y. (2017). Research on the particle breakage of rockfill materials during triaxial tests. *Int. J. Geomech.*, 17(10), 04017085.
- Khalili, A., Wijewickreme, D., and Wilson, W. (2010). Mechanical response of highly gap-graded mixtures of waste rock and tailings. Part I: monotonic shear response. *Can. Geotech. J.*, 47(5), 552-565.
- Kharaz, A.H., Gorham, D.A., Salman, A.D. (2001). An experimental study of the elastic rebound of spheres. *Powder Technology*, 120(3), 281-291.

- Kruggel-Emden, H., Wirtz, S., and Scherer, V. (2008). A study on tangential force laws applicable to the discrete element method (DEM) for materials with viscoelastic or plastic behavior. *Chemical Engineering Science*, 63, 1523-1541.
- Lade, P.V., Yamamuro, J.A., and Bopp, P.A. (1996). Significant of particle crushing in granular materials. *Journal of Geotechnical Engineering*, ASCE, 122(4), 309-316.
- Leduc, M., Backens, M., and Smith, M.E. (2004). Tailings co-disposal at the Esquel gold mine Patagonia, Argentina. *In Proceedings of the SME annual meeting*, Denver, CO.
- Lim, M.S., Wijeyesekera, D.C., Zainorabidin, A. and Bakar, I. (2012). The Effects of Particle Morphology (Shape and Sizes) Characteristics on its Engineering Behaviour and Sustainable Engineering Performance of Sand. *International Journal of Integrated Engineering*, 4 (4), 27-37.
- Luding, S. (1998). Collisions&Contacts between two particles. In: Herrmann, H.J., Hovi, J.P., Luding, S. (Eds). *Physics of dry granular media-NATO ASI Series E350*. Kluwer, Dordrecht, 285.
- Marketos, G., and Bolton, M. (2010). Flat boundaries and their effect on sand testing. *International Journal for Numerical and Analytical Methods in Geomechanics*, 34, 821-837.
- Manso, J., Marcelino, J., and Caldeira, L. (2018). Crushing and oedometer compression of rockfill using DEM. *Computers and Geotechnics*, 101, 11–22.
- Mao, W., Aoyama, S., and Towhata, I. (2019). A study on particle breakage behavior during pile penetration process using acoustic emission source location. *Geosci. Front.*, 11(2), 413–427.
- Maugis, D. and Pollock, H.M. (1984). Surface forces, deformation and adherence at metal microcontacts, *Acta Metallurgica*, 32(9), 1323-1334.
- Maw, N., Barber, J.R., Fawcett, J.N. (1976). The oblique impact of elastic spheres. *Wear*, 38, 101-114.
- McDowell, G.R., and Bolton, M.D. (1998). On the micromechanics of crushable aggregates. *Géotechnique*, 48(5), 667–679.
- McDowell, G.R., Bolton, M. D., and Robertson, D. (1996). The fractal crushing of granular materials. *J. Mech. Phys. Solids*, 44(12), 2079–2101.
- Mindlin, R. (1949). Compliance of elastic bodies in contact. *ASME Journal of Applied Mechanics*, 16, 259-269.
- Mindlin, R. and Deresiewicz, H. (1953). Elastic spheres in contact under varying oblique forces. *ASME Journal of Applied Mechanics*, 20,327-344.
- Munjiza, A. (2004). *The combined finite-discrete element methods*. John Wiley&Sons Ltd., Chichester, UK.

- Nie, Z., Zhu, Y., Zou, J., Gong, J., and Liu, S. (2019). DEM study of the microscopic characteristics and internal stability of binary mixtures. *Powder Technology*, 352, 314-324.
- Ning, Z., and Ghadiri, M. (1996). Incorporation of Rayleigh damping into TRUBAL and determination of the critical time step.
- Okada, Y., Sassa, K., and Fukuoka, H. (2004). Excess pore pressure and grain crushing of sands by means of undrained and naturally drained ring-shear tests. *Eng. Geol.*, 75(3-4), 325-343.
- O'Sullivan, C. (2011). *Particulate discrete element modelling: A geomechanics perspective*, Spon Press (an imprint of Taylor & Francis), London.
- O'Sullivan, C., and Bray, J. (2002). Relating the response of idealized analogue particles and real sands. *In Numerical Modelling in Micromechanics via Particle Methods*, 157-164. A. A. Balkema.
- Potyondy, D.O., and Cundall, P.A. (2004). A bonded-particle model for rock. *International Journal of Rock Mechanics and Mining Sciences*, 41(8), 1329-1364.
- Rahman, M., Shinohara, K., Zhu, H.P., Yu, A.B., and Zulli, P. (2011). Size segregation mechanism of binary particle mixture in forming a conical pile, *Chemical Engineering Science*, 66, 6089-6098.
- Russell, A. R. and Einav, I. (2013). Energy Dissipation from Particulate Systems Undergoing a Single Particle Crushing Event. *Granular Matter*, 15(3), 299-314.
- Shahnazari, H. and Rezvani, R. (2013). Effective Parameters for the Particle Breakage of Calcareous Sands: An Experimental Study. *Engineering Geology*, 159, 98-105.
- Sun, Z., Tang, H., NicolasEspinoza, D., Balhoff, M.T., and Killough, J.E. (2018). Discrete element modeling of grain crushing and implications on reservoir compaction. *Journal of Petroleum Science and Engineering*, 171, 431-439.
- Tapias, M., Alonso, E.E., and Gili, J. (2015). A particle model for rockfill behavior. *Gaceteo de Ingeniería*, 65(12), 975-994.
- Tarantino, A. and Hyde, A.F.L. (2005). An Experimental Investigation of Work Dissipation in Crushable Materials. *Géotechnique*, 55(8), 575-584.
- Teufelsbauer, H., Hübl, J., and Wu, W. (2009). A Revision of the Linear-Dashpot Model Applied in PFC, *Contemporary Engineering Sciences*, 2(4), 165-178.
- Thornton, C. (2000). Numerical simulations of deviatoric shear deformation of granular media. *Géotechnique*, 50(1), 43-53.
- Thornton, C., and Antony, S. (2000). Quasi-static shear deformation of a soft particle system. *Powder Technology*, 109, 179-191.
- Timoshenko, S.P., and Goodier, J.N. (1970). *Theory of Elasticity*. 3rd edn. McGraw-Hill,

New York.

- Tomas, J. (1999). *Proc. Int. Symp. on Reliable Flow of Particulate Solids III*, 641-656, Porsgrunn.
- Tomas, J. (2003). Mechanics of nanoparticle adhesion—a continuum approach. In: Mittal, K.L. (Ed.), *Particles on Surfaces 8: Detection Adhesion and Removal*. VSP, New York, 1-47.
- Tsuji, Y., Tanaka, T., and Ishida, T. (1992). Lagrangian numerical simulation of plug flow of cohesionless particles in a horizontal pipe. *Powder Technology*, 71, 239-250.
- Vallejo, L.E. (2001). Interpretation of the limits in shear strength in binary granular mixtures. *Can. Geotech. J.*, 38(5), 1097-1104.
- Vallejo, L.E., and Mawby, R. (2000). Porosity influence on the shear strength of granular material-clay mixtures. *Engineering Geology*, 58(2), 125-136.
- Vu-Quoc, L., and Zhang, X. (1999). An elastoplastic contact force-displacement model in the normal direction: displacement-driven version. *Proc. R. Soc. Lond. Ser. A*, 455, 4013-4044.
- Vu-Quoc, L., Zhang, X., and Walton, O. (2000). A 3-D discrete element method for dry granular flows of ellipsoidal particles. *Comput. Methods Appl. Mech. Engrg.*, 187, 483-528.
- Walton, O., and Braun, R. (1986). Viscosity, granular-temperature and stress calculations for shearing assemblies of inelastic, frictional disks. *Journal of Rheology*, 30(5), 949-980.
- Wensrich, C.M., and Katterfeld, A. (2012). Rolling friction as a technique for modelling particle shape in DEM. *Powder Technology*, 217, 409-417.
- Wickland, B.E., Wilson, G.W. (2005). Self-weight consolidation of mixtures of mine waste rock and tailings. *Can. Geotech. J.*, 42(2), 327-339.
- Wickland, B., Wilson, G.W., and Johnson, G. (2003). A meso-scale column test for co-mixed tailings and waste rock. In *Application of Sustainability of Technologies: Proceedings of the 6th International Conference on Acid Rock Drainage (ICARD)*, Cairns, Queensland, Australia, 14-17 July 2003. Australian Institute of Mining and Metallurgy, Carlton South, Victoria, Australia, 1171-1173.
- Wickland, B.E., Wilson, G.W., Wijewickreme, D. (2010). Hydraulic conductivity and consolidation response of mixtures of mine waste rock and tailings. *Can. Geotech. J.*, 47(4), 472-485.
- Wickland, B.E., Wilson, G.W., Wijewickreme, D., and Klein, B. (2006). Design and evaluation of mixtures of mine waste rock and tailings, *Can. Geotech. J.*, 43(9), 928-945.
- Williams, D.J., Wilson, G.W., and Panidis, C. (2003). Waste rock and tailings mixtures as a possible seal for potentially acid forming waste rock. In *Application of Sustainability*

- of Technologies: Proceedings of the 6th International Conference on Acid Rock Drainage (ICARD)*, Cairns, Queensland, Australia, 14-17 July 2003. The AusIMM, Carlton South, Victoria, Australia, 427-436.
- Wilson, W.G. (2001). Co-disposal of tailings and waste rock. *Geotechnical News*, 19, 44-49.
- Wilson, G.W., Newman, L.L., and Ferguson, K.D. (2000). The co-disposal of waste rock and tailings. *In Proceedings of the 5th International Conference on Acid Rock Drainage (ICARD)*, Denver, Colo., 21-24 May 2000. Society for Mining, Metallurgy, and Exploration Inc, Littleton, Colo., 2, 789-796.
- Wilson, G.W., Plewes, H.D., Williams, D., and Roberston, J. (2003). Concepts for co-mixing of tailings and waste rock. *In Proceedings of the 6th International Conference on Acid Rock Drainage (ICARD)*, Cairns, QLD, 437-443.
- Wu, C.Y., Thornton, C., and Li, L.Y. (2003). Coefficients of restitution for elastoplastic oblique impacts. *Adv. Powder Technol.*, 14, 435-448.
- Xiao, Y., Liu, H., Ding, X., Chen, Y., Jiang, J., and Zhang, W. (2016). Influence of particle breakage on critical state line of rockfill material. *Int. J. Geomech.*, 16(1), 04015031.
- Xiao, Y., Meng, M., Daouadji, A., Chen, Q., Wu, Z., and Jiang, X. (2020). Effects of particle size on crushing and deformation behaviors of rockfill materials. *Geosci. Front.*, 11(2), 375-388.
- Xu, D., Tang, Z., and Zhang, L. (2019). Interpretation of coarse effect in simple shear behavior of binary sand-gravel mixture by DEM with authentic particle shape. *Constr. Build. Mater.*, 195, 292-304.
- Yasufuku, N., and Hyde, A.F.L. (1995). Pile end-bearing capacity in crushable sands. *Géotechnique*, 45(4), 663-676.
- Zeghal, M. (2009). The impact of grain crushing on road performance. *Geotech Geol Eng*, 27(4), 549-558.
- Zhang, X., and Vu-Quoc, L. (2002). Modeling the dependence of the coefficient of restitution on the impact velocity in elasto-plastic collisions. *Int. J. Impact Eng.*, 27, 317-341.
- Zhao, H.F., and Zhang, L.M. (2013). Effect of coarse content on shear behavior of unsaturated coarse granular soils. *Can. Geo. J.*, 51(12), 1371-1383.
- Zhou, W., Wu, W., Ma, G., Ng, T., and Chang, X. (2015). Undrained behavior of binary granular mixtures with different fines contents. *Powder Technology*, 340, 139-153.
- Zhu, H., Zhou, Z., Yang, R., and Yu, A. (2007). Discrete particle simulation of particulate systems: Theoretical developments. *Chemical Engineering Science*, 62(13), 3378-3396.